UNDERSTANDING THE HUMAN SUBCORTEX

USING ULTRA-HIGH FIELD MRI AND
COMPUTATIONAL COGNITIVE MODELS

Gilles de Hollander

UNDERSTANDING THE HUMAN SUBCORTEX USING ULTRA-HIGH FIELD MRI AND COMPUTATIONAL COGNITIVE MODELS

GILLES DE HOLLANDER

UNDERSTANDING THE HUMAN SUBCORTEX USING ULTRA-HIGH FIELD MRI AND COMPUTATIONAL COGNITIVE MODELS

PROMOTIECOMMISSIE

| **Promotor** | Prof. dr. B.U. Forstmann | Universiteit van Amsterdam |
| **Copromotor** | Dr. L. van Maanen | Universiteit van Amsterdam |

Overige leden	Dr. P.L. Bazin	Max Planck Institute, Leipzig
	Prof. dr. T. H. Donner	University Medical Centre, Hamburg
	Prof. dr. K. R. Ridderinkhof	Universiteit van Amsterdam
	Dr. J.B. Rowe	University of Cambridge, United Kingdom
	Prof. dr. R. Turner	Universiteit van Amsterdam
	Dr. L. J. Waldorp	Universiteit van Amsterdam

| **Faculteit** | Faculteit der Maatschappij– en Gedragswetenschappen |

CONTENTS

1

INTRODUCTION

AN EXCITING TIME FOR NEUROSCIENCE

This thesis was written in an exciting time for human neuroscience. Key technologies such as structural and functional MRI (Ogawa et al., 1990), genomics (International Human Genome Sequencing Consortium, 2004), and machine learning (Bishop, 2006) have rapidly developed in recent years. We can now functionally image the human brain non-invasively with sub-millimeter precision (van der Zwaag et al., 2016), quantify the influence of Neanderthal DNA on the phenotype of the human brain (McCoy et al., 2017), and reconstruct natural movies from BOLD activity in the visual cortex of human subjects (Nishimoto et al., 2011). These technological developments coincided with a general, explosive increase of computational power and data storage capabilities (Manyika et al., 2011). Furthermore, with its promise of groundbreaking discoveries and societal impact, neuroscience has taken center stage in the public eye. This general interest has not only led to a plethora of popular neuroscience books, but also to some very large neuroscience funding initiatives (Markram, 2012; Insel et al., 2013).

A prominent synthesis of this rapid technological development, increased computational power and large funding efforts can be seen in the completion of the Human Connectome Project (HCP; Van Essen et al., 2013). In this 5-year project, over 1200 subjects were scanned using state-of-the-art MRI. High-quality structural MRI, resting state fMRI, task fMRI, as well as diffusion-weighted MRI data were collected, at a cost of approximately 30 million dollars (Glasser et al., 2013; 2016b). Glasser and colleagues (2016a) combined these data to construct a new, big data-driven parcellation of the human brain into 180 functionally and structurally distinct regions, one of the holy grails of human neuroscience (Brodmann, 1909; Nieuwenhuys, 2012). Curiously, however, the parcellation by Glasser and colleagues considered only the very outside of the human brain: the cerebral cortex (see Fig. 1). It ignored other key parts of the telencephalon, such as the striatum (part of the basal ganglia), as well as the five other main regions of the human brain: the cerebellum, diencephalon, mesencephalon, pons, and medulla oblongata (from here cerebellum and "subcortex"; Kandel et al., 2000).
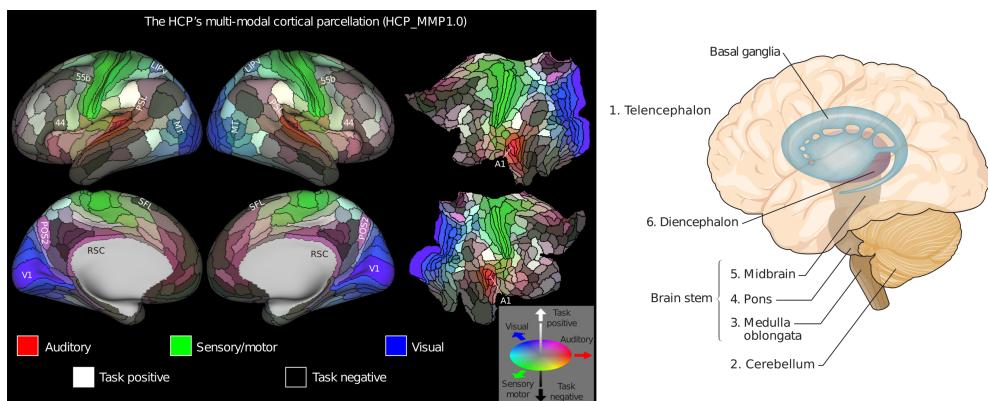
Figure 1. Left panel) a multi-modal parcellation of the human cerebral cortex into 180 areas per hemisphere (Glasser et al., 2016a). Note that parts of the telencephalon, as well as all of the diencephalon and mesencephalon are not ascribed to any specific parcel (light grey). The cerebellum, pons and medulla oblongata are completely absent from the picture. Adapted from Glasser et al. (2016a) **Right Panel)** The six main regions of the brain. Adapted from Kandel et al. (2000).

The complete absence of subcortex in the parcellation scheme of Glasser et al. fits in a larger trend in human neuroimaging and in particular in the expanding field of *human connectomics* (the study of connectivity patterns across the human brain; Behrens and Sporns, 2012; Sporns, 2013). Heidi Johansen-Berg, one of the leading figures in the field, noted this already in a 2013 article on the future of human connectome research: "One curious feature of many connectome studies is that they focus only on regions of the cerebral cortex, ignoring subcortical or cerebellar structures." (Johansen-Berg, 2013).

THE IMPORTANCE OF SUBCORTEX

So why is subcortex so often ignored in neuroimaging studies of the human brain? A first answer that might come to mind is that the subcortex is simply not that important. A persistent misconception is that "what makes us human" is our large cerebral cortex (Rakic, 2009). The human cerebral cortex, however, is actually not that exceptional (Finlay and Workman, 2013). Indeed, the *relative mass* of cerebral cortex is slightly larger than in other primates (approximately 75 – 84% versus approximately 73% in the chimpanzee; Herculano-Houzel, 2012). However, the relative *number of neurons* in cerebral cortex compared to subcortex and the cerebellum is similar to that of other primates (approximately 19% of neurons are in the cerebral cortex; Azevedo et al., 2009). In line with these results, recent work in genomics has shown that the biggest difference in gene regulation between humans and other primates can be found in the cerebellum and subcortex, and the smallest difference in gene regulation is actually found in the cerebral cortex (Vermunt et al., 2016; McCoy et al., 2017). Work from neuroanatomy has shown that 'higher order' areas in the prefrontal cortex, where our superior cognitive resources are presumably located (Fuster, 2001), are densely interconnected with the subcortex in cortico-subcortical loops and that these loops are necessary for higher-order cognition (Alexander et al., 1986; Bhatia and Marsden, 1994; Middleton and Strick, 1994; 2000; 2001; 2002).

When we consider some of the most successful models of human brain function, and their clinical relevance, it also seems ill-advised to ignore the subcortex. For example, a central function of the brain is to learn from the consequences of its actions and adapt future behaviour accordingly (Sutton and Barto, 1998; Glimcher, 2004). A vast literature now shows that dopaminergic nuclei in the subcortex, such as the ventral tegmental area (VTA) and the subtantia nigra, pars compacta (SNc), play a key role in such learning mechanisms (Schultz et al., 1997; Glimcher, 2004; Niv, 2009). Unsurprisingly, the dopaminergic system is also thought to play a role in multiple psychiatric disorders, such as addiction (Di Chiara and Bassareo, 2007) and schizophrenia (Brisch et al., 2014).

Another central function of the brain, next to learning from action, is the selection, chunking, and inhibition of (in)appropriate actions. The basal ganglia, a network of subcortical nuclei, are considered crucial for these processes (Mink, 1996; Graybiel, 1998; Redgrave et al., 1999; Aron and Poldrack, 2006; Frank, 2006). Impaired functioning of the basal ganglia is at the core of multiple movement disorders, such as Parkinson's Disease (PD; Obeso et al., 2008) and an important therapy in the later stages of PD is deep brain stimulation (DBS) of a specific node of the basal ganglia, the subthalamic nucleus (STN; Limousin et al., 1995; Fasano and Lozano, 2015). Surprisingly, after 30 years of clinical use, the underlying mechanism of DBS are still poorly understood (Montgomery and Gale, 2008; Montgomery, 2012; Ineichen et al., 2014). By 2030 almost 10 million people worldwide will suffer from PD (Dorsey et al., 2007). Clearly, the

subcortex is an essential part of the human brain and a better understanding of human subcortex will be crucial in any holistic model of human brain functioning in both health and disease.

THE PROBLEM WITH SUBCORTEX

As we have seen, subcortex is often ignored in human neuroimaging, but this is most likely not because it is not important to study. The reason for its underrepresentation in the MRI literature is probably a merely technical one: subcortical nuclei are much harder to structurally image and parcellate, compared to cerebral cortex. As it turns out, cerebral cortex, unlike subcortex, has some properties that are desirable for structural imaging and parcellation. First, the borders of the cortical sheet are easily identifiable on standard (T1-weighted) structural MRI sequences, because of its good contrast between gray matter (GM), white matter (WM), and cerebral spinal fluid (CSF; Ashburner and Friston, 1997). Furthermore, all of cerebral cortex follows a specific architecture that can be modelled as a folded sheet (Fischl et al., 2004; Glasser et al., 2014), effectively reducing its parcellation to a 2D problem (Glasser et al., 2016a, but see Polimeni et al. (2010) for recent efforts on cortical lamination). Consequently, although the "final" parcellation of cerebral cortex is still a matter of debate (Vogt and Vogt, 1903; Brodmann, 1909; Eickhoff et al., 2005; Nieuwenhuys, 2012; Glasser et al., 2016a), many of the cortical parcellations that have been proposed are readily available in free-to-use packages for neuroimaging research (Fischl et al., 2002; Eickhoff et al., 2005; Heckemann et al., 2006; Shattuck et al., 2008).

For subcortical nuclei, the situation is very different. The borders of these nuclei are often not visible on conventional T1-weighted images, because these borders are not always defined by WM or CSF. Also, the nuclei do not lie on a common cortical sheet, so they need a volumetric (3D) definition rather than a 2D definition (Glasser et al., 2013). To make matters worse, subcortical nuclei are relatively small. They have a volume of only a few dozen up to a few hundred cubic millimeters (Keuken et al., 2014a). When such nuclei are imaged using static MRI protocols, which only look at the structure of the brain, the smallest discrete elements of these images, the "voxels", have a volume of approximately 1 cubic millimeter at conventional field strengths. However, when a researcher is interested in the function of these nuclei and uses dynamic, "functional", protocols, these voxels have a volume of approximately 27 cubic millimeters. Evidently, subcortical nuclei are relatively small compared to conventional MRI resolutions and that makes MRI in these regions susceptible to partial volume effects, where a single voxel can cover multiple subcortical nuclei. In light of these challenges, it is also unsurprising that of the 455 subcortical structures that are defined by the Federative International Community on Anatomical Terminology, only approximately 7% is available in free-to-use neuroimaging atlases (Alkemade et al., 2013).

A NEW DAWN FOR SUBCORTICAL RESEARCH?

In sum, structural and functional neuroimaging of subcortical structures could be key to understanding human brain functioning, but has been hindered by technological limitations. Fortunately, the development of ultra-high field MRI (UHF-MRI; MRI at field strengths of 7 T and above; Duyn, 2012) in recent years offers new opportunities for the study of subcortex. The higher signal-to-noise ratio (SNR) at UHF-MRI, compared to conventional field strengths (at 1.5

and 3 T) can be used to increase the resolution of both structural and functional images to potentially less than 1 mm isotropic (van der Zwaag et al., 2016). Furthermore, because of shorter T_2* relaxation times and stronger field susceptibility effects at higher fields, both T_2* and phase contrast increase markedly at UHF, which could especially be helpful for the delineation of subcortical nuclei (Schäfer et al., 2009). Keuken et al. (2014a) showed these benefits of UHF-MRI for subcortex empirically, by successfully delineating the basal ganglia nuclei in individual subjects. Ultrahigh resolution T2*-weighted images (0.5 mm isotropic) were acquired and combined with a quantitative susceptibility mapping approach (QSM; a phase contrast that is sensitive to local field perturbations and is a marker for iron; Schäfer et al., 2011; Stüber et al., 2014). Importantly, the segmentation procedure of Keuken et al. (Keuken et al., 2014a) also paved the way for functional imaging of specific basal ganglia nodes during experimental paradigms (Keuken et al., 2015).

In another landmark study, Weiss et al. (2015) showed that structural UHF MRI in the subcortex can also be performed on post-mortem tissue and collected T_2*-weighted images of a 2x2x2 cm cube of subcortical tissue, including the STN, with an impressive 0.06 mm isotropic resolution. The considerable increase in resolution compared to in vivo imaging was achieved by extending scanning time to 16 hours, which would not be feasible in living subjects. Crucially, MRI of post-mortem tissue can be combined with other, traditional post-mortem techniques, for example immunohistochemistry, where researchers stain specific proteins that can delineate different neuronal cell populations (Borgers et al., 2014). Such histochemical techniques can help to validate the relationship between estimated local quantitative MRI parameters (T1, T2(*), etc.) and microstructural properties of the brain (Stüber et al., 2014). Ultimately, these multimodal data could be used to construct models that map brain microstructure to MRI parameters, potentially bridging the gap between the mesoscale of functional neuroimaging, and the microscale of classical cyto- and myeloarchitectonic approaches (Weiskopf et al., 2015).

THE TRIPARTITE MODEL OF THE STN

One important issue concerning subcortex that has eluded researchers for decades, and where UHF-MRI might be of help, pertains to the functional architecture of the basal ganglia. Tracing studies in monkeys have shown that large parts of the cerebral cortex project into the basal ganglia via its two input nodes: the striatum (Alexander et al., 1986) and the STN (Hartmann-von Monakow et al., 1978). These projections might play an important role in motor control (DeLong and Wichmann, 2007), higher-order cognition (Middleton and Strick, 2000), and even emotional regulation (Kühn et al., 2005; Péron et al., 2013). The projections are topographically organized: projections from specific cortical areas project to specific corresponding areas in the striatum and this topographic organization is, to some extent, preserved throughout a larger cortico-basal ganglia-thalamo-cortical loop, including the globus pallidus (GP), substanita nigra, pars compacta (SNr), and thalamus (Alexander et al., 1986; Alexander and Crutcher, 1990; Parent and Hazrati, 1993). An influential interpretation of this topographic organization is that of "parallel, segregated loops" of the basal ganglia (Alexander and Crutcher, 1990). For example, Alexander and Crutcher (1990) proposed that there are four main loops throughout the basal ganglia: a 'motor' loop, coming from supplementary and primary motor areas, a 'limbic' loop coming from medial orbitofrontal cortex and the anterior part of the cingulate cortex, an 'oculomotor loop' coming from the frontal and supplementary eye fields, and a 'prefrontal' loop coming from lateral prefrontal cortex. Although topographical organization of the cortico-basal

ganglia projections is undisputed, to which extent the information processing throughout these loops is indeed segregated (Percheron and Filion, 1991), how many loops there are (Middleton and Strick, 2000), and to which extent these loops interact (Joel and Weiner, 1994), remain unresolved issues.
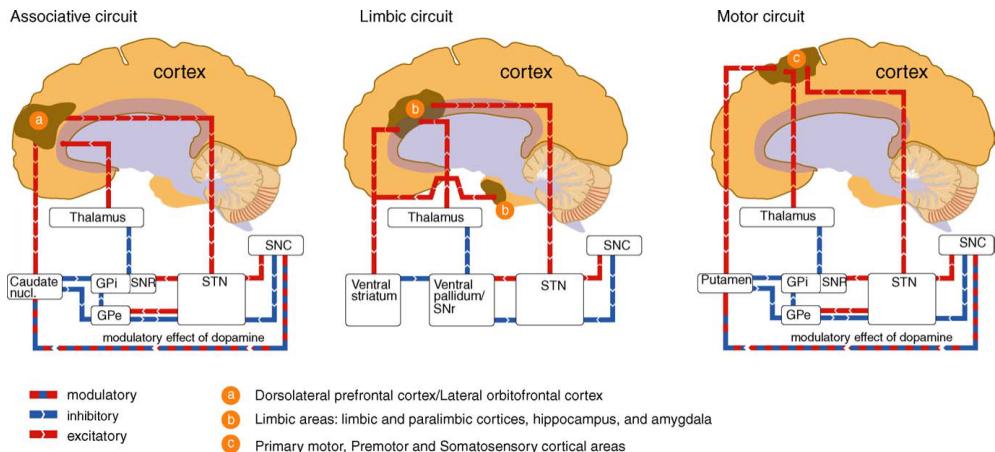

Figure 2. The tripartite model of the STN proposes that the STN takes part in three separate cortico-subcortical circuits that are involved in different functions. Crucially, these loops are represented in separate territories of the STN. The first loop is the associative loop, which is initiated in the dorsolateral and lateral orbitofrontal regions of prefrontal cortex. The limbic circuit is initiated in the hippocampus, amygdala, and limbic and paralimbic cortices. The third circuit is the 'motor' circuit, which originates from premotor, motor and sensorimotor cortices. Adapted from Temel et al. (2005b).

The topographic organization of the basal ganglia also has clinical relevance. As we have seen, DBS of the STN, the smaller input node of the basal ganglia, is an important therapy in later stages of PD (Limousin et al., 1995; Fasano and Lozano, 2015). And although DBS is successful in alleviating motor symptoms of PD (Williams et al., 2014), it can also lead to severe side-effects, including cognitive decline, apathy, and depression (Groiss et al., 2009; Christen et al., 2012; Cyron, 2016). Axonal projections from and into the STN show some topographical organization, just as in other nuclei of the basal ganglia (Parent and Smith, 1987). Temel and coworkers (2005b) proposed that this topological organization can be interpreted as a *tripartite* subdivision of the subthalamic nucleus with a dorsolateral 'motor', central 'associative/cognitive' and ventromedial 'limbic' zone (see Fig. 2). Crucially, Temel and colleagues postulate that 'non-motor' side-effects of DBS are a result of misplacement of the electrode in other parts of the STN than the motor zone (Temel et al., 2005a; 2005c; 2006).

The tripartite STN hypothesis has been corroborated by recent studies using diffusion-weighted MRI (Lambert et al., 2012; Accolla et al., 2014), as well as tracing studies in monkeys (Haynes and Haber, 2013). These structural connectivity studies confirm the topographical organization of the cortical projections into the STN. Furthermore, DBS electrode recordings suggest that neural activity in the "beta"-band, a dominant frequency band in sensorimotor cortical areas, is concentrated in more dorsolateral parts of the STN (Accolla et al., 2016; Horn et al., 2017). Also, there is some evidence that stimulation via the DBS electrode tips that are

located more medioventrally lead to more 'non-motor' side-effects than stimulation via the dorsolateral DBS electrode tips (Mallet et al., 2007; Welter et al., 2014; Accolla et al., 2016).
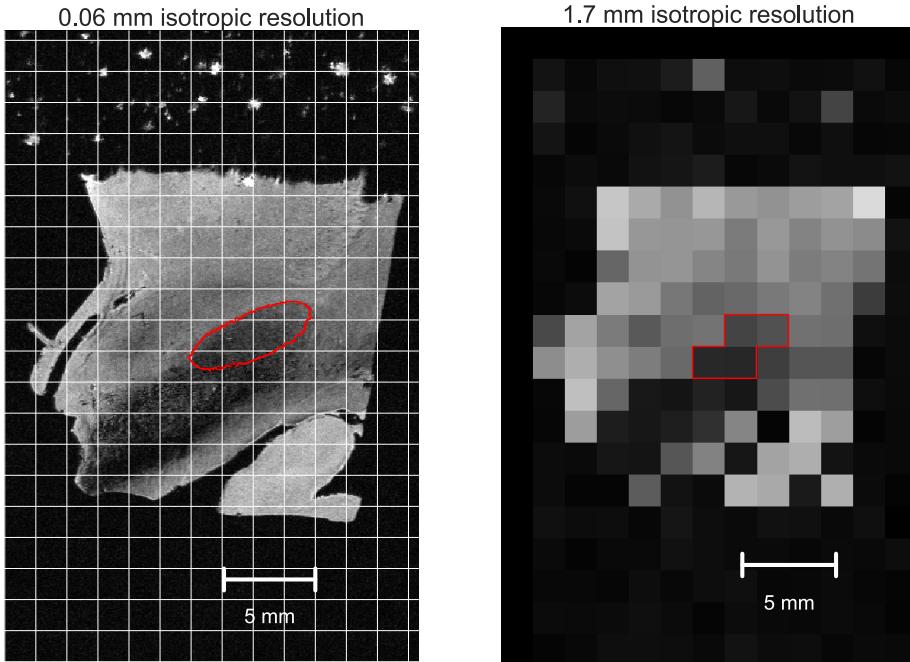
Figure 3. Comparison of an ultra-high resolution 0.06 mm isotropic (coronal) image of a post-mortem tissue block containing the STN, acquired during a 16-hour scan at 7 T (left), and a resampled version at a resolution of 1.7 mm isotropic (on the right). Red lines demarcate the STN. Lambert et al. (2012) and Accolla et al. (2014) used diffusion-weighted MRI data acquired at the latter resolution to infer whether fiber bundles that are adjacent to the STN enter or do not enter the nucleus at specific points. Clearly, partial voluming forms a severe limitation to any such conclusion. White grid in high-resolution image (left) indicate size of 1.7 mm isotropic voxels.

Although recent studies show indirect evidence for the tripartite model of the STN, as summarized above, they should be interpreted with caution. The mentioned DWI studies (Lambert et al., 2012; Accolla et al., 2014) used a resolution of only 1.7 mm isotropic. One could argue that such a resolution is insufficient to resolve whether fiber bundles immediately adjacent to the STN (only a few millimeters long in the dorsal-ventral dimension; see Fig. 3) enter the nucleus or are just passing by. There are major white matter tracts bordering on the STN that do not project into the STN itself. For example, nigrostriatal projections pass through the ventromedial STN, without actually terminating there (Carpenter and McMasters, 1964; Carpenter and Peter, 1972). Similarly, cerebello-rubro-thalamic fibers and the cerebral peduncle, connected to 'associative' and 'motor' cortical regions, pass the STN dorsally, but do not terminate in the STN itself (Martin et al., 1989; Haynes and Haber, 2013; Mai et al., 2015; Contarino et al., 2017). These white matter bundles can cause spurious connections in the tract tracing models used to interpret DWI data (Jones et al., 2013; Thomas et al., 2014). Tracing studies in monkeys also have severe limitations. They provide only a very low numbers of

observations (1-3 animals per cortical area), tend to underestimate the size of termination fields, and cannot always distinguish between passing fibers and terminating fibers (Alkemade, 2013; Haynes and Haber, 2013). Studies employing DBS recordings (Horn et al., 2017) are hindered by considerable difficulty in reliably locating the DBS electrodes. One reason for this is that clinical MRI data is usually acquired at lower fields (Schlaier et al., 2011). In fact, the contact points of DBS electrodes are known to sometimes be located outside the STN (Greenhouse et al., 2013), which might make them unfit for investigation of the functional organization *inside* this nucleus.

In sum, the tripartite model of the STN, although plausible, remains a working hypothesis. There is some indirect evidence for it, but this evidence comes with serious limitations. Ultra-high field MRI, with its superior resolution and potential for functional imaging of the subcortex in action, can offer complementary data that might confirm or refute the tripartite model of the STN.

OUTLINE THESIS

The goal of this thesis was to investigate the internal organization of the STN, using a multidisciplinary approach that includes functional and structural UHF-MRI, immunocytochemistry, and computational cognitive modelling. Specifically, we tried to find evidence for or against the tripartite model of the STN using both structural and functional data. Furthermore, we investigated to which extent potential subdivisions of the STN are overlapping and should be interpreted as functional 'zones' within the STN, rather than discrete subunits. This more nuanced view of a gradual STN organization has gained traction in recent years (Haynes and Haber, 2013; Alkemade and Forstmann, 2014; Lambert et al., 2015). Hopefully, the approaches used and refined in this thesis can also be used in future studies, to help understand also other parts of the vast sea of unchartered subcortical nuclei (Alkemade et al., 2013; Forstmann et al., 2017).

First, **Chapter 2** gives a broader overview of research on the human subcortex using UHF-MRI. It starts with a discussion of the importance of subcortex in the human brain and contrasts its importance with the lack of reliable atlases of subcortical nuclei for MRI research. It then proposes the use of UHF-MRI to study the human subcortex both structurally and functionally and discusses the outstanding technical challenges that hinder such research. Furthermore, we stress the importance of post-mortem validation of MRI contrasts and promote the use of formal cognitive theories to guide the interpretation of neural data. The chapter concludes by highlighting the importance of data sharing, given the considerable costs of high-quality UHF-MRI data.

STRUCTURE OF THE STN

Chapter 3 presents an empirical study that fits in the larger research line laid out in Chapter 2. The study investigates the *structure* of the STN using UHF-MRI in both living subjects and post-mortem samples. Quantitative susceptibility mapping (QSM; Schweser et al., 2011; Langkammer et al., 2012) was used as a proxy for non-heme iron concentration, which is related to cytoarchitecture (Dormont et al., 2004; Fiedler et al., 2007; Massey et al., 2012). Replicating earlier work (Dormont et al., 2004; Massey et al., 2012), we show in four post-mortem samples (0.15 mm isotropic resolution) and thirteen healthy subjects (0.5 mm

isotropic resolution) that iron is heterogeneously distributed throughout the STN. Iron concentration was consistently increased in the anterior, ventromedial tip of the STN compared to more posterior, dorsolateral areas. Furthermore, we tested two alternative formal models of the spatial distribution of iron: one model where there is a sharp transition between areas of high and low iron concentrations ('discrete subdivision hypothesis') and one model where the transition between high and low iron concentrations is more gradual ('gradient hypothesis'). Quantitative analysis of the QSM images and the QSM gradient images suggests that the latter model is more likely, given the data. These results thus speak in favour of overlapping functional zones in the STN, rather than discrete subdivisions.

In **Chapter 4** the structure of the STN is further investigated using an immunoctycochemical approach. Post-mortem samples were scanned using multiple UHF-MRI protocols at ultra-high resolutions (0.06 - 0.2 mm isotropic) and then sectioned and stained using twelve different antibodies. Such antibodies can be used as a proxy for different neuronal populations and could thus demarcate potential subdivisions in the STN. Stained sections were digitally imaged and brought into a common space with the MRI data. We show that different protein markers are consistently expressed in specific parts of the STN, but no clear tripartite organization is evident. Mixture models were fitted to the image intensity distributions of the stainings. The model fits suggest there is no evidence for a specific number of subdivisions. The fits also show that, regardless of their exact number, any potential subdivisions must be highly overlapping. Furthermore, we show that, for some marker proteins, quantitative MRI parameters (T1, T2*, and QSM) can predict staining intensity. This paves the way for forward models that predict cell type and density based on quantitative MRI parameters measured in the STN, potentially *in vivo* (Weiskopf et al., 2015).

FUNCTION OF THE STN

In the remaining chapters, the focus of this thesis shifts from *structural* to *functional* organization of the STN. Are different zones/parts of the STN also involved in different cognitive functions? To answer this question, we needed state-of-the art methodology. Therefore, we first critically reviewed current practices in functional imaging of the STN, developed a 7 T functional imaging protocol optimized to our subcortical needs, and reviewed current model-based cognitive neuroscience approaches to better understand noisy neural activation patterns.

As stated before, the resolution that can be achieved at conventional field strengths of 3 T and below is very limited compared to the size of the STN. A standard resolution for 3 T fMRI is 3 mm isotropic, which amounts to a volume of 27 mm^3 per voxel. That means that the entire STN fits in about 3-5 voxels, ignoring partial volume effects. Still, multiple neuroimaging studies have reported activity in the "STN region" (Aron and Poldrack, 2006). In **Chapter 5**, we present an extensive literature review of such neuroimaging studies at conventional field strengths that report activity in STN and the subtantia nigra (SN). We summarize the reported locations in MNI space, as well as their voxel resolution and the size of used smoothing kernels. We then show, using the probabilistic atlas of Keuken et al. (2014a), that many reported activation coordinates are most likely located outside of the nucleus they are ascribed to. Furthermore, we present simulations that suggest that for most studies that employ smoothing, it becomes impossible to unequivocally assign observed signal changes to a specific basal ganglia node (i.e., STN/SN) and termed this issue the "subcortical cocktail problem". The chapter concludes

with an alternative approach that uses individual anatomical masks without mixing across different anatomical entities.

In **Chapter 6,** a set of 7 T fMRI protocols is compared, to find the optimal combination of scanning parameters that yields robust BOLD sensitivity in the basal ganglia, without sacrificing anatomical specificity. We also compare these protocols to a recently proposed 3 T protocol that has been used to functionally define subdivisions in the substantia nigra (Pauli et al., 2015). We show that standard 7 T fMRI protocols, optimized for cortex, need a reduction of their spatial resolution and echo times, and use only limited parallel imaging, to obtain robust BOLD sensitivity in the subcortex. Our implementation of the 3 T protocol by Pauli et al. (2015) did not show acceptable SNR in the subcortex.

In model-based cognitive neuroscience, formal, mathematical models are used to explain behaviour and quantify interindividual differences in meaningful psychological constructs (Forstmann and Wagenmakers, 2015). For example, sequential sampling models such as the diffusion decision model (DDM; Forstmann et al., 2016) can decompose reaction time distributions and response accuracies of individual subjects into meaningful latent variables such as the rate of information accumulation, response bias, and cautiousness. Recent work has shown that across-subject variability in such latent variables can be related to variability in the BOLD activation of distinct brain networks (Mulder et al., 2014; Keuken et al., 2014b). A model-based cognitive neuroscience approach can be especially useful for the interpretation of noisy neural measurements in the STN, by relating different signal components to specific cognitive processes. In **Chapter 7**, we review different approaches of linking computational cognitive models to neural data and propose a descriptive scale for these approaches that goes from 'loose' and qualitative linking to 'tight' and quantitative linking. Concretely, loose links between cognitive models and neural measurements pertain to qualitative predictions by the cognitive model about general patterns in the neural data, whereas tighter links attempt to quantitatively estimate a mathematical mapping between cognitive model parameters and neural measurements.

In **Chapter 8**, we integrate the insights gained in the preceding chapters into an empirical study. This fMRI study used the anatomical ROI-approach without smoothing promoted in Chapter 5, the optimized fMRI protocol from Chapter 6, and the tight quantitative linking model-based approach outlined in Chapter 7, to learn more about the role of potential STN subdivisions during perceptual decision-making. Specifically, we a-priori subdivided the STN in three subdivisions and investigated their role in implementing response biases, how their activity was affected by stimulus difficulty, and whether they showed lateralized motor activity. We present evidence that the whole STN is involved in implementing response biases, but is not affected by stimulus difficulty and shows no lateralized response-related activity. Furthermore, we find no evidence for functional differentiation between the three segments.

Finally, in **Chapter 9**, the preceding chapters are shortly summarized and their implications for models of STN organization, as well as future work, are discussed.

2

TOWARDS A MECHANISTIC UNDERSTANDING OF THE HUMAN SUBCORTEX

The human subcortex consists of hundreds of unique, small grey matter nuclei (Federative Committee on Anatomical Terminology, 1998) which make up approximately 25% of the entire human brain volume (Dunbar, 1992). Importantly, only approximately 7% of these nuclei are currently represented in standard human brain MRI atlases (Alkemade et al., 2013), owing to the technical challenges in imaging these structures. Indeed, the study of basal ganglia networks and nuclei in humans has been frustrated by the fact that these nuclei are difficult to visualize with MRI at field strengths of 3 Tesla (3T) and below because of their small size and close spatial proximity (de Hollander et al., 2015 Fig. 1b).
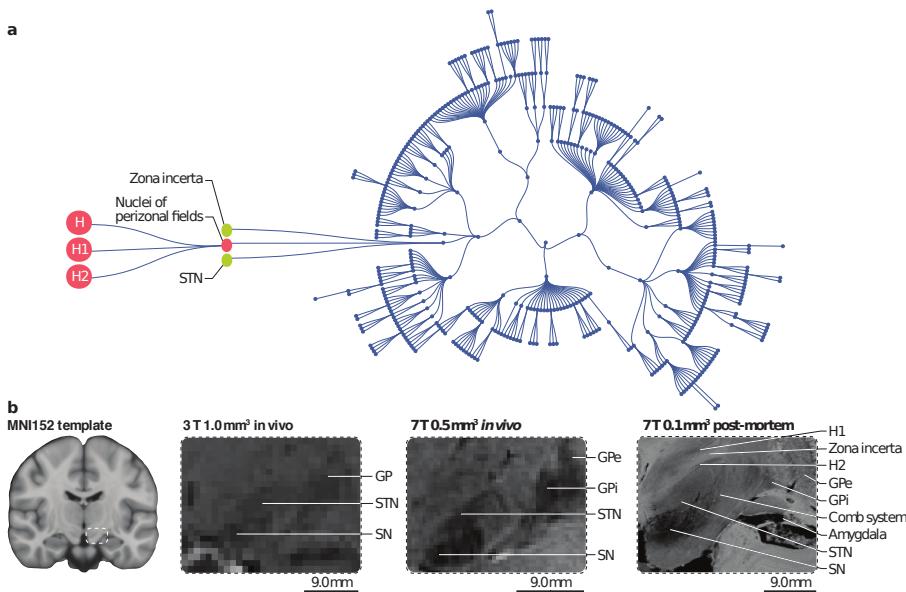
Figure 1. A) Hierarchical tree of the human subcortex. These are the 445 subcortical structures as defined by the FCAT where the outer nodes are nested in the inner nodes. The expanded nodes on the left show three small nuclei (H, H1, H2) which combined are the nuclei of the perizonal fields. The nuclei of the perizonal fields, together with the zona incerta and the subthalamic nucleus combined are the subthalamus. B) Three coronal zoomed in scans displaying the same subcortical region. The in vivo 1mm isotropic resolution 3T T2*-weighted structural MRI scan allows for the identification of the STN, SN, and GP. The in vivo 0.5mm isotropic resolution 7T T2*-weighted structural scan shows increased detail, which now clearly allows the separation of the STN from the SN. The image quality is such that it now also allows the separation of the GPi and GPe. Finally, in the lower right corner, a post mortem 0.1mm isotropic resolution 7T T2*-weighted structural MRI scan. The image allows for clear identification of a number of structures that are not visible in either the 3T or 7T in vivo scans. STN: subthalamic nucleus; SN: substantia nigra; GP: globus pallidus; GPe: globus pallidus externa; GPi: globus pallidus interna.

The human brain may be mapped at three different levels: the macroscopic, the mesoscopic, and the microscopic levels (Amunts and Zilles, 2015). The macroscopic level is measured in centimetres, the scale of large neural networks that spread across the whole brain. The mesoscopic level is measured in millimeters, which is the scale of individual cortical and subcortical nodes, and the microscopic level is measured in micro- and nanometres, which is the scale of individual neurons and neurotransmitters. Here, we argue for an approach that

combines *in vivo* ultra-high field (UHF) 7T MRI, *post mortem* UHF MRI, and *post mortem* histology in a model-based cognitive neuroscience framework to capture neural processes, including decision-making mechanisms, implemented in the human subcortex, ranging from the macroscopic to the microscopic level.

One example of mapping these three levels of the human subcortex comes from the study of the regulatory role of basal ganglia networks in speeded decision-making (Bogacz and Gurney, 2007; Forstmann et al., 2008; van Veen et al., 2008; Bogacz et al., 2010; Forstmann et al., 2012). The relatively well-understood cortico-basal-ganglia-thalamo-cortical loops are particularly important for decision-making processes, including action selection and inhibition (Redgrave et al., 1999; Ding and Gold, 2013). Through the use of the meso- to macroscopic mapping paradigm to assess the role of basal ganglia in action selection, here, we highlight the importance of integrating *in vivo* UHF MRI and post-mortem validation and of placing the resulting data from these approaches into a model-based cognitive neuroscience framework.

We begin by discussing state-of-the art UHF structural MRI and functional MRI (fMRI) technology and how it can be used to map the human subcortex. We then identify and explain techniques to validate MRI data, including those from *post mortem* studies, and end by integrating information from the microscopic, mesoscopic and macroscopic levels into a model-based cognitive neuroscience framework.

IMAGING THE HUMAN SUBCORTEX

Neuroimaging of the human subcortex has been particularly challenging for various reasons. Subcortical nuclei are small, they have particular magnetic properties that hinder anatomical identification and functional imaging, and there has been limited availability of reliable automated parcellation procedures, resulting in a large amount of ambiguous data that must be painstakingly and expertly analysed 'by hand'. Moreover, there has been a lack of validation studies, for example, using *post mortem* specimens, to confirm MRI findings. This hiatus has many potential causes, including the limited availability of human *post mortem* brain specimens, as well as the precariousness of tissue processing, for which the requirements for UHF MRI and histological analyses need to be balanced. Other problems have included a limited knowledge of the function of many subcortical structures, a culture of focusing on cortical structures in MRI-based research (Johansen-Berg, 2013) and the limited availability of UHF MRI scanners and data. Below, we discuss these issues in more depth and offer some potential solutions to improve the imaging, and understanding, of the subcortex.

MRI DATA ACQUISITION.

The subcortex is a highly dense area with many, very small and distinct nuclei (Alkemade et al., 2013) and requires tailored structural MRI contrast images (Keuken et al., 2014a). The use of UHF fMRI combined together with UHF structural MRI increases the spatial specificity that can be achieved compared with 3T approaches (de Hollander et al., 2015). Indeed, previous work directly comparing 3T fMRI with 7T fMRI in subcortical areas indicate that although the latter yields similar activation patterns, it has a higher contrast-to-noise ratio (CNR) and higher spatial specificity (Hale et al., 2010; Hahn et al., 2013; Baecke et al., 2015).

Several studies showed that UHF structural MRI improved the visualization of subcortical structures compared with lower-field strength MRI (Cho et al., 2008; Yao et al., 2009; Cho et al., 2010; Kerl et al., 2012a; 2012b; 2012c; 2013). Several reasons account for this improvement.

The signal-to-noise ratio (SNR) increases linearly with field strength (Edelstein et al., 1986). A high SNR is vitally important as the SNR with structural MRI that can be achieved towards the middle of the brain is substantially lower than the SNR that can be achieved with this technique at the cortical level (Wiggins et al., 2009). It is possible to acquire multiple averages on lower field strengths to improve the SNR. However, this is not always practical as the signal-to-thermal noise ratio with 7T MRI is roughly 2.3 times higher than the value that can be achieved with 3T MRI. This means that to acquire an image on 3T MRI with the same contrast (that is, with the same SNR) as a 7T image, with all else being equal, a 3T MRI scan needs to be roughly 5.3-fold longer (Edelstein et al., 1986). As the scan duration increases, averaging becomes increasingly difficult owing to motion artefacts caused by head movements or internal fluid pulsation, which yield image distortions (Morelli et al., 2011; Federau and Gallichan, 2016). By increasing the SNR, structural imaging with a submillimeter resolution can be achieved and the delineation of small subcortical structures becomes feasible. Benefiting from the SNR gain and optimized MRI sequences, recent *in vivo* UHF MRI studies on the thalamus have yielded promising results, with the visualisation of several thalamic subnuclei (Kanowski et al., 2014; Saranathan et al., 2014; Tourdias et al., 2014).

A further advantage of UHF structural MRI can be seen when standard anatomical T1-weighted scans are acquired. The contrast between white and grey matter is sharper in 7T scans than in 3T scans owing to larger difference in T1 relaxation times between the two tissue types in the former (van der Zwaag et al., 2016).

Finally, the increased sensitivity afforded by UHF structural MRI to small field perturbations, created by the change in composition between different tissues, means that traditional T1-weighted anatomical scans (which are sensitive to white–grey matter boundaries) can be extended with novel contrast mechanisms such as quantitative susceptibility mapping (QSM; Langkammer et al., 2012; Schweser et al., 2016). In QSM, the voxel intensity is linearly proportional to the underlying tissue's magnetic susceptibility, providing a quantitative estimation of iron concentrations (Schweser et al., 2011; Langkammer et al., 2012). As different subcortical nuclei contain different amount of iron and accumulate it at different rates during the adult lifespan (Zecca et al., 2004; Aquino et al., 2009), QSM with high voxel resolution represents an exciting new approach for the visualisation and quantification of the location, shape and morphometric changes of small nuclei (de Hollander et al., 2014a). Indeed, contrast mechanisms such as QSM allow the visualisation of iron-rich structures such as the basal ganglia, which are very hard to distinguish on T1-weighted anatomical scans otherwise (Keuken et al., 2014a; Visser et al., 2016a; 2016b).

UHF diffusion-weighted imaging (DWI) MRI has been conducted in both *post mortem* and *in vivo* studies to visualize the white matter pathways between different grey matter areas (Strotmann et al., 2013; Wargo and Gore, 2013; Dyvorne et al., 2015). High-resolution DWI allows the visualisation and quantification of highly interconnected structural networks (Keuken et al., 2015) and can be used to inform and constrain the architecture of computational models. DWI can deliver insights into the existence and individual connection strength between cortico-subcortical areas. As with other UHF sequences, UHF DWI MRI benefits from a high SNR (Polders et al., 2011; van der Zwaag et al., 2016). This increase in SNR can be used to achieve submillimeter voxel sizes allowing the separation of fine-grained white matter structures such as those found in the thalamus (Heidemann et al., 2012; Calamante et al., 2013). Higher field strengths also result in a decrease in the uncertainty of the diffusor tensor

imaging-estimated parameters, such as fractional anisotropy and the principal eigenvectors (Polders et al., 2011). In future studies, this information could be included in computational models, allowing for concrete predictions about group and individual network dynamics between structures (Michalareas et al., 2016).

UHF fMRI data acquired along with structural UHF MRI data from the same subjects increases spatial and temporal specificity compared with similar 3T approaches (de Hollander et al., 2015). Although previous work showed that lower magnetic field strength MRI can yield a similar spatial resolution to that achieved by UHF fMRI, the latter approach has several advantages (De Martino et al., 2013; DeSimone et al., 2015). Importantly, 7T fMRI studies have a higher CNR and higher temporal specificity (Hale et al., 2010; Hahn et al., 2013; Baecke et al., 2015). In addition, with equal voxel size, UHF fMRI has a superior spatial specificity than lower field strength MRI, owing to a smaller point spread function of the blood-oxygen-level-dependent (BOLD) response (Engel et al., 1997; Shmuel et al., 2007). The BOLD response increases supra-linearly with field strength and translates into a higher temporal SNR within a single voxel, increasing the temporal specificity (Yacoub et al., 2001; Uludağ et al., 2009).

However, the advantages of UHF fMRI are also accompanied by serious challenges (Robitaille and Berliner, 2007; van der Zwaag et al., 2016), some of which are particularly relevant for the subcortex (Barry et al., 2013). First, owing to increased sensitivity to susceptibility-induced field differences, there is a greater relative variability of baseline $T2^*$ relaxation times across the brain (van der Zwaag et al., 2012). This means that the optimal echo times in fMRI are also more variable across the brain, and extremely short in the subcortex; the optimal echo time is approximately 15 milliseconds in the subcortex compared to approximately 30 milliseconds in the cortex at a field strength of 7T (de Hollander et al., 2017). Consequently, 7T fMRI sequences that were originally developed for the cortex are not suitable for fMRI studies of the subcortex. A second, more general challenge of functionally imaging the subcortex is the increased distance to the individual receiving coils and their large overlap in sensitivity profiles compared to cortex. As a consequence, the signal in small subcortical nuclei is weaker than the signal in cortical areas when using acquisition protocols with higher acceleration factors (Pruessmann et al., 1999; de Zwart et al., 2002). It is clear that specifically tailored fMRI sequences are necessary when functionally imaging the human subcortex at ultra-high field.

Combining UHF structural and fMRI has the potential to yield extremely detailed images of the brain: animal studies have already indicated the possibility of single cell imaging (Shapiro et al., 2006), *post mortem* human studies have acquired 0.09 mm isotropic voxels (Makris et al., 2013), and *in vivo* studies have acquired 0.12 x 0.12 x 0.6mm voxels (Stucht et al., 2015). The field of UHF MRI is rapidly advancing and ongoing hardware development together with emerging techniques such as prospective motion correction will ensure continued improvements of the MRI signal (Frost et al., 2015; Stucht et al., 2015).

MRI DATA ANALYSIS.

Automated parcellation procedures aim to enable the automated identification of individual brain structures and provide good results for the cortex, but not for the large number of individual subcortical structures (Alkemade et al., 2013; Visser et al., 2016b). Unlike the subcortex, layering principles are constant across the cortex, therefore, automated segmentation tools are simpler to apply (Cabezas et al., 2011). Subcortical structures vary substantially in their histochemical properties, demanding an increase in the number of identity

validation studies that are required to determine the anatomical accuracy of parcellation procedures. Given the large number of subcortical structures that exist, manual parcellation becomes an exhaustive and time-consuming process. Automated parcellation procedures would greatly speed up the development of probabilistic atlases of individual subcortical brain structures (Visser et al., 2016a). Parcellation procedures that are based on statistical shape and appearance models incorporate previously gathered information about the mean and variance of brain region shape and the intensity of such regions on MRI scans (Heimann and Meinzer, 2009). By providing more detailed information about the anatomical variability, such algorithms result in more accurate parcellation of subcortical structures (Patenaude et al., 2011; Visser et al., 2016a; 2016b). However, to reliably apply these automated procedures, further fine-tuning is warranted.

Until now, functional and structural MRI data are usually registered into a standard anatomical space. Unfortunately, detailed information about the human subcortex, including changes across the lifespan, is currently missing. Standard MRI atlases such as the atlas used by FreeSurfer software (Fischl et al., 2002), the Harvard-Oxford atlas (Heckemann et al., 2006), the LONI Probabilistic Brain Atlas (LPBA40; Shattuck et al., 2008) and the Jülich cytoarchitectonic maps (Eickhoff et al., 2005) lack detailed information about small subcortical structures. Initial efforts from our group provide manually parcellated probabilistic subcortical maps in both young (Forstmann et al., 2012; Keuken et al., 2014a) and elderly healthy participants (Keuken et al., 2013). These efforts have been supplemented with newly developed semi-automatic (Kim et al., 2014) and automatic segmentation protocols (Visser et al., 2016a; 2016b) that can be applied to, for example, the striatum, the globus pallidus (GP), the subthalamic nucleus (STN) and the substantia nigra (SN). However, in light of the large intra- and inter-individual variability in the shape, location and tissue composition of these subcortical structures, including the heterogeneous distribution of iron in subcortical nuclei, carefully cross-validated manual segmentation protocols will remain vitally important (Keuken et al., 2014a; Daugherty et al., 2015).

Another general key issue in fMRI analysis is the smoothing of functional data. Historically, smoothing was needed to compensate for the low SNR resulting from low-field-strength MRI, to meet the assumptions underlying multiple comparison correction techniques, and to accommodate anatomical variability and registration errors. A recent study showed that smoothing should be avoided in MRI studies since the signal is blurred to the point where it cannot unequivocally be attributed to specific regions, layers and subcortical nuclei (Hennig and Speck, 2012; Stelzer et al., 2014; Turner and Geyer, 2014; Geyer and Turner, 2015). The combination of coarse spatial resolution, smoothing, and missing detailed MRI atlases of the subcortex results in a BOLD signal that represents a mix of various neighbouring subcortical nuclei (de Hollander et al., 2015). While this is a problem for fMRI at any field strength, it is particularly important to develop techniques that avoid smoothing or improve the accuracy of smoothed functional data as the field of UHF fMRI develops.

POST-MORTEM VALIDATION

 Even though *in vivo* UHF MRI can deliver excellent spatial resolution, it does not provide the level of microscopic anatomical detail that is obtained using histological and histochemical approaches. As discussed above, identifying small subcortical nuclei is extremely challenging using *in vivo* UHF MRI scans alone. Therefore, comparing *in vivo* results with additional *post mortem* UHF MRI images and histochemical data is an important step for the development of

increasingly accurate UHF MRI techniques, in which an increasing number of small brain structures become visible. Such validation studies entail the scanning of *post mortem* brain tissue using UHF MRI followed by fixation and cutting of the tissue for detailed histological staining. Once scanned and assessed histologically, comparisons between *in vivo* and *post mortem* brains can be made. These studies allow confirmation of the identity of individual brain structures based on neurochemical characteristics and organization of neuronal populations. Unfortunately, the field of histology has not developed at the same pace as the field of *in situ* imaging. The critical importance of 3-dimensional (3D) information for understanding the structure and function of the brain has not yet led to a major shift in the histological approaches used for studying human brains, and histology is still dominated by 2D techniques. Nevertheless, recent developments are helping to modernise histological research, transforming it from a 2D into a 3D discipline (Amunts et al., 2013; Weiss et al., 2015). Creating a 3D histological map allows a more direct comparison between histological and MR images, when care is taken to tailor the fixation process.

Tissue-processing procedures require careful optimization to allow *post mortem* UHF MRI scanning and subsequent histological processing. Formalin immersion fixation is commonly used for human brain specimens, although this approach may result in uneven fixation, which can be minimized by using small tissue blocks. Both under- and over-fixation may negatively influence the MRI signal substantially as well as histological analyses. MRI can be improved by transferring tissues back to a buffered saline solution, and formalin cross-linking can be reversed by heat-induced antigen retrieval to unmask antigens for histochemical purposes (Shi et al., 1991). Under-fixation results in continued autolysis, cracking and shrinking of the tissues, nuclear chromatin condensation and cellular distortion (Chu et al., 2004). Prolonged formalin storage causes coarse hypointensities on $T2^*$-weighted images (van Duijn et al., 2011).

Tailoring fixation procedures to the needs of specific MRI protocols, as well as to the needs of histological processing, is possible, particularly as a variety of techniques can be applied to perform antigen retrieval (Shi et al., 1991). Highly sensitive immunodetection systems are also available, which allow for lenience toward longer fixation periods (Hauptmann et al., 2016). Although long fixation times are unfavourable for histochemical processing, they are crucial to prevent MRI artefacts. Factors such as age, sex, *ante mortem* disease and cause of death can markedly influence the biochemical properties of the brain (Ravid et al., 1992), and matching for these factors between groups is highly important when comparing biochemical properties (Alkemade et al., 2012b). However, in the absence of neurodegenerative disease, these factors will not alter the 3D structure of and the connectivity in the brain. In addition, after death, as biochemical properties begin to change rapidly, morphological characteristics are maintained for prolonged periods (Kretzschmar, 2009).

Further still, quantitative comparisons can be made. Development of novel quantitative contrast measures in MRI (qMRI; Weiskopf et al., 2015) has led to a renewed interest in *post mortem* studies which can be used to validate these techniques. Validation using *post mortem* data provides a direct link between the tissues characteristics and the measured MRI signal. By providing such links it becomes possible to quantitatively assess, for example, the myelination and iron accumulation directly from *in vivo* UHF structural MRI data. Several studies have been published on the quantification of tissue iron concentrations using a variety of approaches both *in vivo* and *post mortem*, and iron concentrations measured in *post mortem* tissue samples are consistently found to correlate to susceptibility measures obtained using QSM (Langkammer et al., 2012; Stüber et al., 2014). Exploiting these *post mortem*-derived

quantitative MRI measures to inform automatic segmentation algorithms for *in vivo* data is not trivial, as the qMRI parameters can change in accordance with how the tissue is processed (Schmierer et al., 2008; Dawe et al., 2009). Additionally, quantifying measures for myelin and neuromelanin have been investigated as markers for neuropathological conditions (Mottershead et al., 2003; Schmierer et al., 2008; Keren et al., 2015). Further studies will have to investigate whether these measures can contribute to our understanding of healthy brain function.

MODEL–BASED COGNITIVE NEUROSCIENCE

Current neuroimaging techniques using UHF 7T or higher MRI can resolve the macroscopic and mesoscopic level with excellent structural and functional detail (Plantinga et al., 2014). At the microscopic level, using post mortem histology, individual neurons can be distinguished. Fusion of post mortem and non-invasive UHF MRI techniques can bridge across all three levels of analysis and provide a holistic framework to study the brain by taking into account mechanisms at all relevant scales (Fig. 2; Weiss et al., 2015).

Formal models can help us make sense of these large complicated data across all levels. These models allow us to study cognitive processes, including memory encoding, response caution, response inhibition and conflict monitoring, in a formal manner. These models can be fit to behavioural data and allow quantification of the computations and latent variables that underlie cognitive processes. Calculating latent variables using a mathematical model has the key advantage of being able to quantitatively reveal relevant information that cannot be directly measured, such as an individual subject's information processing efficiency during a cognitive task. By relating such individual differences to neural signatures (for example, BOLD activation during a decision-making task), we have learned more about where in the human subcortex a task is performed and how the cognitive computations and representations are implemented.

Cognitive neuroscience studies the biological substrate underlying cognition (Gazzaniga et al., 2007). One subfield of cognitive neuroscience that has recently emerged is model-based cognitive neuroscience, which brings together mathematical psychology and cognitive neuroscience, and involves the formalization of cognition through the use of quantitative models (Forstmann and Wagenmakers, 2015). One prominent example of such a model is the diffusion decision model (DDM; Ratcliff, 1978; Forstmann and Wagenmakers, 2015).
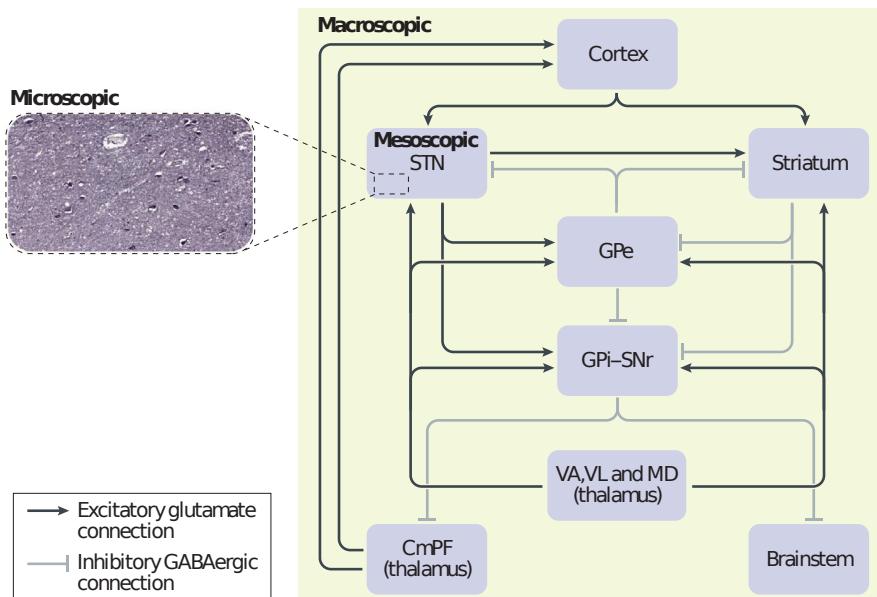
Figure 2. A functional theory on cortico-basal ganglia-thalamo‑cortical network: In their default state, the input nuclei of the basal ganglia - that is, the striatum and the subthalamic nucleus (STN) in combination with the output nuclei of the basal ganglia - that is, the globus pallidus interna (GPi) and the substantia nigra pars reticularis (SNr) - send tonic inhibition to the thalamus, midbrain and brainstem, preventing the premature execution of any action. The black lines indicate excitatory glutamatergic connections, whereas the grey lines indicate inhibitory GABAergic connections. When cortical processes start to favour a certain course of action, this leads to activation of the input nuclei of the basal ganglia (that is, the striatum), which in turn leads to selective suppression of the output nuclei, releasing the brain from inhibition and allowing the action to be executed (Mink, 1996). The intricate interplay between the different basal ganglia nuclei and the cortical brain areas and layers results in an activation‑inhibition network that can generate adaptive changes of response thresholds, thereby allowing swift decision making. The macroscale includes the entire network. The mesoscale focuses on a single nucleus, in this case, the STN. The microscale describes the internal features of a specific nucleus. Detailed knowledge of the microscopic histochemical properties has led to the identification of two types of medium spiny neurons within the substantia nigra, either expressing the dopamine D1 or D2 receptor. The substantia nigra pars compacta is proposed to activate dopamine D1 receptor- expressing cells of the direct pathway and to inhibit the dopamine D2 receptor-expressing neurons of the indirect pathways. The output nuclei GPi and SNr project to the thalamus, which sends efferents completing the cortico‑basal ganglia‑thalamo‑‑ loop. Combining macro-, meso- and micro- scale levels in this way provides a holistic understanding of this network. CmPF, centre median para- fascicular nucleus; GPe, globus pallidus externa; MD, mediodorsal nucleus; VA, ventral anterior nucleus; VL, ventral lateral nucleus.

The DDM models how participants make simple, speeded decisions in the following way: subjects accumulate information until a fixed threshold is reached, after which they make a response. Using the DDM, we can now interpret accuracy and response times as two sides of the same coin. When the response threshold is increased, we expect both the response times to be longer and the accuracy to increase. Information can also be accumulated at a higher

rate, which leads to faster responses and higher accuracy. The DDM can be used to quantitatively estimate these latent cognitive variables, called 'response threshold' and 'rate of accumulation'. Such latent cognitive variables capture the elements of decision-making that researchers try to understand. This gives us a more nuanced understanding of the cognitive process of speeded decisions than raw behavioural measures such as response time and accuracy can provide. More generally, theoretical and empirical simulation work has also shown that correlations between raw behavioural measures and neural signals can sometimes be deceiving, because they might only index emergent properties of a computational process, as opposed to the computations and their variable representations (Marr, 1982; Jonas and Kording, 2017). Other examples of cognitive models deal with learning the value of different choice options (Sutton and Barto, 1998; O'Doherty et al., 2004) or cognitive control (Logan et al., 1984; Cavanagh et al., 2011).

Another class of models used in model-based cognitive neuroscience, the neurocomputational models, provide more focus on how different brain areas interact and could implement cognition, and place little focus on quantitative predictions of behaviour (Frank, 2006; Lo and Wang, 2006). One example is the multi-hypothesis sequential probability ratio test (MSPRT) and the mapping of its various components on different nodes in the basal ganglia (Bogacz and Gurney, 2007). The MSPRT explicitly models the excitatory and inhibitory connections between the cortex, the striatum, the GP, the STN and the SN, and how this network could calculate the probability of different actions being appropriate for a given task. Although this model can show how behaviour could arise from neural interactions, it is currently not possible to estimate its parameters based on behavioural (or neural) data, like the cognitive models discussed above. Its main purpose is, thus, to come up with hypotheses and experiments to validate and/or further test the model predictions.

Both cognitive and neurocomputational models can create a model-based framework in which we can interpret the noisy signals that subcortical fMRI yields, which, when using a model-free approach, may be considered uninterpretable (de Hollander et al., 2016). Recent work in model-based cognitive neuroscience has been successful in linking the role of the basal ganglia to basic cognitive functions as diverse as action selection (Forstmann et al., 2016), cognitive control (Cavanagh et al., 2011) and learning the value of different actions (O'Doherty et al., 2004). This suggests that a model-based approach could potentially be sensitive enough in elucidating the functional role of other subcortical areas, including small nuclei in the brainstem such as the locus coeruleus (for a model-based cognitive neuroscience approach see Mittner et al., 2014).

There are three current approaches that exist for making inferences using model-based analyses of fMRI data (de Hollander et al., 2016; Turner et al., 2017). The first approach is to incorporate neuroanatomical and neurophysiological knowledge in a model. Such models can then yield concrete, testable qualitative predictions by simulation, which can be investigated experimentally. For example, the now classic neural network simulations performed by Frank and colleagues indicate a possible mechanism for how the STN might be involved in inhibiting actions (Frank, 2006). The plausibility of this mechanism was strengthened by the empirical finding that stimulation of the region in and around the STN, using deep brain stimulation (DBS), alters behaviour in a specific way, exactly as predicted by the simulations (Cavanagh et al., 2011). Similar neurocomputational models have been introduced by Bogacz and colleagues (Bogacz et al., 2007) and Wang and colleagues (Lo and Wang, 2006; Wei et al., 2015).

The second approach is to regress the parameters of a cognitive model with a neural signal obtained from the subcortex (Turner et al., 2013; 2015; de Hollander et al., 2016; Turner et al., 2016; 2017). In contrast to the first approach, the link between the model and the data now no longer hinges only on qualitative predictions about experimental conditions, but uses quantitative cognitive models to directly link brain and behavioural data. This second approach provides a mechanistic understanding of cognitive processes implemented in brain regions. For example, we have shown that the trial-by-trial fluctuations in activation in the striatum during a moving dots task can be understood as fluctuations in the amount of 'response caution', a latent decision-making process. This was done by correlating the striatal signal with the trial-by-trial dynamics in the parameters of a mathematical model of decision making (van Maanen et al., 2011).

The third and most recent approach in model-based cognitive neuroscience tries to bridge the gap between cognitive models and neurocomputational models by jointly modelling the cognitive and the neural data together (Turner et al., 2013; 2015; de Hollander et al., 2016; Turner et al., 2017). That is, to model behaviour and neural activations as the result of one and the same process. One elegant example is given in a study in which the authors hypothesized that during a decision-making task, the moment-to-moment evidence for two response options is represented in the firing rate of a specific group of neurons in the frontal eye fields (Purcell et al., 2010). They found support for this hypothesis by using the actual neural firing rates as the evidence variable in a (slightly modified) DDM. This model was then able to predict trial-to-trial variability in response times and the firing rate of downstream neurons that accumulated the evidence. The authors not only correlated parameters estimated by the model to (summary statistics of) the neural data to suggest some abstract relationship, they went one step further by directly inserting (a transformation of) the neural signal into the cognitive model and equating it to one of its internal variables. Models that are currently developed using this 'joint modelling' approach do not only model neural firing rates and behaviour, but also give concrete predictions of the neural firing rates in specific anatomical locations, relating them to specific decision computations (Bogacz and Gurney, 2007).

DATA AVAILABILITY

93% of the human subcortex is missing from human MRI atlases and well-validated segmentation algorithms. Filling in the gaps is a time consuming and costly process. This process would greatly benefit from data-sharing (Poldrack and Gorgolewski, 2014; Candela et al., 2015), which would make UHF MRI datasets available for the entire research community and provide possibilities for groups to work on their brain structure of interest without having to acquire high quality data themselves. In addition, working with existing data allows researchers to conduct power analyses, to simulate MRI parameters to devise new scan sequences tailored to a particular subcortical structure, and to help to perform meta-analyses. Sharing data would thus save both time and funding resources, which could benefit other subcortical research initiatives (see Table 1).

Table 1. Examples of open source UHF MRI datasets. DWI, diffusion weighted imaging; n.s., not stated; rsfMRI, resting state functional MRI; QSM, quantitative susceptibility mapping.

Repository	Example UHF- MRI dataset	Type of data	Demographics	Reference
Dryad Data Repository	dx.doi.org/10.5061/dryad.fb41s	T1, T2* and QSM	n: 54 age range: 19-75 24 females	Forstmann et al., 2014
INDI	dx.doi.org/10.15387/fcp_indi.corr.mpg1	T1 and rsfMRI	n: 22; age range: 21-30; 10 females	Gorgolewski et al., 2015
NITRC	nitrc.org/frs/?group_id=606	T1 and T2*	n: 28; age range: 21-36; 15 females	Tardif et al., 2016
NeuroVault	neurovault.org/collections/550	Probabilistic atlases for the basal ganglia	n: 30; age range: 19-29; 14 females	Keuken and Forstmann, 2015
OpenfMRI	openfmri.org/dataset/ds000113/	fMRI and angiography	n: 20; age range: 21-38; 8 females	Hanke et al., 2014
Human Connectome	lifespan.humanconnectome.org	rsfMRI and DWI	n: 100; age range: 8-75; sex ratio n.s.	Van Essen et al., 2012

To facilitate data sharing efforts, journals entirely dedicated to this purpose have recently been launched, such as Scientific Data and Data in Brief (Poline et al., 2012; Scientific Data, 2014; Wang, 2014; Candela et al., 2015; Eickhoff et al., 2016). The data 'descriptors' or data papers published in these journals are peer-reviewed and aim to provide thorough descriptions of datasets. All these efforts help research groups to compute reproducibility analyses, create subcortical regions of interest for individual studies, and, (practically) overcome the limited access to UHF MRI scanners (Duyn, 2012).

UNDERSTANDING THE HUMAN SUBCORTEX

An in-depth mechanistic understanding of the human subcortex would provide a wide range of benefits to multiple scientific disciplines. What follows is a brief discussion of just a few of these benefits.

First, small nuclei in the human subcortex such as the STN are targets for DBS in patients with Parkinson disease and obsessive–compulsive disorder (Bronstein et al., 2011; de Koning et al., 2011). However, DBS comes at a cost, including some severe adverse effects (Groiss et al., 2009; Christen et al., 2012). One possible reason for these effects is the imprecise placement of electrodes in the brain owing to the use of pre-operative low-field structural MRI images for surgical electrode planning. Another possibility is that potential target structures, which are not visible on lower field structural MRI scans, may prove more effective clinical targets in the future. Testing these hypotheses with a UHF MRI model-based approach would be a step in understanding subcortical mechanisms for the healthy and diseased brain.

Second, neuroscientists around the world collaborate to fill our neuroanatomical knowledge gap. One such large-scale collaborative project is the human connectome project (Sporns et al., 2005; Van Essen et al., 2012). The aim of this project is to investigate the connectivity between grey matter areas in a cohort of 1,200 healthy adults using 3T and 7T MRI with a multi-modal imaging protocol (Van Essen et al., 2012). The human connectome project will undoubtedly provide us with exciting new insights in the functional connections of the human brain. Such a project would evidently benefit from access to well validated segmentations of all subcortical grey matter structures of the human subcortex. A next step is therefore to develop (semi-) automated segmentation algorithms that will help to build a UHF MRI subcortex atlas validated with *post mortem* data.

Finally, knowledge gained from functional and structural UHF MRI efforts in health and disease will facilitate the development of explicit neurocomputational models and ultimately lead to new theories of mechanisms of the human subcortex. The MSPRT, the neurocomputational model of decision making proposed by Bogacz and Gurney (Bogacz and Gurney, 2007) elucidated above, makes specific predictions about excitatory and inhibitory signalling within the cortico-subthalamic-thalamo-cortical network and how they relate to behaviour. An exciting development will be testing concrete model predictions to validate and develop generative cortico-subcortical neurocomputational models for decision-making and action selection.

CONCLUSIONS

In this Opinion article, we discussed current problems and potential solutions charting the '*terra incognita*' that is the human subcortex. It is evident that a highly interdisciplinary approach — bringing together neuroanatomy, physics, mathematical and experimental psychology, and the cognitive and clinical neurosciences — is needed for this challenging endeavour. Such an approach will allow the integration of information over the microscale, mesoscale and macroscale and, as a result, a better mechanistic understanding of the human subcortex (see Fig. 3).
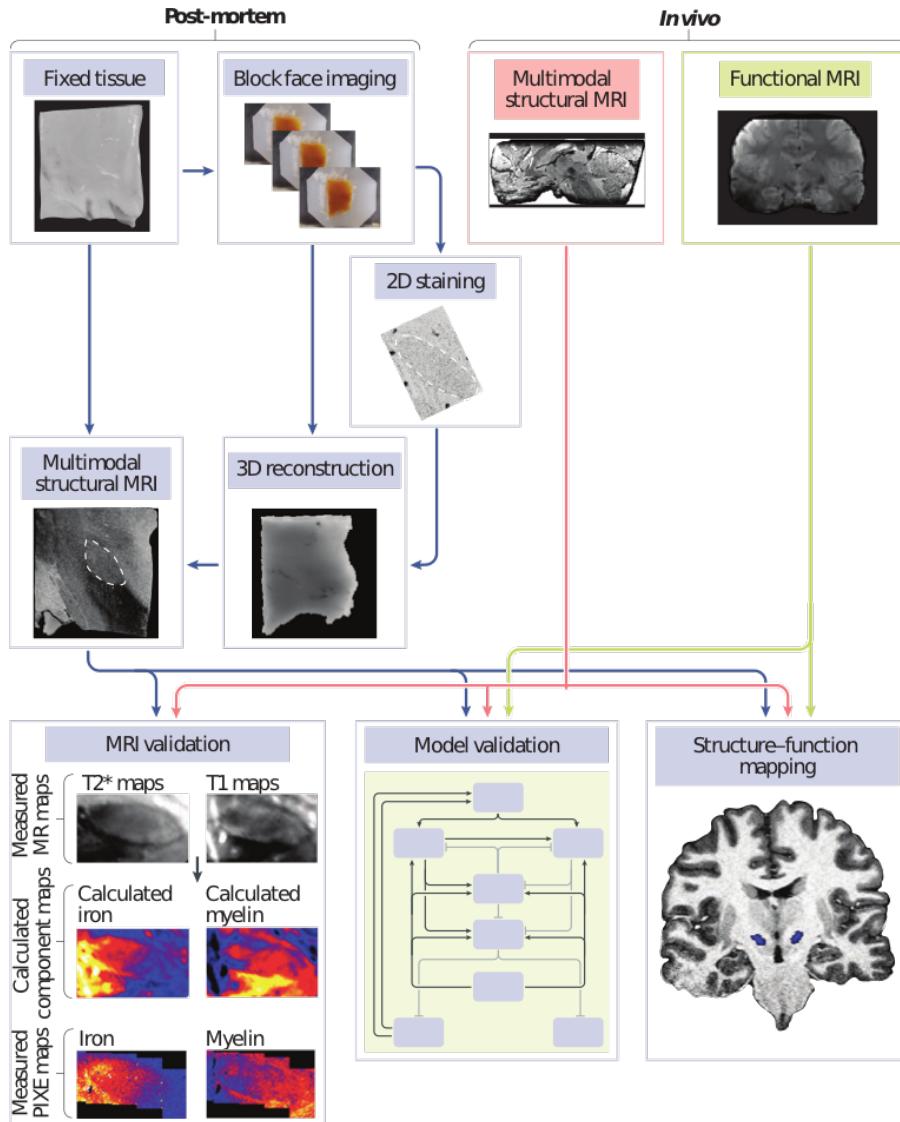
Figure 3. Multi-level data acquisition pipeline. Post mortem histological stained tissue blocks are combined to create a 3D reconstruction of the fixed tissue, showing the chemical composition and borders of the regions of interest in exact cellular detail. This detailed picture is compared qualitatively and quantitatively to post mortem multi-modal structural UHF MRI scans. In vivo multi-modal structural MRI data can also be validated by post mortem data. The histological data not only validates MRI data, but also contributes to validating network models (such as those described in Fig. 2), and structural and functional mapping of the brain. Experimental data from in vivo UHF functional MRI contribute to validating network models and functional mapping. The combination of post mortem and in vivo data acquisition can provide data on macro-, meso- and microscale levels to create an understanding of an entire network, process and/or brain region of interest in exquisite cellular detail. This approach has the ability to address three questions. First, what is the link between the in vivo MRI signal and its underlying

anatomical substrate? An example of such a link whether certain qMRI sequences mainly measure myelin or iron. The subthalamic nucleus is outlined by the dashed line. The second question is: are the biological assumptions built in the neurocomputational model valid? An example of such an assumption comes from the computation model of Bogacz and Gurney in which the presence of glutamatergic neurons in the STN are necessary to predict the activation pattern of the STN during decision-making tasks (Bogacz and Gurney, 2007). The use of histology can test whether glutamatergic neurons are indeed present, whereas the in vivo BOLD measures can be used to test whether the activation patterns match the model's predictions. The third question is: where is the functional activation located exactly? The use of UHF structural MRI scans that allow the visualization of small structural nuclei will facilitate the creating of more precise atlases. The MRI validation subfigure is adapted from Stüber et al. (2014).

3

A GRADUAL INCREASE OF IRON TOWARD THE MEDIAL-INFERIOR TIP OF THE SUBTHALAMIC NUCLEUS

ABSTRACT

The Subthalamic Nucleus (STN) is an important node of the cortico-basal ganglia network and the main target of Deep Brain Stimulation (DBS) in Parkinson's disease. Histological studies have revealed an inhomogeneous iron distribution within the STN, which has been related to putative subdivisions within this nucleus. Here, we investigate the iron distribution in more detail using quantitative susceptibility mapping (QSM), a novel magnetic resonance imaging (MRI) contrast mechanism. QSM allows for detailed assessment of iron content in both in vivo and post-mortem tissue. 12 human participants and 7 post-mortem brain samples containing the STN were scanned using ultra-high field 7 Tesla (T) MRI. Iron concentrations were found to be higher in the medial-inferior tip of the STN. Using quantitative methods, we show that the increase of iron concentration towards the medial-inferior tip is of a gradual rather than a discrete nature.

INTRODUCTION

In this study, the spatial distribution of iron in the STN was investigated using ultra-high resolution 7T MRI and QSM of both in vivo and post-mortem brains. QSM is a novel MR contrast mechanism that provides a map of local tissue magnetic susceptibility, which allows for the quantification of iron content (Schweser et al., 2011; Langkammer et al., 2012; Deistung et al., 2013).

In the basal ganglia (BG), and more specifically the STN, iron is present in relatively high concentrations as compared to other brain areas (Aquino et al., 2009; Schäfer et al., 2011; Deistung et al., 2013). Previous histochemical work has shown that iron is heterogeneously distributed in the STN and that a close relationship exists between iron and cytoarchitectonic features (Dormont et al., 2004; Fiedler et al., 2007; Massey et al., 2012).

The heterogeneous distribution of iron might be related to functional subdivisions in the STN, in line with the influential tripartite model of a (oculo)motor, associative, and limbic network within the BG (Alexander and Crutcher, 1990). In one interpretation of this tripartite hypothesis, the iron-rich medial part of the STN should be related to the limbic circuit, an intermediate level of iron should be found in the associative network, and the posterior-lateral sensorimotor part should reveal the lowest concentration of iron (Dormont et al., 2004). The tripartite hypothesis is at odds with a recently conducted literature review revealing an inconsistent pattern of the precise number and location of subdivisions in both humans and nonhuman primates (Keuken et al., 2012). This inconsistency in the literature might be rooted in the assumption of sharp borders between the projections of functionally distinct circuits in such small nuclei. Instead of discrete subdivisions, projections of distinct networks to the STN might largely overlap and are organized in a continuous manner similar to the striatum (Haber, 2003; Alkemade et al., 2015). Such a model is in line with recent findings that argue for a convergence rather than discrete functional bounds within the STN (Haynes and Haber, 2013) and follows the model previously proposed by Alexander et al. (1986).

Here, iron concentrations in the STN were used as a proxy to test two opposing hypotheses: a) that there are discrete subdivisions of iron distribution in the STN; b) that there is a gradual increase of iron distribution in the STN. These hypotheses make different predictions about the shape of the magnetic susceptibility distributions displayed in QSM as well as the size of the vectors in the gradient field of the QSM (see Fig. 1 for a simulation of these two models). In case of *discrete boundaries*, a *multimodal* distribution of iron concentration is expected (Fig. 1b), as well as the presence of a subset of relatively large gradient vectors (Fig. 1c), reflecting a large increase of iron concentration over small distances. In case of a *gradual increase* of iron concentrations, a *unimodal* distribution of both iron concentration and gradient vectors is expected.
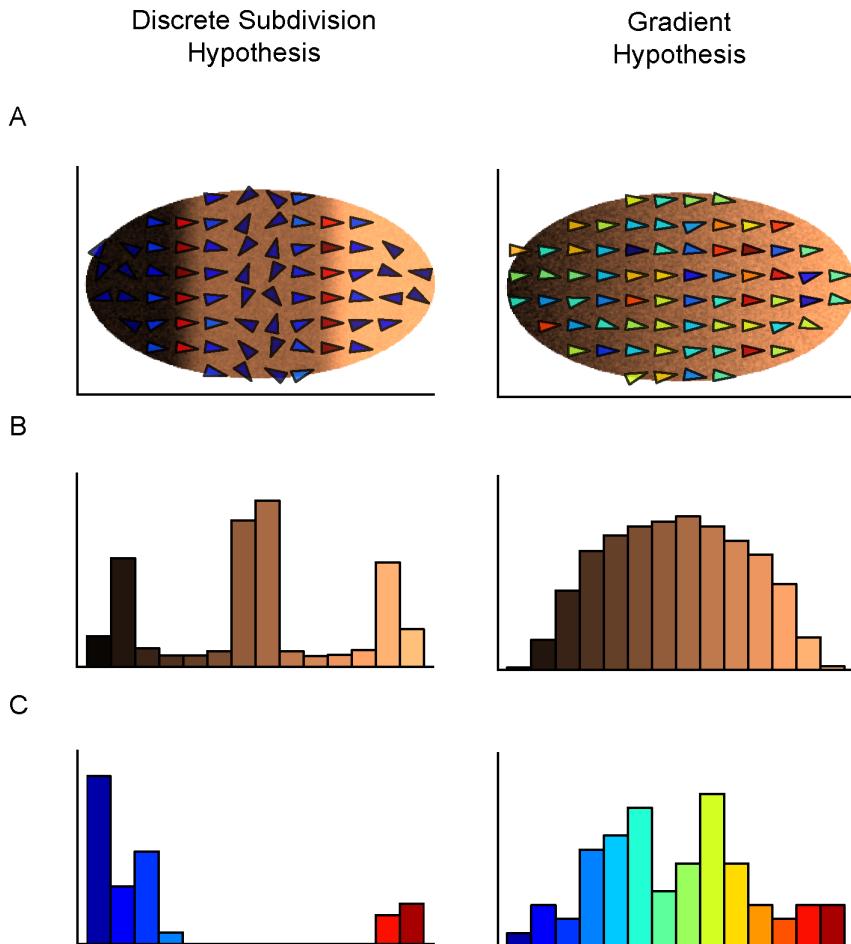
Figure 1. Hypothetical distributions of iron: **(A)** Simulated (2D) data of both the discrete subdivisions and gradient hypothesis. The copper color map indicates iron concentration, the arrows the direction of the gradient and their color the size of the gradient. **(B)** Histograms of raw intensity values. According to the discrete subdivision hypothesis, multiple clusters of susceptibility values should be present. According to the gradient hypothesis, only a single cluster of values is present. **(C)** Distribution of gradient vector lengths. According to the discrete subdivision hypothesis, a small fraction of the vector lengths is much higher and the distribution is bimodal. According to the gradient hypothesis, the vector lengths are distributed unimodal.

In the following we will test these different predictions and show using quantitative measures that there is a consistent increase of iron towards the medial-inferior tip of the STN, but that this increase is of a gradual nature.

METHODS

MR ACQUISITION PROTOCOL AND SEGMENTATION OF THE STN

IN-VIVO DATA

Thirteen healthy young participants (mean age 24.38 years old, range 22-28 years, standard deviation 2.36, six females) were scanned on a 7T Magnetom MRI system (Siemens, Erlangen) using a 24-channel head array Nova coil (NOVA Medical Inc., Wilmington MA, USA). The study was approved by the local ethics committee at the University of Leipzig, Germany. All subjects gave their written informed consent prior to scanning and were given a monetary compensation. One participant had to be excluded due to problems with the orientation of the acquisition matrix, which resulted in uncertainty regarding the anatomical orientation. Whole brain images were acquired with an MP-RAGE (Deichmann et al., 2000) sequence (TR=3000 ms, TE=2.95 ms, TI=1100 ms, voxel size: 0.8 mm isotropic, flip angle=6°, GRAPPA acceleration factor 2). Moreover, multi-echo spoiled 3 dimensional (3D) gradient echo images (GRE) FLASH (Frahm et al., 1986; Elolf et al., 2007) sequence (TR=43 ms, TE=11.22 / 21.41 / 31.59 ms, flip angle=13°, voxel 0.5x0.5x0.6 mm, 56 coronal slices) were acquired. Subsequently, individual QSM of the STN were calculated in the following way: First, the phase images of the FLASH data, which show the field perturbations of a magnetic susceptibility distribution (Schäfer et al., 2009), were unwrapped using a best-path 3D unwrapping algorithm (Abdul-Rahman et al., 2007). Second, the unwrapped phase data were converted in units of ppm and highpass-filtered using the SHARP algorithm (Schweser et al., 2011). To calculate the magnetic susceptibility distribution from filtered phase data, the approach of inversion of the thresholded dipole kernel was applied (Wharton et al., 2010).

POST-MORTEM DATA

Post-mortem tissue blocks obtained from five human brains were scanned on a 7T Magnetom MRI system (Siemens, Erlangen) with a dedicated in-house built RF coil for small tissue samples. For three of the five brains tissue blocks both hemispheres were available resulting in five left and three right STNs in total.

Two tissue blocks were obtained from the Netherlands Brain Bank in Amsterdam, the Netherlands (http://www.brainbank.nl/). The remaining post-mortem tissue blocks were obtained from the Max Planck Institute for Human Cognitive and Brian Sciences, Leipzig, Germany. All post-mortem tissue was obtained in accordance with all legal requirements. Tissue blocks were fixed in 4% formaldehyde for approximately 30 days prior to 7T MRI scanning. See Table 1 for the clinico-pathological data of the post-mortem tissue.

The tissue blocks were placed in an acrylic sphere filled with Fomblin® (Solvay Solexis, West Deptford, New Jersey), a highly viscous fluid of perfluoropolyethers, to avoid background signal. All tissue blocks were scanned using a GRE FLASH sequence (three tissue blocks were scanned with TE=10 ms, TR=30 ms, bandwidth=100 Hz/px, angle=10°, voxel size=0.2 mm³; two tissue blocks were scanned with TE=7 ms, TR=23 ms, bandwidth=120 Hz/px, angle=30°, voxel size=0.15 mm³). Three different orientations of each tissue sample to the main magnetic field were acquired by rotating each sample around the left-right axis of +60 degrees and -60 degrees. The phase information of the resulting three FLASH data sets were unwrapped using best-path 3D unwrapping algorithm (Abdul-Rahman et al., 2007). The magnitude images of the FLASH data sets were co-registered using SPM and the registration matrices were applied to

the unwrapped phase data. The co-registered phase data were highpass-filtered using a fourth order polynomial and converted in units of ppm. The QSM were calculated using the COSMOS approach and the phase data of the three different orientations for each tissue block (Liu et al., 2009).

Table 1. Demographics of the post-mortem tissue. PMD: post mortem delay.

Brain	Sex	Age	Hemisphere	Cause of Death	PMD (hours)	Resolution MRI
1	M	88	L	Aortic stenosis, hypertension, hypercholesterolemia, cardiorenal syndrome, ischeamic cardiomyopathy, atrial fibrillation, rupture of the bowel.	6	0.20 mm^3
2	F	101	L	Hypertension, old myocardial infarction, stomach carcinoma, metastasized, reflux oesophagitis, anemia, coxarthrosis, respiratory insufficiency	5	0.20 mm^3
3	F	91	L	Cardiac insufficiency, urinary tract infection, bronchitis	22	0.20 mm^3
			R			0.20 mm^3
4	F	70	L	Cardiac decompensation	28	0.15 mm^3
			R			0.15 mm^3
5	M	62	L	Sepsis	36	0.15 mm^3
			R			0.15 mm^3

MANUAL SEGMENTATION OF THE SUBTHALAMIC NUCLEUS

Manual segmentation was performed using the FSL 4.1.4 viewer. Segmentation was carried out by two independent researchers. Subsequently, the inter-rater agreement was assessed. Only voxels rated by both raters as belonging to the STN were included in further analyses. Inter-rater reliability for the manual segmentation was assessed using the Dice coefficient (Dice, 1945). For more detailed information regarding the segmentation protocol, see Forstmann et al. (2012) and Keuken et al. (2013).

ANALYSES OF IRON DISTRIBUTION

To allow for earlier findings to be replicated and distinguish between the two main hypotheses of a) discrete subdivisions, or b) a gradual increase of iron within the STN (Fig. 1), QSM and quantitative gradient vector analyses was performed. After the QSM contrast was constructed, the gradient of the QSM image was estimated. Such a field indicates, for every voxel, the direction in which the largest increase of iron concentration is present as well as the magnitude of this increase.

Both hypotheses predict a single direction of iron increase. To test whether this was a plausible assumption for further analyses, the QSM data were tested for one or more gradient directions using the most likely number of clusters according to a spherical clustering algorithm (Maitra and Ramler, 2010). Second, the direction of the mean gradient vector was computed. This mean vector reflects the main direction of the overall increase in iron and allowed the quantitative replication of earlier qualitative findings of increased iron concentrations in the anterior-medial tip of the STN (Dormont et al., 2004; Massey et al., 2012). Third, to distinguish between the two main hypotheses, k-means clustering was performed on the raw QSM values as well as the gradient vector lengths (Fig 1).

GRADIENT VECTOR FIELD ESTIMATION IN THE QSM

The derivatives of the QSM were estimated over all three axes (I_x, I_y and I_z). This was done by convolution with a Gaussian first derivative-operator (Lohmann, 1998; Szeliski, 2010; Solem, 2012), with an absolute sigma of 1.5 times the voxel width of the in-vivo data. To prevent the occurrence of any spurious gradients as a result of differences in intensity with voxels partly outside the STN (partial volume effects), the masks were eroded by one voxel. All voxels outside the resulting masks were interpolated with the magnetic susceptibility value of their nearest neighbor within the mask to ensure that no gradients were rooted in susceptibility values outside the mask. This procedure yielded a vector field indicating the main direction and size of the derivative of the image at every voxel inside the STN.

NUMBER OF DISTINCT GRADIENT VECTOR FIELD DIRECTIONS

To assess whether a single direction of iron increase was plausible, a spherical k-means algorithm was applied to all gradient direction vectors of the QSM gradient vector field within the STN-mask. The likelihoods of different numbers of orientation clusters was assessed using a formal version of the 'elbow method' proposed by Maitra & Ramler (2010).

ANATOMICAL REGULARITY

To test for a regular pattern in gradient direction within the sample population, the *k* main gradient directions according to the maximum likelihood of the spherical k-means algorithms were binned in an 8-bin orientation histogram which was tested for uniformity using a χ^2-test and plotted on a Lambert plane for visual inspection (Mardia and Jupp, 2000).

SUSCEPTIBILITY DISTRIBUTIONS AND GRADIENT VECTOR LENGTH CLUSTERING

To test for distinct clusters of iron concentrations, as predicted by the discrete subdivision hypothesis (Fig. 1b), a standard k-means algorithm (MacQueen, 1967; R Core Team, 2015) was applied to the one-dimensional vector containing the susceptibility values of all voxels within the STN mask. The optimal number of clusters was determined using the gap statistic proposed by Tibshirani (2001).

To test for the presence of any sharp boundaries, as predicted by the discrete subdivision hypothesis (Fig. 1c), the sizes of the gradient vectors were also clustered using the same k-means algorithm and gap statistic. See Fig. 2 for a visual representation of the analysis pipeline.
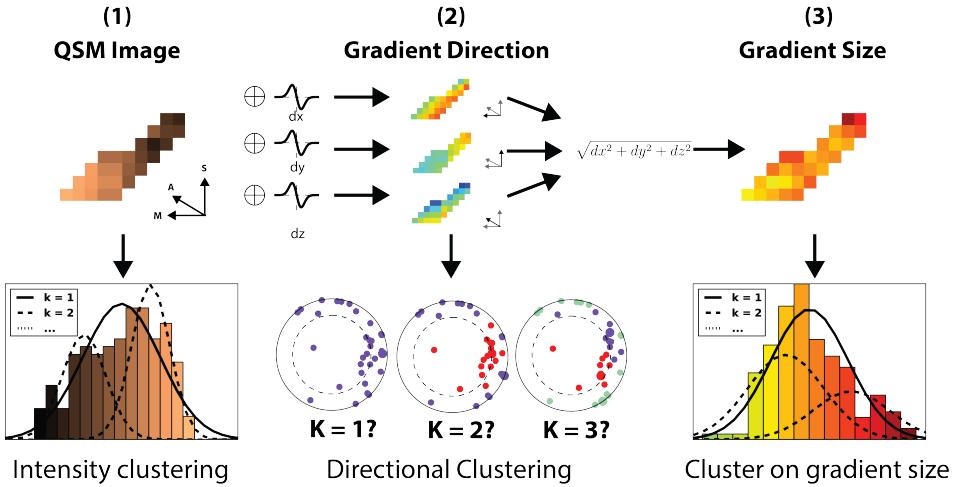
Figure 2. Overview of the analysis pipeline. 1) The input of the pipeline is the QSM image which quantifies the magnetic susceptibility for each voxel and thus the iron content in basal ganglia regions. The susceptibility values are then clustered. **2)** The QSM is convolved with the derivative of a Gaussian separately in all three directions. This yields a vector field indicating, for each voxel, in which direction the iron increases most. These directions are also clustered. **3)** Finally, the length of the gradient vectors is calculated and clustered. Plots in this figure are constructed using the actual QSM data of a representative subject of the in-vivo dataset.

RESULTS

INTER-RATER RELIABILITY COEFFICIENTS OF THE STN MASKS

Across the in-vivo participants and hemispheres, the mean Dice coefficient varied between 0.43 and 0.85 with a mean of 0.73 (SD. 0.09). Across the remaining post-mortem STN tissue and hemispheres the mean Dice coefficient varied between 0.74 and 0.87 with a mean (SD) of 0.83 (0.05). For one of the tissue blocks, i.e., the right STN of case no.3 (see Table 1), both raters agreed on a STN overlap of only 20 mm^3. Given this very small volume, this sample was excluded from any further analysis. In summary, both the in-vivo and post-mortem inter-rater reliability coefficients showed a high overlap across raters. See Fig. 3 for a representational in-vivo and post-mortem QSM scan of the STN.
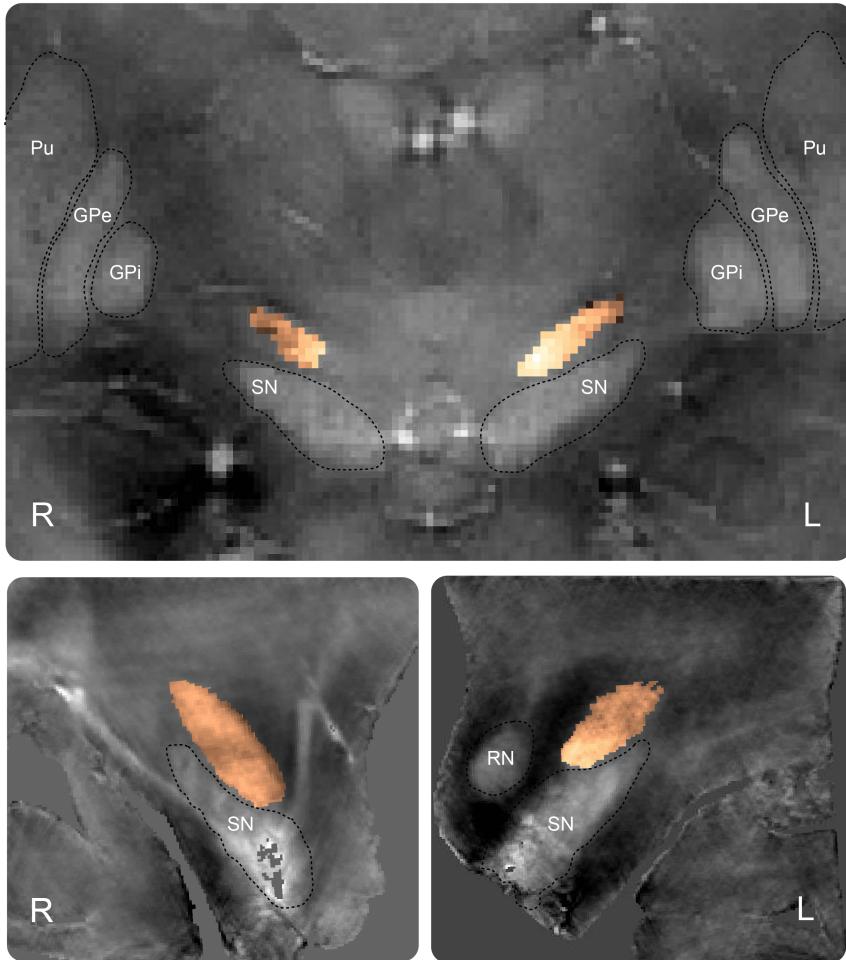
Figure 3. QSM-images of the STN in vivo and post-mortem. Upper panel) QSM-image of a single in vivo participant. Superimposed on the scan are the raw QSM values for the STN mask in copper. **Lower two panels)** QSM images of a right and left hemisphere tissue block of an ex vivo sample. Superimposed on the scans are the raw QSM values for the STN in copper. Note that the voxel size of the ex vivo sample is about 37 times smaller than the voxel size of the in vivo sample (0.15x0.15x0.15mm vs. 0.5x0.5x0.5mm). Pu: Putamen, GPe: Globus Pallidus externa, GPi: Globus Pallidus interna, SN: Substantia Nigra, RN: Red Nucleus.

NUMBER OF GRADIENTS IN THE VECTOR DIRECTIONS

According to the spherical clustering algorithm, a single direction of iron increase across the STN, as predicted by both hypotheses, seemed plausible for the large majority of the data. In the in-vivo data, in the left hemisphere, k=1 was the most likely model for 9 out of 12 participants. For the remaining 3 participants, k=2 was found to be the most likely number of clusters. In the right hemisphere, for 11 participants a single cluster was the most likely and for

1 participant, k=2 was the most likely number of clusters. When clustering the gradient vectors in the post-mortem data, 7 out of the 7 post-mortem samples showed k=1 as the most likely number of distinct gradients.

CONSISTENCY OF THE MAIN IRON GRADIENT DIRECTION ACROSS PARTICIPANTS

The consistency of the main iron gradient direction across participants was tested by plotting the cluster centroids for the most likely number of clusters together on a Lambert azimuthal equal-area projection circle. In such a projection, the surface of a sphere is represented as a circle where relative area is preserved (Mardia and Jupp, 2000, Chapter 9). As can be seen in Fig. 4, the main direction of the iron gradient, for both the in-vivo data sets and post-mortem tissue and both in left and right STN, lie in the medial-inferior direction: iron concentrations increase towards the medial-inferior tip of the STN.

To quantitatively assess whether the distribution of the main gradient directions over participants and post-mortem tissue was non-uniform and consistent, we divided the unit sphere in 8 bins of equal surface representing the $2^3 = 8$ possible combinations of the axes medial vs. lateral, anterior vs. posterior, and inferior vs. superior. A chi-squared test shows that in the in vivo-data, in both hemispheres the main directions are not uniformly distributed over the 8 direction bins ($\chi^2(7, N = 15) = 20.73, p = .0042$) for the left STN, and ($\chi^2(7, N = 13) = 15.92, p = .026$) for the right STN, where for both hemispheres the medial-inferior direction was the preferred direction. In summary, the direction of the individual iron gradient is consistent. The small number of post-mortem cases did not allow the computation of chi-squared test.
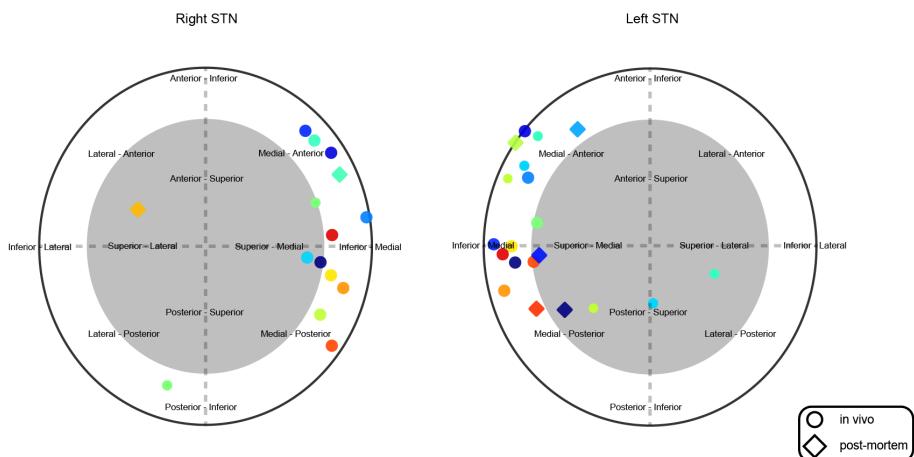
Figure 4. Main directions of the iron gradient for in-vivo and post-mortem data. Every point represents one of the main directions of iron gradients in the left and right STN mask. Markers with the same color and glyph are main directions within the same sample when k=2 was the most likely model (4 out of 24

cases). The size of the glyphs represents the size of the gradient cluster. The diamond glyphs represent the post-mortem brain.

The discrete subdivision hypothesis predicts that multiple discrete clusters of similar susceptibility values exist. However, k-means clustering on the raw QSM yielded k=1 as the most likely number of clusters in all 12 in-vivo data sets, for both the left and right hemispheres. The post-mortem data also showed k=1 as the most likely number of clusters in all 7 post-mortem samples. These analyses suggest a gradual increase of iron rather than discrete boundaries.

For the gradient vector lengths, the discrete hypothesis predicts a multimodal distribution of gradient vector magnitudes with a distinct subset of gradient vectors of large magnitude. Clustering on the magnitudes of the gradient vectors using k-means showed k=1 as the most likely number of clusters in all 12 in-vivo data sets in both hemispheres and all 7 post-mortem tissues. In summary, both in-vivo and post-mortem data confirm the gradient hypothesis.

DISCUSSION

The present study replicates and extends previous findings of heterogeneous iron distributions throughout the STN (Dormont et al., 2004; Massey et al., 2012) by using ultra-high resolution 7T quantitative susceptibility MR mapping of both in-vivo subjects and post-mortem tissue. Single iron gradients, mainly pointing in the medial-inferior direction, were found in the majority of the samples (7/7 in post-mortem, 9/12 for left and 11/12 for right in-vivo STN).

Complementary to the findings of Dormont et al. (2004) and Massey et al. (2012), who reported an increase in iron in the medial-anterior direction, here we show increased iron concentrations in the medial-inferior-anterior direction. This difference might be due to the different methodologies employed in the aforementeiond studies, as both Dormont et al. (2004) and Massey et al. (2012) used histological staining on a limited number of specimens and reported the topology of the employed stainings only qualitatively. Also, histological work is always confined to a single cutting plane eventually inducing biases of changes in intensities in one axis of the plane. Any gradients in the inferior-superior axis will especially be less evident when axial sections are used, as was done in Massey et al. (2012). In Dormont et al. (2004), coronal sections were used so that inferior gradients should be more visible, however, only a single specimen was investigated. Both anatomical variability and the lack of any quantitative measures might explain that an inferior gradient was not found in the Dormont study. Here we present quantitative analyses in the intact STN in 3D on a much larger number of specimens which suggest a similar pattern of increased iron as the abovementioned studies and complementing these findings with the presence of an inferior component to the iron gradient.

Importantly, this quantitative approach allowed the testing of two hypotheses regarding the functional organization of the STN using the iron distribution as a proxy: a) the discrete subdivision hypothesis, and the b) the gradient hypothesis. K-means clustering analysis of the QSM susceptibility values showed no discrete clusters of iron intensities. In addition, the k-means clustering analysis of the gradient vector lengths revealed that there are no sharp boundaries or septa within the STN. Note that these analyses are agnostic towards the number of possible subdivisions because they only reveal a lack of distinct boundaries.

These findings are in favour of the second hypothesis of a gradual increase in iron. We suggest that this reflects that projections of different cortical networks, such as the motor, cognitive, and limbic system converge in the STN and largely overlap, as argued before by Haynes and Haber (2013). This makes sense in light of the integrative function of the STN: a relatively small nucleus, but with a wide array of projections from almost the entire cortex as well as many subcortical areas (Temel et al., 2005b; Lambert et al., 2012). It is, however, at odds with the well-known but inconclusive tripartite subdivision model segregating (oculo)motor, cognitive, and limbic networks (DeLong et al., 1985; Alexander et al., 1986; Alexander and Crutcher, 1990; Parent, 1990; Alexander et al., 1991; Parent and Hazrati, 1993; 1995a; 1995b; Joel and Weiner, 1997; Nakano, 2000; Rodriguez-Oroz et al., 2001; Hamani et al., 2004; Temel et al., 2005c; Obeso et al., 2008; Rodriguez-Oroz et al., 2009; Krack et al., 2010).

Finally, a gradual organization of iron within the STN could have important clinical implications, in particular for the electrode placement in Deep Brain Stimulation (DBS) in Parkinson's patients. DBS of the STN can cause serious 'cognitive' and 'limbic' side-effects, theorized to be due to disturbance of the limbic and associative networks as opposed to the motor network via the STN (Temel et al., 2005b). If these different networks largely overlap within this nucleus, it could be possible to minimize non-motor side effect in DBS by avoiding the region that is least connected to motor-related areas (Lambert et al. 2012). However, it still remains unclear how large these functional areas or transitional zones between areas are. Should the overlap be substantial then it will be significantly more challenging to devise a surgical solution that minimizes non-motor side effects.

LIMITATIONS

Two limitations will be discussed in this section. First, iron is just one of many heavy metal markers of the structural organization in the subcortex. It is possible that other markers such as zinc and copper could show a different distribution. However, there is evidence for a close relationship between iron and cytoarchitectonic features and thereby potentially revealing anatomical subdivisions (Fiedler et al., 2007). Second, iron plays a role in a range of brain functions including myelin production, oxygen transport, and neurotransmitter synthesis (Rouault, 2001; Zecca et al., 2004). Complementary to the role iron plays in cellular functions, there is some evidence linking levels of iron in subcortical structures to higher-level cognitive functions (Sullivan et al., 2009; Penke et al., 2012). It is thus likely that a gradual distribution of iron in the STN is related to its functional organization.

Secondly, four out of 24 participants showed more than one gradient orientation cluster. One explanation for these interindividual differences could be the size of the masks, inducing partial volume effects related to the limited resolution compared to the post-mortem tissue. Partial volume effects might have yielded gradient vectors pointing into the STN, in particular at the dorsal and ventral borders. These gradients are then exactly opposing each other, and will thus be treated as separate clusters by the clustering algorithm. Argueably, this is an artefact and not an actual property of the iron distribution within the STN. A solution for the removal of these artificially induced clusters is to use additional eroding of the masks. However, we decided to leave the original data as unprocessed as possible to avoid any bias towards one of the two hypotheses.

CONCLUSION

In conclusion, the work presented here shows an increased concentration of iron in the medial-inferior tip of the STN. Iron concentrations in the STN increase gradually towards this tip. It is likely that this gradual increase is related to the functional organization of the STN. The current finding of a gradual organization is at odds with the prominent idea of a one-to-one mapping between clearly discernible cytoarchitectonic areas and specific cognitive functions such as the popular tripartite motor-cognitive-limbic model of the STN (Rodriguez-Oroz et al., 2009). We propose to update the tripartite motor-cognitive-limbic model of the STN which, in our opinion, should include transition zones as has been previously proposed by several authors (Alexander et al., 1986; Haynes and Haber, 2013; Alkemade et al., 2015). Still, further experiments, including studies of tissue composition and histology are needed in order to provide more insight into the anatomical organization of the STN.

SUPPLEMENTARY MATERIALS

Histograms of the distribution of iron, histograms of the gradient vector sizes, as well as the amount of explained variance and gap statistics for the different clustering results can be found at http://www.gillesdehollander.nl/gradient_paper/

4

THE FUNCTIONAL NEUROANATOMY OF THE HUMAN SUBTHALAMIC NUCLEUS

ABSTRACT

The subthalamic nucleus (STN) serves as a surgical target for deep brain stimulation (DBS) in movement disorders including Parkinson's Disease. Despite its clinical importance, the internal structure of the STN is not well-understood. Here, we report the results of an unprecedented approach, providing detailed 3-dimensional reconstructions and analyses of extensive immunocytochemical investigations, which are merged with quantitative 7 Tesla magnetic resonance imaging (MRI) data on 7 post-mortem human STNs. Our approach provides a direct link between *post mortem* immunocytochemical and *in vivo* MRI techniques. We found consistent topological patterns in the STN, predominantly along the medioventral-dorsolateral axis. Our data is not in support of the existence of subdivisions within the STN, which form the theoretical underpinning for surgical targeting.

Hidden deep inside the brain under the cortex reside over 450 anatomical structures (Forstmann et al., 2017). Although small, many of these structures have been proven indispensable in our day-to-day functioning. One of these subcortical structures is the subthalamic nucleus (STN) which is reported to be involved in many functions, ranging from speeded decision-making to emotional regulation (Frank, 2006; Herculano-Houzel, 2012; Alkemade et al., 2013; Péron et al., 2013; Aron et al., 2016). Deep brain stimulation (DBS) of the STN effectively alleviates symptoms in a variety of movement disorders including Parkinson's disease (PD; Temel et al., 2005b). However, side-effects, including cognitive decline and emotional instability, are consistently reported (Temel et al., 2006; Christen et al., 2012). These unwanted effects have been ascribed to suboptimal placement of the electrical stimulator within the STN, leading to the unintentional stimulation of circuits involved in cognitive and limbic functions (Temel et al., 2005b). Specifically, it has been suggested that cognitive and emotional side-effects can occur when topologically distinct cognitive/associative and limbic areas of the STN are stimulated (Temel et al., 2005b). The neuroanatomical explanation for the side-effects caused by DBS is rooted in a prominent "tripartite" model of the STN, describing a limbic medial tip, a ventromedial cognitive area, and a dorsolateral motor area (Temel et al., 2005b). However, the internal structure of the human STN is still a topic of ongoing discussion and only limited consistency exists between empirical studies (Keuken et al., 2012; Alkemade et al., 2015).

The principle of functional segregation offers a theoretical framework for defining subdivisions in the STN. According to this principle, neuronal cell types move apart during development, depending on the specializations they acquire (Arendt, 2008). During this process, they form distinct neuronal populations, with potentially distinct functions, as reflected by their individual molecular fingerprint. Immunocytochemical approaches in *post mortem* tissues allow direct visualization of neuronal subpopulations (Forstmann et al., 2017). Despite the impressive molecular anatomical detail, immunocytochemical techniques offer only a static image of the functional neuroanatomy of the human brain (Borgers et al., 2014), and preclude studies on brain function *in vivo*.

Magnetic Resonance Imaging (MRI) offers a complementary, non-invasive technique that can be applied *in vivo*, to study the brain in both health and disease. With the recent advent of Ultra-High Field (UHF) MRI, the spatial resolution required to study the STN has become achievable *in vivo* (van der Zwaag et al., 2016; Forstmann et al., 2017). Recent work by our group has shown that UHF-MRI can be used to quantify interindividual variability in size and location of the STN, to identify consistent topological patterns in non-heme iron using quantitative susceptibility mapping (QSM) both in *post mortem* and *in vivo* images of the STN, and to measure functional activity of the STN during perceptual decision-making (de Hollander et al., 2014a; Keuken et al., 2014a; 2015; de Hollander et al., 2017). However, the precise underlying tissue properties reflected in the MR signal are only scarcely understood (Weiskopf et al., 2015). For example, QSM can also reflect other tissue properties than iron content, such as myelination (Schweser et al., 2016). This hinders the interpretation of observed differences in signal intensities within the STN. Additionally, the spatial resolution obtained with UHF-MRI is substantially lower than that obtained using *post mortem* immunocytochemical approaches, and individual neurons of the STN and their neurochemical characteristics cannot be distinguished.

We have developed a novel multimodal approach integrating immunocytochemical analyses and UHF-MRI in a quantitative fashion, through which we overcome important shortcomings of each individual technique (Forstmann et al., 2017). A major challenge was to optimize the

individual study protocols to allow quantitative comparisons across research disciplines. In the approach, MR images and immunocytochemical data have to be collected from the same sample, and brought in a common space (Weiss et al., 2015; Forstmann et al., 2017). To allow direct comparisons, results from immunocytochemical studies are reconstructed in 3-dimensional space, to which the MRI data is also registered. The next step is to determine what information is shared between these two approaches. The STN topology that becomes apparent in the immunoreactivity patterns can then be transferred to future structural and functional MRI studies performed in living subjects. Here, we present a synthesis of *post mortem* immunocytochemical and MRI data that show that (a) there is a clear functional organization within the STN, which is consistent across subjects; (b) there is little support for any specific number of STN subdivisions, and (c) quantitative MRI (qMRI) can potentially be used as a proxy to identify the functional organization of the STN *in vivo*.

We obtained 10 formalin fixed tissue specimens from non-demented donors via the Netherlands Brain Bank. Clinicopathological data are presented in the Supplementary Materials in Appendix A. The tissue blocks were transferred to Fomblin, and scanned on a 7T Siemens MAGNETOM scanner using a custom built 80mm dual loop miniCP coil (Weiss et al., 2015). Three protocols were acquired: an 0.2mm isotropic magnetization-prepared 2 rapid acquisition gradient echoes (MP2RAGE; Marques et al., 2010), used to extract T_1 maps; an 0.2mm isotropic multi echo gradient echo (GRE) fast low angle shot (FLASH Haase et al., 1985) to calculate T_2* maps; and finally a single echo 0.06mm isotropic GRE FLASH (TA 10.24h) to delineate the STN and obtain quantitative susceptibility maps (QSM). Tissue blocks were then dehydrated and paraffin embedded for further processing. Intermediate block face imaging was performed while cutting serial coronal sections and images were realigned for reconstruction purposes. Sections were systematically sampled, stained, and digitally imaged to produce a 3D reconstruction of the staining profiles in block face space (Fig. 1). The 0.06mm FLASH volume was nonlinearly registered to the stacked block face images using a landmark based approach. All registrations were visually checked for misalignment, and found satisfactory.

Twelve antibodies were used for immunocytochemical stainings within the STN. Antibody selection was based on the ability to label general neuronal features or major neurotransmitter systems, and reports on their expression in the STN (Supplementary Materials and Methods). Consecutive sections containing the STN were stained at 300 μm intervals for Neurofilament H (SMI-32), Synaptophysin (SYN), Myelin Basic Protein (MBP), Tyrosine Hydroxylase (TH), Vesicular Glutamate Transporter 1 (VGLUT1), Glutamate Decarboxylase 65/67 (GAD65/67), GABA-A receptor subunit alpha 3 (GABRA3), Serotonin Transporter (SERT), Parvalbumin (PARV), Calretinin (CALR), Transferrin (TF), and Ferritin (FER). Immunoreactivity was visually inspected and present for all proteins in all tested tissue specimens, and staining intensity showed substantial interindividual variation, which is in line with previous publications (Alkemade et al., 2012b; Borgers et al., 2014). Digital images were created and shape information was used to perform linear transformations for registration to the corresponding block face images. Additionally, manual outlines of the STN were created by two independent raters on PARV and SMI32 sections. These STN outlines and the thresholded staining results allowed the successful reconstruction of 3D densitometric data (arbitrary units) into block face space together with the MRI data in 7 tissue specimens, as illustrated in Fig. 1. For three other blocks, 3D reconstructions were not satisfactory, because of distortions and tissue damage.
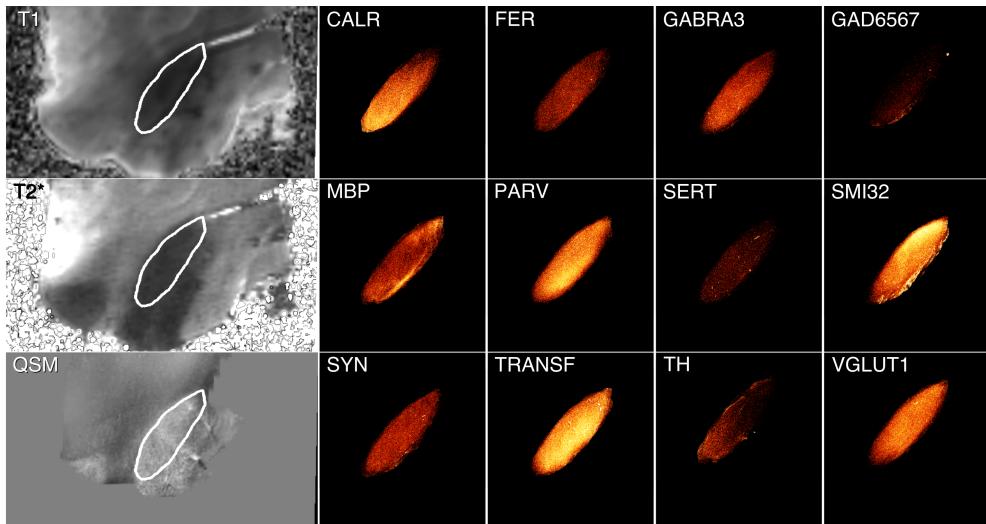
Figure 1: Example of a single STN (#15-033) showing MR contrasts T1, T2* and QSM and immunoreactivity both registered to blockface space. Immunoreactivity is presented as maximum intensity Z-stacks for serotonin transporter (SERT), calretinin (CALR), parvalbumin (PARV), tyrosine hydroxylase (TH), synaptophysin (SYN), transferrin (TF), glutamic acid decarboxylase (GAD65/67), neurofilament H (SMI32), ferritin (FERR), GABA receptor subunit A3 (GABRA3), vesicular glutamate transporter 1 (VGLUT1), myelin basic protein (MBP).

To investigate the consistency of the expression patterns of staining across specimens, each individual 3D reconstruction of an individual staining pattern was divided into 27 sectors of equal volume along 3 axes, i.e., the rostro-caudal axis between slides, and the longest (dorsolateral-ventromedial) axis, and its orthogonal axis within the slides. The majority of markers that showed inhomogeneous patterns show a higher staining intensity in anterior medioventral sectors, and lower staining intensities in the posterior dorsolateral parts of the STN, although there were subtle differences between markers. The pattern was reversed for VGLUT1 and SMI32, which showed higher intensities in the dorsolateral sector of the STN (Fig 2).

The normalized staining patterns in these 27 sectors of equal volume were tested for alterations in staining intensities across subjects using one-sampled t-tests. Statistically significant differences were observed for 10 out of 12 tested markers, identifying a consistent internal organization of these markers within the human STN (Fig. 3).

To identify similar topological patterns between protein markers, a correlation matrix of the staining intensities across space was made for each individual specimen, and these correlation matrices were then averaged across specimens. A hierarchical average-linkage clustering algorithm was applied to the correlation matrix, identifying a number of distinct groups of markers with a higher similarity in their immunoreactivity distributions. The immunoreactivity patterns of SERT and TH are related and show higher staining intensity in anterior slices, in the dorsomedial region of the STN. SMI32 and VGLUT1 also show similar patterns and show predominant expression in posterior slices, at the dorsolateral regions of the STN. GAD6567, CALR, GABRA3, and SYN show highest intensities in the most anterior slices, in the

ventromedial tip of the STN. Finally, PARV, TRANSF, FER, and MBP show a predominantly homogeneous staining distribution, and only marginal correlations between distributions across the STN (Fig. 2). These findings point towards a complex topological organization within the STN with overlapping, but clearly distinct topological patterns of immunoreactivity profiles.
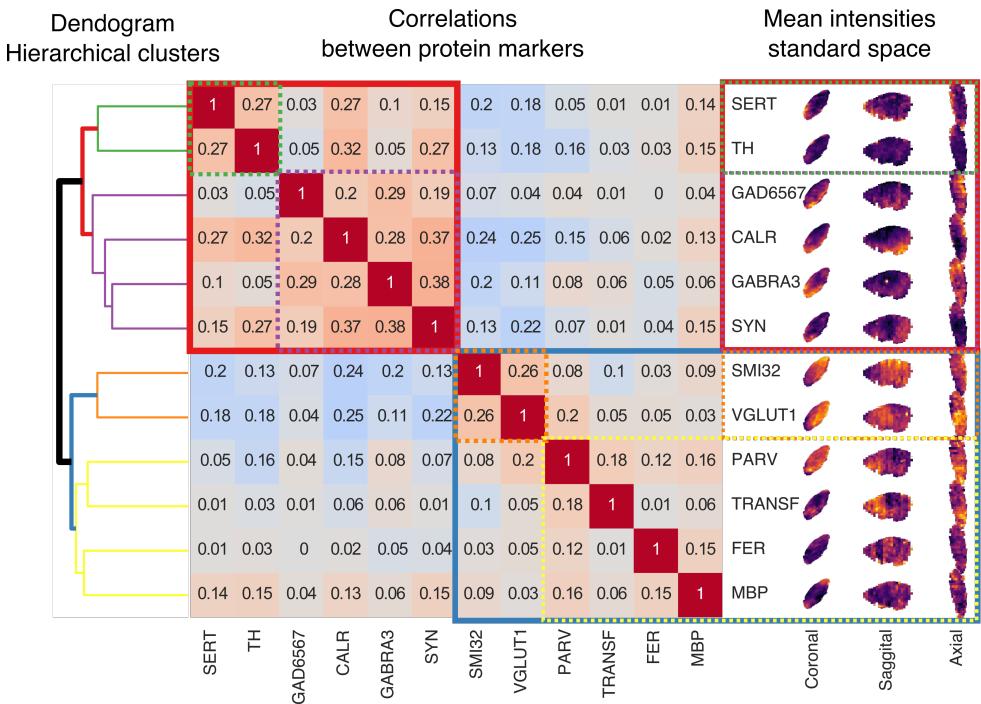
Figure 2. Illustration of main patterns in the immunoreactivity data. The correlation plot visualizes the mean Pearson correlation coefficients across space between the staining intensities of all protein markers. Red squares indicate positive correlations, blue squares indicate negative correlations. The values represent the mean correlation coefficients across specimens. The correlation matrix is subdivided using hierarchical clustering, which yields groups of protein markers that have more similar staining patterns. The resulting clustering tree is visualized in a Dendogram (left). The dendogram shows, for example, that the staining patterns of SERT and TH show a higher similarity compared to that of SERT and SMI32. All normalized staining intensities were registered to a group space and averaged over specimens. The resulting STN representations in a common space are depicted in coronal, sagittal and axial planes (mean intensities standard space; right panel). These images visually illustrate the consistency of staining patterns across specimens.
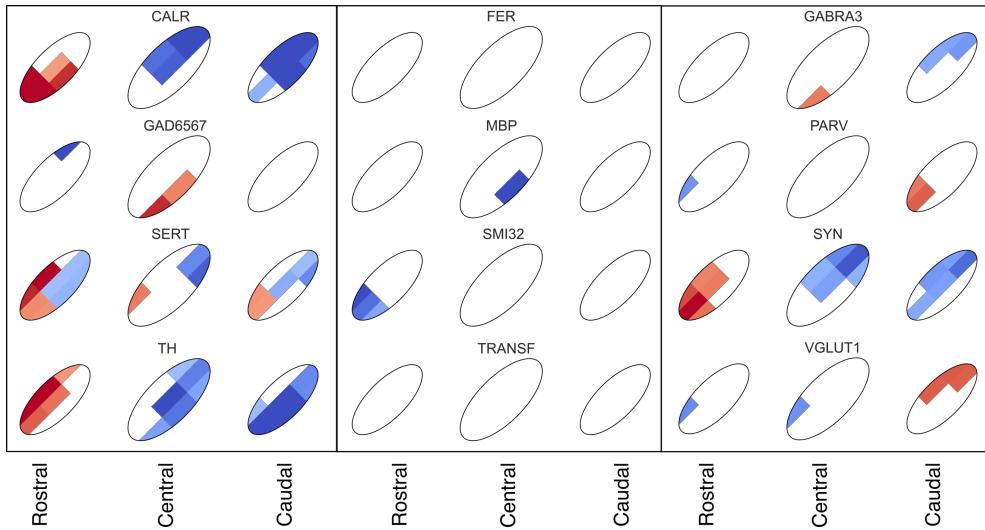
Figure 3. Sectors of the STN that show significantly increased (red) or decreased (blue) immunoreactivity. Significance level at p < 0.05, False Discovery Rate corrected.

Since the number of subdivisions in the STN is a matter of debate, we tested for evidence supporting the existence of subdivisions, using two distinct analytical approaches. In the first analysis, we estimated the number of clusters in the STN by submitting the immunoreactivity data to a quantitative model fitting approach. Mixtures of exponentially-modified Gaussian (ExGauss) distributions were fit in order to compare evidence for the existence of 1 up to 6 subdivisions (see also de Hollander et al., 2014a and Supplementary Materials and Methods). We applied different model comparison techniques, i.e. within- and across-subject cross-validation, Baysian information criterion (BIC), and Akaike information criterion (AIC). Results showed limited consistency across these techniques, as evidenced by varying numbers of subdivisions identified (see Fig. 3 in Appendix A). The conclusion that the number of subdivisions varies strongly across subjects, however, lacks biological plausibility. An alternative explanation is that the immunoreactivity patterns show substantial overlap, explaining the varying number of clusters we observed. Visual inspection of the intensity distributions and corresponding model fits indicate that the mixture models capture the data adequately (see Fig. 4 in Appendix A), as reflected by a single peak in the intensity distributions in the majority of observations. These qualitative assessments are in line with biological variation which is reflected in the diverging model comparisons, rather than true differences in the number of subdivisions. We would like to add a cautionary note by acknowledging inherent limitations of model comparison techniques (Frühwirth-Schnatter, 2006; Marin and Robert, 2014; Gelman et al., 2014b).

Therefore, we subjected the distribution patterns to a second analysis which did not include any prior information on the expected number of clusters. In line with our first analyses, we found that, independent of the number of clusters that was assumed, a substantial overlap of clusters was present. Assuming different number of exGauss components, the majority of regions within the STN did not clearly belong to any specific cluster (see Supplementary Materials and Methods). Using these two approaches, we conclude that the

immunocytochemical data a) offer no clear support for any tested number of subdivisions in the STN, and b) suggest a strong overlap between neuronal populations.

A comparable mixture model was fitted to the gradient size images of the tested protein markers. A gradient image shows, for every voxel, to what extent its value differs from that of its neighboring voxels. High gradient intensities indicate discrete borders in an anatomical structure (Szeliski, 2010). Additionally, a group of voxels showing a substantially higher gradient size as compared to neighboring voxels is indicative for the existence of clear borders within the anatomical structure. We found no evidence supporting clear borders in our data (see also de Hollander et al., 2014a). Again, the estimated parameters indicated strong overlap of neuronal populations.

To compare the protein markers and qMRI data quantitatively, we estimated a regression model where relative staining intensities across the STN were predicted by quantitative MRI parameters, specifically T_1, T_2*, and QSM (similar to Stüber et al., 2014). For the majority of the tested markers, qMRI parameters were predictive for the immunoreactivity patterns (see Table 1). Notably, both T_1 and T_2* values are lower in the medioventral tip and higher in the dorsolateral tip, but in the majority of cases their regression coefficients show an opposite sign. This suggests that these two measures reflect complementary information. The qMRI parameters showed highest predictive value for protein markers that showed a medioventral-dorsolateral distribution gradient (CALR, GABRA3, SERT, SYN, TH, VGLUT1). Additionally, T_1 values were highly predictive of MBP, although MBP expression did not show a strong medioventral-dorsolateral gradient. The relation between T_1 values and MBP is in agreement with the well-established sensitivity of T_1 for myelin (Stüber et al., 2014). Additionally, it shows that qMRI parameters can be related to a number of tissue properties and therefore should not be interpreted as a marker for one specific neuronal characteristic or population. Interestingly, the addition of QSM values to a model including only T_1 and T_2* did not improve the proportion of explained variance (R^2), indicating that QSM values do not provide additional explanatory value over T_2* alone in this dataset (see also Fig. 7 in Appendix A).

Our approach allows the multimodal analysis of human brain tissue and, for the first time, truly merges these two independent neuroimaging disciplines. Immunocytochemical analysis showed that there are consistent topological patterns across the human STN and that these patterns are of a gradual rather than a discrete nature. Quantitative MRI parameters were predictive of a subset of protein markers. This suggests that the topological patterns that were found using immunocytochemistry can, at least partially, be recovered using quantitative MRI.

We have developed a method that overcomes the inherent limitations in spatial resolution present in MRI studies, and the incompatibility of immunocytochemical approaches with *in vivo* investigations. This approach opens the possibility to quantitatively address outstanding questions about the three-dimensional architecture of small brain structures, their neurochemical characteristics, their relation to quantitative MRI measurements, as well as their function. We investigated whether the underlying functional neuroanatomy is in support of the tripartite subdivision hypothesis of the human STN. We found substantial overlap between neuronal populations, and show that quantitative model fits do not show support for any specific number of subdivisions in the STN. Our main conclusion is therefore that the tripartite subdivision hypothesis represents an oversimplification of the complex structure of the STN.

Table 1: Mean and standard deviation of regression slopes of T_1, T_2^*, and QSM values in a general linear model (GLM) predicting relative immunoreactivity intensities, across subjects. Adjusted R^2 is the square of the proportion of explained variance, over and above an intercept model, adjusted for the number of parameters. CALR=calretinin, FER=ferritin, GABRA3=GABA-A receptor subunit alpha 3, GAD6567=glutamate decarboxylase 65/67, MBP=myelin basic protein, PARV= Parvalbumin, SERT=Serotonin Transporter, SMI32=Neurofilament H, SYN=synaptophysin,TF=Transferrin, VGLUT1=vescicular glutamate transporter 1.

	Intercept		T1 (s) slope		T2* (s) slope		QSM (ppm) slope		Adjusted R^2	
	mean	std	mean	std	mean	std	mean	std	mean	std
CALR	0.14	0.21	0.95	1.12	-0.016	0.015	-0.41	0.53	0.24	0.17
FER	0.29	0.28	0.17	0.42	-0.003	0.009	-0.13	0.25	0.08	0.06
GABRA3	0.39	0.37	0.76	1.12	-0.015	0.014	-0.28	0.58	0.16	0.11
GAD6567	0.23	0.28	0.14	0.19	-0.005	0.007	-0.14	0.42	0.08	0.06
MBP	-0.02	0.32	1.38	1.04	-0.006	0.016	-0.37	0.57	0.23	0.13
PARV	0.26	0.34	0.45	0.78	-0.001	0.014	0.11	0.47	0.08	0.06
SERT	0.17	0.31	0.53	0.42	-0.006	0.005	-0.08	0.14	0.10	0.10
SMI32	0.67	0.25	-1.34	1.39	0.009	0.011	0.19	0.53	0.14	0.13
SYN	0.18	0.32	0.83	1.09	-0.009	0.007	-0.18	0.35	0.12	0.14
TH	0.10	0.29	0.54	0.69	-0.007	0.005	-0.30	0.25	0.11	0.09
TF	0.21	0.32	0.52	0.77	0.003	0.006	-0.16	0.32	0.16	0.19
VGLUT1	0.57	0.26	-0.63	0.61	0.007	0.008	0.01	0.15	0.11	0.08

5

THE SUBCORTICAL COCKTAIL PROBLEM; MIXED SIGNALS FROM THE SUBTHALAMIC NUCLEUS AND SUBSTANTIA NIGRA

ABSTRACT

The subthalamic nucleus and the directly adjacent substantia nigra are small and important structures in the basal ganglia. Functional magnetic resonance imaging studies have shown that the subthalamic nucleus and substantia nigra are selectively involved in response inhibition, conflict processing, and adjusting global and selective response thresholds. However, imaging these nuclei is complex, because they are in such close proximity, they can vary in location, and are very small relative to the resolution used in most fMRI studies. Here, we investigated the consistency in localization of these nuclei in BOLD fMRI studies, comparing reported coordinates with probabilistic atlas maps of young human participants derived from ultra-high resolution 7T MRI scanning. We show that the fMRI signal reported in previous studies is likely not unequivocally arising from the subthalamic nucleus but represents a mixture of subthalamic nucleus, substantia nigra, and surrounding tissue. Using a simulation study, we also tested to what extent spatial smoothing, often used in fMRI preprocessing pipelines, influences the mixture of BOLD signals. We propose concrete steps how to analyze fMRI BOLD data to allow inferences about the functional role of small subcortical nuclei like the subthalamic nucleus and substantia nigra.

INTRODUCTION

The subthalamic nucleus (STN) and substantia nigra (SN) are small subcortical nuclei in the basal ganglia (Marani et al., 2008). Many cognitive neuroscience studies using BOLD functional magnetic resonance imaging (fMRI) have shown that the STN and SN are involved in a range of tasks such as response inhibition (Aron et al., 2007; Duann et al., 2009; Boehler et al., 2011a), conflict processing (Beauregard and Lévesque, 2006), force production (Vaillancourt et al., 2004; Spraker et al., 2007), working memory (Yoon et al., 2013; Yu et al., 2013), and the adjustment of global and selective response thresholds (Mansfield et al., 2011 Table 1). While several studies have shown the involvement of either the STN or the SN in tasks such as the stop-signal task or Simon task, several neurocomputational models make distinct functional predictions for these nuclei (Bogacz and Gurney, 2007; Frank et al., 2007). For instance, Frank et al. (2005; 2007) propose that the STN acts as a general brake, whereas the SN, through the release of dopamine, is activated by the correct response and inhibits the incorrect response. However, the small size and close proximity of the STN to the SN, as well as to the surrounding brain structures, frustrates precise localization and makes it challenging to attribute the BOLD signal to either STN or SN, respectively. A common procedure is to place a box of 10x10x10 mm on a center coordinate in the STN and extract the mean BOLD fMRI signal in this box, to estimate the signal change in the STN (Aron and Poldrack, 2006; Aron et al., 2007; Coxon et al., 2012). Note that the volume of such a box is about 7.5 times larger than the average STN volume reported in the literature (1000 mm3 compared to a weighted average of 119.88 mm3 and a weighted median of 131.75 mm3; Bonin and Shariff, 1951; Fussenich, 1967; Lange et al., 1976; Hardman et al., 1997; 2002a; Yelnik, 2002; Lévesque and Parent, 2005; Shen et al., 2009; Colpan and Slavin, 2010; Forstmann et al., 2012; Lenglet et al., 2012; Keuken et al., 2013; 2014a; Weiss et al., 2015). In combination with often-used smoothing procedures, the signals originating from the STN and SN will get mixed, making it difficult to unequivocally attribute signal to either structure (Lancaster et al., 2007; Stelzer et al., 2014).

The goal of this study was to investigate the consistency of the coordinates found in fMRI studies on the STN and SN, summarize the methods employed in these studies, and assess the severity of the problems with localization and mixture of signals. In a first step, we conducted a comprehensive literature search to characterize the methods resulting in significant functional activation in the STN and SN. In a second step, the peak coordinates of the STN and SN derived from these studies were compared to the location of recently published probability STN and SN ultra-high resolution 7T MRI atlas (Keuken et al., 2014a). Thirdly, using ultra-high resolution individual anatomical MRI masks, a simulation study was performed to test the influence of different smoothing kernels on the mixture of BOLD fMRI signals from both the STN and SN.

MATERIALS AND METHODS

SELECTION OF STN AND SN BOLD FMRI STUDIES

A comprehensive search for relevant neuroimaging studies in the field of BOLD fMRI studies including the STN and SN was carried out using Google scholar (http://scholar.google.com/). The main keywords utilized were 'fMRI + substantia nigra', 'fMRI + SN', 'fMRI + subthalamic nucleus', 'fMRI + STN', as well as all combinations of the aforementioned terms.

Based on the information contained in the abstracts of all the papers returned, empirical studies were selected to meet the following inclusion criteria: (1) Studies were published in peer-review English language journals between January 2000 and March 2014; (2) the studies used BOLD fMRI; (3) the studies reported a functional coordinate that could be attributed to either the SN or STN; and (4) the studies reported the location of activation as 3D coordinates in stereotactic space of Talairach or the Montreal Neurological Institute (MNI).

All empirical studies included were cross-referenced and all papers citing these empirical studies were searched, using the Google scholar citation index tool. The whole selection process was repeated for the newly obtained empirical papers until no new studies were found. This resulted in the inclusion of 52 papers (see Table 1).

All activation foci of the included studies that were originally reported in Talairach space were converted to the MNI stereotactic space using the Lancaster et al. transformation algorithm, which has been validated and shown to substantially reduce any bias between the two reference spaces (Lancaster et al., 2007).*

PROBABILISTIC ULTRA-HIGH RESOLUTION 7T MRI ATLAS MAPS

For analysis of the comparison between STN and SN coordinates reported in the literature (see Table 1), we used previously reported ultra-high resolution 7T MRI probability maps (Keuken et al., 2014a). The probability maps are based on 30 participants (14 females) with a mean age of 24.2 year (SD 2.4). The STN and SN masks were manually segmented by two raters for each individual on 7T zoomed multi-echo 3D FLASH MRI data with an isotropic voxel size of 0.5 mm (Haase et al., 1985). Only voxels rated by both raters as belonging to the STN or SN were included in further analyses. Note that no differentiation between the SN pars compacta and the pars reticulata was made because the voxel resolution and used scan sequence did not allow for identification of the two subparts. The individual masks were then linearly registered to MNI standard space and combined to create a probabilistic atlas. For more information regarding the segmentation, MRI scanning sequence, and registration procedure see Keuken et al. (2014a) and Forstmann et al. (2014). The structural data can be found on http://www.nitrc.org/projects/atag_mri_scans/ and on http://dx.doi.org/10.5061/dryad.fb41s. The probabilistic masks can be found on http://www.nitrc.org/projects/atag

Table 1. Literature overview of BOLD fMRI STN and SN studies.

M.S. Manual segmentation, TSE: Turbo spin echo, PD proton-density weighted, MT: Magnetization transfer, * a slice gap was used, ±: coordinates not displayed in Figure 1. The age is given in the mean years if provided, otherwise the range is given. N.S. not specified.

Author	Task	Age	Field Strength	fMRI resolution (mm)	voxel size (mm^3)	FWHM (mm)	Structure	Definition of ROI	MNI peak coordinate		
									x	y	z
Aron, 2004	Feedback-driven classification-learning	20-33	3	3.125x3.125x6*	58.59	8	SN/VTA	Search space: 15mm3 sphere (0,-15,-9)	-6	-21	-9
Aron and Poldrack, 2006	Stop-signal paradigm	29.2 (4.5)	3	3.125x3.125x4	39.06	5	STN	ROI: 10mm3 box (10,-15,-5)	8	-20	-4
							STN		6	-18	-2
							STN		10	-14	-4
							STN		14	-18	-4
		23.8 (3.7)		1.56x1.56x3	7.3	2	STN	M.S. TSE sequence	N.S.	N.S.	N.S.
Aron et al., 2007	Stop-signal paradigm	28.1 (4.1)	3	3.125x3.125x4	39.06	5	STN	ROI: 10mm3 box (10,-15,-5)	6	-18	-4
							STN		8	-16	-6
							STN		14	-8	-4
							STN		10	-14	-4

Table 1 (continued)

Author	Task	Age	Field Strength	fMRI resolution (mm)	voxel size (mm³)	FWHM (mm)	Structure	Definition of ROI	MNI peak coordinate		
									x	y	z
Baudrexel et al., 2011	Resting State	63.2 (8.7)	3	3x3x3*	27	5	STN	M.S. EPI sequence of 2 axial slices (z: -6 & -8)	-12	-14	-8
							STN		-14	-8	-6
Beauregard and Lévesque, 2006	Counting stroop	10.2 (0.8)	1,5	3.36x3.36x4	45.16	12	SN	Talairach atlas	-11.9	-19.3	-8.1
	Go/No-go		1,5	3.36x3.36x4	45.16	12	SN	Talairach atlas	-2.3	-12.3	-13.4
Boecker et al., 2008	Automated four-digit finger sequence	25.8 (4.7)	3	3.6x3.6x3.6	46.66	8	SN	Talairach atlas	-2.3	19.1	-18.3
							SN	Talairach atlas	1.2	-18.9	-15.6
Boehler et al., 2011a	Stop-signal paradigm	24.5 (n.s.)	3	3x3x3.3*	27	4	SN	Sig. voxels in the SN region	10	-22	-20
			3	3x3x3	27	8	SN	Sig. voxels in the SN region	12	-24	-14
							STN	Sig. voxels in the STN region	10	-16	-2
Boehler et al., 2011b	Visual discrimination	26 (n.s.)	3	2x2x3.6	14.4	6	SN	Visual inspection on mean PD sequence	8	-20	-14
							SN		-6	-18	-16

Table 1 (continued)

Author	Task	Age	Field Strength	fMRI resolution (mm)	voxel size (mm³)	FWHM (mm)	Structure	Definition of ROI	MNI peak coordinate		
									x	y	z
Brunenberg et al., 2012	Resting State	29.9 (n.s.)	3	1.56x1.56x3	7.3	3	STN	Talairach atlas	N.S.	N.S.	N.S.
Brydon et al., 2008	Checker board	18-35	1,5	N.S.xN.S.x3*	-	8	SN		-10	-16	-10
	Cognitive color-word stroop		1,5	N.S.xN.S.x3*	-		SN	ROI: 8mm sphere on peak voxel	-12	-2	-8
Bunzeck and Düzel, 2006	Visual oddball	23.9 (4.2)	3	3x3x3.3*	29.7	4	SN/VTA	M.S. sequence MT	8	-20	-18
							SN/VTA	M.S. sequence MT	12	-18	-20
Bunzeck et al., 2007	Visual oddball	65.3 (6.3)	3	3x3x3.3*	29.7	4	SN/VTA	M.S. sequence MT	0	-14	-12
Chase and Clark, 2010	Slot machine	33.7(1.8)	3	3.1x3.1x3	28.83	10	SN/VTA	Coordinates of Duzel et al. 2008	-8	-20	-14
						4	SN/VTA		-8	-18	-18
							SN/VTA		12	-16	-12
							SN/VTA		-6	-18	-16
Corlett et al., 2004	Three-stage retrospective revaluation	25 (5)	3	3.1x3.1x5*	48.05	8	SN	Pickatlas	14	-20	-5
							SN		-10	-18	-8
Coxon et al., 2010	Motor task switching	25.2 (n.s.) / 67.9 (n.s)	3	2.5x2.5x2.83*	17.69	10	STN	ROI: 10mm3 box (10,-15,-5)	10	-15	-5

Table 1 (continued)

Author	Task	Age	Field Strength	fMRI resolution (mm)	voxel size (mm³)	FWHM (mm)	Structure	Definition of ROI	MNI peak coordinate		
									x	y	z
D'Ardenne et al., 2012	AX-CPT	20-53	3	1.5x1.5x1.9	4.28	3	SN/VTA	Talairach atlas	-5.5	-11.1	-12.4
D'Ardenne et al., 2013	Sequential decision making	19-53	3	1.5x1.5x1.9	4.28	3	SN/VTA	M.S. sequence PD	-1.3	15.3	-17.3
							SN/VTA	M.S. sequence PD	-3.5	17.3	-18.6
							SN	M.S. sequence PD	13.8	22.6	-20.5
Duann et al., 2009	Stop-signal paradigm	22-45	3	3.4x3.4x4	46.24	10	STN	AAL atlas	N.S.	N.S.	N.S.
Fleming et al., 2010b	Perceptual decision making	23.9 (n.s.)	3	3x3x3*	27	8	STN	N.S.	-15	-18	0
Fleming et al., 2010a	Perceptual decision making	25.3 (n.s.)	3	3x3x3*	27	8	STN	ROI: 10mm3 box (10,-15,-5)	10	-15	-5
Guitart-Masip et al., 2011	Go/No-go	23 (1.72)	3	1.5x1.5x1.5	3.38	6	SN/VTA	M.S. sequence MT	8	-9	-10
							SN/VTA	M.S. sequence MT	-12	-19	-7
Guitart-Masip et al., 2012	Go/No-go	23.3 (5)	3	1.5x1.5x1.5	3.38	6	SN/VTA	M.S. sequence MT	12	-18	-10
							SN/VTA	M.S. sequence MT	-7	-22	-14
							SN/VTA	M.S. sequence MT	7	-20	15

Table 1 (continued)

Author	Task	Age	Field Strength	fMRI resolution (mm)	voxel size (mm³)	FWHM (mm)	Structure	Definition of ROI	MNI peak coordinate		
									x	y	z
Herz et al., 2014	Simon task	23 (3.9)	3	N.S.xN.S.x3.7*	-	8	SN/STN	ROI: 12 mm sphere (-10,-15,-5)	16	-8	-10
							STN		-14	-12	-6
Hu et al., 2013	Stop-signal paradigm	27.6 (5.5)	3	3.4x3.4x4	46.24	8	STN	Pickatlas	3	-25	-2
							STN		6	-13	-5
Jahfari et al., 2011	Simon task / Stop-signal paradigm	23.6 (n.s.)	3	2.3x2.3x3.3*	17.46	N.S.	STN	Anatomical ROI centered on 8,-9,-11	8	-9	-11
Kirsch et al., 2003	Nonaversive differential conditioning	23.3 (n.s.)	1,5	3x3x5	45	6	SN	Talairach atlas	-8.4	-15.8	-15.7
							SN	Talairach atlas	10.7	-24.9	-11.9
							SN	Talairach atlas	-8.3	-18.6	-10
							SN	Talairach atlas	10.7	-22.1	-17.6
Krebs et al., 2009	Reward anticipation paradigm	25 (2.9)	3	3.5x3.5x3.5	42.88	6	SN/VTA	N.S.	9	-18	-18
							SN/VTA		9	-12	-18
							SN/VTA		15	-15	-9

Table 1 (continued)

Author	Task	Age	Field Strength	fMRI resolution (mm)	voxel size (mm³)	FWHM (mm)	Structure	Definition of ROI	MNI peak coordinate x	y	z
Krebs et al., 2011	Reward anticipation paradigm	24.7 (2.1)	3	1.5x1.5x2	4.5	3	SN		12	-17	-8
Krebs et al., 2012	Spatial attention	21.7 (3.2)	3	3x3x3	27	6	STN	ROI: 2mm sphere on peak voxel	8	-16	-6
							SN/VTA		4	-14	-12
							SN/VTA		-2	-16	-14
							SN/VTA		2	-20	-16
							SN/VTA		-4	-14	-12
							SN/VTA		4	-12	-12
Lehericy, 2005	Complex motor sequence	22.9 (3.9)	3	1.5x1.5x2.5	5.63	10	STN	Atlas by Yelnik et al. 2003	-13.6	-16.2	-4.6
							STN		-11.5	-12.1	-7.1
							STN		11.7	-12	-9.4
							STN		-11.5	-12.1	-7.1

Table 1 (continued)

Author	Task	Age	Field Strength	fMRI resolution (mm)	voxel size (mm³)	FWHM (mm)	Structure	Definition of ROI	MNI peak coordinate		
									x	y	z
Lehericy, 2005	Complex motor sequence	22.9 (3.9)	3	1.5x1.5x2.5	5.63	10	STN		15.9	-11.9	-7.3
							STN		11.7	-12.1	-9.4
Lévesque et al., 2006	Counting stroop task	10.2 (1.3)	1,5	N.S.xN.S.x4	-	N.S.	SN	-	-11.9	-19.3	-8.1
Leunissen et al., 2012	Motor task switching	24.5 (n.s.) / 25.3 (n.s)	3	2.5x2.5x3.08*	19.25	10	STN	ROI: 10mm3 box (10,-15,-5)	8	-10	-8
							STN		-5	-10	-8
Mansfield et al., 2011	Task switching	23.4 (4.8)	1,5	4x4x4	64	8	STN	ROI: Forstmann et al. 2010 masks	N.S.	N.S.	N.S.
Marchand et al., 2012	Complex motor	27.7 (2.4)	3	3.4x3.4x3.3*	38.15	6	STN	Talairach atlas	N.S.	N.S.	N.S.
Menz et al., 2012	Probability discount	26.6 (4.2)	3	2x2x3*	12	8	SN/VTA	Coordinates of Schott et al. 2006	6	-20	-10
							SN/VTA		-8	-16	-12
							SN/VTA		-10	-16	-12
Monchi et al., 2006	Montreal card-sorting	23.4 (n.s.)	1,5	4.7x4.7x4.7	103.82	6	STN	Talairach atlas	-11.9	-24.3	-4.2
							STN		-9.8	-23	-13.4

Table 1 (continued)

Author	Task	Age	Field Strength	fMRI resolution (mm)	voxel size (mm³)	FWHM (mm)	Structure	Definition of ROI	MNI peak coordinate		
									x	y	z
Monchi et al., 2006	Montreal card-sorting	23.4 (n.s.)	1,5	4.7x4.7x4.7	103.82	6	STN		14	-20.1	-7.3
Murray et al., 2007	Reward learning	26 (3)	3	3.1x3.1x5*	48.05	6	SN/VTA	N.S.	10	-8	-6
							SN/VTA		-4	-16	-6
							SN/VTA		-8	-20	-6
							SN/VTA		12	-22	-4
							SN/VTA		-8	-20	-8
							SN/VTA		14	-16	-6
							SN/VTA		8	-22	-8
Preuschoff et al., 2006	Gambling	21.4 (n.s.)	3	3.28x3.28x3	32.28	8	STN	Talairach atlas	16	-18	-4.6
							SN		2.2	-18.8	-14.5
Prodoehl et al., 2008	Force production	20-37	3	3.125x3.125x3	29.3	N.S.	STN	BGHAT template	-10.5	-14.1	-5.8

Table 1 (continued)

Author	Task	Age	Field Strength	fMRI resolution (mm)	voxel size (mm³)	FWHM (mm)	Structure	Definition of ROI	MNI peak coordinate		
									x	y	z
Ray Li et al., 2008	Stop-signal paradigm	22-45	3	3.4x3.4x4	46.24	6	STN	ROI: 10mm3 box (10,-15,5)	-6	-21	-3
							STN		-6	-21	-3
							STN		9	-21	-6
							STN		-12	-12	-6
							STN		12	-12	-3
							STN		-12	-12	-3
							STN		12	-12	-3
							STN		-12	-15	-3
							STN		12	-15	-9
Robinson et al., 2009	Resting state	26 (5)	3	3.3x3.9x4*	51.48	0	STN	N.S.	N.S.	N.S.	N.S.
							SN	N.S.	N.S.	N.S.	N.S.
Schott, 2004	Associative memory	n.s. / 18-31	1,5	3.13x3.13x6*	58.78	8	SN	M.S. sequence MT	N.S.	N.S.	N.S.
Schott et al., 2008	Delayed monetary incentive task	22.8 (1.5)	3	3.5x3.5x2	24.5	6	SN/VTA	M.S. sequence PD	-7	-23	-18
Shohamy et al., 2008	Face scene association learning	18-24	3	3.125x3.125xN.S.	-	8	SN/VTA	ROI: 10mm3 sphere on peak voxel Adock et al. 2006	3	-18	-12

Table 1 (continued)

Author	Task	Age	Field Strength	fMRI resolution (mm)	voxel size (mm³)	FWHM (mm)	Structure	Definition of ROI	MNI peak coordinate		
									x	y	z
Spraker et al., 2007	Force production	20-35	3	3.125x3.125x3	29.3	5	STN	Talairach atlas	-10.5	-14.1	-5.8
Vaillancourt et al., 2004	Force production	21-35	3	3.125x3.125x5	48.83	N.S.	STN	Talairach atlas	N.S.	N.S.	N.S.
Vaillancourt et al., 2007	Force production	21-35	3	3.125x3.125x3	29.3	0	STN	Talairach atlas	-10.5	-14.1	-5.8
Wen et al., 2012	Resting state	55.3 (n.s.)	3	4x4x5	80	8	STN	ICA	9	-11	-3
							STN	Talairach atlas	-9	-12	-3
							SN	ICA	-9	-18	-12
Wittmann et al., 2005	Reward anticipation	22.9 (3)	1,5	3.13x3.13x6*	58.78	8	SN	Talairach atlas	7.4	-22.1	-16
							SN		11	-19.4	-12.8
Wittmann et al., 2007	Novelty	24.5 (4)	3	3x3x3	27	4	SN/VTA	Talairach atlas	5.3	-23.2	-15.8
							SN		14	-24.8	-10.2
							STN		-7.6	-11.7	-6.7
Yoon et al., 2013	Working memory paradigm	33.1 (10.7) / 28.8 (7.3)	1,5	3.4x3.4x4	46.24	2	SN	Pickatlas	-8	-16	-12
							SN		8	-16	-14
Yu et al., 2013	Working memory updating	28 (4.4)	3	3x3x3	27	4	SN/VTA	M.S. sequence MT	10	-12	-12

SIMULATION STUDY

A simulation study was performed to assess the amount of signal that originates from neighboring nuclei that can be introduced into a region of interest (ROI) by smoothing. Sixty STN and sixty SN masks (thirty masks in both hemispheres) from the ATAG (Atlas of The bAsal Ganglia) dataset (Keuken et al., 2014a) were used in a total of 60 simulations. All simulations used one STN and one SN mask at a voxel resolution of 0.5 mm isotropic. It was assumed that every voxel in each mask contained a signal of unit strength. Then, smoothing kernels of different sizes were applied, and for every voxel and for every nucleus, the amount of signal in that voxel originating from that nucleus was determined. If the entire signal came from the same nucleus, the value was 1. If no signal from that nucleus reached that voxel, the value was 0. The sum of the signal strengths of the two nuclei in a voxel could never surpass 1.

We focused on the mixture of signal in the center voxel of both masks, to emulate a ROI study where the ROI would be placed in the best possible voxel according to the ground truth. This is a very optimistic scenario considering the difficulty of STN/SN localization as discussed earlier. For every center voxel, two quantities were computed:

$$\text{mass}_{SN} = \sum_x \sum_y \sum_z \exp\left(-\left(\frac{(x - x_{com})}{2\sigma^2} + \frac{(y - y_{com})}{2\sigma^2} + \frac{(z - z_{com})}{2\sigma^2}\right)\right) \text{SN\_mask}[x, y, z]$$

and

$$\text{mass}_{STN} = \sum_x \sum_y \sum_z \exp\left(-\left(\frac{(x - x_{com})}{2\sigma^2} + \frac{(y - y_{com})}{2\sigma^2} + \frac{(z - z_{com})}{2\sigma^2}\right)\right) \text{STN\_mask}[x, y, z]$$

corresponding to the amount of signal originating from the SN and the amount of signal originating from the STN.

$[x_{com}, y_{com}, z_{com}]$ is the coordinate of the center-of-mass of the mask-

of-interest in millimeters. $\text{STN\_mask}[x, y, z]$ was either 1 or 0, corresponding to the coordinate $[x, y, z]$ being in the STN or not, $\text{SN\_mask}[x, y, z]$ analogously for the SN. σ is the standard deviation of the Gaussian kernel, which can be calculated for a given FWHM (full width at half maximum) by using the following formula:

$$\sigma = \frac{\text{FWHM}}{2\sqrt{2\ln(2)}}$$

RESULTS

OVERVIEW OF FUNCTIONAL MRI STN AND SN STUDIES

52 functional MRI studies were included in the present study (Table 1), published between 2003 and 2014. These studies employed for instance resting state, the stop-signal task, decision-making tasks including reward and outcome manipulations, and threshold adjustments in cognitive control tasks. Smoothing kernels ranged between 0 mm – 12 mm and data was collected on either 1.5T or 3T scanners. Note that not all studies report extensive methodological or procedural information, which limits the assessment of their anatomical specificity (Poldrack et al., 2008).

STN AND SN COORDINATES IN MNI SPACE COMPARED TO ULTRA-HIGH RESOLUTION 7T ATLAS MAPS

The reported STN and SN-coordinates were compared to the center-of-mass coordinates of the previously published 7T MRI probabilistic masks (Keuken et al., 2014a). Results are summarized in Table 2.

Table 2. Average deviation of reported coordinates from center of mass ATAG masks.
Distance of reported MNI coordinates from the center of mass of the corresponding ATAG STN probabilistic mask (for STN coordinates) or ATAG SN probabilistic mask (for all other coordinates, "SN", "SN/STN" and "SN/VTA") in millimeters (standard deviation). A coordinate with a higher X-value lies more to the right. A coordinate with a higher Y-value lies more anterior. A coordinate with a higher Z-value lies more superior

	N of reported coordinates (n of studies)	Distance in x	Distance in y	Distance in z	Total distance
Left hemisphere					
SN	12 (9)	1.0 (3.4)	0.5 (4.9)	0.6 (3.6)	5.6 (4.0)
SN/VTA	17 (11)	2.9 (2.8)	2.6 (11.8)	-0.3 (4.2)	9.1 (9.6)
STN	20 (12)	-0.9 (2.8)	-1.2 (4.4)	1.3 (2.8)	5.2 (3.3)
Right hemisphere					
SN	18 (10)	-0.9 (3.7)	-1.6 (11.1)	-1.8 (4.0)	8.9 (8.6)
SN/STN	1 (1)	5.5 (-)	8.2 (-)	2.2 (-)	10.1 (-)
SN/VTA	17 (11)	-2.6 (4.1)	-1.3 (4.5)	0.2 (3.8)	7.1 (2.6)
STN	17 (14)	-1.6 (2.9)	-3.7 (4.2)	3.0 (5.1)	7.3 (4.7)

On average, reported STN activity coordinates lay 5.2 mm (left hemisphere, std. = 3.3) and 5.7 mm (right hemisphere, std. = 2.8) from the center-of-mass of the 7T MRI probabilistic mask. Several studies include older participants (Bunzeck et al., 2007; Coxon et al., 2010; Baudrexel et

al., 2011; Wen et al., 2012). This might result in a mismatch between the reported coordinates and the probabilistic atlas because it is known that the STN shifts in lateral direction with age (Dunnen and Staal, 2005; Kitajima et al., 2008; Keuken et al., 2013). Note, however, that this lateral shift (on average 1.6 mm more lateral for elderly than for young participants; Keuken et al., 2013) is considerably smaller than the mismatch in location reported in the present study. The mismatch in location is predominantly observed in the dorsal-ventral and anterior-posterior direction such that the reported coordinates were on average 1.3 / 1.5 (left/right, std. = 2.8/2.5) mm more dorsal and 1.2 / 2.5 (left/right std. = 4.4/4.0) mm more anterior than the center-of-mass of the 7T probabilistic STN masks.
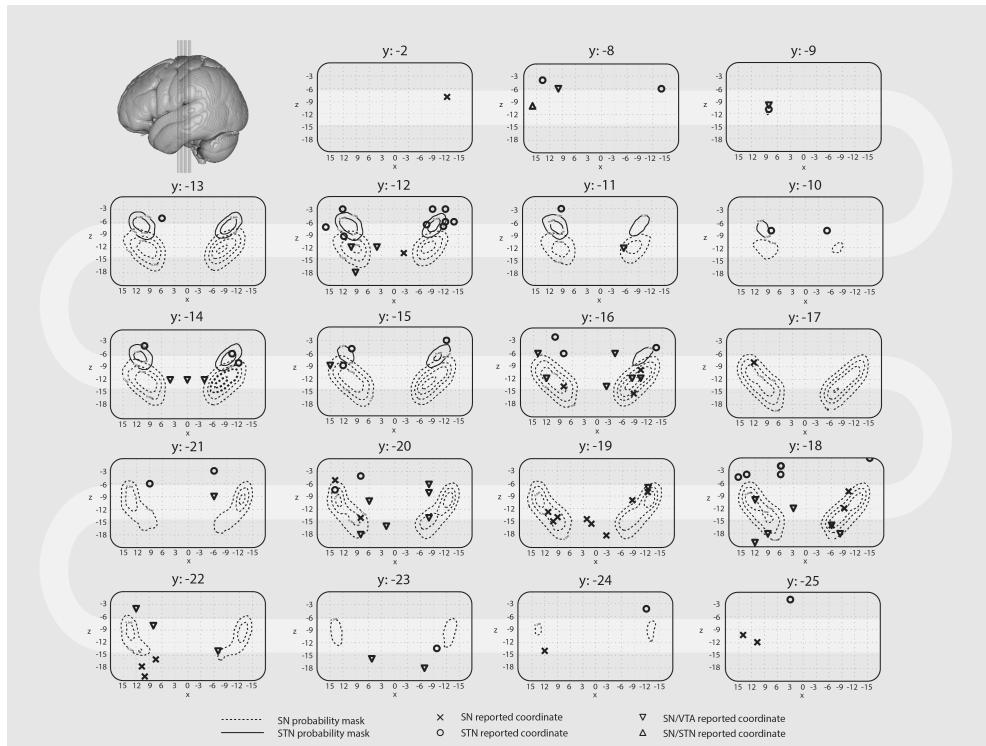
Figure 1. Location of individual peak coordinates of the STN and SN. Coronal slices in anterior to posterior direction are displayed together with functional coordinates of the STN, SN, SN/VTA, and SN/STN as reported in Table 1. Overlaid onto these coordinates is the probabilistic atlas of the STN and SN. The isolines reflect the percentage overlap across the 30 young subjects taken from Keuken et al. (2014a). The outermost isolines reflects a 10% probability of containing the SN at the population level, the more inner lines represent 30%, 50%, and 70% probability of containing the SN. The outermost isolines for the STN reflects a probability of 20% containing the STN, the inner line represent 40% probability of containing the STN. The grid size corresponds to a voxel size of 3x3 mm. All coordinates are in MNI standard space.

The left STN coordinates were on average 0.9 mm (std. = 2.8) more medial than the center-of-mask of the 7T MRI probabilistic mask, and the right STN coordinates lay on average 0.4 mm (std. = 3.2) more lateral. The average distance between the centers-of-mass of the SN and STN of the probabilistic masks is in the same order of magnitude as the distance between the

average reported STN fMRI location and the actual STN center-of-mass (6.4 mm left, 6.7 mm right; std. = 0.7 / 0.7).

Reported SN activity coordinates were on average 5.6 (left hemisphere, std. = 4.0) and 8.9 (right hemisphere, std. = 8.6) mm away from the center of mass of the 7T MRI probabilistic mask. Shifts occurred in all three directions.

Figure 1 shows coronal plots of the probabilistic maps with the reported coordinates rendered onto them. Only coordinates that lay within the MNI coordinate range of x: 18,-18 / z: 0,-21 / y: -2,-25 were plotted. The coordinates that fell outside of this range are marked in Table 1.

The average FWHM of the smoothing kernel was 6.3 mm (median 6 mm). A smoothing kernel of 8 mm FWHM was used most frequently (16 out of 52 studies: see Figure 2 for the relative size of the kernels used compared to the STN and SN). There was no relationship between the nucleus of interest and the smoothing kernel used.
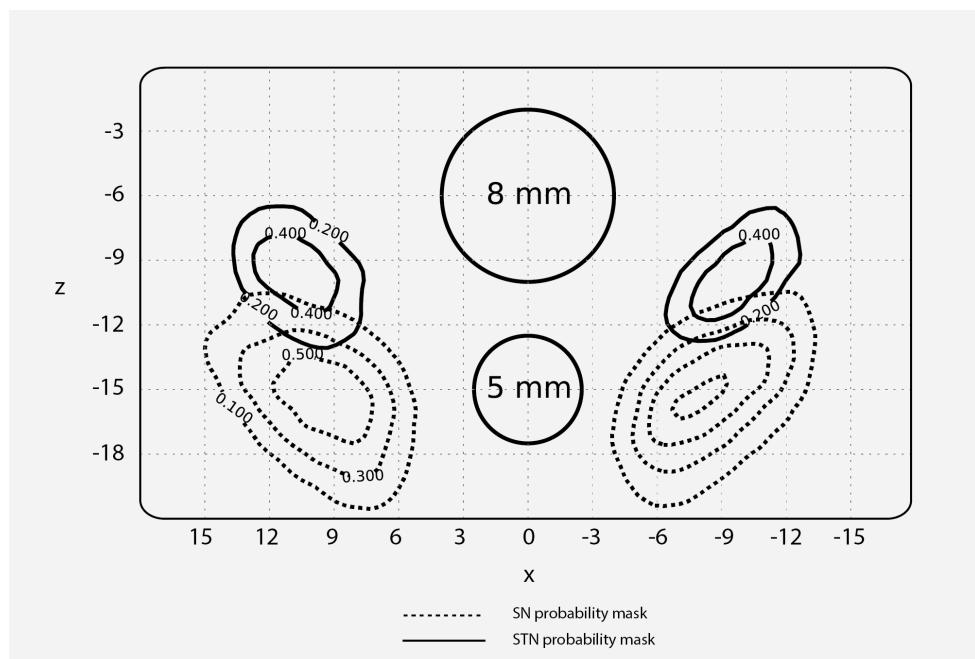

Figure 2. Relative size of a standard FWHM diameter compared to the STN and SN.
A zoomed-in coronal slice (MNI y-coordinate: -14) showing the STN and SN. Two circles are shown in the middle to indicate the diameter of 2 frequently used FWHM smoothing kernels. The isolines reflect the percentage overlap across the 30 young subjects taken from Keuken et al. (2014a).

To test for any spatial biases introduced by smoothing, as reported by e.g. Sacchet et al., (Sacchet and Knutson, 2013) for the nucleus accumbens, MNI coordinates were correlated with the size of the smoothing kernel employed. No correlations were found except for the SN ($r(45)=.83$, $p <0.05$, uncorrected), which lay more superior as a function of a larger smoothing kernel. The majority of studies (47 out of the 52) reported the voxel resolution. The voxel resolution was on average 34 mm^3 (median 32 mm^3, std. = 21 mm, range 3.4 – 103.8 mm).

SN probability mask
STN probability mask
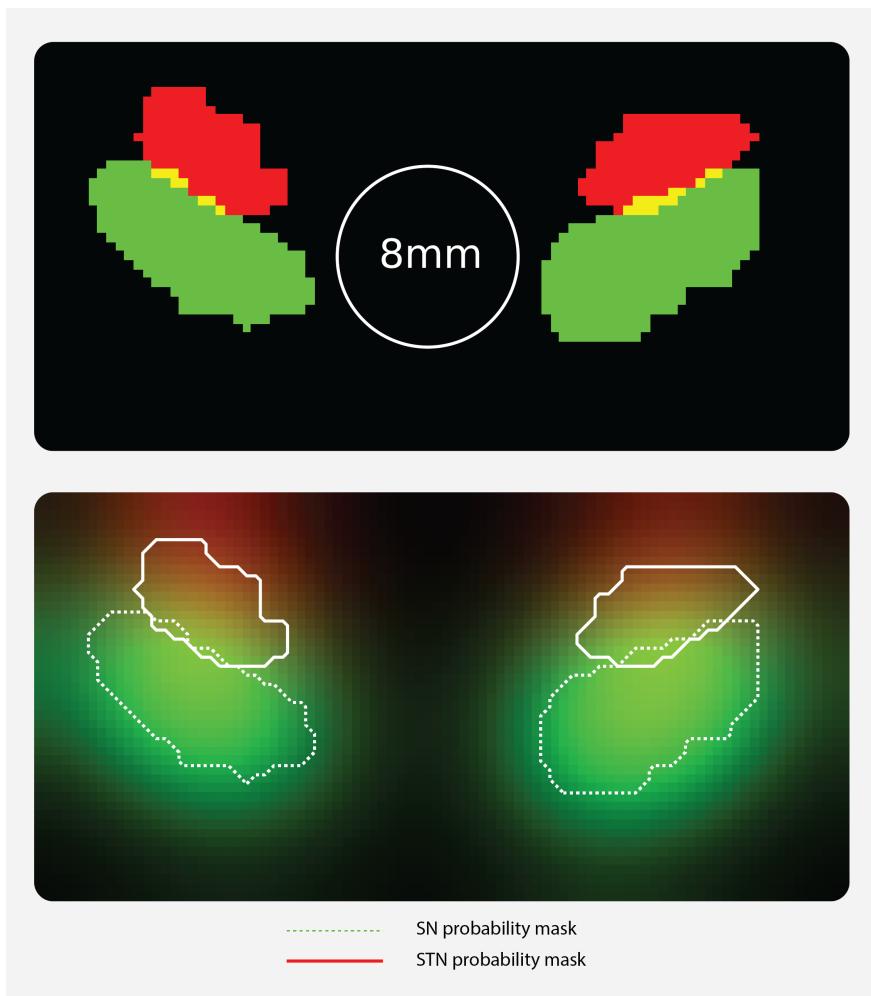
Figure 3. Illustration of effect of smoothing on mixture of BOLD signals between SN and STN. Four binary, individual masks are displayed of one representative participant smoothed with an 8 mm FWHM smoothing kernel.

Figure 3 qualitatively illustrates the effect of an 8 mm FWHM smoothing kernel on individual masks of the left and right STN and SN. The result shows that signal originating from each nucleus spreads widely, also across its neighbor's boundaries (Figure 4).

After a smoothing kernel with an FWHM of 0mm is applied, the signal in the center voxel still originates completely from its nucleus. When a 4 mm FWHM smoothing kernel was used, 30% of the signal in the center voxel of the STN was found to originate from outside the STN and SN, while 10% originated from the SN and 60% from the STN itself. With an often-used 8 mm FWHM smoothing kernel, 75% of the signal in the center voxel of the STN mask originated from outside the STN and SN, 10% originated from the SN and only 15% from the STN itself. For this

simulation, the strength of the STN signal in the center voxel was assumed to be similar in size to the signal originating from the SN. Note that the results would vary if different signal strengths in both nuclei were assumed. However, the precise ratios have little effect on this finding. Importantly, this simulation shows that with large smoothing kernels it becomes impossible to disentangle the origin of the measured signal, even when focusing on the most central voxel. In empirical fMRI studies this is an unlikely scenario, because the voxel resolution is at an average of 34 mm3, instead of the 0.064 mm3 (0.4 mm isotropic) used here. In sum, the mixing of signals is likely to be substantially worse in empirical fMRI studies compared to this simulation study.
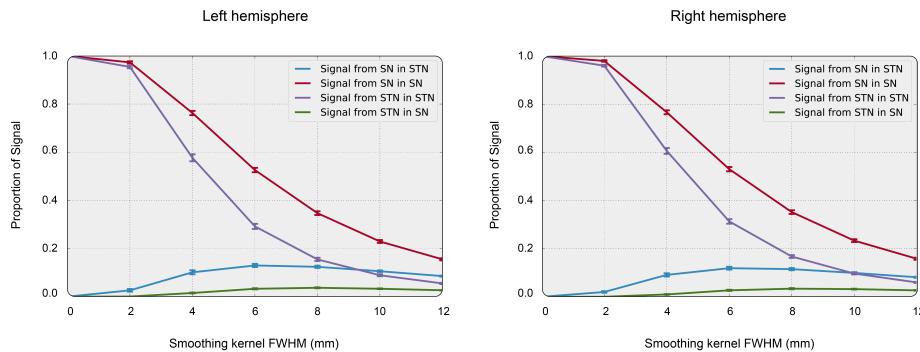

Figure 4. Simulation results: Effect of smoothing on mixture of BOLD signals between SN and STN. Summary of the smoothing simulation study. For both hemispheres, in 30 subjects taken from Keuken et al. (2014a), the effect of smoothing on the mixing of signals in STN and SN in their respective center voxels was estimated. The lines show the amount of signal for different source-destination pairs of STN and SN as a function of smoothing kernel size. When no smoothing is applied, all signal in the SN originates from SN and all signal in STN originates from the STN. When more smoothing is applied, the amount of signal originating from the nucleus that is measured sharply decreases, and within the STN the amount of signal from the SN becomes equal in size to the signal originating from the STN itself.

DISCUSSION

In the present study, we showed that there is large variability in previously reported fMRI coordinates attributed to the STN and SN. We also show a discrepancy between individual coordinates of empirical studies and probabilistic atlas maps derived from ultra-high resolution 7 T MRI (Keuken et al., 2014a). The resolution of the fMRI sequences reported in the included studies was usually low. The average voxel resolution was 34 mm^3 (median 32 mm^3; std 21 mm^3). Over the past years, the voxel resolution has increased on 3T scanners. For all studies published since 2010 on 3 T, mean voxel size was 22 mm^3 (median 23 mm^3; std 18 mm^3). There is a significant correlation between year-of-publication and voxel size (r(115) = -0.31, p<0.001). However, half of the studies published in 2013 and later (n=9) still use a coarse voxel resolution; on average they used a resolution of 24 mm^3 (median 27 mm^3, std 20 mm^3), which results in only approximately 5 voxels covering the STN.

The simulation results reveal that when smoothing kernels of commonly used sizes are applied, the amount of signal from neighboring nuclei that get smoothed into a region of interest is of similar size as the signal from the region itself. This is particularly important when analyzing data from a small nucleus such as the STN, which borders the larger SN.

These results add empirical data to the recent discussion about smoothing in functional neuroimaging. Stelzer et al. (2014) suggested that smoothing fMRI data should be abandoned altogether, because it (1) causes incorrect estimation of the true spatial extent of brain activation, (2) blurs away signals of limited spatial extent, and (3) frustrates the detection of low-intensity signals in the vicinity of non-active tissue. Our results illustrate quantitatively how large these effects can be, specifically for subcortical nuclei: we show that reported MNI coordinates largely non-overlap with anatomical masks (point 1) and that smoothing can induce substantial mixing with signal from outside the nucleus (point 2 and 3).

The use of smoothing can increase the signal-to-noise ratio in fMRI when the signal is more spatially correlated than the noise on the scale of the smoothing kernel employed. However, in the case of subcortical nuclei, the used smoothing kernels are often too large and mix in signal and noise from neighbouring structures. Yoon et al. (2013) provide an empirical example of the influence of kernel size in their supplemental information: the activity in the SN only reached a significance threshold when a smoothing kernel with a very minor FWHM of 2 mm was employed. When a smoothing kernel with an FWHM of 8 mm was used, the effect disappeared. Because the voxel size of this study was rather large, 3.4x4x4 mm, the effect of a 2 mm smoothing kernel was negligible and could have been abandoned altogether. When one applies such a relatively large smoothing kernel to data of such a relatively coarse resolution, the amount of signal in a voxel in the smoothed image originating from outside this voxel is less than 0.2%[1]. The results by Yoon et al. thus clearly show that smoothing is not necessary to find significant effects in the substantia nigra region, even at 1.5 T (Yoon et al., 2013).

It has been suggested that a lack of spatial resolution and anatomical specificity could be overcome by using unsupervised clustering algorithms such as principal component analysis (PCA) or independent component analysis (ICA). These methods might 'detect' the nucleus of interest by exploiting the different covariance structures of the BOLD signal in different nuclei. We think, however, that such an approach is not appropriate. First and foremost, it assumes that the task-related BOLD activity in the STN and SN are uncorrelated. This is highly unlikely because both nuclei are part of the same functional networks, e.g., the basal ganglia motor control loops. Secondly, even if the signal could be separated to some extent, there is no objective way of finding out which cluster component belongs to which nucleus and to which extent they account for only one nucleus. Third, independent components might represent non-BOLD signals such as physiological noise. Fourth, the most adequate procedure of defining the actual signal of the nucleus of interest by means of, e.g., a demixing matrix (van Maanen et al., 2011) or a Gaussian sphere (Erika-Florence et al., 2014) remains elusive.

Therefore, we suggest that during functional imaging of small subcortical nuclei, standard smoothing strategies should be avoided altogether. More complex, adaptive smoothing approaches (Tabelow et al., 2009) might be useful, but analysis protocols that do not require smoothing should be preferred. A-priori ROI analyses (Poldrack, 2006) do not require smoothing, nor do whole-brain univariate analysis approaches that make use of False

---

[1] See http://nbviewer.ipython.org/gist/Gilles86/0c093962de8cf05f76c8

Discovery Rate (FDR) as multiple comparison correction, as well as multivariate analysis strategies (O'Toole et al., 2007; Stelzer et al., 2013; 2014).

Concretely, we propose an approach that maximizes both anatomical specificity and signal-to-noise. Researchers are advised to use individual anatomical masks based on an appropriate MR contrast (i.e., T_2*(-weighted) or quantitative susceptibility mapping, QSM) that allows for detailed visibility and segmentation of the structures of interest (Forstmann et al., 2010; 2012; Keuken et al., 2013; Lefranc et al., 2014; Keuken et al., 2014a). When individual segmentation is not feasible, researchers can use probabilistic atlas maps, as provided for the STN and SN in Keuken et al. (2013; 2014a) and Forstmann et al. (2012). If the research question does not focus on anatomical patterns within the nucleus itself, the mean signal across all voxels in the nucleus can be analysed. This maximizes SNR and removes both the multiple comparisons problem, as well as the need for registration to a standard space. When different activation patterns within the nucleus are expected, a voxel-wise analysis within the anatomical mask can be computed.

Given the variability in reported coordinates and smoothing, one may question the validity of earlier fMRI findings in the STN/SN. It is important to note that studies with Parkinson Disease patients using deep-brain stimulation (DBS; Cavanagh et al., 2011) or lesioning of the STN (Jahanshahi et al., 2015) deliver important causal evidence for the functional role of the STN in motor control. Functional MRI studies that report BOLD activity in motor control paradigms are thus likely to be sensitive to actual task involvement. However, we believe that caution is warranted in interpreting the anatomical specificity of these findings. In conclusion, the mixing of signals might be most prominent in studies that 1) use smoothing kernels with a FWHM of more than 4 mm, 2) do not use anatomical masks that are based on individual anatomy, either individually segmented or based on a population probabilistic map like the ATAG dataset (Keuken et al., 2014a), and finally, 3) use voxel resolutions that are in the same order of magnitude as the nucleus itself.

Finally, the present study provides evidence for the importance of accounting for individual anatomy when attempting to understand the functional role of small subcortical areas such as the STN and SN. Moreover, the combination of ultra-high resolution fMRI with a very high voxel resolution and zoomed-in acquisition protocols help to unmix signals arising from small subcortical structures in very close proximity. Lastly, the simulation results indicate that spatial smoothing should be avoided.

6

COMPARING FUNCTIONAL MRI PROTOCOLS FOR SMALL, IRON-RICH BASAL GANGLIA NUCLEI SUCH AS THE SUBTHALAMIC NUCLEUS AT 7 T AND 3 T

ABSTRACT

The basal ganglia (BG) form a network of subcortical nuclei. Functional magnetic resonance imaging (fMRI) in the BG could provide insight in its functioning and the underlying mechanisms of Deep Brain Stimulation (DBS). However, fMRI of the BG with high specificity is challenging, because the nuclei are small and variable in their anatomical location. High resolution fMRI at field strengths of 7 Tesla (T) could help resolve these challenges to some extent.

A set of MR protocols was developed for functional imaging of the BG nuclei at 3 T and 7 T. The protocols were validated using a stop-signal reaction task (Logan et al., 1984). Compared to sub-millimeter 7 T fMRI protocols aimed at cortex, a reduction of echo time and spatial resolution was strictly necessary to obtain robust Blood Oxygen Level Dependent (BOLD) sensitivity in the BG. An fMRI protocol at 3 T with identical resolution to the 7 T showed no robust BOLD sensitivity in any of the BG nuclei.

The results suggest that the subthalamic nucleus, as well as the substantia nigra, red nucleus, and the internal and external parts of the globus pallidus show increased activation in failed stop trials compared to successful stop and go trials.

INTRODUCTION

The basal ganglia (BG) are a set of subcortical nuclei (the subthalamic nucleus, STN; the substantia nigra, SN; the globus pallidus, pars interna, GPi; the globus pallidus, pars externa (GPe); and, outside of the subcortex, the striatum, STR), that play a crucial role in functions such as action selection, cognitive control, and response inhibition (Alexander and Crutcher, 1990; Parent and Hazrati, 1995a; Redgrave et al., 1999; Middleton and Strick, 2001; Frank, 2006; Redgrave et al., 2010; Aron, 2011). These nuclei project to large parts of the cortex, possibly within discrete "cortical-subcortical loops" that correspond to different functional domains such as cognition, motor control, and emotion (Alexander and Crutcher, 1990; Temel et al., 2005b; Keuken et al., 2012). Malfunctioning of the BG is implicated in many clinical conditions, including Parkinson's disease (PD), Huntington's chorea, schizophrenia, attention deficit disorder (ADHD), and addiction.

Deep brain stimulation (DBS) of BG nuclei, in particular the STN, is an important therapy in PD. However, the precise underlying mechanisms of this therapy are poorly understood and severe side-effects can occur, possibly because of modulations of different cortical-subcortical loops than the motor control loop (Temel et al., 2005b; Ineichen et al., 2014; Fasano and Lozano, 2015).

Functional neuroimaging in healthy and clinical human populations could help elucidate the functional mechanisms of the BG in health and disease, as well as provide a mechanistic explanation of therapeutic benefits and side-effects of DBS. However, in the BG the anatomical specificity of traditional functional Magnetic Resonance Imaging (fMRI) techniques is limited, because the nuclei in the BG are very small compared to the voxel size of most functional MRI protocols. For example, with a voxel size of 3 mm isotropic, a commonly used voxel size in 3 T fMRI studies, the entire STN can be covered in 4-5 voxels, assuming only small partial volume effects (the STN has a volume of approximately 100 mm3; Keuken et al., 2014a; de Hollander et al., 2015; Zwirner et al., 2017). This is especially problematic because a related nucleus, the SN, lies directly adjacent to the STN (and also other related nuclei, such as the red nucleus, RN, are only a few millimeters away). At lower resolutions, it becomes very likely, due to partial volume effects, that functional signals from the SN are intermixed with those from the STN (de Hollander et al., 2015). A related problem is that individual anatomy is usually not taken into account: it is assumed that whole-brain registration to a standard space (e.g., MNI152), based mostly on image contrast between gray and white matter in cortex, is sufficient to achieve millimeter precision and perfect across-subject anatomical overlap of subcortical nuclei in the standard space. This assumption is problematic. An anatomically more precise approach would entail labelling the nuclei-of-interest in individual space. However, visualizing the location of the nuclei of the BG in the individual brain at lower field strengths than 7 T is very challenging (Schäfer et al., 2011; Plantinga et al., 2014; de Hollander et al., 2015).

The use of Ultra-High Field Magnetic Resonance Imaging (UHF-MRI; MRI with field strengths of 7 T and above) could help increase the anatomical specificity of functional neuroimaging of the BG, because its increased signal-to-noise ratios (SNR) potentially allow for substantially decreased voxel sizes of less than one millimeter isotropic (van der Zwaag et al., 2016). The increased spatial specificity, combined with the high-quality structural images at UHF-MRI, permits the testing of hypotheses about the functional specialization of the different BG nuclei, as well as putative subdivisions within these nuclei. For example, a prominent theory about the

STN is that it has three subdivisions, distinctly connected to 'motor', 'cognitive', and 'limbic' cortical networks (Temel et al., 2005b; Keuken et al., 2012).

However, experiences in and outside of our lab suggest that "off-the-shelf" fMRI protocols at 7 T, originally developed for functional imaging in the cortex, do not achieve an acceptable temporal signal-to-noise ratio (tSNR) in the BG, precluding robust Blood Oxygen Level Dependent (BOLD) sensitivity (see also Barry et al., 2013).

The low tSNR obtained in the BG with UHF fMRI is most likely due to a combination of at least three complicating factors. First, the BG have very high concentrations of iron, which leads to substantially reduced T_2* relaxation values, especially at higher field strengths (Aquino et al., 2009; Schweser et al., 2011; Langkammer et al., 2012; Deistung et al., 2013; Keuken et al., 2013; de Hollander et al., 2014a). The phenomenon underlying all common fMRI measurements is the so-called BOLD-effect (Ogawa et al., 1990): a difference in T_2* relaxation values between paramagnetic deoxyhemoglobin and diamagnetic oxyhemoglobin (Logothetis, 2008). The theoretically optimal echo time (TE) for a single-echo T_2* weighted fMRI protocol is therefore equal to the baseline T_2* of the tissue-of-interest (Norris, 2006). At this point during the decay, the shift in signal resulting from a small change in T_2* is greatest (see Figure 1). One of the main advantages of UHF-MRI is the increased contrast in T_2* weighted images, because there is more variance in T_2* relaxation values across the brain (Peters et al., 2007; van der Zwaag et al., 2016). However, this increase in variability of baseline T_2* relaxation times across the brain also comes with increased variability in the optimal TE for fMRI. The baseline T_2* relaxation value for the cortex is approximately 25-35 ms at 7 T, whereas the baseline T_2* relaxation value for the STN in young healthy participants, as well as many other BG nuclei in the subcortex, is roughly 15 ms (Yacoub et al., 2001; Peters et al., 2007; van der Zwaag et al., 2009; Keuken et al., 2013). Hence, the TE of most echo-planar based (EPI) protocols at 7 T targeted at cortex is too long to acquire a reliable BOLD contrast in the BG: the MR signal has almost completely decayed by the time of signal readout.

A second complicating factor for UHF fMRI in the BG is their location deep in the brain. As a consequence, the BG lie relatively far from all the receive elements of a typical head coil, as well as approximately equidistant to them. The sensitivity of the different receiver coils to signal from the BG is therefore not only relatively low, but also roughly equal across coils. Therefore, parallel imaging techniques, such as GRAPPA and SENSE are less effective in the BG, because they exploit differences in the sensitivity profiles of the receiver coils. This well-known issue of having a higher noise level in the center of the brain when using parallel imaging techniques is called the "g-factor penalty" (Sodickson and Manning, 1997; Pruessmann et al., 1999; de Zwart et al., 2002; Griswold et al., 2002; Setsompop et al., 2016). In whole-brain UHF fMRI this is especially unfortunate, because at such high field strengths, parallel imaging is essential. The increased resolution in UHF fMRI, resulting in prolonged echo trains, in combination with reduced T_2* relaxation values calls for parallel imaging to overcome geometric distortions and to achieve sufficiently short TE's and an acceptable temporal resolution (de Zwart et al., 2002; Setsompop et al., 2016; van der Zwaag et al., 2016).

A third complicating factor is the relatively increased physiological noise at UHF compared to lower field strengths (Triantafyllou et al., 2005). It is well known that cardiac and respiratory artefacts are especially prominent in the more inferior parts of the brain, close to areas of major cerebral spinal fluid (CSF) flow, such as the interpeduncular fossa, and junctions of major arteries such as the circle of Willis. However, Barry and colleagues (2013) showed that although

signal variance is much higher in the subcortex than in cortex, only little of this variance can be explained by cardiac, respiratory, and CSF dynamics in 7 T fMRI. The authors speculated that these unexplained sources of noise might have a neural origin and are related to intrinsic functional connectivity, unrelated to the particular task at hand (Barry et al., 2013). Independent of the source of the noise, these results suggest that the task-related BOLD contrast is contaminated with noise that is difficult to filter out using physiological regressors.
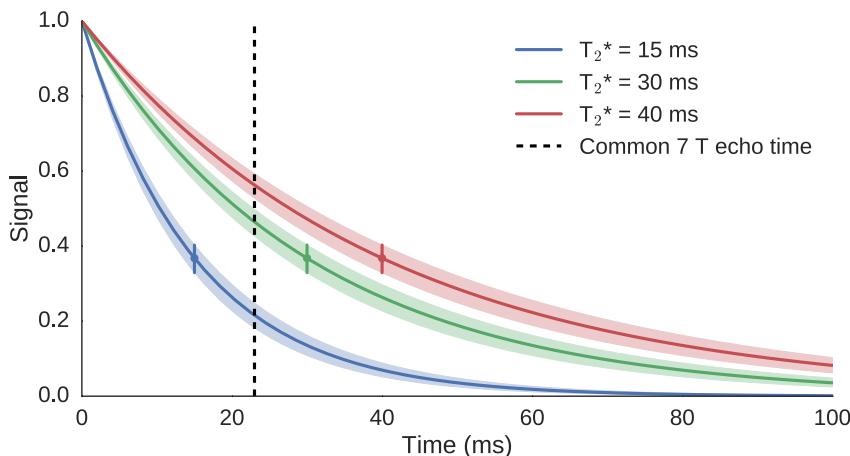

Figure 1. Signal decay curves for different T_2* relaxation value. At 7 T, the T_2* relaxation value for STN is approximately 15 ms, whereas the relaxation time in the cortex is approximately 30 – 40 ms. The dotted line indicates a common echo time at 7 T of 22 ms. Clearly, the signal in the cortex is still strong at this point in time, but the signal in the STN has largely faded. Colored dots indicate the signal of the T_2* curve at its respective T_2* value. The shaded area shows the change in signal corresponding to a T_2* value up- or downshift of 10%. Note that this signal change is largest around the baseline T_2* value.

Therefore, in order to detect neural activity in the STN, in this study we investigated the BOLD sensitivity of multiple fMRI protocols with different parameter sets using 7 T MRI in the BG. We asked how TE and resolution can be adjusted such that the aforementioned problems can be overcome and an optimal combination of BOLD sensitivity and spatial and temporal resolution is achieved (see Table 1). In addition to TE and resolution, acceleration factors were also systematically covaried with resolution. Higher resolutions lead to longer readout times. Therefore, the acceleration factors of the protocols at the highest resolution also had to be increased, to obtain sufficiently short TEs. The protocols were evaluated while participants performed a stop-signal task, a prominent paradigm in cognitive neuroscience and for which ample work suggests that especially the STN plays an important role (Aron and Poldrack, 2006; Aron, 2007; Aron et al., 2014a). Drawing on other prominent neurocomputational models of the role of the BG in perceptual decision-making and action control, we speculated that other BG nuclei would likely also show heightened activity in all conditions when compared to baseline (Gurney et al., 2001; Frank and Claus, 2006; Bogacz and Gurney, 2007).

Recently, BOLD activity has been reported in small subcortical nuclei in the subcortex at lower field strengths (3T and below; de Hollander et al., 2015), and even functional subdivisions in the substantia nigra were reported in a study using 3T (Pauli et al., 2015). As fMRI at 3 T is much

less costly and challenging than fMRI at higher fields, ultra-high field fMRI should only be used when lower-field strengths cannot provide the necessary BOLD sensitivity and anatomical specificity. Therefore, to justify the need for 7T fMRI, we also directly compared BOLD sensitivity of a 3 T protocol to the best-performing 7 T protocol, using the same resolution and an identical experimental paradigm, but otherwise parameters optimized for 3 T. The 3 T protocol was as similar as possible to the protocol reported in the recent study by Pauli and colleagues (2015) that reported functional subdivisions in the SN.

METHODS

STRUCTURAL MRI

Identifying the nuclei of the BG in individual anatomical scans is crucial to distinguish BOLD signals from different nuclei, but remains a challenge, especially at 3 T (de Hollander et al., 2015). Therefore, for 14 participants, high-quality anatomical scans acquired at 7 T and individual anatomical BG masks of an earlier study by Keuken et al. (2014a) were used. The masks were based on a set of multi-echo T_2* weighted anatomical FLASH volumes at a resolution of 0.5 mm isotropic (Haase et al., 1985; Forstmann et al., 2014). These T_2* weighted images were used to draw masks of the SN, STN, and red nucleus (RN) following a strict protocol (see Keuken et al., 2014 for details). They were also used to calculate Quantitative Susceptibility Mapping images (QSM; Langkammer et al., 2012). These QSM images were used to draw individual anatomical masks of the GPi and GPe. The masks were drawn by two independent, trained raters. The conjunct voxels of these two masks were used as the final Region-of-Interest (ROI) in all analyses. In other words, only voxels that were labeled as inside the nucleus-of-interest by both raters were used for signal extraction. Exploratory analyses using disjunctive masks (containing all voxels rated as in-the-nucleus by at least one of the raters) showed comparable results as those with the conjunct masks, indicating that the choice for conjunct masks is not crucial for our results.

For the remaining 6 participants, an identical anatomical 7 T scan and anatomical labeling protocol as in the original Keuken et al. (2014) study was performed specifically for this study.

For all participants, a 0.7 mm isotropic T_1 weighted image was acquired using the MP2RAGE sequence at 7 T (Marques et al., 2010) with the following parameters: repetition time (TR) = 5000 ms; TE = 2.45 ms; inversion times TI1= 900; TI2 = 2750 ms; flip angle 1 = 5°; flip angle 2 = 3°. This anatomical scan was used to allow for registration and transformation of statistical parametric maps (SPMs) to MNI152 standard space.

Also at the 3 T scanner anatomical images were collected. The anatomical images used here were based on a 4-echo 1 mm isotropic FLASH protocol (128 slices; TEs of 9.84 ms, 17.22 ms, 24.60 ms, and 31.98 ms; TR = 43 ms, flip angle = 15°). The resulting T_2*-weighted images were used to estimate T_2*-relaxation times for the different nuclei-of-interest at 3 T. Also, these data were registered to the 7 T FLASH images and the 3T functional data. The resulting transformation matrices were used to transform the individual anatomical masks based on the 7 T FLASH images to the 3 T functional data.

FUNCTIONAL MRI PROTOCOLS

Three different 2D-EPI protocols were tested at 7 T (see Table 1). Protocol 1 and 2 were designed to have a relatively high spatial resolution (1.2 mm isotropic) and were equal in all parameters, except TE (22 vs 15 ms). Protocol 1 and 2 were thus designed to investigate the effect of TE on the detected BOLD signal. For protocol 3, to increase SNR at the cost of spatial specificity, the voxel resolution was considerably reduced to 1.5 mm isotropic. This led to smaller matrices and readout times, so the GRAPPA factor and echo time could be decreased, resulting in an even higher SNR. We chose to optimize parameters as much as possible for a given resolution, rather than doing an exhaustive, full parameter sweep, which would be extremely expensive. In other words: we chose not to run protocol 3 with a GRAPPA-factor of 4, like protocol 1 and 2, because it was not necessary at that resolution and would be detrimental to the image quality.

Table 1 Parameters of the fMRI protocols that were tested

	Protocol 1	Protocol 2	Protocol 3	Protocol 4
Field strength	7 T	7 T	7 T	3 T
Resolution	1.2x1.2x1.2 mm^3	1.2x1.2x1.2 mm^3	1.5x1.5x1.5 mm^3	1.5x1.5x1.5 mm^3
TE	22 ms	15 ms	14 ms	30 ms
TR	2 s	2 s	2 s	2 s
Flip Angle	75°	75°	60°	81°
Grappa factor	4	4	3	2
Matrix size	150 x 150	150 x 150	128 x 128	64 x 64
Number of slices	38	38	60	26
Bandwidth	1450 Hz/Px	1450 Hz/Px	1446 Hz/Px	1396 Hz/Px
Partial Fourier	6/8	6/8	6/8	-
Number of subjects	5	5	20	10

Protocols 1-3 were acquired at a Siemens MAGNETOM 7 T system (Siemen Medial Solutions, Erlangen, Germany), using a 32-channel head array Nova coil (NOVA Medical Inc., Wilmington MA). For protocol 1, which consisted of 3 runs of 515 volumes with 38 slices, respectively, the acquisition time was 17:10 min per run. The other parameters were as follows: TR = 2000 ms, TE = 22 ms, flip angle = 75°, bandwidth 1450 Hz/Px, echo spacing 0.81 ms, voxel size = 1.2 mm isotropic, Field-of-View (FOV) 180 x 180 x 45.6 mm, phase encoding direction A >> P, partial Fourier 6/8, GRAPPA acceleration factor 4, matrix size 150 x 150.

Protocol 2 was identical, except that the TE was decreased to 15 ms.

Note that the Ernst angle for the STN is approximately 80°, assuming a T1 value of approximately 1200 ms (Keuken et al., 2017). However, because of limitations due to the Specific Absorption Rate (SAR), for protocol 1 and 2, a flip angle of 75° was used.

Protocol 3 also consisted of 3 runs of 515 volumes and it also took 17:10 min to acquire. This protocol entailed 60 slices with a voxel size of 1.5 mm isotropic. This allowed for a FOV that covered almost the entire brain, but excluded the most superior part of the brain for most participants. The other parameters were as follows: TR = 2000 ms, TE= 14 ms, flip angle = 60°, bandwidth 1446 Hz/Px, echo spacing 0.8 ms, FOV 192x192x97mm, phase encoding direction A >> P, partial Fourier 6/8, GRAPPA acceleration factor 3, matrix size 128 x 128. Again, because of SAR restrictions, it was not possible to use the Ernst angle for imaging the STN. Instead, because of the higher number of slices compared to protocols 1 and 2, for protocol 3, the flip angle had to be further decreased to 60°. Due to its larger FOV, protocol 3 contained large parts of the cortex. These cortical areas are more affected by geometrical distortions due to field inhomogeneities than is the subcortex. Therefore, when acquiring protocol 3, a corresponding B0 field map with the same FOV was acquired (TR = 1500 ms, TE_1= 6 ms, TE_2 = 7.02 ms).

Protocol 4 was set up to be able to assess the BOLD sensitivity at 3 T, for a similar resolution as the 7 T protocol. It was an adaptation of the protocol reported by Pauli and colleagues (2015) and was acquired at a Siemens MAGNETOM Verio 3 Tesla system with a 24-channel head coil. This protocol also consisted of three runs of 515 volumes, but only 26 slices, and at a resolution of 1.5mm isotropic. The other parameters were: TR of 2000 ms, TE= 30 ms. flip angle = 81°, bandwidth 1396 Hz/Px, echo spacing 0.95 ms, FOV 96x96x39mm with 50% oversampling in the phase-direction, phase encoding direction A >> P, no partial Fourier, GRAPPA acceleration factor 2, matrix size 64 x 64.

All four protocols were planned in such a way that all nuclei-of-interest (STN, SN, GPe, GPi, and RN) fell well within the FOV. This was achieved by a slightly tilted axial slice orientation. For protocol 3 we ensured that the inferior frontal gyrus also fell within the FOV. The inferior frontal gyrus has been implicated in response inhibition in many previous studies and used as a 'control region' for the BOLD sensitivity in cortical regions (Erika-Florence et al., 2014; Aron et al., 2014a; 2015).

PHYSIOLOGICAL DATA

For estimating the effects of physiological noise on the fMRI data, we recorded physiological data for 6 of the participants in protocol 3. For these 6 participants, the fit of a 32-regressors RETROICOR model (Glover et al., 2000) showed high explained variance in inferior regions around the brainstem and circle of Willis, indicating that the physiological noise modelling was successful. However, analyses showed that the effects of physiological filtering on BOLD sensitivity were very limited (in accordance with Barry et al., 2011; van der Zwaag et al., 2015). In the 6 participants for which physiological data was collected, ROI-wise tSNR increased only very marginally after physiological filtering: from 89.2 (std. 22.2) to 95.8 (25.1) in left STN and from 90.3 (sd 21.5) to 96.9 (24.0) in right STN. This is a very limited increase, considering that 32 physiological regressors were filtered out. Accordingly, the statistics of the ROI-based contrast between go trials and failed stop trials were not meaingfully affected. The t-statistic of the contrast slightly increased after filtering in left STN (t(5) = 1.97, p = 0.10 before, t(5) = 2.3, p = 0.07), whereas it slightly decreased in right STN (t(5) = 2.93, p = 0.03 before filtering, t(5) = 2.62, p = 0.05 after filtering). The other nuclei showed similar results. We therefore decided to analyze all data in the same way, without the application of any physiological noise filtering.

PARTICIPANTS

A total of 20 participants (10 female; mean age 26 (SD 2.6), age range 22 – 32) took part in the experiment. Participants had normal or corrected-to-normal vision, and none of them had a history of neurological, major medical, or psychiatric disorders as indicated by self-report and structured clinical interview. All participants were right handed, as confirmed by the Edinburgh Inventory (Oldfield, 1971).

The participants that were scanned using the different protocols were largely overlapping. All 20 participants were scanned using protocol 3. Of these 20 participants, 5 participants were also scanned using protocol 1 and 2. Out of these 5 participants, 4 participants were also scanned using protocol 4 (and thereby were scanned using all 4 protocols). Finally, a group of 6 participants (out of the pool of the aforementioned 20 participants) were scanned using protocol 3 and 4 (see also Table 2).

Table 2: Subgroups of participants that were scanned using the different protocols

	n	Protocol 1	Protocol 2	Protocol 3	Protocol 4
Group A	4	x	x	x	x
Group B	1	x	x	x	
Group C	6			x	x
Group D	9			x	

The study was approved by the local ethical committee of the University of Leipzig, Germany. All participants gave written informed consent and received a monetary reward for their participation.

EXPERIMENTAL PARADIGM

The experimental paradigm consisted of a classic auditory stop-signal task (Logan et al., 1984; Aron and Poldrack, 2006), where participants are instructed to indicate the direction of an arrow using two spatially compatible buttons, as fast as they can. On a subset of trials (25%), participants hear, at some time after stimulus onset (the stop signal delay; SSD), an auditory cue that indicates that they should inhibit their response and not press any button. Longer SSDs usually lead to more failures to stop, because less time remains to inhibit an ongoing response. Following the study of Aron and Poldrack (2006), the SSD is dynamically adapted during scanning, in steps of 50 ms, using a staircase procedure to make sure that each participant successfully stops on approximately 50% of the trials (see also Logan and Cowan, 1984).

Participants performed 384 trials per session (three blocks of 128 trials), including 96 stop trials (32 per block). During protocol 3, one participant performed only 256 out of the 384 trials and another participant performed only 345 out of the 384 trials. Both participants quit because of fatigue (note that the total task time of 3 runs was 51 minutes). We chose to still include these 2 participants in the final analysis of protocol 3, because a) these participants performed the

large majority of the trials, b) their data could improve the statistical power of this study, c) the larger variability in their estimates could be modeled in the level 2-analyses.

Each trial lasted 8 seconds (4 fMRI volumes) in total. A trial started with the presentation of a white circle. After 500, 1000, 1500, or 2000 ms, an arrow pointing to the left or right was presented in the middle of the circle, indicating the desired response. The stimulus always disappeared after 1000 ms regardless of a stop signal or (an inhibited) response. For the remaining 5000 to 6500 ms, a blank screen was presented. The relatively long inter-trial interval was chosen to allow for deconvolving the BOLD signal related to each trial in a model-free manner using finite impulse response functions (FIR; Poldrack et al., 2011).

BEHAVIORAL ANALYSIS

Standard analyses of behavior during the stop-signal task were performed. The stop-signal task has three conditions of interest: trials in which no stop signal was delivered and the subject gave the correct response (*go* trials), trials in which a stop signal was delivered and the participant gave no response (*successful stop* trials), and trials in which a stop signal was delivered and the participant gave the correct response (*failed stop* trials). There was a small proportion (0.90%) of trials were the participant gave an incorrect response. These trials were excluded from the analysis. Responses that were faster than 150 ms or slower than the stimulus duration of 1000 ms were also excluded (1.5%). For every participant and experimental session, we calculated the median response time (RT) for go trials, the median RT for failed stop trials and the proportion of successful stops, both per SSD and over all trials.

Lastly, we also calculated the stop signal reaction time (SSRT): an estimate of the average amount of time it takes a participant to inhibit their response after the stop signal has been presented, assuming an independent race between a go and stop process. By mathematically formalizing the cognitive process underlying the stop signal task as a race, we can estimate this SSRT. Specifically, the SSRT was estimated using the so-called "mean method". This method takes the percentile of the Go RT distribution corresponding to the rate of unsuccessful stops (close to 50% for all subjects), and subtracts the mean SSD from this value (Logan et al., 1984; Aron and Poldrack, 2006; Verbruggen and Logan, 2009).

IMAGE REGISTRATION

For all protocols at 7 T, the mean functional signal intensity images were registered to the middle echo (20.39 ms) of the 0.5 mm isotropic T_2*-weighted FLASH images using linear affine transformations, optimized by the ANTS registration algorithm and the mutual information cost function (version 2.0.0; Avants et al., 2009). Visual inspection revealed that the automatic registration was sufficient.

Multiple registration algorithms and cost functions in FSL FLIRT (Jenkinson and Smith, 2001), MIPAV (Bazin et al., 2007), and ANTS (Avants et al., 2009) were applied to register the 3 T functional data (protocol 4) to the 3 T and 7 T FLASH images. However, after visually inspecting the results, we concluded that it was not feasible to register the 3 T data automatically, because of a lack of contrast-to-noise and the small FOV of the 3 T functional 2D-EPI images. We therefore opted for a manual landmark-based approach. Concretely, one rater (MCK) indicated in both the anatomical 3 T FLASH images and the mean functional 1.5 mm isotropic 3 T 2D-EPI images the location of the following landmarks: (1) the top indentation of the pons, (2) the posterior part of the 4th ventricle, (3) the ventral point of the bilateral RN, and (4) the most

anterior-dorsal-lateral part of the bilateral GPe. Then, MIPAV (McAuliffe et al., 2001; Bazin et al., 2007) was used to find the linear transformation that minimizes the distance between these manually indicated landmarks in both image modalities. This linear transformation was used in all further processing. The average 3 T FLASH images were also registered to the average 7 T FLASH images using linear registration in FSL FLIRT, to allow for using the anatomical masks drawn on the latter modality for the 3 T data.

The linear transformation matrices from the functional scans to the anatomical T_2*-weighted FLASH images were inverted and all the individual anatomical masks (left and right STN, SN, RN, GPi, and GPe) were transformed into individual functional space using nearest-neighbor interpolation. When anatomical masks were transformed to different spaces, nearest neighbor-interpolation was preferred over other interpolation algorithms, such as trilinear and spline interpolation, because otherwise the edges of the masks get smoothed out and mask size can increase arbitrarily.

PREPROCESSING FMRI DATA

All data was preprocessed using the FSL FEAT preprocessing pipeline (version 5.09; Smith et al., 2004; Woolrich et al., 2009), as implemented in the NiPype fMRI pipeline framework (create_featreg_preproc(); Gorgolewski et al., 2011). This pipeline motion-corrects the data using the MCFLIRT algorithm, makes a brain mask in individual functional space using BET, and normalizes the data such that the median voxel intensity within the brain is 10,000. Then, depending on the subsequent analysis, a 1.5 mm full-width-half-maximum (FWHM), a 5.0 mm FWHM, or no Gaussian smoothing kernel was applied. The data were high-pass filtered with a cutoff of 128 seconds. Lastly, the motion parameters obtained by the MCFLIRT algorithm and their first derivatives were used as regressors in a voxelwise general linear model (GLM) to filter out motion-induced noise. The residuals of this GLM were used as input to all further analyses. As an (almost) whole-brain volume was acquired using protocol 3 (see 2.6), these data were corrected for B_0 field inhomogeneities using FSL's FUGUE and the obtained B_0 fieldmaps, before it was submitted to the FEAT preprocessing pipeline. Visual inspection suggested that the influence of this correction was negligible in the subcortex.

FMRI DATA ANALYSIS

Voxelwise tSNR maps of the unsmoothed data were created by taking, for every voxel, its mean intensity across a run, and dividing it by the standard deviation of its intensity across the run. Mean voxelwise tSNR, averaged over all voxels inside a mask, was then extracted for every protocol, participant, run, and ROI.

To investigate whether the decreased tSNR at higher voxel resolutions could be mitigated by the increased number of voxels measured per ROI, we also calculated ROI-wise tSNR. For every ROI-mask, the signal of every voxel inside that mask was averaged, to get a mean ROI signal time course. The ROI-wise tSNR was calculated by dividing the mean intensity of this signal by the standard deviation through time of this signal.

All tSNR measures were calculated on unsmoothed, but otherwise completely preprocessed data. Therefore, the found tSNR values were corrected for, e.g., subject movement and slow signal drifts. Furthermore, the signal that was used in the ROI GLM analysis was identical to the signal used to calculate tSNR, enabling us to relate the found tSNR and percent signal change estimates of the GLM to simulation studies of Murphy et al. (2007).

We also deconvolved and visualized the task-locked signal of the ROI signal time courses for different conditions by fitting a GLM with finite impulse regressors (Poldrack et al., 2011) implemented in the Python package pyFIR (version 0.1; https://github.com/Gilles86/pyFIR). This analysis was performed on the mean ROI signal described above, to visually assess the BOLD sensitivity of the different protocols in the different ROIs. Three conditions (go trials, failed stop trials, and successful stop trials) were modeled with each 9 regressors corresponding to offsets of 0, 2, 4, 6, 8, 10, 12, 14, and 16 seconds after task onset. The parameter estimates for the different regressors were averaged across participants and plotted as a function of their offset. For protocols with good BOLD sensitivity, we expected to see a typical hemodynamic response function in all conditions and ROIs, with a peak at around 4-6 seconds. When BOLD sensitivity was sufficient, we expected the estimated height of this peak to be highly significantly different from zero.

We also created an event-related GLM design matrix with canonical HRF regressors using Nipy (0.4.0 Brett et al., 2009). The design matrix contained three regressors of interest, corresponding to go, failed stop, and successful stop trials. One second block functions at trial onset were convolved with a canonical double-gamma haemodynamic response function (HRF) (Worsley and Friston, 1995; Glover, 1999). A constant, the first-order derivatives of the HRFs, and a second-order polynomial were also added to the model, to account for individual differences in the hemodynamic responses and slow signal drifts. The GLM was fitted to the ROI-signal time series of every block using GLSAR AR(1) estimation, as implemented in Statsmodels (Seabold and Perktold, 2010), to account for temporal autocorrelation in the signal. For every participant, ROI, protocol, and the mean value of every beta-regressor over the three runs was used as input in a one-sample t-test against baseline, or a paired t-test between conditions. They were also used as input to a Bayesian t-test (Morey and Rouder, 2015) to estimate the Bayes factor (BF) between a model where the different conditions lead to different BOLD responses versus a model where they do not. In contrast to traditional frequentist p-values, BFs offer a natural interpretation as the amount of evidence the researcher has for one hypothesis over another, without being biased toward rejecting the null hypothesis (Wagenmakers, 2007; Rouder et al., 2012). However, there is not a straightforward way to control for the multiple comparisons problem without substantial additional modelling (Neath and Cavanaugh, 2006; Stephens and Balding, 2009). We therefore chose not to perform multiple comparison correction on the Bayesian analysis, but leave it to the reader to interpret the resulting BF in a cautious manner.

We performed statistical analyses both on the entire samples of protocol 1-4 (with 5, 5, 20, and 10 subjects, respectively), as well as on a subset of 5 subjects, to keep the number of subjects equal over the (analysis of) the four protocols.

T_2* ESTIMATION

To obtain an empirical estimate of the T_2* relaxation values of the different BG nuclei at both 3 T and 7 T MRI, an exponential decay function was fitted to the signal intensities at different echo times of the FLASH sequence images (see section above on "Structural MRI"). This estimate was calculated using voxelwise Ordinary Least Squares (OLS) regression in log-space (Weiskopf et al., 2013; 2014). We opted not to use robust regression since the number of data points was too limited to do this effectively (3 and 4, respectively) and the young and healthy participants of this study were specifically selected for minimal movement during scanning.

The voxelwise estimates were subsequently extracted and averaged within the anatomical masks of the nuclei-of-interest.

After performing the analysis described in section 2.4.4, only protocol 3 turned out to have sufficient BOLD sensitivity in the BG ROI. Therefore, we also performed a voxelwise analysis on the data resulting from protocol 3, but not the other protocols, in both subcortex and cortex. Ideally, the protocol should have sufficient sensitivity in both cortical (although TE was not optimal for cortex) and subcortical regions to test task-related activations. To investigate the sensitivity in cortical areas, we used a conventional group-level voxelwise analysis in MNI152 space. To address possible subcortical activations outside of the a-priori selected ROIs, we also used a custom groupwise template with high contrast in subcortex.

To investigate the BOLD sensitivity of protocol 3 in MNI152 space, the mean functional images of protocol 3 were registered to the uniform T_1 weighted image of the whole-brain MP2RAGE, using linear affine registration as implemented in ANTS (version 2.0.0; Avants et al., 2009). The T_1 weighted images were brain-extracted using the brain mask created by the FSL BET-algorithm applied to the INV2-image (Smith, 2002), and then registered to the 1 mm isotropic MNI152 standard brain using non-linear registration via the SyN-algorithm, as implemented in ANTS (version 2.0.0; Avants et al., 2009). The combined transform of these two transformations (from the mean EPI to T_1-weighted anatomical image and from T_1-weighted anatomical image to 1 mm isotropic MNI152 standard brain) was used to transform the statistical parametric maps in individual space to MNI152 standard space using nearest-neighbor interpolation.

Preferably, the fMRI data can be transformed to a space where voxels originating from a particular anatomical location in one individual (e.g., the subthalamic nucleus of participant 1) have a very high overlap with voxels from other individuals originating from the same anatomical location (e.g., the subthalamic nucleus of participant 2). As, the individual T_1-weighted images have little tissue contrast in subcortex, which hampers the anatomical overlap between functional EPI data and a standard template in this region, in addition a study-specific group T_2*-weighted FLASH template was created by by non-linearly registering (using the SyN-algorithm implemented in ANTS) all the individual T_2* weighted FLASH images (middle echo time of 20.39 ms) to the FLASH image of the first participants, and then iteratively registering all anatomical images to the mean image of all individual transformed images. After 5 iterations, the mean of the transformed images did not considerably change anymore. The mean of these images showed very high contrast in the subcortex, and the different nuclei-of-interest are clearly visible.

The functional images of protocol 3 were, in addition to the MNI152 space, also registered to this group FLASH space, to investigate the topology of activation clusters in the subcortex with high anatomical specificity without constraining the analysis to a- priori selected ROIs.

A voxelwise GLM group analysis was performed both in the study-specific 0.5 mm T_2* weighted FLASH space, as well as in 1 mm standard MNI152 space. The data was smoothed with either a 1.5 mm (for the study-specific template analysis) or 5.0 mm (for MNI152 1mm space) FWHM Gaussian smoothing kernel. Go, failed stop, and successful stop trials were modeled as separate conditions. First-order derivatives of the canonical HRF were included as nuisance

regressors. The estimated contrasts were: (1) successful stop – go, (2) failed stop – go, (3) successful stop – failed stop, (4) failed stop – successful stop. A mixed-effects level 2 analysis was performed using FSL's FLAME1. For the analysis in MNI152-space, multiple comparison correction was performed using Gaussian Random Field (GRF) Theory, as implemented in FSL's *smoothestimate* and *cluster*, using a voxelwise threshold of z > 3.1 and GRF cluster-threshold of p < 0.05. For the analysis in the group template space, we believed the assumption of a Gaussian random field was not tenable, because the smoothing of the data had been very limited. Therefore, for this analysis, we opted for a voxelwise false discovery rate (FDR) correction (*fdr*-function of FSL, q < 0.05).

EXPLORATORY CONNECTIVITY ANALYSES

An exploratory connectivity analysis was conducted to test whether the different protocols were capable of recovering functional connectivity patterns in the BG. In this connectivity analysis, a correlation matrix representing the correlations between the measured signals of the different BG nuclei was computed. The inputs of the correlation matrix were the preprocessed mean ROI timeseries (task-related activity was not modeled here). If BOLD sensitivity and specificity were high, we would expect to see high connectivity between homologous BG nuclei across the two hemispheres (e.g., a high correlation between left and right STN), preferably more so than between spatially closer, but functionally distinct nuclei (e.g., left STN and left SN).

RESULTS
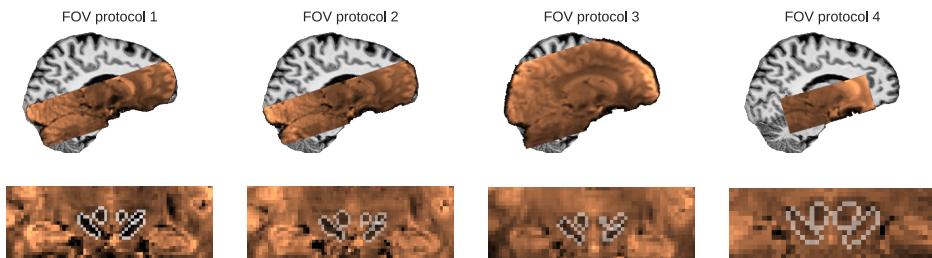
Figure 2 Illustration of the Field-of-views of the four protocols and anatomical masks. The top row shows, for a representative subject, a sagittal slice of the mean functional images overlaid on the T1-weighted anatomical image. The bottom row shows the outlines of the individual masks for RN, STN, and SN, overlaid on coronal slices of the mean functional image (radiological convention). The coronal slices are chosen such that they correspond to the center-of-mass of the right SN mask.

BEHAVIOR

The median correct go RT and the estimate of the SSRT in all experiments were typical for young adults (Aron and Poldrack, 2006), and the inhibition rates were close to 50% (see Table

3). As expected, median RTs of failed stops were faster than correct go trials, and inhibition rate was around 50%. Median go RTs were not correlated with SSRTs, in line with the independence assumption of the race model (Logan and Cowan, 1984; Aron and Poldrack, 2006; see also Shenoy and Yu, 2011).

Table 3 Mean values of behavioral measures per protocol

Behavioral measure	Protocol 1	Protocol 2	Protocol 3	Protocol 4
Median correct Go RT (ms)	420.3 (43.3)	440.5 (61.9)	477.2 (97.9)	531.5 (128.3)
Median failed stop RT (ms)	387.5 (29.8)	407.9 (54.8)	438.0 (79.5)	490.1 (120.1)
Percentage go discrimination errors	0.07 (0.16)	0.30 (0.30)	0.36 (0.43)	0.29 (0.70)
Mean SSD (ms)	200.3 (46.7)	204.6 (91.8)	247.2 (91.0)	317.0 (122.1)
Percentage successful inhibition	52.6 (3.0)	51.2 (6.3)	56.1 (6.4)	58.1 (6.8)
Mean SSRT (ms)	215.3 (31.6)	231.4 (71.2)	211.8 (33.2)	192.7 (25.9)

TRANSFORMATION OF ANATOMICAL MASKS

The transformation of the anatomical masks from the 7 T-FLASH-space to the four functional spaces was visually inspected for all participants. A representative example of the individual anatomical masks transformed to individual space for the four protocols can be found in Figure 2.

The volumes of the anatomical masks and the between-rater agreement, as indicated by the Dice-coefficient (Dice, 1945), can be found in Table 4.

T_2* ESTIMATES

At 3 T, the T_2* relaxation value in the left STN was on average 34.2 ms (std 6.7) and 35.6 ms in right STN (std 6.8). This is considerably lower than the 66 ms, the approximate T_2* relaxation value for cortex at 3 T (Peters et al., 2007 see Table 4 for the T2*-estimates for the different nuclei).

As expected, the T_2* value in the BG is even shorter at 7 T, on average 15.2 ms (std. 1.7) in the left STN and 14.9 ms (std. 2.0) in the right STN, as compared to approximately 33 ms in cortex (Peters et al., 2007). This confirms that, especially at 7 T, functional protocols that are optimized to functional imaging of the cortex might have too long echo times to have robust BOLD sensitivity in iron-rich subcortical nuclei, such as the BG.

Table 4 Mean and standard deviations of interrater consistency (Dice coefficient) and anatomical mask sizes (mm^3)

	Dice	Volume (mm^3)
STN_L	0.73 (0.16)	54 (13)
STN_R	0.74 (0.14)	58 (12)
SN_L	0.79 (0.07)	297 (123)
SN_R	0.77 (0.05)	298 (129)
RN_L	0.89 (0.03)	269 (44)
RN_R	0.89 (0.02)	261 (46)
GPi_L	0.80 (0.05)	367 (79)
GPi_R	0.81 (0.06)	357 (71)
GPe_L	0.86 (0.03)	1020 (156)
GPe_R	0.86 (0.04)	958 (146)

Table 5 Estimated T_2* relaxation time estimates at 3 T and 7 T

|	T2* at 3T in ms (std)	T2* at 7T in ms (std)
mask		
STN_L	34.2 (6.7)	15.2 (1.7)
STN_R	35.6 (6.8)	14.9 (2.0)
SN_L	36.6 (4.3)	14.1 (1.7)
SN_R	36.6 (10.0)	13.8 (1.4)
RN_L	42.4 (5.0)	16.9 (1.5)
RN_R	40.1 (3.9)	16.9 (1.5)
GPi_L	34.3 (2.1)	13.1 (1.3)
GPi_R	34.4 (2.0)	12.8 (0.8)
GPe_L	31.8 (2.4)	13.1 (1.2)
GPe_R	32.4 (2.7)	12.9 (0.9)

TSNR

Voxelwise temporal signal-to-noise ratios were extremely low for protocol 1 (1.2 mm/TE = 22 ms/7 T), 2 (1.2 mm/15 ms/7 T), and 4 (1.5 mm/30 ms/3 T). For left / right STN, tSNR was 8.2 (std 0.8) / 8.3 (1.2) for protocol 1, 12.4 (0.9) / 12.8 (1.6) for protocol 2, and 9.2 (1.0) / 9.2 (1.3) for protocol 4. Temporal SNRs in other BG nuclei were comparable (see Figure 3). Earlier simulation studies suggest that a tSNR in these ranges makes it virtually impossible to detect activations patterns in the individual brain within an acceptable scan time (Murphy et al., 2007).

Protocol 2 showed a significantly higher tSNR than protocol 1 ($t(4)$ = 13.6, p = 0.0002 for left STN and $t(4)$ = 7.7, p = 0.002 for right STN), suggesting that the reduction of TE indeed increases the tSNR.

Only protocol 3 (1.5 mm/14 ms/7 T) showed an acceptable tSNR: 48.6 (11.1) for left STN, and 50.5 (11.1) for right STN, see also Figure 3 (top). Temporal SNR in such a range should allow for detecting neural activation in the individual brain in a reasonable amount of time (Murphy et al., 2007).

Higher spatial resolutions always lead to decreased tSNR but also to smaller partial volume effects. Furthermore, as the tSNR can be increased by spatial averaging over a certain region, the temporal SNR of the mean time series per ROI was also calculated. This showed that the ROI-wise tSNR is still highest for protocol 3 (140.3, (std. 57.2) for left STN, 160, (91.7) for right STN). But, as expected, protocol 1 (88.2 (47.4) for left STN, 154.3 (47.5) for right STN) and 2 (62.3 (12.0) for left STN, 101.1 (39.9) for right STN) show tSNRs that are closer to that of protocol 3 when the signal is averaged over all voxels (see also Figure 3, bottom). This suggests that most of the noise was uncorrelated across voxels, and most likely consists of image noise, rather than physiological noise (Triantafyllou et al., 2006).
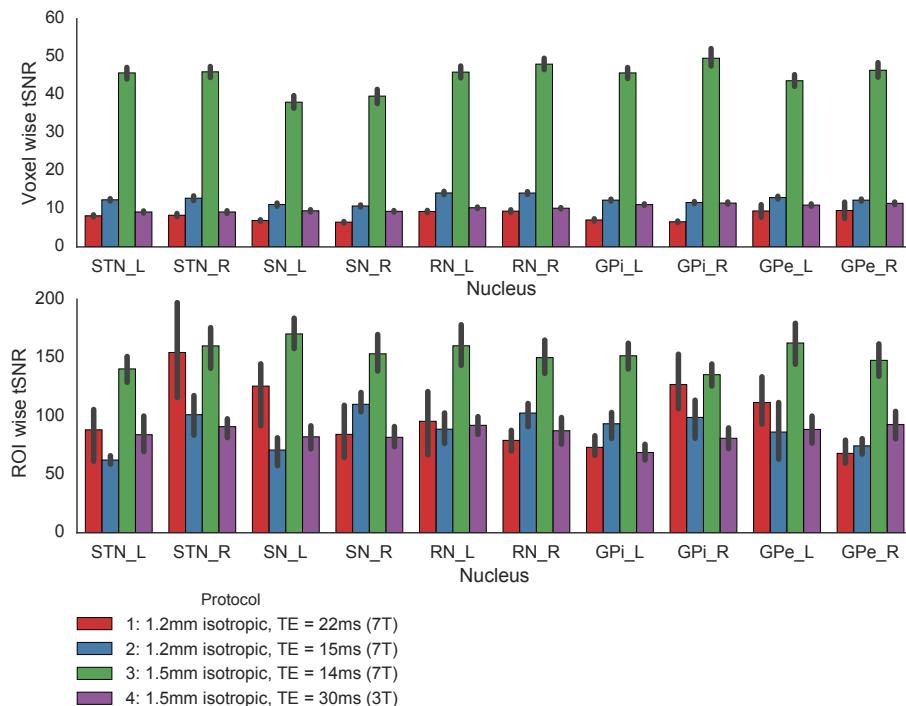
Figure 3 Voxel- (top) and ROI-wise (bottom) temporal signal-to-noise ratios (tSNR) in the basal ganglia for the four protocols. Error bars represent bootstrapped 67% confidence interval.

Four representative coronal slices of the tSNR maps are depicted in Figure 4. They clearly show the improved tSNR in protocol 3 (1.5 mm/14 ms/7 T), as well as the relative drop in tSNR in the subcortex as compared to cortex at 7 T, especially in protocol 1 (1.2 mm/22 ms/7 T) and 2 (1.2 mm/15 ms/7 T), which had a relatively high acceleration factor (see Table 1).
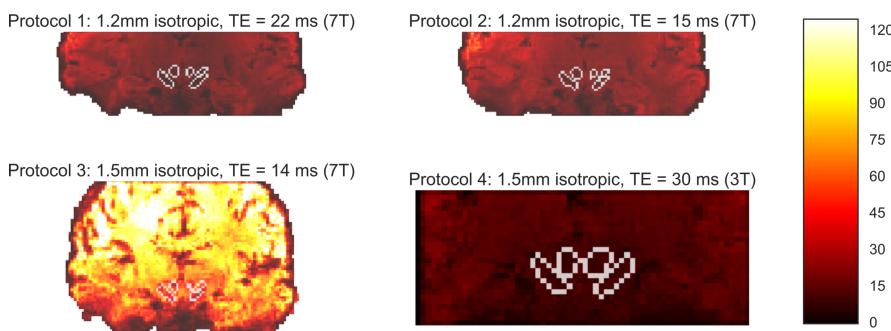

Figure 4 Coronal slices of the voxelwise tSNR-maps for the four protocols in a representative subject.

TASK-LOCKED ROI ANALYSES

FINITE IMPULSE RESPONSE (FIR)-ANALYSIS

To keep things concise and easy to compare, for the FIR and traditional GLM, we report analyses on the same five subjects in protocol 1, 2, and 3, and five subjects in protocol 4, of which four subjects overlap with protocol 1-3 (specifically, group A and B for protocols 1-3, and group A and a randomly picked participant of group C for protocol 4; see Table 2).

Qualitative inspection of the task-locked ROI time series suggested that protocol 1 (1.2 mm/22 ms/7 T), 2 (1.2 mm/15 ms/7 T), and 4 (1.5 mm/30 ms/3 T) show no robust task-related BOLD responses in left or right STN (see the top panel of Figure 5). They lack the prototypical HRF pattern of a peak at 4-6 seconds after task onset. Such a pattern was, in contrast, clearly present in the STN time series of protocol 3, already with five subjects (Figure 5, top panel; see also Supplementary Materials S3 in Appendix B). This suggests that the higher tSNR in protocol 3 also leads to robust BOLD sensitivity.

ROI GLM

For protocol 1 (1.2 mm/22 ms/7 T) and 2 (1.2 mm/15 ms/7 T), no parameter estimates were significantly different from 0 after FDR correction (all $p > 0.05$, see Figure 5 and supplementary materials S1 for additional statistics). All Bayes Factors suggested limited evidence for the null hypothesis (BF10 range 0.42 – 1.02). This suggests that there was no reliable task-related BOLD activity detected in any of the conditions. Accordingly, there were also no significant differences between the task conditions in any of the nuclei (see Supplementary Material S2 for details).

For protocol 3 (1.5 mm/14 ms/7 T), all three parameters estimates were significantly different from zero in both left and right STN, as shown by t-tests (all $p < 0.05$, FDR corrected; Bayesian t-tests showed Bayes factors in favor of an effect, BF10 range 4 - 784; see also Figure 5 and Supplementary material S1 in Appendix B). In other words: in both left and right STN, and in every condition, after task-onset there was a significant BOLD response, detected already with five subjects. Also, the contrast "failed stop" > "go" was significant in both left and right STN in five subjects ($t(4) = 8.3$, $p = 0.0011$ for left STN, BF10 = 34, $t(4) = 9.17$, $p = 0.0008$, BF10 = 45 for right STN).

For protocol 4 (1.5 mm/30 ms/3 T), using five subjects (all four subject of group A and a randomly selected participant of group C; see table 2), and after FDR correction, no parameter estimates were significantly different from zero according to t-tests.

Bayes Factors were in the range of 0.40 – 2.75, where all Bayes Factors showed evidence for the null hypothesis, except for the "go"-condition in the right STN. No contrasts between conditions were significant.
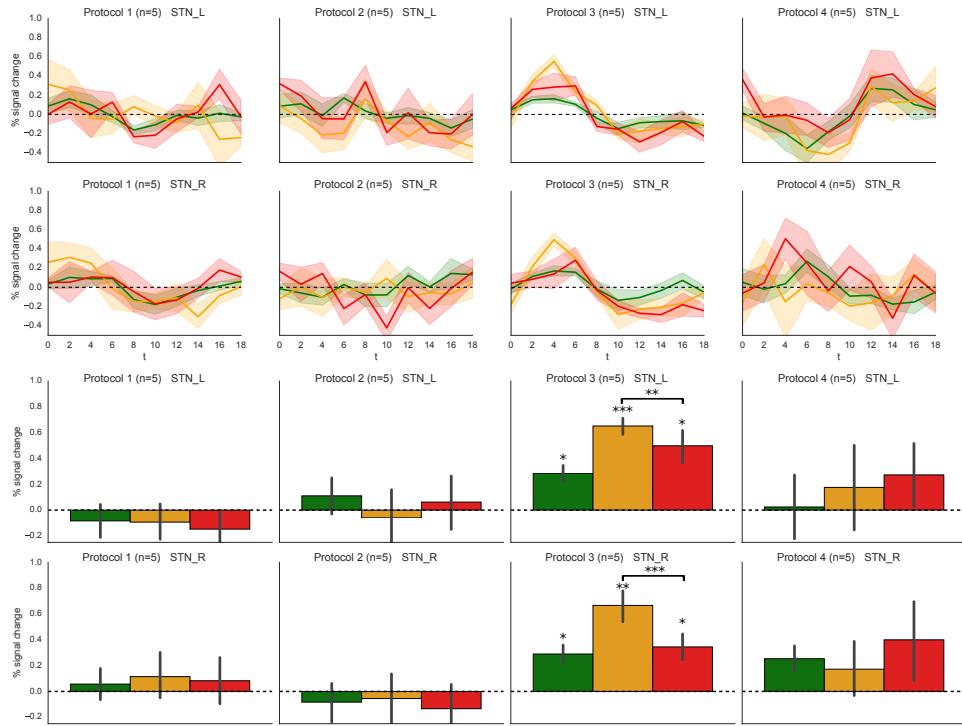
Figure 5 Raw task-locked mean time series (top) and corresponding GLM parameter estimates (bottom) for all four protocols in left and right STN for five subjects. For protocol 1-3 all five subjects are overlapping. For protocol 4, four out of five subjects are overlapping. Shaded area and error bars indicate 67% bootstrapped confidence interval, corresponding to the standard error of the mean (SEM). Green corresponds to go trials, orange to failed stop trials, and red to successful stop trials. Only for protocol 3 are any parameters significantly different from zero after FDR correction. (q < 0.05). * = p < 0.05, ** = p < 0.01, *** = p < 0.001

When all 20 subjects were included for protocol 3 (1.5 mm/14 ms/7 T), similar patterns were found, albeit with more robust p-values and Bayes Factors. All nuclei except for the left and right GPi and left GPe showed a higher BOLD response during failed stop trials compared to go trials (FDR corrected; see also Table 6 and Figure 6). Also, left and right STN, right SN, the left and right RN, and left and right GPe showed a higher BOLD response during failed stops than successful stop trials. None of the nuclei showed a larger activation for successful stop trials than for go trials (see also supplementary Table S2 in Appendix B).
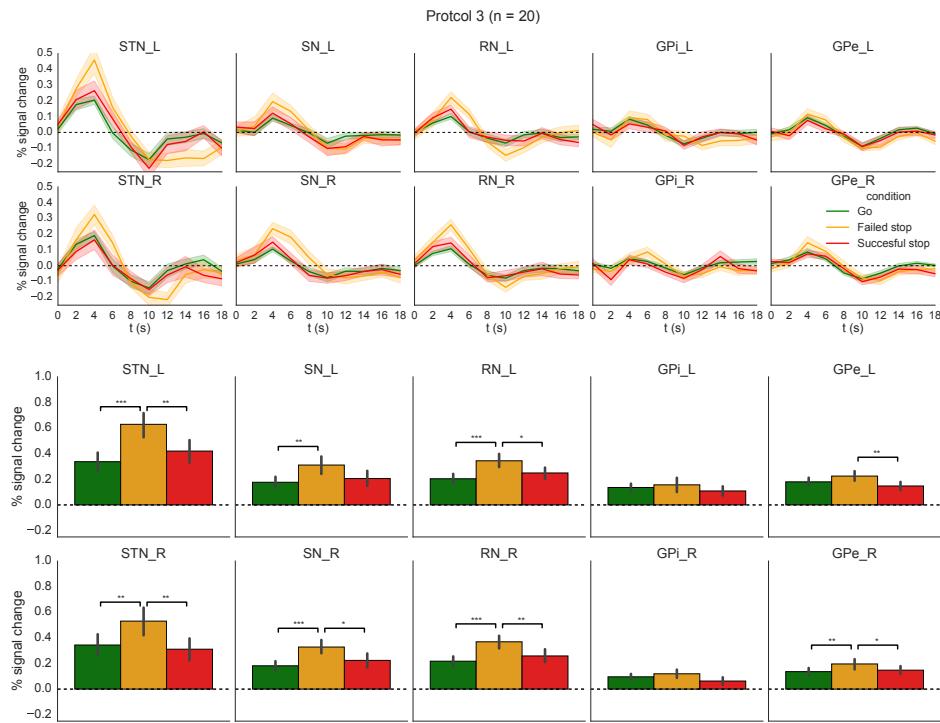
Figure 6 Raw task-locked mean time series (top) and corresponding GLM parameter estimates (bottom) for protocol 3 across all basal ganglia masks for 20 subjects. Shaded area and error bars indicate 67% bootstrapped confidence interval, corresponding to the standard error of the mean (SEM). Green corresponds to go trials, orange to failed stop trials, and red to successful stop trials. * = p < 0.05, ** = p < 0.01, *** = p < 0.001

When all 10 subjects were included for protocol 4, after FDR correction, none of the parameter estimates were significantly different from zero. However, a Bayesian t-tests, agnostic to the multiple comparisons, suggested limited evidence in favor of a model where BOLD activity was different from baseline for left STN (successful stop; BF_{10} = 2.49), right STN (go trials; BF_{10} = 16.00; failed stops; BF_{10} = 3.16), left GPi (failed stops; BF_{10} = 1.14), and right RN (failed stops; BF_{10} = 3.45; see also Supplementary Material S1 and S3). However, no significant differences between conditions were found (all p > 0.05, BF10 in range 0.4 – 1; see also Supplementary Material S2 and S3 in Appendix B).

Table 6 Frequentist and Bayesian statistics for main task contrasts using protocol 3. A Bayes factor (BF10) larger than 1 means evidence for an effect, a Bayes factor less small 1 means evidence in favor of no effect. See also Figure 6 and supplementary Tables S1 and S2. * = significant effect after FDR-correction (q < 0.05).

	Successful stop > go		Failed stop> go		Failed stop> successful stop	
	frequentist	BF10	frequentist	BF10	frequentist	BF10
GPe_L	t(19) = -1.52, p=.144	0.63	t(19) = 1.40, p=.176	0.54	t(19) = 3.36, p=.003*	13
GPe_R	t(19) = 0.57, p=.577	0.27	t(19) = 3.08, p=.006*	7.63	t(19) = 2.58, p=.018*	3.12
GPi_L	t(19) = -1.13, p=.271	0.41	t(19) = 0.55, p=.591	0.27	t(19) = 1.14, p=.267	0.41
GPi_R	t(19) = -1.42, p=.173	0.55	t(19) = 0.74, p=.466	0.3	t(19) = 1.68, p=.110	0.76
RN_L	t(19) = 1.57, p=.132	0.67	t(19) = 4.66, p<.001*	173	t(19) = 2.38, p=.028*	2.2
RN_R	t(19) = 1.16, p=.260	0.42	t(19) = 5.22, p<.001*	531	t(19) = 3.70, p=.002*	25
SN_L	t(19) = 0.83, p=.416	0.32	t(19) = 3.26, p=.004*	11	t(19) = 1.93, p=.069	1.08
SN_R	t(19) = 1.26, p=.224	0.46	t(19) = 5.72, p<.001*	1423	t(19) = 2.38, p=.028*	2.19
STN_L	t(19) = 1.48, p=.154	0.6	t(19) = 4.29, p<.001*	82	t(19) = 2.95, p=.008*	6.05
STN_R	t(19) = -0.87, p=.394	0.33	t(19) = 3.35, p=.003*	13	t(19) = 3.18, p=.005*	9.23

VOXELWISE ANALYSIS MNI152-SPACE (PROTOCOL 3)

We computed a voxelwise GLM analysis only on the data of protocol 3 (1.5 mm/14 ms/7 T), since only this protocol showed robust BOLD sensitivity in the BG, and, importantly, only this protocol allowed for scanning the majority of cortex and could potentially be used to investigate cortico-subcortical interactions. For these analyses, all 20 subjects were included.

For the "failed stop > go" contrast, many significant activation clusters were found in cortex and subcortex in both hemispheres. These include inferior frontal gyrus (pars operculum, IFG), pre-supplementary motor (pre-SMA), anterior cingulate cortex (ACC), early visual cortex (V1, V2), the middle and superior temporal gyrus, primary auditory cortex, insular cortex, and two clusters that covered almost the entire subcortex and brainstem bilaterally (see Figure 7, top; Figure 8; top; Table 7a).

Failed stop > Go

Successful stop > Go


Failed stop > Successful stop
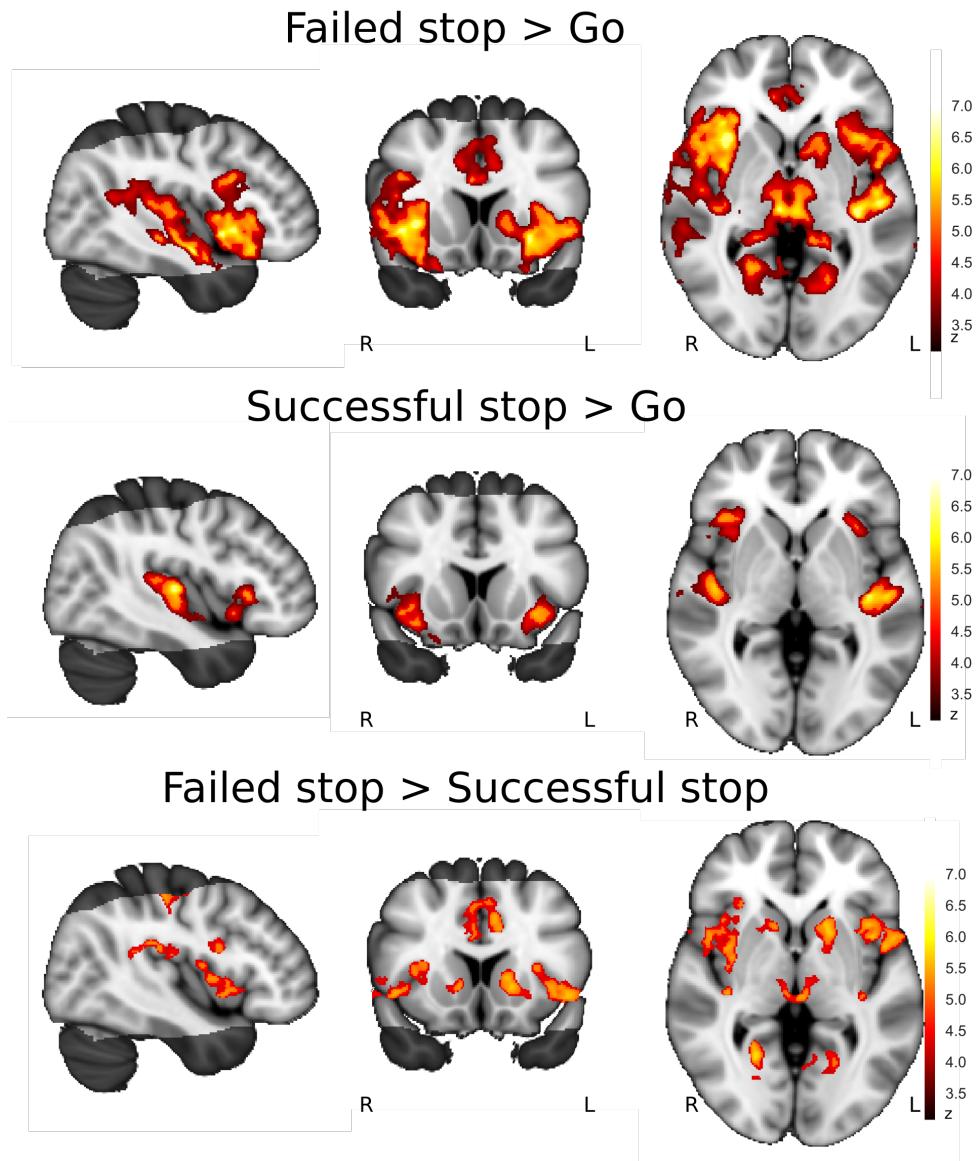
Figure 7 Whole-slab SPMs for main task contrasts in protocol 3. From left to right: sagittal (MNI152 X=43), coronal (MNI152 Y = 14), and axial (MNI152 Z=0) slices. Parts of the MNI brain that did not overlap with the functional data of all 20 participants were not included in the statistical tests and are darkly shaded.
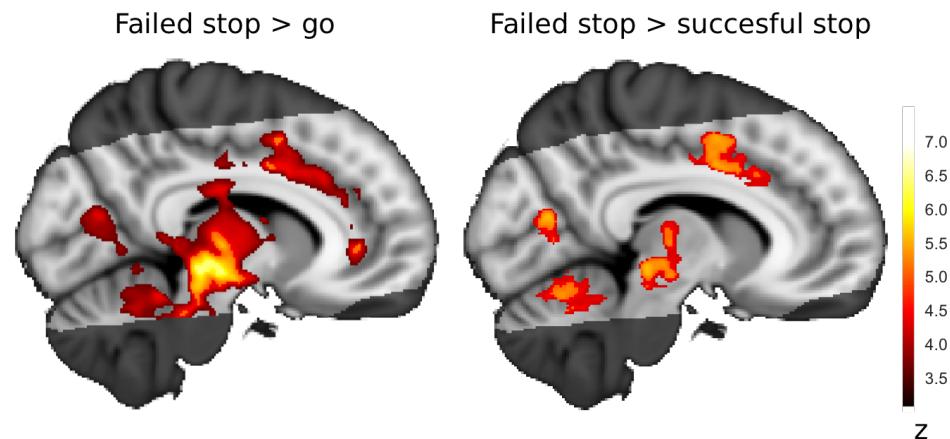
Figure 8 Sagittal slices (MNI152 X = 9) of two contrasts that show extensive activated clusters across the subcortex and brainstem for protocol 3. This illustrates the lack of anatomical specificity of conventional voxelwise GLM with moderate (5.0mm FWHM) smoothing.

The "failed stop > successful stop" contrast also showed a very large set of significant activation clusters across cortex and subcortex, where, again, the subcortical clusters were very large and showed little anatomical specificity (see Figure 7; Figure 8 and Table 7b).

For the "successful stop > go" contrast, the spread of significant activation clusters is much sparser. Only the left and right primary auditory cortex and left and right insula show a significant activation pattern, which is to be expected as there was an auditory stop signal (see Figure 9, middle row; Table 7c).

For the "successful stop > failed stop" contrast, no significant activation clusters were found.

Table 7 Significant clusters of the whole-slab voxelwise GLM analysis on protocol 3 for three main contrasts (failed stop > go, successful stop > go, and failed stop > successful stop). The contrast successful stop > failed stop showed no significant activation clusters. MNI-coordinates are those of the voxel with the highest z-score.

(a) Failed stop > Go

Name	MNI X	MNI Y	MNI Z	Volume (mm3)	Max z-value
Left insular cortex / subcortex / brainstem	-40	-6	-11	34321	6.79
Right insular cortex / subcortex / brainstem	32	17	-7	27849	6.44
Anterior cingulate cortex (ACC)	-3	23	23	3014	5.15
Right primary visual cortex (V1)	23	54	-2	1476	5.41
Left primary visual cortex (V1)	-19	-61	2	700	4.67

Name	MNI X	MNI Y	MNI Z	Volume (mm3)	Max z-value
Left posterior cingulate cortex (PCC)	-11	-18	39	638	5.04
Pre-supplementary motor Area (pre-SMA)	6	7	45	532	4.74
Left middle temporal gyrus (MTG)	44	-28	-7	440	5.44
Left posterior cingulate gyrus	-13	-39	-2	417	4.97
Right superior temporal gyrus (STG)	63	2	2	347	5.15
Right posterior cingulate cortex (PCC)	5	-15	25	155	4.47
Right anterior cingulate cortex (ACC)	7	42	1	80	4.67
Right middle temporal gyrus (MTG)	54	-59	6	71	4.45
Left insular cortex	-32	-19	18	69	4.28
Right cerebellum	9	-43	-18	69	4.24
Left temporal pole	-46	2	-18	44	4.68
Left anterior cingulate cortex (ACC)	-6	37	7	42	4.37
Right anterior cingulate cortex (ACC)	4	38	12	41	4.22

(b) Failed stop > successful stop

Name	MNI X	MNI Y	MNI Z	Volume (mm3)	Max z-value
Left posterior cingulate cortex (PCC)	-11	-17	38	9931	5.32
Right inferior fronal cortex/ frontal operculum (IFG)	47	2	5	8837	5.39
Left striatum	-14	12	2	7879	5.36
Left cerebellum	-25	-59	-23	7221	5.23
Subcortex / brain stem	8	-25	-6	6229	5.3
Left primary motor cortex (M1)	-38	-25	52	4186	5.46
Right primary auditory cortex	34	-31	18	3957	5.33
Left primary auditory cortex	-50	-20	17	3292	5.75
Right primary visual cortex (V1)	23	-56	0	2561	5.46
Left primary visual cortex (V1)	-12	-73	11	1689	4.83
Right primary motor cortex (M1)	41	-25	50	915	4.97
Left insular cortex	-31	-24	8	449	4.66
Right primary somatosensory cortex / motor cortex (M1/S1)	57	-13	44	369	5.04
Right primary somatosensory cortex / motor cortex (M1/S1)	55	-3	42	320	5
(c) Successful stop > go					
Left primary auditory cortex	-50	-25	7	14226	6.29
Right primary auditory cortex	44	-17	5	12266	6.15
Right insular cortex	32	21	-10	6115	5.09
Left insular cortex	-31	17	-7	3792	5.44
Right striatum	12	15	0	276	4.82

VOXELWISE ANALYSIS ON T2*-WEIGHTED GROUP TEMPLATE

The registration to the MNI152-standard brain via the T_1-weighted images and the 5.0 mm FWHM smoothing does not allow for high anatomical specificity in the BG. The T_1-weighted

images show only little anatomical detail in the subcortex, which causes the registration to standard space to rely mostly on cortical structures. The extensive smoothing might obfuscate small activation clusters by introducing perturbing noise from adjacent areas that are not involved in the task, as well as erroneously join distinct clusters together (Stelzer et al., 2014).

Therefore, we also created a group-specific T_2*-weighted template at a resolution of 0.5 mm by iteratively registering the individual FLASH images towards each other and repeated the group-level analysis in this space. This template has much higher anatomical contrast in the subcortex. Also, we used only limited smoothing (1.5 mm FWHM).

This analysis (see Fig. 9-11) showed, comparable to the MNI152-analysis, extensive activation clusters in the inferior parts of the brain for the "failed stop > go" contrast, extending well outside the border of the STN, SN, and RN. We found a large cluster immediately dorsal to the STN and RN, probably reflecting the involvement of thalamic nuclei. We also found a cluster medial of the SN and ventral of the RN, which could be attributed to the ventral tegmental area (VTA; Eapen et al., 2011), an important dopaminergic nucleus (Arsenault et al., 2014; Haber, 2014). The cluster posterior to the RN might be attributed to a number of nuclei in the brainstem, such as the locus coereleus, an important neuromodulatory node (Keren et al., 2015), or the periaqueductal gray (Linnman et al., 2012), amongst others.

The "failed stop > successful stop" contrast shows very comparable clusters to the "failed stop > go" contrast, but they are less extensive and have lower z-values. This suggest that maybe very similar networks are involved, albeit less heavily.

The activation clusters in the "successful stop > go" contrast are, again, comparable to the MNI152-analysis, and show no clear clusters in the subcortex or brainstem. Still, a set of clusters in the thalamus and VTA survived the FDR correction, even though they have the size of only a few voxels and relatively low z-values, so a cautious interpretation is warranted.
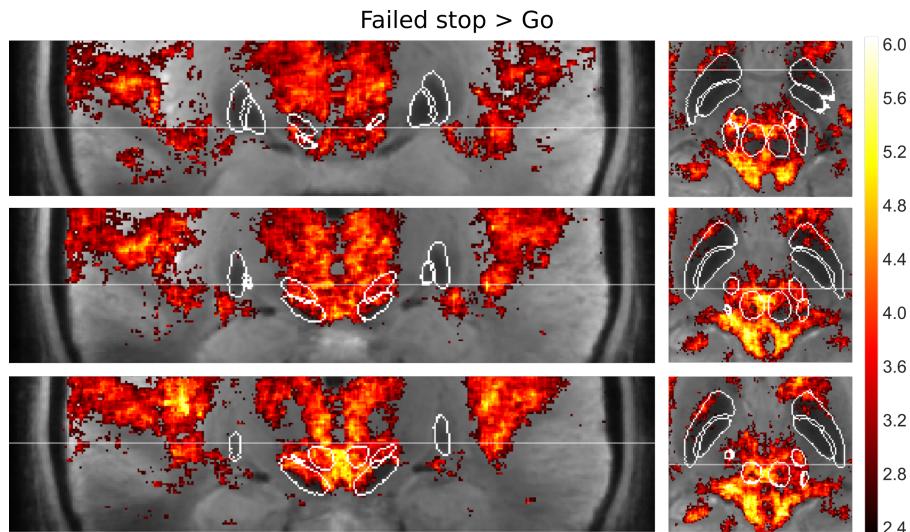
Failed stop > Go

Figure 9 Slices of the voxelwise analysis of the "**Failed stop > Go**" contrast in the T_2* weighted group template (no MNI152 coordinates) for protocol 3, showing both average anatomy and a SPM of the z-values. Outlines of the anatomical masks are overlaid in white. These masks indicate the area that corresponds to voxels that have been labeled as the nucleus-of-interest nucleus in at least 18 out of 20 participants. The two lateral nuclei are the Globus Pallidus interna (GPi, medial) and externa (GPe, lateral), the most-medial, sphere-like areas are the red nuclei (RN). These lie just dorsal of the substantia nigra (SN), and slightly posterior to the subthalamic nucleus (STN).

Failed stop > Successful stop
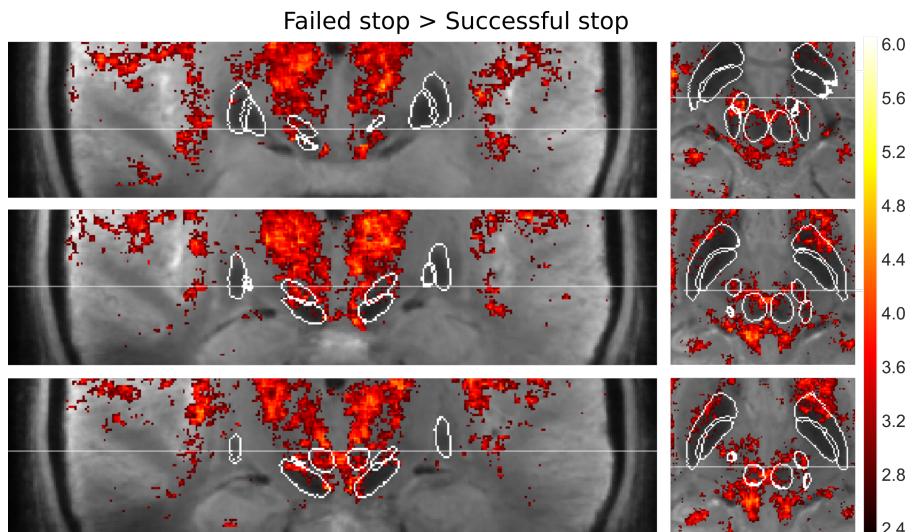
Figure 10 Slices of the voxelwise analysis of the "**Failed stop > Successful stop**" contrast in the T_2* weighted group template for protocol 3, showing both average anatomy and a SPM of the z-values. Outlines of the anatomical masks are overlaid in white. These masks indicate the area that corresponds to voxels that have been labeled as the nucleus-of-interest nucleus in at least 18 out of 20 participants. The two lateral nuclei are the Globus Pallidus interna (GPi, medial) and externa (GPe, lateral), the most-medial, sphere-like areas are the red nuclei (RN). These lie just dorsal of the substantia nigra (SN), and slightly posterior to the subthalamic nucleus (STN).
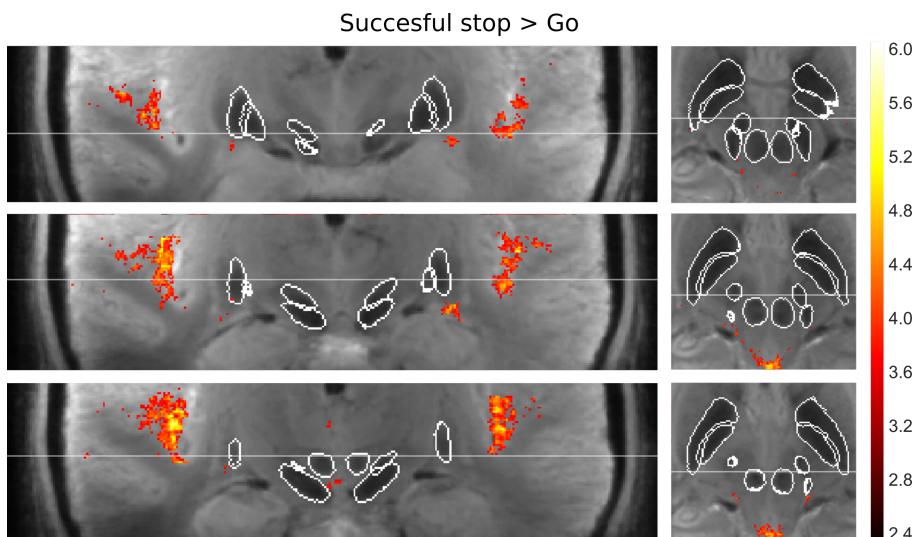
Figure 11 Slices of the voxelwise analysis of the "**Successful stop > Go**" contrast in the T$_2$* weighted group template for protocol 3, showing both average anatomy and a SPM of the z-values. Outlines of the anatomical masks are overlaid in white. These masks indicate the area that corresponds to voxels that have been labeled as the nucleus-of-interest nucleus in at least 18 out of 20 participants. The two lateral nuclei are the Globus Pallidus interna (GPi, medial) and externa (GPe, lateral), the most-medial, sphere-like areas are the red nuclei (RN). These lie just dorsal of the substantia nigra (SN), and slightly posterior to the subthalamic nucleus (STN).

CONNECTIVITY ANALYSES

Since the specificity of task activation patterns of the different BG nuclei was rather limited, we also investigated node-to-node functional connectivity. If the anatomical masks would correspond to distinct functional signals, they should show clear correlational patterns with higher correlations for functional homologous nuclei across the hemispheres, compared to functionally different nuclei in the same hemisphere. Subcortex BG node-to-node signal correlations were computed, without additional modelling of task-related activity. For the 7 T protocols 1-3 (1.2 mm/22 ms/7 T; 1.2 mm/15 ms/7 T; 1.5 mm/14 ms/7 T), but not the 3 T protocol 4 (1.5 mm/30 ms/3 T), robust correlation patterns were found. Importantly, correlations between contralateral functional homologous nodes tended to be higher compared to functionally distinct nodes that were spatially closer. For example, for protocol 3 (1.5 mm/14 ms/7 T), the correlations between left and right STN (mean r = 0.52. std. 0.15) and left and right SN (mean r = 0.54, std. 0.14), were on average considerably higher than those between left STN and left SN (mean r = 0.28, std. 0.22; t(19) = 4.9, p < 0.001 and t(19) = 5.3, p < 0.001) and right STN and right SN (mean r = 0.34, std. 0.2; t(19) = 3.2 , p < 0.001 and t(19) = 4.3, p < 0.001). These correlational patterns suggest that these connectivity measures adhere to functional anatomy and are not just an artefact of spatially correlated noise.

Importantly, the correlation sizes were in general higher in protocol 3 (1.5 mm/14 ms/7 T), especially in STN, SN, and RN (see Figure 14). These higher correlations are to be expected because of the higher tSNR of this protocol compared to protocols 1 (1.2 mm/22 ms/7 T), 2 (1.2 mm/15 ms/7 T), and 4 (1.5 mm/30 ms/3 T).
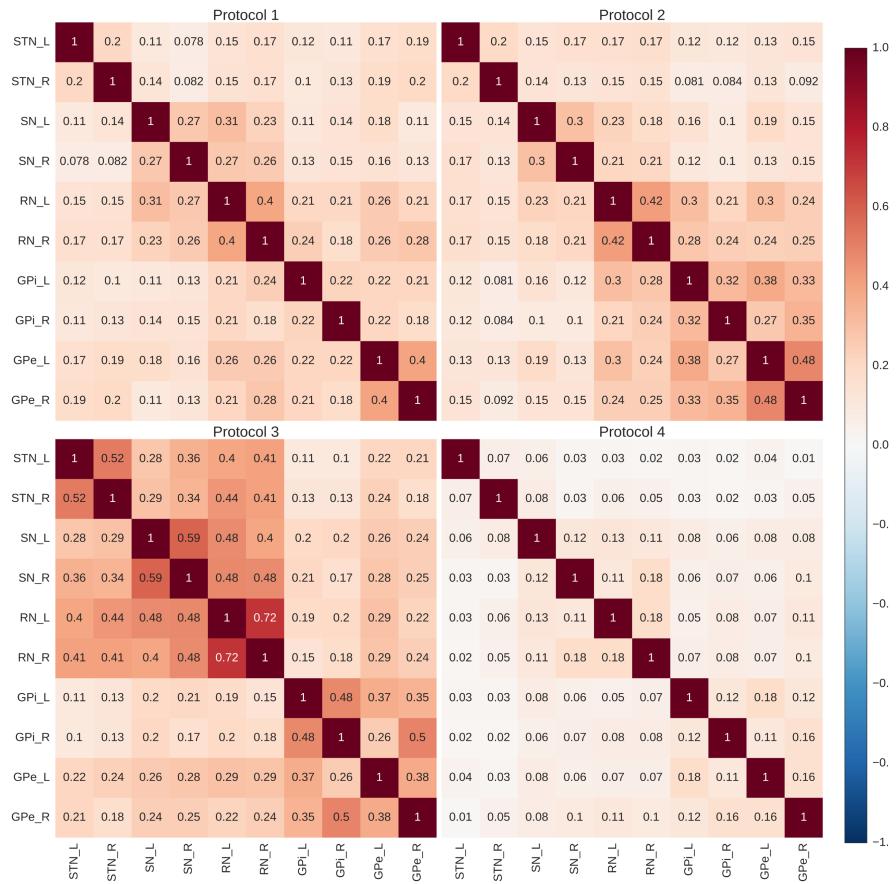
Figure 12 Mean Basal Ganglia functional connectomes for the four protocols. Note how in protocol 1-3 (and especially in protocol 3) contralateral homologues are more strongly correlated than ipsilateral nodes that are spatially much closer. For example, the timeseries in left and right STN are more correlated than those of left STN and left SN, even though they lie adjacent to each other. This suggests some functional relevance of the found correlations, more than just spatially correlated (physiological) noise.

DISCUSSION

The BG play a crucial role in many cognitive paradigms and they are thought to subserve diverse cognitive functions such as decision-making and learning. However, it remains a challenge to functionally image the BG with sufficient anatomical detail to attribute measured signals to specific nodes and their putative subdivisions (de Hollander et al., 2015). Here we

tested three fMRI protocols at 7 T, as well as a comparable protocol at 3 T, to quantitatively test which set of scanning parameters (most notably echo time, resolution, and field strength), deliver robust BOLD sensitivity with maximal anatomical specificity.

First and foremost, our work establishes that, compared to functional neuroimaging of the cortex, some modesty in terms of resolution is necessary. Also, special care should be taken to accommodate the short effective T2* relaxation values in and close to the iron-rich BG nuclei, especially at higher field strengths. Using a spatial resolution of 1.2 mm isotropic and a GRAPPA factor of 4, parameters that are frequently used in 'cortical' 7 T functional neuroimaging studies (van der Zwaag et al., 2016), we found no robust BOLD sensitivity in subcortical BG nuclei. Even when the echo time was specifically optimized for these nuclei (protocol 2), voxelwise tSNRs were very low. The average task-locked signal did not resemble a hemodynamic response and statistical tests showed no task-related activity or significant differences between task conditions. A different picture emerged for the 1.5 mm isotropic 7 T fMRI protocol with a GRAPPA factor of 3 (protocol 3). This protocol showed significant task-related activity in all conditions, with the same limited number of subjects (5). This protocol is similar to earlier work that showed activations in the BG nuclei (Keuken et al., 2015; Mestres-Missé et al., 2017).

We also tried to replicate a high-resolution 3 T fMRI protocol with 1.5 mm isotropic resolution focusing on BG nodes (Pauli et al., 2015). This protocol showed no robust BOLD sensitivity. More specifically, voxelwise tSNR was very low, the average task-locked signal did not resemble a hemodynamic response, and, after FDR correction, no BG nuclei showed significant activation. One may argue that the differences between the findings by Pauli and colleagues and our findings can be attributed to differences in the analysis, preprocessing, and experimental paradigm as follows: (a) we performed a relatively stringent a-priori anatomical-region-of-interest analysis. This was different from the voxelwise analysis without (explicit) multiple comparison correction in Pauli et al. In their study, the data were thresholded at arbitrary and relatively lenient (especially considering the high resolution and limited smoothing) one-sided thresholds of p < 0.005 and p < 0.001; (b) here, no physiological filtering of the fMRI data was performed (since no physiological data were available for this protocol); (c) we used a different experimental paradigm that taps into action selection and response inhibition, rather than (passive) reinforcement learning.

Despite our current findings, it is important to note that functional neuroimaging at a lower field strength of 3 T still has some advantages over UHF MRI in terms of lower costs, reduced geometrical distortions, less T_2* variability, and higher T_2* values across the brain (attenuating the need for very short echo times). However, it is also evident from the current results that the 7 T MRI protocol used in the present study provides superior tSNR at an appropriate spatial resolution to achieve sufficient anatomical specificity in BG nodes. We suggest that special care should be taken in future studies investigating the subcortex, in particular BG nodes, with 3 T fMRI.

Secondly, this study suggests that the BG nuclei are highly similar in their activation patterns during the different conditions of the stop-signal task. Specifically, all nodes show increased activity compared to baseline in both go and failed stops, as well as during successful stopping trials. Moreover, most of the BG nuclei showed increased activity during failed stop compared to go and successful stop trials. Contrary to the findings of Aron and colleagues (2006) in an "STN region" that probably corresponds to a combination of the subcortex BG nuclei studied

here, no BG nuclei showed heightened activity in successful stop trials compared to go trials (for similar findings see Jahfari et al., 2011; but see Aron et al., 2014b; Cai et al., 2014; Erika-Florence et al., 2014; Aron et al., 2015; Hampshire, 2015; Hampshire and Sharp, 2015). A difference in activation between failed stop and go trials, but no difference between successful stop and go trials in the "STN region" has been reported before in other studies (Ray Li et al., 2008; Jahfari et al., 2011). Multiple theoretical frameworks have been developed that might help further interpret these findings in future work (Shenoy and Yu, 2011; Hampshire and Sharp, 2015).

Thirdly, the present study shows that the traditional analysis approach where individual SPMs are transformed to a MNI152 standard space using T_1-weighted anatomical images after smoothing with a moderate 5 mm FWHM Gaussian kernel, leads to a severe loss of anatomical detail. The activation clusters that were found in the "failed stop > go" contrast cover almost the entire subcortex and brainstem. A more specific approach that uses a-priori defined individual anatomical masks and/or a group-specific T_2*-weighted template provided more fine-grained anatomical specificity. Such specificity is necessary for the validation of current detailed models of BG functioning. Theoretical, simulation, and meta-analysis papers have all stressed the negative influence of smoothing on anatomical specificity (Stelzer et al., 2014; Turner and Geyer, 2014; de Hollander et al., 2015).

Lastly, the explorative voxelwise analysis in the group template shows that areas other than the main BG nuclei are involved in the stop signal task, mostly in the thalamus and brainstem, and possibly in the VTA. Unfortunately, the field of neuroimaging is currently lacking detailed subcortical atlases that allow us to probe these areas in more detail and this work motivates further work on the extension of subcortical MRI atlases (there are potentially hundreds of distinct subcortical areas; Alkemade et al., 2013; Keuken et al., 2014a).

FUTURE WORK

The current results shed new light on the pressing issue to develop new UHF fMRI protocols specifically tailored to subcortical brain structures (van der Zwaag et al., 2016). The greatest challenge will be to increase the SNR, allowing for higher resolutions and the sensitivity to detect small differences in activity due to experimental manipulations in cognitive paradigms. There are several directions that future work could help to increase the SNR in the subcortex: (1) rapid acquisition techniques, such as simultaneous multi slice (SMS) and accelerated 3D image encoding. These techniques do not subsequently acquire single 2D slices, but multiple slices or entire brain volumes simultaneously (Boyacioğlu et al., 2015; Setsompop et al., 2016). This allows for reducing TR and the collection of more volumes and/or slices per experiment; (2) the use of multi-echo protocols that yield multiple images with different echo times, collected virtually at the same time. These different images could be used to have an optimal signal across the entire brain, including areas with vastly different T_2* baseline values (Koopmans et al., 2011; Kundu et al., 2012); (3) coil setups tailored towards deep brain structures. Currently, multi-channel coil arrays have a high number of coils that are locally sensitive, which facilitates parallel imaging techniques, but effectively only in the 'outer' parts of the brain (Pruessmann et al., 1999; de Zwart et al., 2002; Setsompop et al., 2016). This local sensitivity can be detrimental to the sensitivity in the deeper parts of the brain, since they are relatively distant from all the coils in the array.

Furthermore, the effective resolution of fMRI can also be further improved by using contrast mechanisms that are more tightly localized than the default BOLD contrast. One promising candidate would be the Vascular Space Occupancy sequence (VASO) that is sensitive to cerebral blood volume (CBV), affording higher spatial specificity to the activated nuclei, especially at higher field strengths (Lu et al., 2003; Huber et al., 2013; 2016). Unfortunately, the increased specificity comes at a cost of reduced signal sensitivity, and future work should test whether VASO can be an effective functional measure not only in cortical, but also subcortical areas. Another candidate might be the use of Spin Echo-based protocols (SE), because of the large amount of large vessels present in the subcortex. The T_2 contrast these sequences offer are less sensitive to draining veins and thus would be more spatially specific to activation of the nuclei themselves (Parkes et al., 2005; Uludağ et al., 2009). Furthermore, Spin Echo-based sequences are less sensitive to susceptibility effects induced by iron deposition. However, those advantages come with a decreased overall BOLD sensitivity and an increased specific absorption rate, especially at UHF, limiting the spatial coverage of the acquisition.

Parallel efforts could focus on improving the sensitivity of functional MRI at the lower field strength of 3 T. Although the SNR is inherently lower at 3 T compared to 7 T, 3 T scanners are much more widely available and have lower operating costs. Future work should thoroughly establish whether robust BOLD sensitivity can or cannot be achieved at 3 T without severely sacrificing anatomical specificity. One possible approach would be to slightly reduce the resolution of the functional images but still use high-quality anatomical data for precise localization of the nuclei-of-interest. The problem of lower SNR might also be somewhat overcome by longer acquisitions and massive averaging, but note that one needs roughly $(7/3)^2$ = 5.4 times more data to obtain similar signal estimation at 3 T versus 7 T, ignoring issues like subject movement and fatigue (the subjects already performed the task for 51 minutes in the protocols described in this paper), as well as a general higher BOLD sensitivity at 7T (van der Zwaag et al., 2009). Although some 3 T studies have convincingly shown activation clusters in subcortical BG nodes, the issue of anatomical specificity of activation clusters has oftentimes been overlooked (de Hollander et al., 2015).

CONCLUSION

In sum, the Basal Ganglia play a crucial role in theories of cognition and disease and studying their functioning could help elucidate the neural underpinnings of therapies such as DBS and cognitive processes such as response inhibition. Functional imaging of these nuclei with sufficient anatomical detail in the living human is, however, a challenging endeavour. Special caution should be taken in the development of UHF fMRI protocols targeting the BG, because the magnetic properties of these small iron-rich nuclei are considerably different from cortical regions, the usual focus of UHF fMRI studies. The study described here provides a first recipe for a validated fMRI protocol at 7 T that can disentangle signals originating from different subparts of this subcortical network.

7

DIFFERENT WAYS OF LINKING BEHAVIORAL AND NEURAL DATA VIA COMPUTATIONAL COGNITIVE MODELS

ABSTRACT

Cognitive neuroscientists sometimes apply formal models to investigate how the brain implements cognitive processes. These models describe behavioral data in terms of underlying, latent, variables linked to hypothesized cognitive processes. A goal of model-based cognitive neuroscience is to link these variables to brain measurements, which can advance progress in both cognitive and neuroscientific research. However, the details and the philosophical approach for this linking problem can vary greatly. We propose a continuum of approaches which differ in the degree of tight, quantitative, and explicit hypothesizing. We describe this continuum using four points along it, which we dub "qualitative structural", "qualitative predictive'", "quantitative predictive'", and "single model" linking approaches. We further illustrate by providing examples from three research fields (decision making, reinforcement learning, and symbolic reasoning) for the different linking approaches.

INTRODUCTION

In recent years, cognitive neuroscientists have applied formal, computational cognitive models to more effectively understand how the brain implements cognitive processes such as decision making, reinforcement learning, and symbolic reasoning. Such formal cognitive models can decompose effects in behavioral data by description in terms of underlying latent cognitive processes and associated variables. "Model-based cognitive neuroscience" links these variables to brain measurements. This approach can, on the one hand, constrain the development of cognitive models, while, on the other hand, also refine models that explain how cognitive processes are implemented in the brain (Forstmann et al., 2011). Linking brain measurements to psychological constructs has been conceptualized as identifying a *bridge locus*: to link some mental capacity to a neural substrate (Teller, 1984; Schall, 2004). A researcher can identify *bridge loci* by empirically testing probable *linking hypotheses*. An example of a linking hypothesis is that the ventral striatum represents how much reward a subject expects during a task.

The scope of this paper is limited to the neural linking of computational cognitive models and excludes (much more common) conceptual verbal theories of cognition. A main strength of computational models of cognition over verbal theories is that they force the modeler to be explicit and precise in their assumptions about cognition. This reduces the potential for miscommunication and misunderstanding of what a cognitive theory entails and reduces the potential for vague statements that are hard to test empirically (Lewandowsky and Farrell, 2010; Forstmann and Wagenmakers, 2015; Hawkins et al., 2015b). Additionally, because of their quantitative nature, computational cognitive models offer the possibility of assigning hard numbers to abstract cognitive concepts like "response caution" or "learning rate". These numbers allow the integration of cognitive theory with quantitative neural data in a statistical framework. Ultimately, we believe that this quantitative, statistical approach can bring us much tighter integration between the cognitive and neural domain than verbal theories, supporting more stringent tests of the theories and of the links between neural and behavioral data.

David Marr (1982) famously subdivided the problem of understanding how the brain works into three levels: 1) a computational level that describes what computational problem a brain aims to solve in a given context, 2) an algorithmic level that describes how the problem can be solved, and 3) an implementational level that describes how this algorithm can physically be performed. Linking cognitive models to neural data can inform theories at all three levels.

For example, at the algorithmic level, cognitive models of speeded decision making make clear predictions about how subjects can lower the distance an evidence accumulator has to travel from the start of a trial to the end. However, for many models, it is not possible to investigate whether this is achieved by increasing the starting point or the finishing threshold of the accumulator, with only behavioral data. Clearly, neural data can help to distinguish between these different algorithms and needs to carefully be related to the cognitive models that are successful in explaining behavior (Bogacz et al., 2010; Forstmann and Wagenmakers, 2015).

Similarly, more elaborate explanations at the implementational level are only possible with a firm understanding of what problem the brain is actually solving and what possible strategies are. This point is made again in Marr's original proposal of the three levels, and also eloquently put in the following analogy of David A. Robinson (Robinson, 1992): "Trying to understand

perception by studying only neurons is like trying to understand bird flight by studying only feather: it just cannot be done. In order to understand bird flight, we have to understand aerodynamics; only then do the structure of feathers and the different shapes of birds' wings make sense". We believe the linking of cognitive models, explaining how computational problems the brain is faced with can be solved, to neural data, rooted in the physical substrate of the algorithms.

Another advantage of linking cognitive models to neural data might be the sheer wealth of additional information that neural data can provide in comparison to behavioral data. By any measure, the amount of information in behavioral data is extremely limited. Because many behavioral experiments provide not much more than choices and reaction times, literally all the data of a behavioral experiment can usually be summarized in a few hundred (only choice) up to a few thousand bytes (also reaction times). Compare that to ultra-high resolution fMRI data from 7 Tesla MR scanners, which can easily occupy a few billion bytes per subject. Of course, the picture is more complicated than this: the neural data is much more ambiguous. However, recent efforts in both sequential sampling models as well as models of value-based learning have taught us that to reliably estimate the parameters of more complicated cognitive models and dissociate between different versions of them, the amount of information of most behavioral datasets is very limited (Turner and Sederberg, 2014; Hawkins et al., 2015a; Steingroever et al., 2016). Thus, even disregarding the conceptual benefits, cognitive modelers should welcome the practical benefits arising from the wealth of extra information in neural data, as it provides an opportunity to develop richer models of cognition than has been possible so far.

But how do we link cognitive models to functional brain measurements most effectively? In the past decade, parameters of formal cognitive models have been linked to many measures of neural activity, such as EEG, fMRI, and single-cell recordings. These studies have employed wildly varying approaches, connecting variability in behavior and brain measurement at the level of subjects, conditions, and even trials. In some studies, cognitive models are used to set up testable hypotheses about brain activity. In other studies, cognitive model parameters are directly correlated against measurement models of neural data, after both models have been fit to their respective data domain. Some studies make a single model of both brain and behavior and try to predict both at the same time.

In this review, we aim to provide a particular taxonomy of possible methods of linking neural data to cognitive models. We think this taxonomy is useful to describe the work that has been done so far and understand how it progressed. Additionally, it offers cognitive neuroscientists a set of handles on where to start when linking neural data to cognitive models, as well as what to strive for in the long run (see also the discussion).bWe then give some examples of the four categories of linking in three subfields of cognitive neuroscience from the literature. Finally, we will discuss the strengths and weaknesses of different points on the continuum and lay out future challenges and developments.

LOOSER AND TIGHTER LINKS

There are many approaches to linking formal models of cognition to neural data. These approaches differ in how explicit and precise the link is made between neural, physiological

processes on the one hand, and cognitive, phenomenal processes on the other hand. We propose a continuum of "tightness" of linking. At the loosest level, cognitive models can be linked with neural data simply by constraining the kinds of structural assumptions allowed in the models in order to respect data about neural structures. Tighter links can be created by comparison of predictions for neural and behavioral data, or neural and behavioral model parameters. The very tightest and most explicit links are specified by "joint" models, which make quantitative predictions about both neural and behavioral data at the same time.

Table 1 provides some illustrative examples which are elaborated below. These examples highlight four commonly-used points on the continuum between loose to tight linking. Below, we first provide definitions for those four different commonly-used levels of linking. Following that, we give detailed examples of these approaches in practice, with each level of linking illustrated in up to three different research domains: perceptual decision-making; reinforcement learning, and symbolic reasoning.

Qualitative structural linking: Neural data on the structure of the brain are used to constrain the structure of a cognitive model. An example of this is the leaky competing accumulator model (LCA): "the principles included in the modeling effort have neurobiological as well as computational or psychological motivation, and the specific instantiations of the principles are informed by additional neurophysiological observations" (Usher and McClelland, 2001).

Qualitative predictive linking: A cognitive model is tested using qualitative predictions about both neural and behavioral data. For example, Borst et al. (2010) used the symbolic reasoning modeling framework of ACT-R to make predictions about the difference in fMRI-signals between conditions which differed in behavioral measures associated with task difficulty, separately for different brain regions: "the model does not predict a general increase in BOLD response with task difficulty; instead, it predicts lower but more persistent activation levels for the more difficult conditions in the visual and manual modules, and higher and more persistent activation levels for the more difficult conditions in the problem state and declarative memory modules" (Borst et al., 2010).

Quantitative predictive linking: the predictive output of a cognitive model is quantitatively related to some aspect of neural data. In an early example of this approach, fMRI data was acquired during a Pavlovian conditioning task. The signal that was measured by fMRI was correlated with the error signal of a temporal difference (TD) algorithm performing the same task: "we used the actual output of a TD learning algorithm to generate a PE (or δ) response at two main time points in a conditioning trial: the time of presentation of the CS and the time of presentation of the reward. The output of this algorithm was then entered into a regression model of fMRI measurements from subjects who underwent appetitive Pavlovian conditioning. This enabled us to test for brain regions that manifested a full range of TD error-related PE response'" (O'Doherty et al., 2003).

Single model: a single generative model predicts a joint distribution over both cognitive and neural data. For example, Purcell et al. (2012) used single-cell recordings from monkeys: "Models using actual visual neuron activity as input predicted not only the variability in observed behavior but also the dynamics of movement neuron activity. This union of cognitive modeling and neurophysiology strengthens the interpretation of visual neuron activity as a representation of perceptual evidence of saccade target location and the interpretation of movement neuron activity as the accumulation of that evidence".

We will now present the four levels of linking in greater detail, by using examples from the fields of evidence accumulation models, value-based decision-making models, and symbolic reasoning models.

Table 1. Examples of four different approaches to linking models of evidence accumulation, reinforcement learning, and symbolic reasoning to neural data

Linking type			
Qualitative structural linking	**Usher and McClelland** (2001): the leaky competing accumulator model assumes that in evidence accumulation, accumulators corresponding to different choice options inhibit each other and also passively decay. This is inspired by the neural observations of mutual inhibition between neurons and passive decay of membrane potentials.	**Frank and Claus** (2006) a neural network model simulates dopaminergic basal-ganglia-cortical interactions. This is a neurocomputational model that makes qualitative predictions about both brain activity and behavior.	**Anderson** (2007): the general ACT-R framework has, in its later versions, been explicitly linked to fMRI brain research. The framework assumes distinct cognitive modules and relates them to different parts of the brain.
Qualitative predictive linking	**Ho, Brown, and Serences** (2009): evidence accumulation models predict distinct fMRI time courses for different drift rates. This qualitative prediction was supported by differences in the HRF across the entire brain.	**Berns, McClure, Pagnoni, and Montague** (2001): neural recordings from two conditions with differing predictability in upcoming response with a certain associated value, as estimated by a temporal difference learning model are contrasted.	**Borst, Taatgen, Stocco and van Rijn** (2010): a priori predictions about differences across conditions in cognitive modules predict cortical activations, that are tested using fMRI.
Quantitative predictive linking	**van Maanen et al.** (2011): trial-to-trial fluctuations in response caution as estimated by STLBA are correlated with single-trial BOLD estimates. &	**O'Doherty, Dayan, Friston, Critchley, and Dolan** (2003): an error signal as estimated by a reinforcement learning model was regressed against BOLD activity. OFC and ventral striatum coded for this signal.	**Borst, Taatgen, and van Rijn** (2011): An ACT-R model predicted activity patterns for different cognitive modules during a multitasking paradigm. The activity of these modules was convolved with an HRF and regressed against fMRI volumes, to identify brain regions corresponding to the different cognitive modules.

Table 1 (Continued)

Linking type	
Single model	**Purcell, Schall, Logan and Palmeri** (2012) constructed a model that takes raw neural data of a visual area as input. This model can then predict distributions of both behavioral data as well as neural data in a downstream evidence accumulation areas.
	Anderson (2012): a simple RT-model of cognition was linked to a multivariate model of neural activation in fMRI by a Hidden semi-Markov model. The resulting joint model made predictions about cognitive states and neural recordings.

EXAMPLES OF QUALITATIVE STRUCTURAL LINKING

QUALITATIVE STRUCTURAL LINKING IN MODELS OF EVIDENCE ACCUMULATION

Recently, attempts have been made to link evidence accumulation models with neural data. The earliest attempts, such as seminal work by Usher & McClelland (Usher and McClelland, 2001), defined qualitative structural links. These links were structural in the sense that the constraints were applied to the structure of the model, not to the model's predictions, and the links were qualitative in the sense that the constraints revolved around the inclusion/exclusion of model elements, not to the quantitative parametric values taken. For example, the leaky competing accumulator model (LCA) of Usher & McClelland (2001) specifically included structural elements such as mutual inhibition between competing accumulators. This inclusion was motivated by neural data which demonstrate the prevalence of inhibitory connections between nearby neurons within the same cortical stratum. Similarly, the LCA included passive decay of accumulated evidence, to respect the neural observation that membrane potential decays back to baseline in the absence of input. Evidence in favor of these links was inferred by the observation that the resulting cognitive model provided a good fit to behavioral data.

QUALITATIVE STRUCTURAL LINKING IN MODELS OF REINFORCEMENT LEARNING

The classic parallel distributed processing models provided cognitive descriptions of learning including structural constraints from neural data (PDP; Rumelhart et al., 1986a; 1986b). The models assumed massive parallelism and distributed information representation, reflecting key findings in the emerging neural literature on cortical structure. The models also used learning rules such as back-propagation, which were inspired by neural findings such as Hebbian plasticity.

QUALITATIVE STRUCTURAL LINKING IN MODELS OF SYMBOLIC REASONING

The ACT-R production framework (Anderson, 1992) is a domain-general model of human cognition. ACT-R began as a cognitive model purely aimed at behavioral data, but has since been extended in great detail to jointly consider behavioral and neural data (Qin et al., 2003; Sohn et al., 2003) . The earliest linking of the ACT-R model to neural data was qualitative structural linking, which identified links between different cognitive modules in ACT-R and different brain regions. These links respected findings about the localization of brain function that were emerging at the time from the then-new method of fMRI. For example, the "visual module" of ACT-R was linked with lower occipital brain regions, and the "motor module" with motor cortices in the parietal and temporal lobes. These links defined the structure of the model and allowed the investigation of hypotheses about deficits due to brain lesions, for example.

EXAMPLES OF QUALITATIVE PREDICTIVE LINKING

QUALITATIVE PREDICTIVE LINKING IN MODELS OF EVIDENCE ACCUMULATION

Hanes and Schall (1996)recorded single-cell activity in the frontal eye fields (FEF) in behaving macaques. The activity of "movement neurons" predicted the execution of saccades. Hanes and Schall showed that the ramping activity of these neurons preceding a saccade always ended with the same firing rate, but the rate of increase of firing rate was variable. The authors related these qualitative patterns to evidence accumulation models. In certain evidence accumulation models, evidence builds up gradually before a response is made, with two key properties: the rate of build-up (the "drift rate") differs from decision to decision, but the amount of accumulated activity just before a response is issued (the "threshold") is always the same. This is qualitatively similar to the pattern observed by Hanes and Schall.

QUALITATIVE PREDICTIVE LINKING IN MODELS OF REINFORCEMENT LEARNING

The field of reinforcement learning and value-based decision-making has a long history of computational cognitive modelling (Sutton and Barto, 1998). These computational models made it possible to design experiments that manipulated model parameters across conditions and compare the corresponding neural and behavioral data qualitatively (Berns et al., 2001; Knutson et al., 2001). An example is given by Nieuwenhuis et al. (2002),who observed that the Holroyd and Coles' model could mirror the impaired performance of older adults in a probabilistic learning task, as well as the accompanying reduced error-related negativity (ERN) measured by EEG. It could do so by varying only one parameter in the model that represents to the efficiency of dopaminergic connections to the anterior cingulate cortex (ACC).

QUALITATIVE PREDICTIVE LINKING IN MODELS OF SYMBOLIC REASONING

The ACT-R model assumes distinct cognitive modules that perform different parts of cognitive tasks (Anderson, 2007). For example, the cognitive steps necessary for performing some symbolic logic operation might be modeled as involving the visual module (to perceive the stimulus), the procedural and declarative memory modules (to remember the logical rules), and the motor module (to produce the desired behavioral response). From these assumptions, ACT-R can make predictions about differences in reaction time and accuracy between conditions. Many neuroimaging studies have related cognitive ACT-R models to fMRI data to localize the cognitive modules within the brain. Such localization assumptions are linking hypotheses, and subsequent studies have used qualitative predictive approaches to test those. For example, Borst et al. (Borst et al., 2010) constructed an ACT-R model of a task where both a subtraction operation had to be performed at the same time as a text entry task. The model made priori predictions about which modules (e.g., ``Problem State'', ``Declarative Memory'', ``Manual'', and ``Visual'') would be more activated during different combinations of easy/hard versions of the two tasks. These predictions were then tested by comparing them to brain area activations during the task measured by fMRI.

EXAMPLES OF QUANTITATIVE PREDICTIVE LINKING

QUANTITATIVE PREDICTIVE LINKING IN MODELS OF REINFORCEMENT LEARNING

Using quantitative outputs of a computational model of cognition to predict neural activity has been a successful strategy in the study of value-based decision-making and neuroeconomics (Glimcher, 2004). Especially prominent has been the *single-trial regression approach*, in which parameters of a reinforcement learning model are estimated from choice behavior during tasks involving the learning of reward values associated with different choices. These subject-specific parameter estimates can be used to calculate estimates of the subjective values of the different choice options to the subject, for every individual trial during the experiment. These subjective, trial-by-trial values can then be used as a hypothetical cognitive signal that tracks, for example, the difference between the expected reward after a choice and the reward that was actually delivered (the so-called "prediction error" or "delta'' signal"). To investigate a linking hypothesis, the researcher then hypothesizes that this cognitive signal is represented in the brain, at the *bridge locus*. Neural signals from the bridge locus should correspond to the phenomelogical concept under study, and to the hypothetical cognitive signal in this case (Teller, 1984). For example, the bridge locus of the prediction error signal might be some area in the brain where the neural signal consistently tracks the difference between the expected reward and the actual reward in a reinforcement learning task. At a practical level, the hypothetical cognitive signal, as estimated by the reinforcement learning model, can be transformed to a hypothetical BOLD fMRI-signal, by convolution with a hemodynamic response function (Glover, 1999). This creates a hypothetical fMRI signal corresponding to the prediction error signal, which can be used as a regressor in a general linear model (GLM), with additional regressors for other task-related activity (for example stimulus presentation). The parameters of this GLM are then estimated for all voxels in the brain. This yields a statistical parametric mapping of the brain that shows for which areas of the brain BOLD activity correlates with the hypothetical neural signal representing stimulus value, and offers candidates for the bridge locus. This approach was used to show that the BOLD activity in orbitofrontal cortex (OFC) and in ventral striatum was correlated with the temporal difference error signal as estimated by a reinforcement learning model (O'Doherty et al., 2003).

QUANTITATIVE PREDICTIVE LINKING IN MODELS OF SYMBOLIC REASONING

Recent versions of the ACT-R architecture predict quantitative differences in activation in different cognitive modules during a task. These predictions can be convolved with a canonical hemodynamic response function, generating quantitative hypotheses about which areas of the brain modulate their activity in correspondence with the activity of the proposed cognitive modules in the model. Such time courses can be fitted to all the voxels throughout the entire brain. For example, Borst et al. used a multitasking paradigm, where either a subtraction or a text entry task had to be performed, while at the same time performing a listening comprehension task (Borst et al., 2011). The ACT-R model predicted, for every trial, the relative activity of "Problem State", "Declarative Memory", "Vision", and "Manual" modules. These relative activities correlated with the measured BOLD signal in corresponding brain areas.

QUANTITATIVE PREDICTIVE LINKING IN MODELS OF EVIDENCE ACCUMULATION

Linking evidence accumulation models of speeded decision-making to neuroimaging data is more difficult than for the models of reinforcement learning and symbolic reasoning reviewed above. One reason for this is that, in order to explain random variability in reaction times, models of speeded decision-making are stochastic. Across trials, the models assume variability in the amount of evidence that is necessary to make a decision, as well as variability in the speed of evidence accumulation (LBA; Brown and Heathcote, 2008), possibly amongst even more variability (Ratcliff and McKoon, 2008). This means that, unlike in most reinforcement learning models, there is no one-to-one correspondence between data and the parameters of the model at the level of a single trial. This precludes the very popular single trial regression approach, at least for "out-of-the-box" evidence accumulation models, although different alternatives to resolve this issue have been proposed and performed.

One alternative is to change the unit of analysis from single trials to single subjects, focusing on the covariance of differences between subjects in neural and behavioral parameter estimates. In an fMRI study of decision-making, Forstmann et al. (2008) instructed subjects to stress either the speed or accuracy of their decisions. The difference in BOLD-activity between accuracy- and speed-stressed trials in the striatum and the presupplementary motor area (pre-SMA) was correlated across subjects with the difference in model parameters related to response caution, estimated from behavioral data via the LBA model. In other words, participants who made large changes in their cognitive settings (for speed vs. caution) also showed large changes in fMRI responses, and vice versa. This provides some evidence for a role of these brain areas in setting a response threshold before a decision is made.

More recent approaches to linking evidence accumulation models to neural data start with the neural signal, and use this as input to an extended evidence accumulation model. Cavanagh et al. estimated, separately for each trial in a decision-making experiment, the power in the theta frequency band from recorded EEG signals. These single-trial estimates of theta power were then used to inform parameter estimates in an extended version of the drift diffusion model (HDDM; Cavanagh et al., 2011). This model allowed different estimates of the threshold parameter on different trials, and a covariate model to assess the association of single-trial theta power with single-trial threshold estimates. Parameters estimated from data suggested that the coefficient of the covariate was probably larger than zero, which provides evidence that response caution (measured by the threshold parameter) is related to fluctuations in theta-power in medial prefrontal cortex.

SINGLE MODEL APPROACH

SINGLE MODEL APPROACHES IN EVIDENCE ACCUMULATION

In some work in neurophysiology, the link between neural data and cognitive model is more explicit. The most complex models can take as input neural data from one source, and then predict neural data from another source, as well as behavior. Purcell et al. (2012) identified and recorded from different clusters of cells in the frontal eye fields (FEF) in awake macaque monkeys during a visual search task. Some neurons in the FEF only respond to specific visual inputs ("visual" neurons), while other neurons respond only just before a saccade ("motor"

neurons), and some neurons respond to both ("visuomotor" neurons). Considered from the perspective of an evidence accumulation model of decision-making, the visual neurons might be interpreted as providing a continuous, noisy, representation of decision evidence, and the motor neurons might be interpreted as the accumulators which process that evidence. Purcell et al. used the spike trains recorded from visual and visuomotor neurons as input to the accumulators of an evidence accumulation model. The model used these inputs to reliably predict the behavioral data of the monkeys (response proportions and reaction time distributions).

Purcell et al. also investigated the predictive performance of the model on neural data. For this, they used nine different architectures for evidence accumulation. These architectures differed in details like the presence or absence of leakage in the accumulation process, or mutual inhibition between accumulators. Interestingly, the response proportions and response time distributions were well explained by many of the different model architectures, even though those architectures made very different assumptions about neural structure. However, Purcell et al. showed that only one class of evidence accumulation architectures was also able to predict all the quantitative patterns in the neural data coming from the motor neurons.

SINGLE MODEL APPROACHES IN SYMBOLIC REASONING

Simple symbolic reasoning models have been combined with functional neuroimaging data in a single model using Hidden Semi-Markov Models (HSMMs). Such models assume that, in order to perform a task, subjects move through a discrete set of cognitive steps, or "states", until they finish the trial (usually by giving a response). A HSMM can be fit to both behavioral and neuroimaging data, where it is assumed that both are dependent measurements of the same sequence of states.

Anderson, Betts, Ferris, and Fincham (2010; 2012) first applied this approach to a dataset where students solved linear algebra problems in an MRI scanner, where every step in solving the problem was made explicit using the task interface. Given both reaction times and functional neuroimaging data, the model reliably predicted in which state of solving the linear algebra problem the subject was for a given moment in time.

DISCUSSION

A growing number of researchers are working towards linking formal cognitive computational models with neuroscientific data. This linking effort is made in vastly different fields of cognitive modeling, ranging from perceptual and value-based decision-making to symbolic reasoning models. These models are also linked to neural data coming from very different neuronal imaging modalities, including single-cell recordings, EEG, and fMRI. We described different kinds of linking that are applied in four discrete categories that vary along a continuum of how tight and how explicit the link between cognitive model and neural data is made. However, it is clear that even within these categories, different analyses are applied.

The great majority of studies using model-based links between neural and behavioral data, so far, are based on a regression analysis. This analysis tests for relationships between parameters estimated by a cognitive model and some aspect of a neural signal -- often a

parameter estimated using a neural measurement model. In such approaches, the exact mapping from cognitive parameter to neural signal is typically left implicit, but upon closer inspection the link is almost always a linear relationship between a parameter of the cognitive model and a parameter of an easy-to-use, traditional measurement model of the neural signal. The role of the measurement model is to reduce the raw neural data to a single number (per subject, per condition, or per trial) that can be submitted to a standard regression analysis. For example, in fMRI this measurement model is most often a standard GLM used to model BOLD responses via a canonical hemodynamic response function. The GLM allows the estimation of coefficients which index the height of the hemodynamic response function, or the difference in height between conditions, and it is these coefficients that are later correlated against the parameters of a cognitive model. In EEG, the measurement model is often just the mean signal intensity in a predefined stimulus-locked time window.
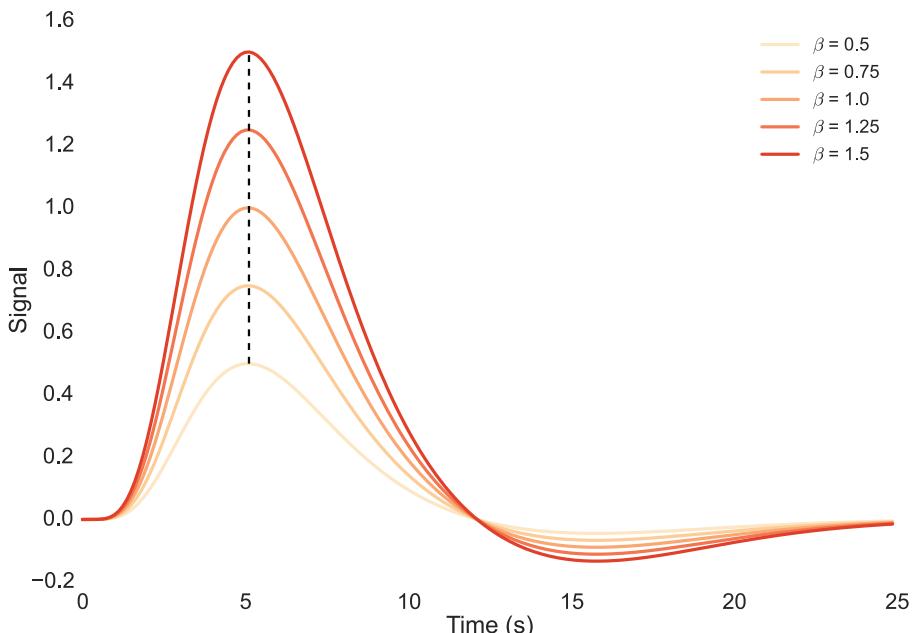
Figure 1. Standard canonical hemodynamic response function model of blood oxygen level-dependent activity. In regression-based approaches, it is assumed that the only way the blood oxygen level-dependent response is modulated is that the canonical shape is multiplied by some factor β.

The assumptions underlying these linking functions are rarely tested, even though there is ample evidence that they are probably often violated. For example, a central assumption of the canonical hemodynamic response function (HRF) model used in fMRI is that the HRF is identical across brain areas and subjects, but of course this is not true (Gonzalez-Castillo et al., 2012). Even more problematic is that cognitive processes, as modeled by computational models, are typically assumed to modulate only the *amplitude* of the task-locked hemodynamic response. Figure 1 illustrates just how simplistic this assumption is. Contradicting this assumption, the main finding of multiple linking papers was a relationship between an estimated cognitive parameter and the *delay* (Ho et al., 2009) or *dispersion* of the HRF (Borst et al., 2011). We have also seen in our own data (Forstmann et al., 2008), that cue-locked

differences in the height of the HRF across conditions are often accompanied by differences in the onset-till-peak, as well as the dispersion of this HRF. These problems of violated or untested assumptions are not unique to fMRI measurement. For example, a frequent assumption in analyses of single-cell recordings is that recordings taken over different trials, cells, or conditions, are independently and identically distributed, but this is often not true (Aarts et al., 2014).

The more advanced linking approaches we have reviewed, particularly the quantitative predictive approach and the single-model approach, enable future work to focus on more complex relationships and formally incorporate such links in quantitative models. In functional neuroimaging, for example, one possible strategy is to move away from voxels as the single unit-of-analysis, and move towards analyses that use anatomically-informed regions-of-interest. First of all, such a unit of analysis is often more appropriate, because anatomical boundaries are much less arbitrary than an artificial voxel-grid and they respect the close relationship between anatomical structure and function (Smith et al., 2009; Lohmann et al., 2013; Alkemade et al., 2015). For instance, a hypothetical relationship between degree-of-surprise and activity in the rostral part of the anterior cingulate cortex is to many neuroscientists much more interpretable than a relationship between degree-of-surprise and a blob thresholded at a z-value of 3.1, with a volume of 3300 mm^3 at MNI coordinate (2, 16, 32). Secondly, such an anatomically-informed approach aligns with the goal of tighter, single models that take as much neural data into account as possible. Ultimately, one would like to find bridge loci of cognitive processes that correspond to anatomical regions that have been described, validated and related to function for more than a century, rather than the smoothed and arbitrarily threshold activations blobs that frequently differ between fMRI studies (Brodmann, 1909; Derrfuss and Mar, 2009). Thirdly, there is also an important practical benefit to this: by reducing the huge dimensionality of all the voxels in the brain to the number of anatomical constructs one is interested in, the number of neural signals that need to be analyzed is reduced by multiple orders of magnitude. The corresponding reduction in computational burden allows the use of more sophisticated mathematical models, and more complete statistical treatments. Some of the more computationally demanding studies that have been published the past years would not have been feasible without dimensionality reduction of the neural data (Wiecki et al., 2013; Frank et al., 2015; Turner et al., 2015).

A possible drawback of this strategy is the lack of "negative controls", which provide divergent validity. By exclusively focusing on a subset of a priori regions-of-interest, a researcher could potentially miss other brain areas that should be of interest. Clearly, the set of brain areas that is investigated should be narrowed down only after more exploratory research uncovered the set of potential bridge loci within all brain areas.

Even if these quantitative links between model parameters and neural signals are made more explicit, researchers must still remain circumspect in the conclusions they draw from any of these statistical links they find between the two. Clearly, computational models that were developed in cognitive psychology are there to explain *cognition*. At best, they give a formalization of the kind of cognitive processes the human brain can perform, how they differ in different circumstances, and formalize differences in cognition across subjects. They describe the algorithms that take place in the brain and which quantities it therefore has to compute, but these models usually remain agnostic about the precise implementation of these algorithms at the level of neural signals (Moore, 1956; Marr, 1982; Schall, 2004; Mars et al., 2012).

When a brain region is identified that shows a correlation between neural signal and a cognitive parameter, this area may be involved in computing the quantity that corresponds to that parameter. Nevertheless, it is still very unlikely that such a cognitive parameter is a cognitive process in itself, and that is has a simple one-to-one, cognitive-process-to-brain-area mapping (O'Reilly and Mars, 2011; Mars et al., 2012). This is because many other hypotheses can be generated which are consistent with the observed link, but differ in the mechanics that explain the link (e.g., perhaps the identified region simply relays or mirrors the signal of interest). Finding relationships between cognitive models and neural measurements is just a first step toward more detailed neurocomputational models (Bogacz et al., 2010).

WHEN IS A LINKING APPROACH NOT GOOD ENOUGH?

It is difficult to avoid the appearance of value judgments in our proposed continuum of loose-to-tight linking. However, we would like to stress that it is not true that tighter linking is always preferable to looser linking. The ideal point on the continuum depends on many things, but most importantly on the status of the formal quantitative models in the research paradigm of interest. Tighter linking approaches are only feasible when there exist well-understood and settled quantitative models of both the behavioral data and the neural data in the paradigm of interest. Even more, these models must be computationally or analytically tractable, for any level of linking, and they should preferably be specified at the level of distributions and likelihood functions for the tightest possible linking. Where these assumptions are not met, linking approaches beyond the simplest qualitative structural or qualitative predictive are not likely to succeed (e.g., this was the case for models of perceptual decision-making in the late 1990s and early 2000s). Conversely, in areas for which tractable quantitative models do exist, it is incumbent on researchers to strive for the tightest possible linking approaches (e.g., it is no longer reasonable for perceptual decision-making models to be linked to neural data using qualitative approaches).

We propose the following guidelines for researchers searching for the right way to link their behavioral and neural data via cognitive models. First of all, when a researcher is interested in how a cognitive model relates to computations performed in the brain, it is always a good idea to come up with qualitative predictions. One should always ask themselves the question of what aspects of a model correspond to structural aspects of the brain (qualitative structural linking), as well as how variability in the parameters of the model across subjects, conditions or trials, would relate to differences in neural functioning (qualitative functional linking). These intuitions can then be tested empirically by clever experimental design, modulating some aspect of either the neural or cognitive domain and measuring the corresponding change in the other one.

Only after such qualitative predictions have been made and possibly tested, one should wonder if these predictions can be phrased in a quantitative way. Is there a neural measure that possibly corresponds to variability in the neural process we hypothesize? And can we come up with a parameter estimate from the model that it can be related to? If so, a wealth of literature has shown relatively straightforward methods of relating the two to each other, which we have reviewed under quantitative functional linking. If it's possible to use more elaborate models of the neural data, this is usually a good idea, especially in an explorative setting, because it allows for relaxing and testing the assumptions about the links between neural and cognitive models (e.g., maybe the dispersion of the HRF in the striatum and not so much the height is modulated by response caution).

Third, only when such exploratory, but quantitative, efforts have been successful, one can start thinking about how to unify the findings into a single model. This is a very challenging enterprise, as we understand little about how the brain actually computes anything, but recent successes suggest that concepts from cognitive and neural models can to a surprising extent just be equated. For example, the decision-related signal in single neurons in LIP is not just a correlate of the decision variable, but may be the decision variable itself (Purcell et al., 2010). And maybe cognitive states and neural states during problem solving are two sides of the same coin (Anderson, 2012). While the exercise of developing single models explaining both behavioral and neural data has only just begun, it will be very interesting to see what new models the scientific community can develop and extend in the coming future.

CONCLUSIONS

Linking formal cognitive models to neural data can improve our understanding of how the brain functions. However, the precise technical details and philosophical approach to tackling this linking problem can vary greatly. We have focused on one important attribute of linking: the degree of tight, quantitative, and explicit hypothesizing. In each field of cognitive research, the earliest approaches to linking behavioral and neural data are typically qualitative. As knowledge is accumulated, and as formal models become more settled, linking approaches become more quantitative and more explicit. Even in that case, however, model parameters are most frequently estimated separately for the behavioral and neural models, and the two models are brought together only at the very end, in a simple linear regression on model parameters. Future work should explicitly model how differences in cognitive parameters modulate differences in the signal in the neural domain, thereby acknowledging the richness of the data in the neural domain and exploit more than the most common parameter of the simplest measurement model in that domain.

8

A MODEL-BASED 7 T FMRI STUDY INVESTIGATING THE ROLE OF DIFFERENT SEGMENTS OF THE SUBTHALAMIC NUCLEUS DURING PERCEPTUAL DECISION-MAKING

ABSTRACT

A prominent model of the subthalamic nucleus (STN) posits that the STN can be functionally subdivided into a dorsolateral 'motor', central 'associative', and ventromedial 'limbic' part. Here, we tested this tripartite model using ultra-high field functional MRI at 7 Tesla on 19 subjects performing a perceptual decision-making task using a random dot motion discrimination task (RDM). The RDM task was extended with a response bias cue and a difficulty manipulation. Both manipulations are known to modulate BOLD activity in different brain networks. Furthermore, subjects responded with their left and right index finger. Motor responses are known to initiate contralateral activity in the motor network and possibly also the STN. We analyzed the BOLD signal in three subregions of the STN, using individual, anatomically-defined masks. We also related BOLD activity to parameter estimates of the diffusion decision model (DDM). We found converging, but anecdotal evidence that the STN is involved in implementing response biases, with similar effect sizes in all three segments. STN activity in all segments was the same for easy and hard trials and was not related to inter- or intra-individual differences in the rate of evidence accumulation. Lastly, activity in left and right STN was the same for motor responses using the left and right hand in all three subregions. Taken together, these findings do not support the functional tripartite model of the STN.

INTRODUCTION

The subthalamic nucleus (STN) is a small, subcortical brain structure and an input node of the basal ganglia (BG). It is a target for deep brain stimulation (DBS), which reduces the motor symptoms of Parkinson's Disease (PD) by electrically stimulating the STN (Lozano and Lipsman, 2013; Fasano and Lozano, 2015). However, DBS can lead to severe side-effects such as cognitive decline, depression, and (hypo)mania (Temel et al., 2006; Groiss et al., 2009; Christen et al., 2012).

The so-called tripartite model of the STN explains these side-effects by a subdivision of the STN into three parts with different functional roles. These parts are hypothesized to be connected to three cortical networks, which can be characterized as a "limbic" network, an "associative" network, and a "motor" network. Consequently, the proposed subdivision of the STN also consists of limbic, associative, and motor parts, which can be found in the ventromedial, central, and dorsolateral parts of the STN. The tripartite model proposes that misplacement of the electrode in the limbic or associative parts of the STN, rather than the motor part, is the origin of "non-motor" side-effects (Temel et al., 2005b; Karachi et al., 2009). Although empirical studies provide indirect evidence that the tripartite model is plausible in the human brain (Mallet et al., 2007; Lambert et al., 2012; Greenhouse et al., 2013; Haynes and Haber, 2013), a recent systematic review of the neuroanatomical literature on the STN in the non-human primate shows little consistency in the number of subdivisions and their topological organization (Keuken et al., 2012). Moreover, we know of no study that shows direct evidence in a healthy human population that different subparts of the STN are involved in different cognitive functions. Currently, the evidence for putative subdivisions in the STN comes exclusively from neuroanatomical data, rather than functional data obtained during the execution of relevant tasks (but see Greenhouse et al., 2011, 2013 for results of a cognitive paradigm in a clinical group). The current study overcomes this gap in the empirical literature by imaging the STN during a perceptual decision-making task using ultra-high field (UHF) 7 Tesla (T) functional MRI. Unlike fMRI at lower fields, UHF fMRI can potentially resolve fine activation patterns within the STN, because of its increased spatial resolution (van der Zwaag et al., 2016; de Hollander et al., 2017).

Participants performed a perceptual discrimination task (Britten et al., 1992), in which they indicated the main direction of motion of a noisy cloud of moving dots (RDM; Forstmann et al., 2008; 2010; van Maanen et al., 2011; Mulder et al., 2012; Keuken et al., 2015). To validate the STN subdivision hypothesis, the RDM task was extended with two standard experimental manipulations that are known to modulate different cortico-basal ganglia networks. The first manipulation tapped into response biasing processes. On half of the trials, subjects were cued to a response with a higher potential payoff. Such response bias manipulations have been associated with a limbic network including orbitofrontal cortex, hippocampus, and ventral striatum (Forstmann, 2010; Mulder et al., 2012; 2014; Keuken et al., 2014b).

The second manipulation tapped into the rate of evidence accumulation during decision-making, by changing the difficulty of stimulus discrimination. On some trials, the coherence of the dots on the screen was relatively high (easy trials), whereas on other trials the coherence was relatively low (hard trials). This manipulation has been shown to modulate activity in frontal areas such as the dorsolateral prefrontal cortex (Heekeren et al., 2004), but also other cortical areas in both the limbic and motor domain (Mulder et al., 2014; Keuken et al., 2014b).

The third experimental factor-of-interest tapped into the response direction. The STN is considered part of a cortico-basal ganglia-thalamic 'motor' loop, including primary motor cortex (M1; Alexander and Crutcher, 1990; Temel et al., 2005b; 2005c). A benchmark fMRI finding is the lateralization of activity related to response hand. Right M1 shows increased activity for left responses and left M1 for right responses and we hypothesized that such a lateralization might also occur in the STN (Sasahira et al., 1995; Kleinschmidt and Toni, 2004; Devos et al., 2006).

To maximize anatomical specificity of our functional measurements, we used anatomically-defined masks of the STN, based on ultra-high resolution (0.5 mm isotropic) structural images (Keuken et al., 2014a). These STN masks were automatically subdivided in three parts of equal volume along their dorsolateral-ventromedial axis, using an automated procedure (see also Chapter 4). Our main hypothesis was that, if the STN has functional subdivisions that are relevant for perceptual decision-making, these three segments should be differentially modulated by the three task factors. The most concrete hypotheses were that (a) the ventromedial 'limbic' segment would be most sensitive to the response bias cues (Forstmann, 2010; Mulder et al., 2012), (b) the central 'associative' segment would be most sensitive to the difficulty manipulation (Heekeren et al., 2004), and (c) the dorsolateral 'motor' segment would be most sensitive to the response hand (Sasahira et al., 1995; Kleinschmidt and Toni, 2004).

To test these hypotheses, we applied four sets of analyses of increasing complexity. In the first set of analyses, we contrasted the BOLD responses during the main task conditions, i.e., "neutral cue" vs. "potential payoff cue", "easy stimulus" vs. "hard stimulus", and "left response" vs. "right response". We then tested whether these contrasts had different sizes across the three segments.

In the second set of analyses, we adopted a model-based cognitive neuroscience approach, capitalizing on individual differences in behavior. This approach potentially increases sensitivity and specificity to differential activation patterns (Forstmann and Wagenmakers, 2015; de Hollander et al., 2016; Forstmann et al., 2017). Concretely, we fitted the diffusion decision model (DDM; Forstmann et al., 2016) to the behavior of the subjects. According to the DDM, subjects shift their 'starting point' towards the cued response option and show a reduction of the 'drift rate' (rate of evidence accumulation) from easy to hard trials. We correlated the behavioral effects as quantified by the DDM to the size of the individual fMRI contrasts. In this way, we tested the hypothesis that the different segments were specifically related to the two latent processes (starting point shift and drift rate reduction) underlying the two task manipulations (potential payoff cues and increased difficulty; de Hollander et al., 2016; Forstmann et al., 2017; Forstmann and Wagenmakers, 2015).

A third set of analyses also adopted a model-based approach, but capitalized on trial-to-trial variability within the same subject, rather than variability between subjects. Specifically, we tested whether trial-to-trial variability in STN activity was linearly related to trial-to-trial variability in response bias and rate of evidence accumulation (van Maanen et al., 2011; Wiecki et al., 2013; Turner et al., 2015).

A fourth set of analyses tested changes in functional connectivity between the STN segments and other parts in the brain, in response to the task manipulations. We tested two hypotheses: First, whether activity in the central, 'associative' segment of the STN was more correlated with prefrontal activity during hard trials than during easy trials. Second, whether the ventromedial

'limbic' segment of the STN showed increased correlations with activity in limbic and premotor areas during potential payoff cues, compared to neutral cues.

METHODS

SUBJECTS

Nineteen healthy subjects were scanned (10 males; mean age 26.9, std. age 2.4, range 23 – 32). All subjects had normal or corrected to normal vision and no history of neurological or psychological disorders. All subjects were right-handed, as confirmed by the Edinburgh Inventory (Oldfield, 1971). All subjects participated in an earlier study using both structural and functional MRI in the basal ganglia (de Hollander et al., 2017). The study was approved by the local ethical committee of the Max Planck Institute for Human Brain and Cognitive Sciences in Leipzig, Germany. All subjects gave written informed consent and received a monetary reward for their participation, as well as an additional monetary reward based on their task performance.

EXPERIMENTAL PARADIGM

On every trial, before the stimuli were presented, subjects were cued with an arrow pointing to the left (25 % of the trials) or right (25 % of the trials), or a cross ("neutral" condition, remaining 50 % of the trials). Subjects could earn additional monetary reward based on their performance. The cue indicated different *potential payoffs:* different responses yielded different payoffs, provided that the response was correct. Specifically, if a response was correct *and* congruent with the direction of the cue arrow, the subject earned 0.04 euro for that trial. However, if the response was correct, but incongruent with the cue arrow, the subject earned only 0.01 euro for that trial. If a response was correct on a neutral trial, the subject earned 0.025 euro. When subjects gave the incorrect response, they did not gain any reward, regardless of the cued direction (see Fig. 1).

The RDM consisted of a cloud of dots in a circle with a diameter of 5 degrees (visual angle) and with on average 16.7 dots per square degree. The dots moved around with a speed of 5 degrees per second. Frames were presented at a speed of 60 frames per second. On the first three frames, the dots were randomly positioned within the circle. The task then subsequently looped over three frames while the dots of the presented frame were repositioned. Before a frame was drawn, one portion of dots, determined by the 'coherence' parameter (determining the difficulty of the trial), was repositioned a fixed amount to the left or right (making sure that the speed was 5 degrees per second). The remaining portion of dots was moved by the same amount, but in a random direction. The RDM was always presented for 1500 ms, independent of the subject responses, to prevent visual stimulus duration from confounding response behavior. On 50% of the trials, the dot coherence was 35 % ("easy trials"). On the remaining 50% of the trials, the dot coherence was 15 % ("hard trials").

After subjects gave a response, feedback was presented on whether they were correct and how much money they earned on that trial "+€0.01" (incongruent cue), "+€0.025" (neutral cue), or "+€0.04" (congruent cue) for correct trials, or "+€0.00" for incorrect trials. If subjects responded

in less than 250 ms, or needed more than 1250 ms, they received the feedback "too fast" or "too slow", respectively.
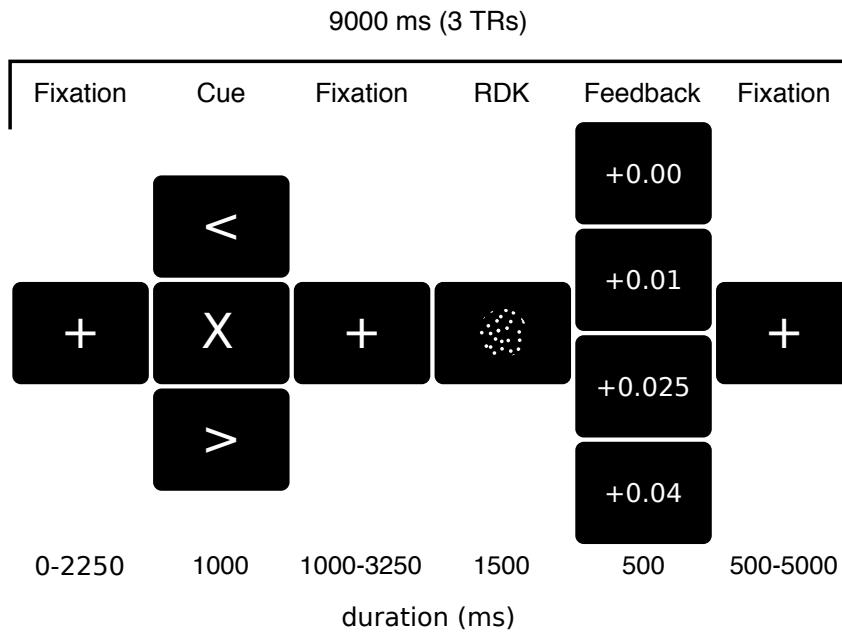
Figure 1: Illustration of the experimental paradigm. After seeing a fixation cross, subjects were presented a cue, indicating whether the left (<) or right (>) response option had a higher potential payoff when correct, or whether both response options had identical potential payoff (X). After another fixation cross, a random-dot kinematogram was presented for 1500 ms and the subject was instructed to indicate the main direction of motion using their left and right index finger. Immediately after stimulus presentation, the subject was presented feedback on the amount of reward collected on that trial. This was 0.00 euro for incorrect responses, or 0.01 (incongruent cue), 0.025 (neutral cue), or 0.04 euro (congruent cue) for correct responses. A trial always took 3 TRs in total, corresponding to 9 seconds.

GENERAL PROCEDURE

After the participants were screened for MRI, they were introduced to the task on a laptop. They were explicitly explained how the cue payoffs work with a few examples. The participants were then also explained why, with limited information, following the cues is a rational strategy. After this introduction, subjects performed 384 trials of a RDM task with potential payoff cues, divided over 3 runs, each consisting of 128 trials in 19 minutes and 21 seconds. Over these 384 trials, subjects could gain an additional monetary reward, based on their performance, of at most 9 euro and 60 cents. A trial always took 9 seconds (3 TRs) in total. It started with a fixation cross for 0, 750, 1500, or 2250 ms (pseudo-randomly sampled), after which a response payoff cue was presented (see also section Experimental Paradigm). The cue was always presented for 1000 ms. After the cue, a second fixation cross was presented for 1000, 1750, 2500, or 3250 ms. After this second fixation cross, the dots were presented for 1500 ms and the subject had

to respond with their left or right index finger. Immediately after the task, feedback was presented for 500 ms. It showed how much the subject earned on that trial. For the remaining 500 – 5000 ms, a blank screen was presented.

MRI SCANNING PROTOCOL

Neuroimaging of the basal ganglia at UHF is challenging compared to most cortical brain regions (de Hollander et al., 2015; Forstmann et al., 2017). Therefore, we drew upon earlier validated MRI protocols for both structural (Keuken et al., 2014a), as well as functional (de Hollander et al., 2017) imaging of the STN. Specifically, we used multi-echo T_2*-weighted FLASH images with a resolution of 0.5 mm isotropic that were collected during earlier studies (Keuken et al., 2014a; de Hollander et al., 2017) for visualization of the STN and its neighboring structures. We also acquired 0.7 mm isotropic T1-weighted images using a MP2RAGE sequence (Marques et al., 2010) for registration to 1 mm isotropic MNI152 space and identifying cortical structures.

For the functional imaging, we used a recently developed BOLD fMRI protocol that balances spatial resolution with subcortical SNR and has a relatively short echo time, accounting for the relatively very short T_2*-relaxation values in the STN (de Hollander et al., 2017). A T_2*-weighted 2D-EPI protocol with a resolution of 1.5 mm isotropic, TR = 3000 ms, slice thickness 1.5 mm, 90 slices, interleaved acquisition, TE= 14 ms, flip angle = 60°, bandwidth 1446 Hz/Px, echo spacing 0.8 ms, FOV 192x192x97mm, phase encoding direction A >> P, partial Fourier 6/8, GRAPPA acceleration factor 3, matrix size 128 x 128 was used. Due to the increased number of slices compared to the protocol presented in de Hollander et al. (2017; 90 vs. 60), the acquired volume now covered the entire brain for all subjects.

To correct for field inhomogeneities, a corresponding B0 field map with the same FOV was acquired (TR = 1500 ms, TE_1= 6 ms, TE_2 = 7.02 ms).

ANATOMICAL LABELLING

For every subject, the left and right STN were segmented on the 0.5 mm isotropic T2* weighted FLASH images by two independent raters, following a previously published protocol (Keuken et al., 2014a; de Hollander et al., 2017). Similar to earlier studies, only voxels that were labeled as part of the STN by both raters were included in further analyses.

In a previous study (de Hollander et al., 2017), we created a T2* weighted group space of the subjects included in this study, by iteratively registering their T2* weighted FLASH images towards each other. In this group space, the STN is clearly visible, as well as its neighboring structures.

Because of the heavy computational burdens of the model-based analyses and to increase the limited functional signal-to-noise ratio in the STN without resorting to spatial smoothing, we subdivided the STN in smaller segments a-priori. For both the left and right STN, the masks of the 19 individuals were transformed to the group space reported in de Hollander et al. (2017). Subsequently, the sum of these masks was taken and thresholded at 14, leaving only voxels in the group space where for at least 73% of the subjects the voxel was labeled as being inside the STN. This thresholded mask resembled the ellipsoid shape and volume of an individual STN. On the mean-subtracted coordinates of these voxels, we performed principal components

analysis (Bishop, 2006) to find the 3D vector (direction) that explained the most variance in the coordinates (see Fig. 2 for a projection of this vector in the group space). We interpreted this vector as the "main ventromedial-dorsolateral" axis of the STN (Temel et al., 2005b; Haynes and Haber, 2013; de Hollander et al., 2014a).
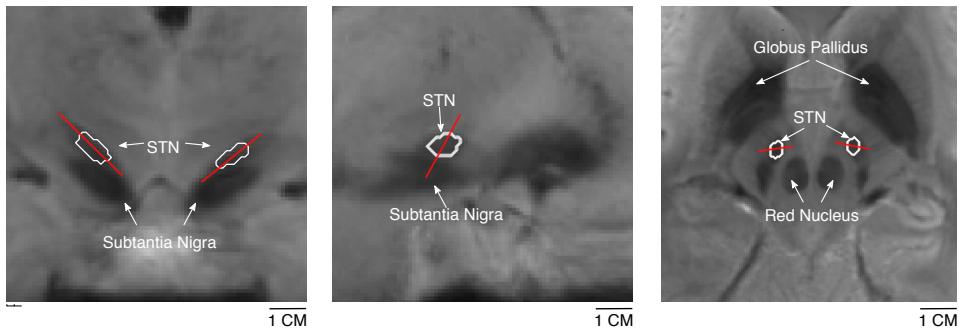
Figure 2: A coronal, sagittal and axial slice (neurological convention) of the 0.5mm isotropic group space. The outlined region is the summed STN group mask, thresholded at 14/19 subjects. The red line indicates the main vector from the PCA coordinate analysis and that was used to subdivide along the STN in three segments.

Then, for every individual subject mask *separately*, all voxel coordinates on this axis were given a "ventromedial score". This voxel-wise score allowed us to divide individual left and right STN masks into three segments: the "posterior-dorsolateral" (segment A), the "central" segment (segment B), and the "anterior-ventromedial" segment (segment C; see Fig. 3). Note that these segments always covered the entire individual anatomical mask for each subject separately, with an equal volume. The segments were transformed to individual functional (EPI) space using linear registration as implemented in ANTS (Avants et al., 2014) and used as a region-of-interest (ROI) in all further analyses. In the individual functional space at 1.5 mm isotropic resolution, the segments had a volume of on average 5.5 voxels (18.56 mm^3; std. 2.0 voxels, 6.75 mm^3) and never overlapped with other segments.
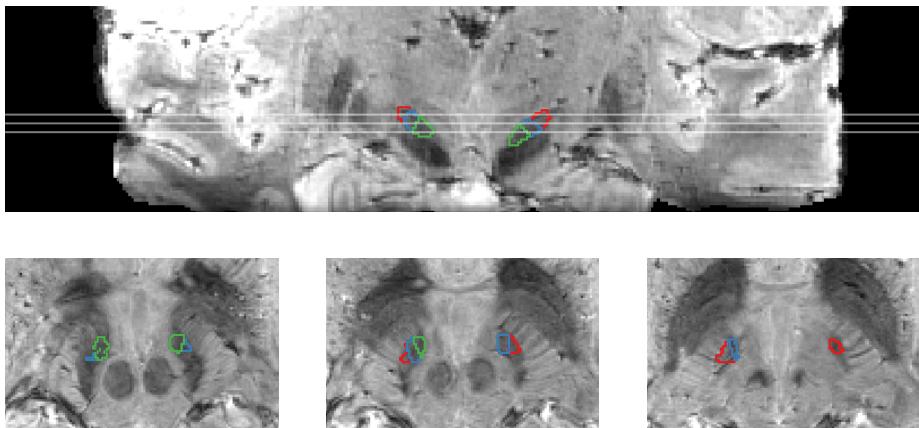
Figure 3: PCA segments in individual space overlaid on the 0.5 mm isotropic averaged multi-echo FLASH image (neurological convention). Top row corresponds to a coronal view, where three white lines indicate the axial cuts illustrated on the bottom. The red region corresponds to the "dorsolateral" segment A, the blue region corresponds to the "central" segment B, and the green region corresponds to the "ventromedial" segment C.

PHYSIOLOGICAL DATA

For 15 of the 19 subjects, physiological data was collected using finger pulsometry and a respiratory band. For four subjects, these data were not acquired due to technical problems.

For the 15 subjects for which physiological data were collected, the fMRI signal was filtered using a 32-regressors RETROICOR model (Glover et al., 2000). This model showed high explained variance in inferior regions around the brainstem and circle of Willis, indicating that the physiological noise modelling was successful. However, in line with earlier work (Barry et al., 2013; de Hollander et al., 2017), no effect of physiological noise filtering on estimated task activity in the STN was found. We extracted the filtered signal from the entire left and right STN mask and fitted three GLM models: one with only a cue-regressor, one with only a stimulus regressor, and one with both a cue and stimulus regressor. None of the GLMs yielded a significant difference in the R^2 of the model fit on physiologically filtered data and the R^2 of the model fit on unfiltered data. Also, none of the parameter estimates were significantly different between filtered vs. unfiltered data.

Since we were able to acquire data from only a limited number of subjects and the physiological noise filtering did not to improve the statistical sensitivity or quality of the GLM fits, we chose to include all 19 subjects and not filter any of the data using linear regressors based on physiological data.

DATA ANALYSIS

PREPROCESSING

The data were corrected for inhomogeneities in the main magnetic field (B0) using the acquired B0 field map and the FUGUE procedure as implemented in FSL (Jenkinson, 2004). After the field map correction, the data were slice-time corrected for the different acquisition times of the different slices along the z-direction (Huettel et al., 2009; Sladky et al., 2011). The data were then further processed using the standard FSL FEAT preprocessing pipeline (Smith et al., 2004; Woolrich et al., 2009) as implemented in the NiPype pipeline framework (Gorgolewski et al., 2011). This pipeline motion-corrects the data using FSL's MCFLIRT algorithm, creates a brain mask in individual functional space, and normalizes the data such that the median voxel intensity within the brain is 10,000. Depending on the subsequent analysis, a 5.0 mm full-width-half-maximum (FWHM), or no Gaussian smoothing kernel was applied. The data were high-pass filtered with a cutoff of 128 seconds. Lastly, the motion parameters obtained by the MCFLIRT algorithm and their first derivatives were used as regressors in a voxelwise general linear model (GLM) to filter out motion-induced noise. The residuals of this noise-modelling GLM were used as input to all ROI-analyses.

BEHAVIORAL ANALYSIS

To test whether the experimental manipulations were successful, behavioral data were analyzed using a repeated-measures ANOVA. There were two main task manipulations: (a) cue congruency (congruent, neutral, incongruent), and (b) difficulty (easy, hard). We tested whether the percentage of correct responses was modulated by cue congruency or difficulty, after an arcsine-transform, to account for the non-normality of the accuracy scores. We also tested whether response times were significantly affected by congruency and difficulty. For this second test, we also included "correct/error response" as an additional factor in the ANOVA. The DDM predicts that if subjects shift their accumulation starting point as a result of the cue, the reaction times are influenced by cue congruency in opposite ways for correct and error responses. Specifically, congruent cues compared to incongruent cues lead to faster correct responses, but slower errors responses (Mulder et al., 2012).

Furthermore, fifteen versions of the DDM (Forstmann et al., 2016) were hierarchically fit using the HDDM-package (Wiecki et al., 2013). The models differed on two (independent) dimensions: first, they were made increasingly more complex by allowing for more across-trial variability. Specifically, the first set of models included no across-trial variability. A second set only included across-trial variability in drift rate (Ratcliff, 1978), a third set of models only allowed for variability in start point, a fourth set of models allowed for across-trial variability in drift rate *and* start point (Ratcliff and Rouder, 1998), and finally, a set of models allowed for across-trial variability in all three main parameters in the DDM: drift rate, start point, and non-decision time. The last version of the DMM is known as the *full* DDM (Ratcliff and Tuerlinckx, 2002). The second dimension determined how the cue-induced biases were modeled. The first possibility was that only drift rate was affected, increasing by a quantity δv towards the cued bound. The second set of models modeled the bias as a shift of start point of δz towards the cued bound, and the third, and final set of models allowed for both a drift rate shift δv and a start point shift δz towards the cued bound (similar to Mulder et al., 2012).

These fifteen models were quantitatively compared to each other using the deviance information criterion (DIC; Gelman et al., 2014b), as well as qualitatively, by plotting the

predicted RT quantiles for correct and incorrect responses, versus the quantiles that were actually observed. Based on earlier work (Mulder et al., 2012), we expected a model that allowed for both start point shifts and drift rate shifts to account for the data best.

Importantly, the HDDM fits yielded individual parameter estimates for all subjects. These parameters for the best model (with lowest DIC) would, at a later stage, be correlated with differences in BOLD activity in the STN across subjects.

FMRI ANALYSIS

The general goal of the STN fMRI analyses was to test for differences in task-related activity across the three segments of the STN, i.e., segment A (dorsolateral), B (central), and C (ventromedial). We performed four sets of analyses that addressed this issue ("is the activity in different parts of the STN differentially related to the different cognitive processes underlying the task-at-hand?"), but used different operationalizations of the processes-of-interest. The first set of analyses tested for differences in task-related activity across conditions: e.g., was a particular STN segment more activated during hard vs. easy trials (or vice versa)? The second set of analyses took a model-based approach and related these differences to *interindividual variability* in task activity (across subjects) to variability in DDM model parameters (similar to Mulder et al., 2012). For example, did a particular STN segment show a larger difference of activity between hard vs. easy trials for subjects that had a larger reduction of drift rate in response to the difficulty manipulation? The third set of analyses were also model-based but related within-subject variability in BOLD activity to trial-by-trial variability in DDM parameters (van Maanen et al., 2011; Wiecki et al., 2013; Turner et al., 2015). For example, was a particular segment more activated on trials that were more likely to have a higher drift rate? The last set of analyses investigated differences in functional connectivity between the STN segments and other parts of the brain, as a function of task conditions (O'Reilly et al., 2012).

For all analyses, the main neural measurement of interest was the average signal time course for the three different segments in the left and right STN (i.e., six time courses per task run; see section 2.5). The first test in all three sets of analyses was always done for each STN segment separately, i.e., segment A (dorsolateral), B (central), or C (ventromedial). Crucially, we always performed a second 'interaction test', to investigate if segment A was *related more* (bigger effect size) to the task modulation than segment B or C. This interaction test is essential for the statement that segment A is more involved than the other segments. For example, if segment A would show a significant effect, but segment B would not, this alone would not be sufficient evidence to say that there is a difference between the two segments (The Difference Between "Significant" and "Not Significant" is not Itself Statistically Significant; Gelman and Stern, 2006; Nieuwenhuis et al., 2011; de Hollander et al., 2014b).

TASK CONTRASTS

The first set of analyses tested whether there were significant differences in the BOLD response between task conditions. Therefore, a set of general linear models (GLM) were fit to the extracted STN segment time series. The first model (GLM1a) contained the following task condition regressors: (a) neutral cue, (b) payoff cue, (c) easy stimulus, and (d) hard stimulus. Its first main contrast of interest was 'payoff cue > neutral cue' (and neutral cue > payoff cue), to test whether any segments were involved in processing the cue information. The other main contrast was 'hard stimulus > easy stimulus' (and 'easy stimulus > hard stimulus'), which should reveal activity related to the speed of evidence accumulation.

Cue-related BOLD effects might be lateralized and represent some a-priori motor facilitation or suppression towards a left or right response. Such a bias cue-related lateralized signal has been shown before in the putamen (Forstmann, 2010) and could potentially cancel out cue-related effects when cue direction is ignored. We therefore also fitted a variant of the model (GLM1b), which took into account the direction of the cue. This GLM contained the following task regressors: (a) neutral cue, (b) payoff cue (left), (c) payoff cue (right), (d) easy stimulus, and (e) hard stimulus. The contrast of interest was "payoff cue (left) > payoff cue (right)".

It is well-known that limbic structures show heightened activity after an error has been made (Alexander and Brown, 2011). Therefore, "drift-rate"-related activity in limbic areas such as the Insula (Mulder et al., 2014; Keuken et al., 2014b) might be a result of a larger number of errors in trials with a lower drift rate. To test this hypothesis, we fitted a third variant of the GLM (GLM 1c), that de-confounded the task difficulty from error trials. It included the following regressors: (a) neutral cue, (b) payoff cue, (d) easy stimulus (correct), (e) easy stimulus (error), (f) hard stimulus (correct), and (g) hard stimulus (error). The main contrast-of-interest for this GLM was 'hard stimulus (correct) > easy stimulus (correct)'.

To test for lateralized motor activity in the STN, we also fitted a GLM focusing on responses (GLM 2). It included the following regressors: (a) neutral cue, (b) potential payoff cue, (c) easy trials, (d) hard trials, (e) left responses, and (f) right responses. We hypothesized that potential STN 'motor' segments should show lateralized motor activity. Specifically, we expected to find increased activity for left versus right responses for right STN versus the left STN, and vice-versa.

ACROSS-SUBJECT VARIABILITY IN BEHAVIOR AND BOLD

The second set of analyses tested whether across-subject variability in DDM parameters was related to across-subject variability in corresponding BOLD effects. The first hypothesis pertained to cue-related response bias and STN activity. The mean shift in starting point of every subject (as estimated by HDDM) was correlated with the contrast 'payoff cue > neutral cue' (GLM1a). We expected the STN segment involved in implementing response biases (the putative 'limbic' area) to show such an across-subject correlation.

The second hypothesis pertained to the difficulty manipulation and the resulting drift rate reduction. Specifically, the reduction in drift rate for hard trials compared to easy trials was correlated, across subjects, with the size of the contrast 'hard stimulus > easy stimulus' (GLM1a). We expected that activity in the central, 'associative' STN segment, should show a significant correlation with the drift rate effect of the difficulty manipulation.

WITHIN-SUBJECT VARIABILITY IN BOLD AND BEHAVIOR

Recent technical developments have made it possible to relate not only subject-to-subject, but also trial-to-trial variability in BOLD activity to DDM parameters (van Maanen et al., 2011; Wiecki et al., 2013; Turner et al., 2015). Here, we used the "regression approach", implemented in the HDDM (Wiecki et al., 2013). In this approach, DDM parameters can be different from trial-to-trial and are modeled as a linear function of some neural measure. For example, the drift rate v at trial t can be modeled as a sum of an intercept (mean drift) $v_{intercept}$ and a regression coefficient times v_{BOLD} times the estimated BOLD activity at that trial $BOLD(t)$:

$$v(t) = v_{intercept} + v_{BOLD} * BOLD(t)$$

Here, $v_{intercept}$ and v_{BOLD} are free parameters that are estimated using both the behavioral response time data, as well as a trial-to-trial measure of neural activity within a Bayesian framework (Kruschke, 2011; Gelman et al., 2014a). The Bayesian framework yields posterior distributions (rather than maximum likelihood point estimates) of the free parameters. The rationale is that if the drift rate is meaningfully related to BOLD activity, a large part (e.g., at least 97.5%; Kruschke, 2011) of the posterior probability mass of the parameter v_{BOLD} should be higher or lower than zero. In that case, the data provide evidence that trial-to-trial fluctuations in BOLD can predict specific underlying variables that lead to choice behavior.

To take such an approach, a trial-wise regressor representing neural activity of the different STN segments is needed. Therefore, two "single trial" GLMs were fit to obtain trial-wise estimates of the height of the task-related BOLD response in the different STN segments (Mumford et al., 2012; Frank et al., 2015; Keuken et al., 2015). Specifically, we obtained 'cue-locked' single trial estimates by fitting a GLM with 128 regressor accounting for the different trials, with their onset locked to the cue presentation, as well as one regressor accounting for all easy stimmulus presentations and one regressor accounting for all hard stimulus presentations (amounting to 130 regressors in total) to each run. We also obtained 'stimulus-locked' single trial estimates, again by fitting a GLM with one regressor for every trial, but now with the onsets locked to the stimulus presentation onset. This GLM also contained one regressor accounting for all neutral cue presentations and one for all potential payoff cue presentations (again, amounting to 130 regressors in total per run).

We used the HDDM regression approach to test two hypotheses, analogous to those tested with the across-subject variability DDM analyses presented in section 2.7.3.2. The first hypothesis pertained to starting point variability. A model was estimated in which the starting point variability was a function of a term accounting for startpoint shifts during congruent and incongruent cues, as well as an additional regressor modelling the influence of cue-related trial-wise BOLD activity.

We hypothesized that STN activity should reveal "shifts towards the cued direction":

$$z(t) = 0.5\,b + cue(t){:}z_{congruency} + cue(t){:}z_{bold} * BOLD_{cue}(t)$$

The intercept of the starting point was set at precisely halfway the lower (0) and upper (b) bound of the diffusion process. Additionally, the starting point was increased toward the correct bound by an amount of $z_{congruency} + z_{bold} * BOLD_{cue}(t)$ for congruent cues, and decreased by $z_{congruency} + z_{bold} * BOLD_{cue}(t)$ for incongruent cues. When an STN segment was involved in implementing response biases as a result of the cue, one would expect the credible interval of the posterior of the parameter z_{bold} to be different from 0.

The trial-wise BOLD-parameters were z-scored (demeaned and divided by their standard deviation), *over subjects and cue-validity conditions*. This was done to prevent the trial-wise analysis from being contaminated by subject-wise and condition-wise variability in BOLD responses (those effects were already investigated in the first two sets of analyses).

In addition to trial-to-trial variability in response bias, we also related trial-to-trial differences in drift rate to BOLD activity in the three STN segments. Specifically, we hypothesized that the activity of some STN segments would be related to the speed of the accumulation process (drift rate). Therefore, the model was extended such that the trial-wise drift rates $v(t)$ was the

sum of an intercept and a regressor v_{bold} times the estimated BOLD activity at trial t; the BOLD regressor was fitted separately for easy and hard trials:

$$v(t) = v_{intercept}(difficulty) + v_{bold}(difficulty) * BOLD_{RDM}(t)$$

We hypothesized that areas in the STN that were involved in evidence accumulation ("associative" areas in the central segment) would show a robust relationship to trial-to trial variability in drift rate. We allowed for the regression coefficients to be different for easy and hard trials. Again, trial-wise BOLD-parameters were z-scored (demeaned and divided by their standard deviation) over subjects and difficulty conditions, to prevent spurious correlations due to inter-subject or condition effects.

For every model, 15 independent chains were run, with 4000 samples each, after 1000 samples used as a burn-in. A total of 60,000 samples were used for estimation of the posterior parameter distributions.

SUBTHALAMIC–CORTICAL CONNECTIVITY ANALYSES

Using psychophysiological interaction analysis (PPI; O'Reilly et al., 2012), we asked to what extent trial-to-trial BOLD variability in the STN explained trial-to-trial BOLD variability in cortical areas during different task conditions, over and above task-related activity. Therefore, for every STN segment separately, as well as the two complete STN masks, we fitted a voxel-wise GLM to all voxels in MNI152-space, with the following regressors: (a) neutral cue, (b) potential payoff cue, (c) hard (correct), (d) easy (correct), (e) easy (error) (f) hard (error) (g) STN segment activity, (h) neutral cue * STN segment activity, (i) potential payoff cue * STN segment activity, (h) hard (correct) * STN segment activity, and (k) easy (correct) * STN segment activity.

The first hypothesis was that BOLD activity in STN segments that were related to starting point variability would be more correlated to limbic areas during potential payoff cues than during neutral cues. Thus, limbic areas should show a significant "potential payoff cue * STN segment activity > neutral cue * STN segment activity" contrast, for the ventromedial segment C.

The second hypothesis was that associative STN segments would be more functionally correlated to associative areas, during hard trials vs. easy trials (or vice versa). Specifically, we expected the contrast "hard stimulus * STN segment activity > easy stimulus * STN segment activity" to be significantly different from zero in associative areas, especially when the PPI regressor was sampled from segment B.

To test these hypotheses, the aforementioned PPI contrasts were estimated using the entire left STN and right STN as a seed mask on the preprocessed fMRI data, after smoothing with a 5.0 mm FWHM Gaussian kernel. The resulting contrasts were thresholded at z > 2.6 and then corrected for multiple comparisons using a cluster-wise threshold of p < 0.05, using Gaussian Random Field theory, as implemented in FSL. The resulting clusters in the thresholded z-map were used as a mask for the PPI maps based on the six STN separate segments used as a seed. This yielded, for every STN segment, a slope parameter that indicates to which extent that STN segment was more correlated with another brain area, during a specific task condition. We then tested, using an interaction test, whether the effect sizes of the three different segments had a different size. If these effect sizes would be different, then such a difference could be taken as evidence for a specific segment of the STN to be more functionally connected to cortex than the other segments of the STN.

BAYESIAN STATISTICS

If possible, Bayesian statistics were used. An important advantage of Bayesian statistics over traditional statistics is that it allows to quantify evidence in favor of the null-hypothesis (Wagenmakers, 2007). Since the aim was to validate the tripartite neuroanatomical model of the STN using functional MRI, one hypothesis was that there is *no* functional specialization, i.e., no evidence in favor of subdivisions. Traditional statistics do not allow to quantify evidence for this hypothesis. However, for completeness, where appropriate, we also report p-values.

For Bayesian hypothesis testing we used the JZS Bayes Factor, as implemented the 'BayesFactor' package (Morey and Rouder, 2015). We always report the BF_{10}: the posterior odds of a model including an effect versus a model where this effect is not present. Thus, a BF_{10} that is smaller than 1 suggest absence of an effect, whereas Bayes Factors bigger than 1 suggest evidence for an effect.

RESULTS

BEHAVIORAL RESULTS

One subject performed only 256, instead of 384 trials, due to fatigue (the entire experiment took approximately an hour). After careful inspection of the data set, this subject was still included in the analyses to improve statistical power.

DESCRIPTIVE STATISTICS

Both experimental task manipulations had a significant effect on both error rates and response times. Subjects made significantly more errors on hard versus easy trials (BF_{10} = 245; t(18) = 4.9, p<0.001;). Also, there was a main effect of cue congruency on the number of errors (BF_{10} = 98; F(2, 36) = 8.74, p < 0.0001). There were significantly less errors on congruent versus incongruent trials (BF_{10} = 7.3; t(18) = 3.06, p < 0.01).

Subjects were faster on easy compared to hard trials (BF_{10} = 34.4; t(18) = 3.88; p = 0.001). Consistent with a shift in start point in the DDM, there was a significant interaction effect of cue congruency and response error on reaction time (BF_{10} = 39; F(1, 17) = 5.75, p<0.01). There was also a main effect of correctness of the response (BF_{10} = 101; F(1, 17) = 9.88, p < 0.01), but no main effect of cue validity (BF_{10} = 0.10; F(2, 36) = 0.378, p=0.69). As predicted by a start point shift in the DDM, congruent correct trials were significantly faster than incongruent correct trials (BF_{10} = 5.5; t(18) = 2.9, p<0.01), whereas congruent error trials were slower than incongruent error trials, although this effect was inconclusive (t(18) = 1.93, p=0.07; BF_{10} = 1.1; see also Fig. 3 for the effect sizes of the main behavioral effects).
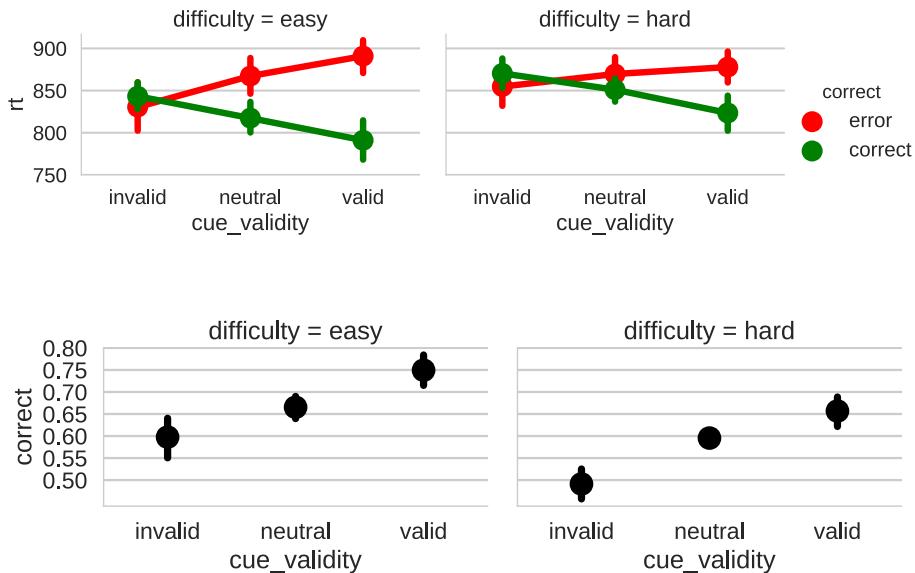
Figure 3: Main behavioral effects of task manipulations on RT (top) and correct responses (bottom). Error bars indicate 67% bootstrapped confidence interval corresponding to the standard error of the mean (SEM).

DDM FITS

Increasingly complex versions of the DDM were fitted to the behavioral data. Quantitative model comparison using the DIC (Vandekerckhove et al., 2014; DIC; Gelman et al., 2014b) showed that models that allowed for across-trial variability in all three main parameters (non-decision time, starting point, and drift rate) explained the data better than models containing only two or less across-trial variability parameters. The winning model also allowed for the potential payoff manipulation to shift both the drift rate and starting point towards the cued response option, similar to the model presented in Mulder et al. (2012; see the Supplementary Materials in Appendix C for more details).

FMRI IN THE STN

MAIN TASK CONTRASTS

The main contrasts of GLM 1a (see Figure 4) showed that there is substantial evidence that the most dorsolateral sectors A and B in both left and right STN do not show different BOLD activity on potential payoff cues versus neutral cues (all BF10 < 0.3; see also Table 1). There is anecdotal (BF10 = 1.68) evidence for increased activity in the ventromedial segment C of the left STN during potential payoff cues, as well as the ventromedial segment C of the right STN

(BF10 = 2.73; see also Table 1). To test whether the different segments were differentially activated in response to a cue (i.e., an interaction of segment and cue condition), the effect of STN segment on the size of the contrast was. A model that assumed all STN segments had an equal effect size was about three times more likely for left STN (BF10 = 0.33; p = 0.33; see also Table 1). For right STN, the data provided only inconclusive evidence, but pointed towards differentially activated segments (BF10=1.14; p=0.06). For all segments, we found anecdotal-to-substantial evidence that the direction of the cue had no effect on BOLD activity (model 1b; all BF < 0.5; see also Table 1).

We found evidence for all STN segments that activity during stimulus presentation was not modulated by the difficulty of the stimulus. This was found both when the analysis included error trials (GLM1a; all BF < 0.5; see also Table 1), as well as when error trials were excluded (GLM1c; all BF10 < 0.5; see also Figure 5 and Table 1).

The contrast of left versus right responses (GLM 2) provided evidence that there is no lateralized motor response in the STN (all BF10 < 0.75). Only for (ventromedial) segment C in the left STN, inconclusive evidence was found that there is a lateralized signal during the motor response (BF10 = 1.17). However, this effect was in a different direction than hypothesized (larger activity during left responses). Also, the effect did not replicate in segment C of the right STN.

In sum, the task contrasts suggest that the three STN segments are not differentially activated as a result of task difficulty, or response hand, in either hemisphere. There is anecdotal evidence that the ventromedial segment C of the left and right STN is more activated during potential payoff cues than neutral cues. However, an interaction test showed that it is not possible to conclude that segment C was modulated more by the cue than other segments.

Table 1: JZS Bayes factors and uncorrected p-values for main task contrasts in the 6 STN segments, as well as the complete mask; * significant p-value (p<0.05; uncorrected).

Segment		A	B	C	whole mask	A	B	C	whole mask
		Left STN				**Right STN**			
Model 1a									
Payoff cue > neutral cue	BF_{10}	0.26	0.28	1.68	0.54	0.26	0.27	2.73	0.32
	p-value	0.65	0.56	0.04*	0.19	0.68	0.59	0.02*	0.43
Hard > easy	BF_{10}	0.24	0.25	0.36	0.25	0.49	0.26	0.25	0.42
	p-value	0.98	0.76	0.34	0.74	0.21	0.69	0.70	0.26
Model 1b (includes cue direction)									
Left cue > right cue	BF_{10}	0.30	0.36	0.50	0.27	0.32	0.25	0.28	0.28
	p-value	0.49	0.34	0.20	0.61	0.42	0.79	0.55	0.55
Model 1c (includes error factor)									
Difficulty effect	BF_{10}	0.31	0.26	0.23	0.25	0.51	0.47	0.32	0.53
	p-value	0.46	0.42	0.83	0.67	0.06	0.10	0.43	0.09
Error effect	BF_{10}	0.51	0.41	1.86	0.64	0.99	0.34	1.3	0.99
	p-value	0.40	0.46	0.05	0.31	0.18	0.52	0.10	0.18
Model 2 (Response direction)									
Left > right	BF_{10}	0.32	0.3	1.17	0.50	0.55	0.28	0.72	0.63
	p-value	0.42	0.49	0.06	0.20	0.18	0.54	0.12	0.15
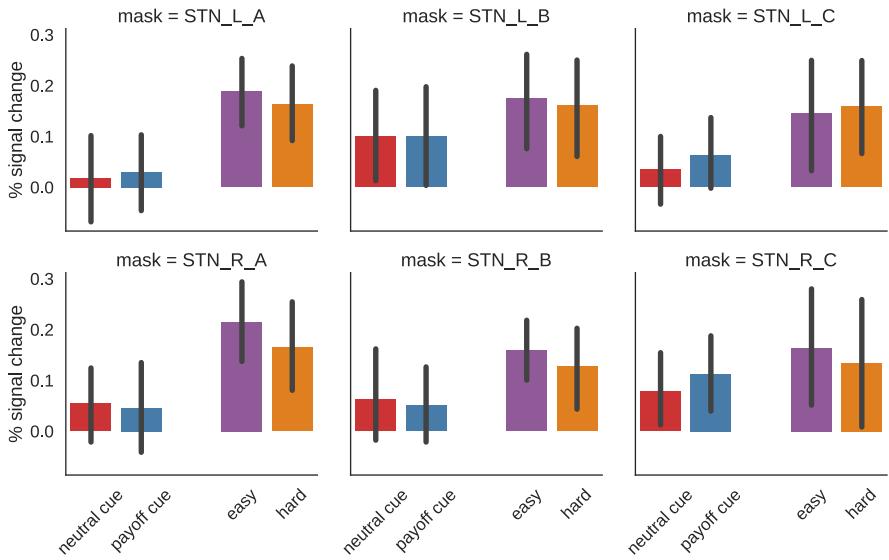
Figure 4: Mean parameter estimates of four task conditions in GLM 1. Error bars indicate 95% bootstrapped confidence interval.
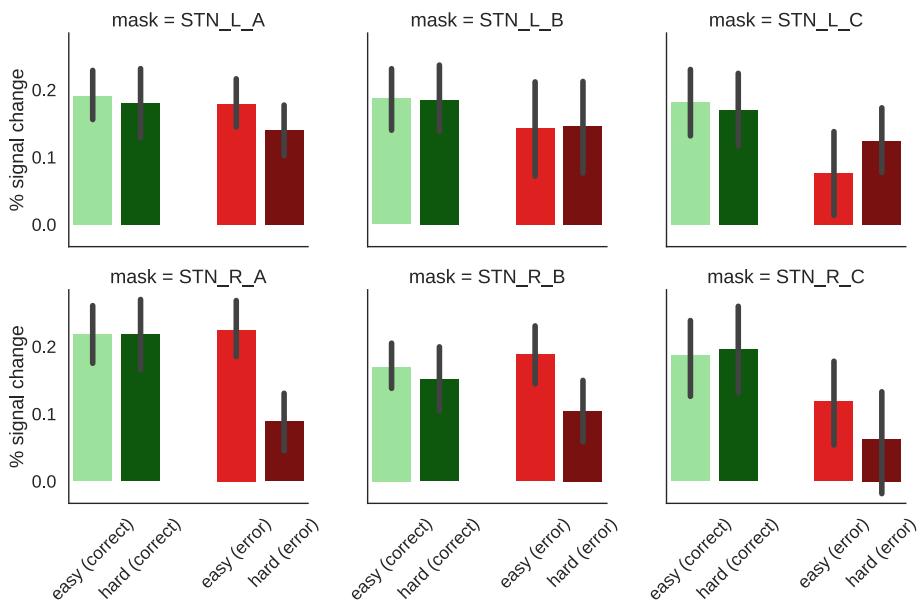
Figure 5: Mean parameter estimates of four task conditions in GLM 1c. Error bars indicate 95% boostrapped confidence intervals.

INTERINDIVIDUAL VARIABILITY AND DDM PARAMETERS

We correlated DDM parameter differences (start point shift and drift rate reduction), to the size of the corresponding BOLD contrast (potential payoff cue > neutral cue and hard stimulus > easy stimulus), across individuals, separately for the different STN segments.

This provided anecdotal evidence that starting point shifts towards the cued bound correlate with the size of the "potential payoff > neutral cue"-contrast across subjects in segment A and B of the left STN, and segment A of the right STN. For the other segments, there was anecdotal evidence for no correlation (see Table 2 and Fig. 6 for details).

To test if the correlation of segment A of the left STN was larger than that of segment C, we obtained 100,000 samples from the posterior of the slopes of a linear model including all three segments. It turned out that for 85% of the posterior, the slope of segment A was bigger than the slope of segment C (5.7 times more probability mass). For the right STN, this was only 66% of the posterior (2 times more probability mass). Therefore, there is no evidence that the correlation between X and Y in segment A was stronger than in segment C.

Table 2: Correlations, p-values, and relative Bayes factors for across-subject variability in start point shifts.

Start point shift (DDM) ~ potential payoff cue > neutral cue (BOLD)

	Left STN			Right STN		
	r	p	BF10	r	p	BF10
Segment A	0.44	0.06	1.53	0.42	0.07	1.35
Segment B	0.41	0.08	1.28	0.2	0.41	0.52
Segment C	-0.07	0.78	0.42	0.32	0.19	0.77
Combined mask	0.39	0.1	1.09	0.43	0.06	1.46

Drift rate reduction (DDM) ~ hard stimulus > easy stimulus (BOLD), no errors

	Left STN			Right STN		
	r	p	BF10	r	p	BF10
Segment A	-0.2	0.42	0.51	0.36	0.38	0.93
Segment B	0.01	0.96	0	-0.05	0.55	0.41
Segment C	-0.51	0.02	2.76	0.08	0.25	0.42
Combined mask	0.28	0.24	0.96	-0.3	0.21	0.63
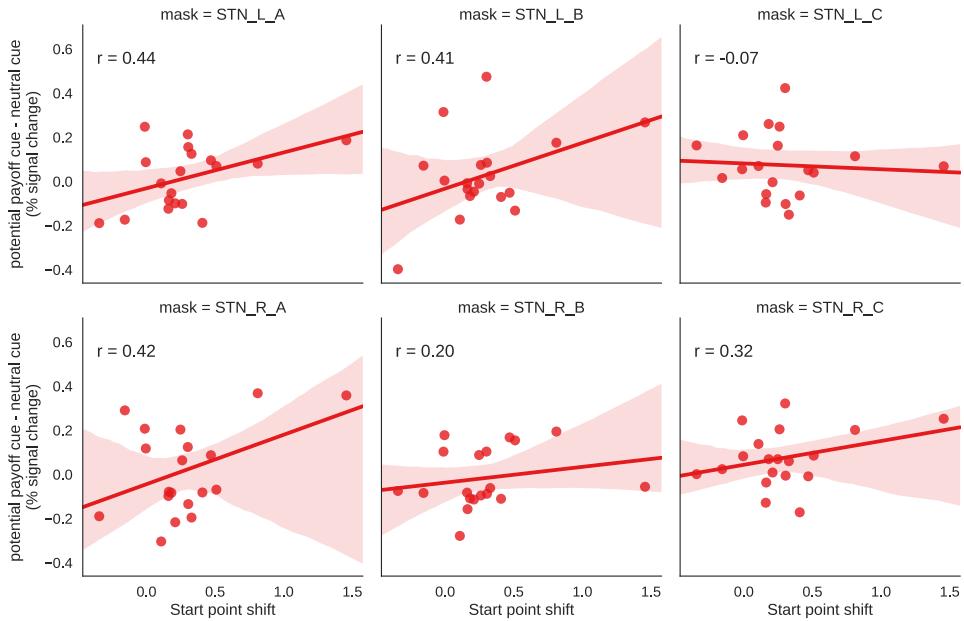
Figure 6: Correlations between individual start point shifts as estimated by the DDM and the % signal change between potential payoff cues and neutral cues. Shaded area represents the 95% bootrsrapped confidence interval on regression coefficient.

For segment C in the left STN, there was anecdotal evidence (r=0.51, BF10 = 2.75; see Table 2 and Fig. 7) that the "hard stimulus (correct) > easy stimulus (correct)" contrast positively correlated with the amount of drift rate reduction. For all other segments in both left and right STN, there was anecdotal evidence for no correlation.

Again, we obtained 100,000 samples from the posterior of the slopes of a linear model where all three left STN segments predicted individual differences in drift rate reduction due to the difficulty manipulation. For 83% of the posterior, the slope of segment C was bigger than that of segment A. For 100% of the posterior, the slope of segment C was bigger than the slope of segment B. This is evidence that BOLD activity in segment C is to a higher degree related to difficulty effects than segment A and B. However, this pattern does not replicate in the right hemisphere.

In sum, there was anecdotal evidence that the dorsolateral tip (segment A) of the left and right STN are involved in implementing starting point shifts, since these shifts correlate across subjects with corresponding BOLD activity. There was also anecdotal evidence that the ventromedial tip (segment C) of the left STN is correlated with difficulty effects. However, this effect did not replicate in the right STN. For both the start-point in segment A, as well as the drift-rate correlation in segment C (left hemisphere), there was some evidence that the effect was larger than in other parts of the STN.
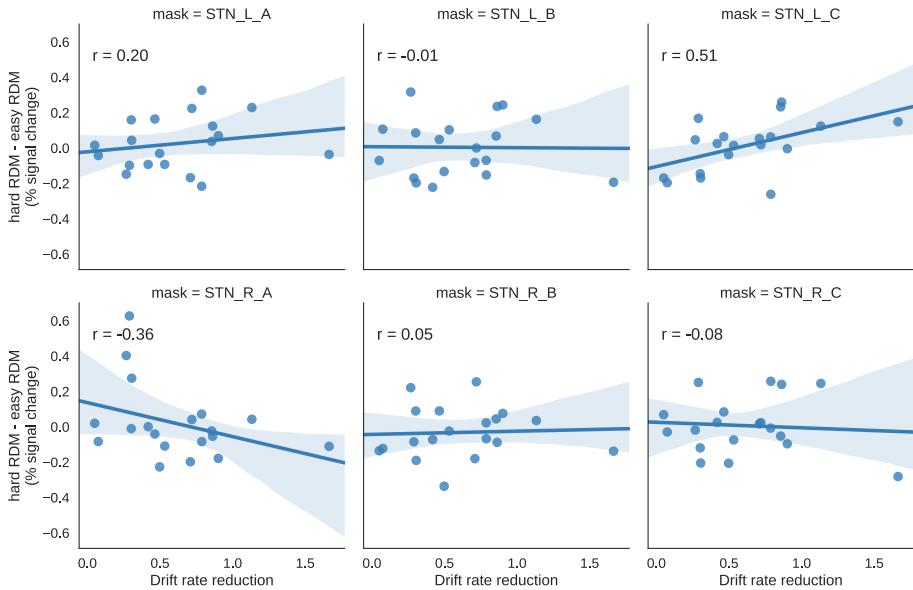
Figure 7: Correlations between individual drift rate reductions as a result of increased difficulty and the BOLD contrast "hard stimulus > easy stimulus".

FMRI IN THE STN – TRIAL-TO-TRIAL VARIABILITY AND DDM PARAMETERS

The posterior estimates of the DDM parameters suggest that all segments are positively correlated to the starting point shifts, although not robustly. For segment A of the left STN, 95% of the posterior was larger than zero, for segment B this was 88% of the slope posteriors, and for segment C this was 85% (see Fig. 8). For the right STN, a similar pattern was found: 92% of segment A was larger than zero, 66% for segment B, and 92% for segment C (see Fig. 8). However, with a cutoff of the 95% highest posterior density credible interval (Kruschke, 2011), none of the posteriors is credibly different from 0 (see Table 3). Fig. 8 also shows that the posteriors of all segments were also overlapping to a large degree, so we conclude that there is no evidence for different parts of the STN to be differentially involved in implementing response biases.

For the trial-to-trial variability in drift-rate, we fitted models where drift rates were a linear function of the trial-to-trial BOLD amplitude after stimulus-onset for each segment separately. Slopes were always fit separately for easy and hard trials. These model fits suggested that trial-to-trial variability in BOLD is not predictive of variability in drift rate in any of the segments in left or right STN (see Fig. 9 and Table 3).

In sum, the regression HDDM analysis shows anecdotal evidence that the STN is involved in implementing response biases, but there is no evidence that different segments of the STNs are more involved than others. The regression HDDM analysis also suggests that there is no effect of trial-to-trial fluctuations in the rate of evidence accumulation on the activity in the STN.
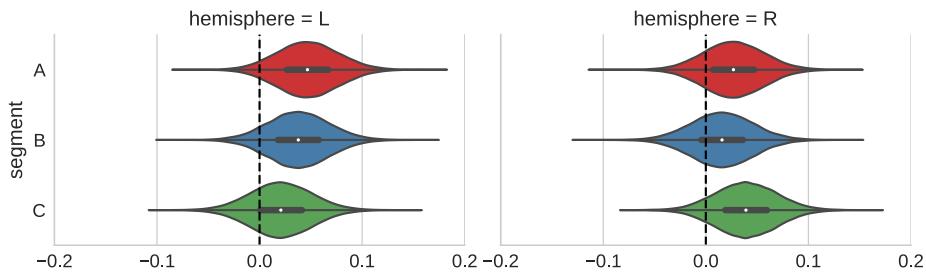
Figure 8: Estimated posterior distributions for the group slope parameter of the trial-to-trial variability BOLD activity, regressed on the *start point* in the HDDM.
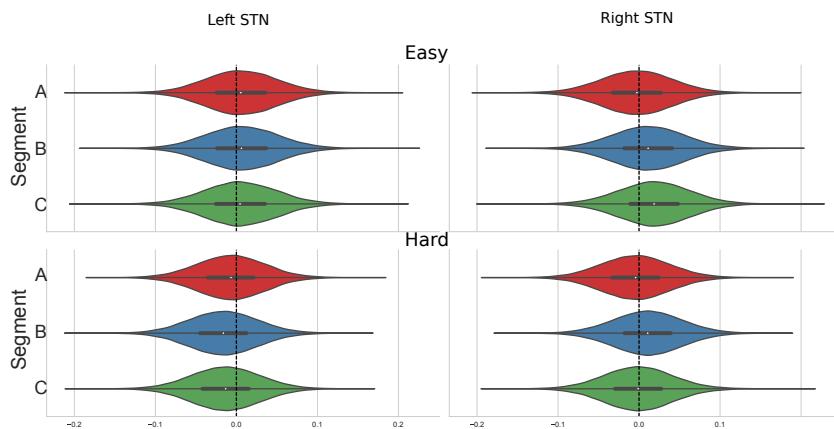
Figure 9: Estimated posterior distributions for the group slope parameter of the trial-to-trial variability BOLD activity, regressed on the *drift rate* in the HDDM. The top row visualizes the slopes in the easy condition, the bottom row visualizes the slopes in the hard condition.

Table 3: Mean, standard deviation and HPD 95% credible intervals for slopes of regression HDDM models using single trial BOLD amplitude estimates.

Cue-induced Start point shift ~ BOLD activity

Left STN	Mean slope	Std	95% Highest Posterior Density Credible interval		Percentage posterior larger than 0
Segment A	0.049	0.03	-0.009	0.108	94.6
Segment B	0.035	0.03	-0.024	0.094	88.1
Segment C	0.032	0.03	-0.027	0.092	85.5

Right STN					
Segment A	0.042	0.03	-0.016	0.099	92.1
Segment B	0.012	0.03	-0.046	0.072	66.1
Segment C	0.044	0.031	-0.016	0.104	92.2

Drift rate (Easy) ~ BOLD acitivity

Left STN

	Mean slope	Std			
Segment A	0.01	0.04	-0.081	0.094	54.9
Segment B	0.01	0.04	-0.08	0.094	55.5
Segment C	0	0.04	-0.082	0.094	54.2

Right STN

Segment A	0	0.04	-0.09	0.084	47.7
Segment B	0.01	0.04	-0.076	0.097	60.2
Segment C	0.02	0.04	-0.07	0.103	66.7

Drift rate (hard) ~ BOLD activity

Left STN

Segment A	-0.01	0.04	-0.09	0.075	43.6
Segment B	-0.02	0.04	-0.102	0.064	35.2
Segment C	-0.01	0.04	-0.094	0.073	37.7

Table 3 (continued)

Drift rate (hard) ~ BOLD activity

Right STN	Mean slope	Std	95% Highest Posterior Density Credible interval		Percentage posterior larger than 0
Segment A	0	0.04	-0.086	0.081	45.9
Segment B	0.01	0.04	-0.074	0.093	59.9
Segment C	0	0.04	-0.087	0.081	48.9

PSYCHOPHYSIOLOGICAL INTERACTION (PPI)-ANALYSIS

PPI analyses using the entire left STN mask as a seed region revealed that BOLD activity in the left STN in response to a potential payoff cue is *less* correlated with the insular/opercular cortex than during neutral cues (see Fig. 10). For the PPI analysis using the right STN as a seed mask, no significant clusters were found.

The reduction of functional connectivity during potential payoff cues was present in all three segment of the left STN (t(18) = 4.3, p=0.00039 for segment A, t(18) = 3.9 p=0.0012 for segment B and t(18) = 3.35, p=0.0035 for segment C). There was substantial evidence that these effects are not different across the three segments (F(36, 2) = 0.92, p=0.409; BF10=0.26).

Finally, the PPI analyses showed no significant clusters that differed in their functional connectivity with the left or right STN during hard versus easy trials.

PPI analysis neutral cue > potential payoff cue (seed = left STN)
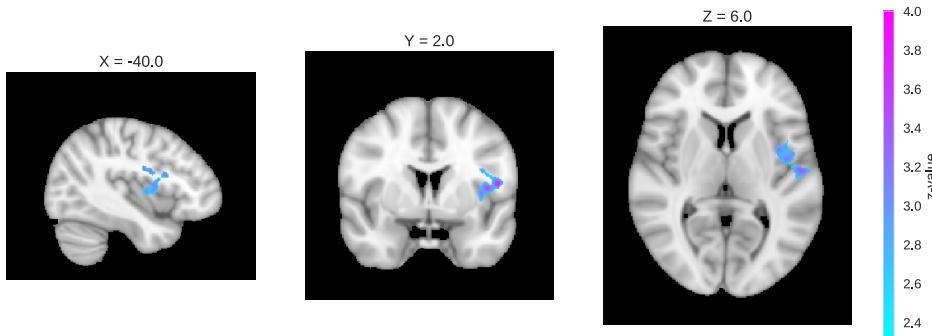
Figure 10: Thresholded statistical parametric map with z-values for the PPI contrast neutral cue > potential payoff cue in MNI152-space. Functional connectivity between let STN and left insular/opercular cortex is reduced during potential payoff cues versus neutral cues.

DISCUSSION

In this study, we investigated putative functional subdivisions in the STN using UHF fMRI during perceptual decision-making. The experimental paradigm had three main factors: (1) a potential payoff manipulation that taps into response biasing processes, known to modulate activity in limbic structures. (2) A difficulty manipulation that taps into evidence accumulation processes, known to be related to associative structures. (3) The hand that was used to respond, depending on the trial-to-trial choices of the subject, inducing lateralized motor activity. We tested the hypothesis that different parts of the STN were differentially involved in the processes underlying these three manipulations. The STN was split up a-priori in three segments of equal volume along its main dorsolateral-medioventral axis, resulting in a posterior, dorsolateral segment A, a central segment B, and an anterior, ventromedial segment C. We tested whether these different segments showed different activity patterns in the main task contrasts and whether their activity showed different relationships to variability in behavior. Finally, we tested STN functional connectivity patterns to other areas in the brain.

RESPONSE BIAS MANIPULATION

In line with the hypothesis of a ventromedial 'limbic' tip implementing response biases, we found anecdotal evidence that the ventromedial segment (C) of the STN is more activated after a biasing cue versus a neutral cue. However, there was no substantial evidence that this cue-related activity in STN segment C was different from other segments. Interestingly, albeit not as predicted, activity in the dorsolateral segment A and not in the ventromedial segment C showed the most-robust correlation to individual differences in HDDM starting point shifts ($BF10 = 1.53$ for left STN; $BF10 = 1.68$ for right STN). Furthermore, a comparison of the posteriors of the slopes suggested that the regression slope in the dorsolateral segment A was larger than in segment C. This finding suggests that it is the dorsolateral segment A of the STN that is most-involved in implementing response biases.

When testing trial-to-trial variability in response bias, as quantified by the starting point parameter in the DDM, a different pattern was found: Activity in all three segments and in both STNs was marginally related to starting point shifts towards the cued bound. However, the posteriors of the different segments were highly overlapping.

Testing the functional connectivity of the STN during potential payoff cues versus neutral cues, yielded reduced connectivity between the left STN and left insular/opercular cortex during potential payoff cues, compared to neutral cues. This reduction in functional connectivity was the same across the three segments ($BF10 = 0.26$). This was not in line with our hypothesis of increased "limbic" connectivity when a response bias needs to be implemented. Also, this pattern was not present for the right hemisphere.

In sum, the present study provides marginal but converging evidence that the STN is involved in implementing response biases. However, there was no consistent evidence for a specific STN segment to be more involved in this process than other segments.

DIFFICULTY MANIPULATION

Anecdotal evidence was obtained for all STN segments to be equally involved in easy and hard trials (all BF10 < 0.53). This result did not depend on the inclusion of error trials in the analysis. Contrary to the hypothesis of an 'associative' central segment coding for stimulus difficulty, we found a correlation between the ventromedial segment C of the left STN and the reduction of drift rate from easy to hard trials across subjects (BF10 = 2.76). The posterior of the slope of this correlation suggested that this correlation is meaningfully bigger than in the other segments of the left STN. However, this correlation was not found in the right hemisphere. Furthermore, a model-based analysis focusing on trial-to-trial differences in drift rate suggested that none of the segments in either STN were related to fluctuations in drift rate across the task. Lastly, the functional connectivity analyses showed no regions that were robustly more correlated to STN during easy trials versus hard trials, or the other way around.

In sum, we found anecdotal and mostly converging evidence that none of the three STN segments showed activity patterns that are related to the rate of evidence accumulation.

RESPONSE HAND

We tested whether the left or right STN showed differential activity to the response hand. We found anecdotal evidence that BOLD activity was the same for left and right responses in almost all segments (BF10 0.28 – 0.72). Only for the ventromedial segment C of the left STN there was inconclusive evidence that activity differed depending on response hand (BF10 = 1.17), but the observed activation pattern was opposite to our hypothesis: activity in segment C of the left STN was higher for left than for the right responses. In sum, we find no evidence for a specific 'motor' region in the STN showing lateralized activity.

LIMITATIONS

The current study has some limitations. First, the study appears underpowered. This is reflected in Bayes Factors that are close to 1 which means that the evidence for the presence of effects was always only "anecdotal" (BF10 < 3). The number of subjects and estimated amplitude of the BOLD response was in the same range as found in earlier fMRI studies in the STN (Mestres-Missé et al., 2012; de Hollander et al., 2017), but showed higher across-subject variance. One explanation for this is that the volume TR was relatively long, at 3 seconds (though similar to Keuken et al., 2015). Also, an event-related design was employed where cue and stimulus were presented in close succession, which might have hindered deconvolution of the HRF and reduced statistical power (although these cue-stimulus intervals were comparable to earlier work; van Maanen et al., 2011; Mulder et al., 2012).

A second limitation is that UHF fMRI (and fMRI in general) is bounded to physiological limits in effective spatial resolution, in addition to native image resolution. Both physiological, as well as measurement noise contribute to a point-spread function (PSF) that blurs local neural activity across the image (Engel et al., 1997). This spatial blurring might reduce the specificity with which we can ascribe BOLD activation differences to specific underlying neuronal populations, and also the sensitivity with which we can dissociate two subpopulations. Recent work estimates the full-width-half-maximum of the point spread function at 7 T in a range of 1.5-2

mm (Shmuel et al., 2007), which is a few times smaller than the length of the STN in its longest axis (roughly 1cm), although it remains to be seen how well these results from cortex generalize to subcortical nuclei.

COMPARISON TO OTHER STUDIES

There is quite some empirical evidence for the tripartite STN hypothesis that contradicts the results presented here. Firstly, neuroanatomical studies using neural tracers (Karachi et al., 2005; Haynes and Haber, 2013), as well as studies employing diffusion-weighted imaging (Brunenberg et al., 2012; Lambert et al., 2012; Accolla et al., 2014) find at least three subdivisions in the STN. Second, there is evidence that DBS of the STN using more ventral, rather than dorsal contacts, increases the risk of 'limbic' side-effects like hypomania (Mallet et al., 2007; Welter et al., 2014; Accolla et al., 2016) and modulates different aspects of cognition (Greenhouse et al., 2011; 2013). Third, electrophysiological recordings using DBS electrodes show that the more dorsolateral part of the STN shows higher neuronal activity in the beta band (13-30 Hz) than ventromedial parts (Kühn et al., 2008; Lourens et al., 2013). Fourth, STN regions with higher beta-activity are connected more strongly to motor and premotor areas. In contrast, STN regions with relatively high neuronal activity in the alpha spectrum (3-7 Hz), located more ventromedial, are more connected to medial temporal areas, like hippocampus (Accolla et al., 2016; Horn et al., 2017).

In light of the aforementioned studies, one may ask why the present study did not deliver evidence for subdivisions. There may be four tentative answers:

First, it is possible that there are subdivisions in the STN, but this study was unable to detect them. Potentially, we did not employ task manipulations that robustly modulate activity across different subdivisions in the STN. In that case, a different experimental paradigm might have shown differences in activation across the STN.

Second, the present study might not pick up on subdivisions because the activity of different neuronal populations was smoothed together, due to neurovascular coupling (see also limitations section; Shmuel et al., 2007).

A third potential answer could be that other techniques might be biased to find subdivisions. For example, tracing studies usually underestimate the volume of the terminal fields of the cortical projections and obtain only 1-4 samples per seed region (Alkemade, 2013; Haynes and Haber, 2013). Such small sample sizes preclude these data from providing conclusive evidence on potential subdivisions. Diffusion-weighted imaging (DWI) studies offer larger sample sizes, but the spatial resolution of DWI is very limited compared to the size of the STN and partial volume effects could lead to spurious subdivisions (Jones et al., 2013). For example, white matter bundles ascribed to the 'limbic tip' of the STN probably belong to the medial forebrain bundle, a key part of the mesolimbic dopamine system. However, these bundles might not terminate in the STN, but originate from nearby limbic structures such as the lateral hypothalamus, substantia nigra, and ventral tegmental area (Coenen et al., 2009; Haynes and Haber, 2013). In line with such an explanation, it has been shown that nigrostriatal projections can pass through the STN, without actually terminating there (Carpenter and McMasters, 1964; Carpenter and Peter, 1972). Similarly, the dorsal part of the STN lies close to cerebello-rubro-

thalamic fibers and cerebral peduncle, which are connected to 'associative' and 'motor' cortical regions, but do not necessarily terminate in the STN itself (Martin et al., 1989; Haynes and Haber, 2013; Mai et al., 2015; Contarino et al., 2017). Results from electrode recordings and stimulation of the STN are also limited by spatial resolution. It is very challenging to precisely locate DBS electrodes after placement, and it is common for "dorsal" and/or "ventral" electrodes to be located outside of the STN (Greenhouse et al., 2013). Recording or stimulating regions inside versus outside the STN will likely show different effects and this could be clinically relevant. However, such differences in stimulation between regions within and outside the STN say little about subdivisions within the STN.

A final answer as to why the results of this UHF fMRI study diverged from earlier empirical work might be that there are, indeed, differences in *structure* across subregions within the STN (for example, as defined by their connections to cortex), but that these differences are not *functionally* relevant. Brain function has to follow from brain structure, but this does not mean that this mapping is trivial (Jonas and Kording, 2017). The tripartite model of the STN currently fails to comprehensively describe how the three subdivisions of the STN differ in their underlying computations and consequently affect behavior. An alternative account to the tripartite model is that, although projections on the STN are spatially organized, neurons in different regions of the STN do not differ in their functional role. One empirical observation that is in line with such a 'fully integrative' account is that dendrites of subthalamic neurons are oriented along the main axis of the STN and can span large parts of it (Yelnik and Percheron, 1979). Furthermore, projections from the STN into the GPe are highly diffuse (Parent and Hazrati, 1995b). Another observation in favor of a fully integrative account is that projections from different cortical areas, although topologically organized, are probably highly overlapping (Lambert et al., 2012; Alkemade, 2013; Haynes and Haber, 2013; Alkemade and Forstmann, 2014; Lambert et al., 2015).

In sum, the number of subdivisions in the STN is, in our view, still an open question. Furthermore, it is useful to make a distinction between structural subdivisions and their functional relevance. The study presented here studied the latter and showed evidence that, even if there is structural organization within the STN, it might not be functionally relevant for the processes underlying perceptual decision-making, response bias, and response execution.

FUTURE WORK

We are currently planning future work that involves replicating the results of this study. We will adapt the design of the study to improve sensitivity. Specifically, we will (a) strive for a larger sample size, (b) remove the response deadline put on the subjects to better accommodate the assumptions of the DDM, (c) increase the inter-trial interval between cue and stimulus presentation to better facilitate deconvolution of their event-related BOLD response, and (d) decrease the volume TR (increase temporal resolution) of the fMRI protocol by reducing the field-of-view, to better facilitate deconvolution, filtering, and connectivity analyses. Furthermore, we will use a Bayesian approach to integrate the results of this study and a future study in a principled way (Verhagen and Wagenmakers, 2014).

Other work on functional subdivisions in the STN should also focus on increasing the sensitivity of fMRI in the subcortex (Forstmann et al., 2017), further define the connectivity pattern of the

STN and its putative subdivisions (Lambert et al., 2012; Haynes and Haber, 2013), and construct new hypotheses about which experimental paradigms could dissociate activity of different putative subdivisions. It is essential that such work allows for the possibility to falsify the subdivision hypothesis, which calls for the pre-registration of study protocols and applying Bayesian statistics (Wagenmakers et al., 2012; Wagenmakers and Forstmann, 2014; Chambers et al., 2017).

CONCLUSION

The goal of the present study was to validate the tripartite model of the STN, consisting of a "motor", "associative", and "limbic" subdivision. We applied UHF fMRI during a perceptual decision-making task with a response bias and difficulty manipulation. We found anecdotal, but converging evidence that the STN is involved in implementing response biases equally in all STN segments. We also found anecdotal evidence that activity in the STN is not modulated by the difficulty of the stimulus nor by the hand that is used for a response. Furthermore, functional connectivity patterns did not differ across different segments of the STN. These results speak against a functional subdivision of the STN in the context of perceptual decision-making. Future work is necessary to replicate the results presented here, as well as to generalize them to experimental paradigms that tap into cognitive processes other than perceptual decision-making.

9

GENERAL DISCUSSION AND FUTURE DIRECTIONS

In this thesis, novel approaches for understanding the human subcortex using Ultra-High field MRI (UHF-MRI) were explored. The approaches were also applied to empirically validate the tripartite model of the subthalamic nucleus (STN). In **Chapter 2**, current state-of-the-art UHF-MRI methods and their relevance for the study of the human subcortex were reviewed. In **Chapter 3**, the iron distribution of the STN was visualized with quantitative susceptibility mapping (QSM) in both living subjects, as well as post-mortem tissue. We showed that the spatial distribution of iron is heterogeneous throughout the STN, but that there are no hard borders or clear subdivisions in the spatial distribution of iron across the STN. In **Chapter 4** we investigated post-mortem STN samples using multiple MRI sequences, as well as immunocytochemical stainings. We showed that the histochemical structure of the STN is complex, gradual, and shows no clear tripartite subdivision. In **Chapter 5** we turned to functional imaging of the STN and critically reviewed the methods used in the empirical neuroimaging literature on the STN. Conventional methods turn out to often be inadequate for distinguishing between signals from adjacent subcortical nuclei. We promoted a ROI-approach where individual anatomy is taken into account and cautioned against spatial smoothing. In **Chapter 6**, a set of 7 T fMRI protocols was compared, to assess which spatial resolution is feasible for functionally imaging iron-rich subcortical nuclei at UHF. We show that also at 7 T, some modesty in terms of resolution is necessary for functional imaging of subcortex and that 3 T fMRI shows inferior BOLD sensitivity at equal resolution. In **Chapter 7** we reviewed different approaches for linking cognitive computational models to neural measurements. Such a model-based approach might aid in the interpretation of noisy neural signals, such as BOLD measurement in subcortex. Finally, in **Chapter 8**, we tested the tripartite model of the STN with an empirical study on how BOLD activity in different parts of the STN is related to different aspects of perceptual decision-making. We show that the STN is involved in implementing response biases, but found no evidence for functional differentiation across different parts of the STN.

In sum, we have shown that UHF-MRI offers new possibilities for the investigation of the structure and function of subcortical nuclei and can be combined with post-mortem techniques to study subcortex at the microscale. Furthermore, multiple streams of data, both structural and functional, did not confirm the tripartite model of the STN. The structural data suggest a more complex and gradual internal organization of the STN and the functional data show evidence against the idea that different parts of the STN play different functional roles, at least in the context of perceptual decision-making and motor responses.

In what follows, the relevance of our empirical findings for the tripartite model of the STN, as well as the limitations of these findings will be summarized. I will then critically review the literature that led up to the tripartite model of the STN and highlight an alternative view that fits the empirical data presented in this thesis. The chapter concludes with a discussion of the most important technological limitations that currently hinder neuroimaging of the subcortex, in particular the STN, and lays out future directions for research.

THEORETICAL DISCUSSION

THE TRIPARTITE MODEL OF STN

The empirical work presented in this thesis is at odds with the prominent 'tripartite' model of the STN. Both the QSM data (Chapter 3), as well as the immunocytochemical stainings (Chapter 4), and the fMRI study (Chapter 8) show no consistent evidence for three subdivisions or any other number of subdivisions. Also, all three data streams suggest that any potential subdivisions must be highly overlapping: iron concentration, closely linked to cytoarchitecture, gradually increases towards the medial tip of the STN, without any strict borders. Immunocytochemical stainings show neuronal populations that are overlapping and that lack sharp borders. Most of the stainings show a dorsolateral-ventromedial gradient, just as the QSM data. The fMRI study suggested that the function of different parts of the STN is homogeneous.

LIMITATIONS OF THE EMPIRICAL WORK IN THIS THESIS

I will discuss some limitations to the empirical data presented in this thesis. First, Chapter 3 presented data that quantified magnetic susceptibility to infer the spatial distribution of iron across the STN. It should be noted that magnetic susceptibility is only a proxy of non-heme iron (iron that is not bound to a protein), rather than a direct measurement of iron concentration. Although a close relationship with iron has been established, specifically in the STN (Dormont et al., 2004; Langkammer et al., 2012; Stüber et al., 2014), opposite relationships with myelin and calcium concentrations have also been shown (Schweser et al., 2016). Furthermore, although there are good reasons to believe that iron concentrations are tightly related to cytoarchitecture (Fiedler et al., 2007), the functional significance of differences in iron concentrations remains elusive and is possibly highly complex (Zecca et al., 2004; Penke et al., 2012). For example, the substantia nigra can functionally be divided into a dopaminergic pars compacta, and a non-dopaminergic pars reticulata, but these subdivisions are not clearly distinguishable on QSM images (Keuken et al., 2014a). The relationship between QSM and iron concentration also depends on the precise chemical form of iron. The complexity of the relationship between magnetic susceptibility and iron was illustrated in Chapter 4, where we showed that there is no robust statistical relationship between QSM values and the staining intensity for ferritin, an intracellular protein that stores iron. Still, the spatial iron distribution pattern was consistent across living subjects, as well as in post-mortem tissue. Furthermore, the pattern was in agreement with the 'main' posterior, dorsolateral-anterior, ventromedial axis of organization we found in most of the immunocytochemical stainings.

In Chapter 4, we applied immunocytochemistry (Alkemade et al., 2012a; Borgers et al., 2014) to study the internal structure of the STN. Some methodological limitations to the results of Chapter 4 should be mentioned as well: (a) We investigated a limited number of antibodies (twelve). Additional antibodies could have shown different patterns. Note, however, that in pilot studies seven additional protein markers were also investigated, but showed no expression within the STN. (b) The staining images were very noisy, as reflected in the inconsistent mixture modelling results across samples. Possible causes for the noise are the inherently limited strength of the signal-of-interest, as well as artefacts such as tissue shearing and misregistration. On the other hand, the high correlation between staining intensities of different antibodies, as well as moderate correlations with the quantitative MRI parameters show that

the noisy data do reflect meaningful information about the internal structure of the STN. (c) The mixture models only included the intensity distributions of the staining images and did not (explicitly) model any spatial information. Arguably, more complex spatial statistical models might be more appropriate for these data (Gaetan and Guyon, 2010). However, gradient image analyses indicated that the intensity changes between adjacent pixels are very similar across the STN. Arguably, this will limit the benefits of including the spatial structure of the pixel intensities into a statistical model, since this structure will add little information. (d) The mixture models were fitted for each antibody and sample separately. The use of a hierarchical and/or multivariate approach might capitalize on consistencies across antibodies and samples, and accommodate for some of the noise in these data (Lee and Wagenmakers, 2014; Gelman et al., 2014a). However, implementing such an approach will be highly challenging, because of the need for a common spatial and intensity space, as well as a generative model for how different antibody staining intensities are related. Initial efforts on constructing such a multivariate model stranded on the definition of an appropriate linker function to join the highly non-normal intensity distributions of the individual stainings into a single multivariate distribution.

In Chapter 8, an empirical fMRI study showed that different parts of the STN are equally involved in different aspects of perceptual decision-making. Again, some general limitations should be mentioned; (a) First, one could argue that our experimental paradigm might not tap into the distinct cortico-basal ganglia networks that define the three subdivisions of the STN (Temel et al., 2005b; Lambert et al., 2012). Note that the task manipulations were related to specific and distinct brain networks, implied in the tripartite STN model (Temel et al., 2005b), in two earlier meta-analyses (Mulder et al., 2014; Keuken et al., 2014b). However, we cannot rule out that different experimental paradigms would show differential activity across different STN subregions. (b) A second limitation of the empirical fMRI study is the limited effective spatial resolution of fMRI (in addition to image resolution). When we consider that putative subdivisions in the STN are potentially highly overlapping (as in the concept of "functional zones"; Lambert et al., 2012), their neural activity will probably also overlap. This will hinder the identification of these different subdivisions in functional data, especially when we consider the additional inherent blurring in fMRI, due to neurovascular coupling and spin dephasing during signal readout. The point spread function (PSF), which quantifies the severity of such blurring, is estimated to have a full-width-half-maximum of approximately 2 mm at 7 T, in cortical gray matter (Shmuel et al., 2007). This is relatively minor compared to the longest axis of the STN, which is approximately 13.2 mm (Yelnik and Percheron, 1979). However, the reduced echo time that is necessary for fMRI in the basal ganglia increases the weighting of signal from larger veins, which could potentially increase the width of the point spread function. Furthermore, the vasculature in the subcortex is organized differently from cortex (Pollock et al., 1997) and we currently do not know how this influences the PSF. (c) A third, related point is the limited BOLD sensitivity in subcortex. Functional MRI studies at 7 T in cerebral cortex routinely show significant stimulus-related BOLD activation clusters in unsmoothed/minimally smoothed z-maps of individual subjects (Martuzzi et al., 2012; Trampel et al., 2012; Derey et al., 2015). However, we did not find such robust activation clusters in the subcortex. One major reason for this is the substantially increased noise in subcortex which is discussed at length in Chapter 2 and 6. A second reason is the severely reduced size of the BOLD response in subcortex, compared to cerebral cortex. In cerebral cortex, task-related BOLD responses are routinely found with a size of 5.0 – 10.0 percent signal change at 7 T (Pfeuffer et al., 2002; van der Zwaag et al., 2009). In our stop-signal (Chapter 6) and random dot motion task (Chapter 8) paradigms, we found much smaller task-related BOLD responses in the STN, of approximately only 0.5 and 0.3 percent signal change, respectively. Similarly, Keuken et al. found cue-related activity of only

0.1 percent signal change in the STN (Keuken et al., 2015). This limited signal change is in line with recent work using calibrated BOLD experiments in visual cortex, pallidum, and striatum, which suggests that the BOLD response in subcortical areas in response to increased rate of oxygen consumption (CMRO2) is considerably smaller than in cortical areas (Ances et al., 2008). Because of these very small task-related effects (as well as for computational issues), in Chapter 8, we used three a-priori defined ROIs within a larger anatomically-defined STN ROI, rather than a voxelwise analysis in an individual or group space. One could argue that these three ROIs, defined along the main axis of the STN, might not accurately capture the three functional subdivisions in the STN and that we therefore failed to pick up on functional differences across these three regions. However, even when the a-priori ROIs would not exactly overlap with the functional subdivisions, one would still expect to find different effect sizes across the three ROIs. We found consistent evidence against any difference in effect size across these ROIs.

THE PROBLEM WITH THE TRIPARTITE MODEL

Two recent reviews by Keuken et al. (2012) and Alkemade et al. (2015) highlighted that, in the empirical literature as a whole, there is little consensus on the precise number of subdivisions in the STN, or their topography. However, in the recent human neuroimaging literature on the STN, the tripartite model of the STN has been very influential and is often presented in the introduction of papers as a mere fact. One example is the recent DTI study of Lambert et al. (2012), which was presented as a "confirmation" of three functional zones in the STN (Lambert et al., 2012). Accordingly, the study included rather biased clustering analyses: the 10 out of 24 STNs where more or less clusters than 3 were found were simply discarded as noise (see Alkemade and Forstmann, 2014 for critique). Where does this strong belief in the tripartite model come from? The review articles by Temel et al. (2005b; currently approximately 302 citations) and Hamani et al. (2004; currently approximately 448 citations) have been very influential references. Both Hamani et al. and Temel et al., cite review articles by Alexander et al. (1986; 1990; 1991), Parent & Hazrati (1993; 1995a; 1995b), and Joel & Weiner (1997) to substantiate the claim that the STN can be divide in *three* subdivisions and work from that premise to interpret a large body of empirical literature. A closer look into these older review articles that led up to the tripartite model reveals some interesting details.

First, almost all these review articles have as main subject the parallel organization of the *basal ganglia in general* and half of them say little to none about the STN. The paper by Alexander and Crutcher (1986), one of the first papers that proposed the concept of closed segregated loops in the basal ganglia, was based on anatomical tracing studies concerning the pallidum and the striatum. The authors mention the STN only twice as part of a "subsidiary basal ganglia network". The follow-up article from 1990 (Alexander and Crutcher, 1990) contains only a single paragraph that discusses the STN as part of the 'indirect pathway' in the different segregated loops. Neither of these two papers discusses any topographical organization in the STN. Parent and Hazrati (1995b) do discuss the place of the STN in the cortico-basal-ganglia-thalamic loops at length and propose a tripartite subdivision of the STN. However, this model of STN organization is largely based on where the STN projects to in other basal ganglia nuclei, namely the globus pallidus, pars externa (GPe), globus pallidus, pars interna (GPi), and subtantia nigra, pars reticulata (SNr) and how these subareas in *other* basal ganglia nuclei are, in turn, connected to 'associative', 'motor', and 'limbic' cortical areas. Joel & Weiner (1997) also propose such a subdivisions scheme, based on similar reasoning.

Another interesting aspect of these older review articles is that, although they are sometimes lumped together as evidence for *three* subdivisions in the STN (Hamani et al., 2004; Temel et al., 2005b; Lambert et al., 2012), they propose different numbers of subdivisions in the basal ganglia. The original proposal of "closed segregrated loops" in the basal ganglia by Alexander et al. (Alexander et al., 1986) contained *five* different loops: a 'motor', 'oculomotor', 'dorsolateral prefrontal', 'lateral orbitofrontal', and 'anterior cingulate' loop, whereas the follow-up paper (Alexander and Crutcher, 1990) presented *four* subdivisions in the basal ganglia: 'motor', 'oculomotor', 'limbic', and 'prefrontal'. The review articles from Parent & Hazrati (Parent and Hazrati, 1995a; 1995b) subdivide the cortico-basal ganglia loops into *three* subdivisions: 'associative', 'sensorimotor', and 'limbic' areas, similar to the review article by Joel & Weiner (1997). Interestingly, a more recent review by Middleton & Strick (Middleton and Strick, 2001) suggests the basal ganglia contains even *ten* parallel loops.

THE STN AS A TOPOGRAPHIC REPRESENTATION OF CORTEX AND A GENERAL–PURPOSE INTEGRATOR

So how do we reconcile the existing literature with the empirical results presented in this thesis? One helpful idea might be that of the 'topographic connectome' (Jbadbi et al., 2013). Jbadbi et al. argue that modelling the brain as a limited number of discrete nodes and edges is often useful, but in some cases too simplistic. Many discrete brain areas are connected to other discrete brain areas in a topographic way. Such connections are organized following "point-to-point mappings that preserve spatial arrangements: Nearby locations in a source region connect to nearby location in the target" (Jbabdi et al., 2013). Famous examples of such connections are found in the retinotopic maps throughout visual cortex (Wandell and Winawer, 2011), but similar arrangements can be found throughout the rest of the brain as well (Thivierge and Marcus, 2007). Clearly, such topographic connections cannot be captured by a single graph-theoretical edge, or even a limited set of edges (Sporns et al., 2005). Rather, there is a whole continuum of subconnections between both sides of the edge, and any subdivision in a specific number of edges/subregions is arbitrary (see Fig. 1). When we apply the concept of the topographic connectome to the STN, we might propose that the STN has a *single* topographic representation of a large part of cerebral cortex, rather than *three* (Joel and Weiner, 1997), *four* (Alexander and Crutcher, 1990), or *five* (Alexander et al., 1986) discrete 'subdivisions' corresponding to distinct cortical regions.

What could be the functional relevance of such a topographic organization? One speculative answer I will propose here is that the relevance of the topographic organization for STN functioning is not that significant. Maybe the topographic organization of cortical projections into the STN is just a natural consequence of the inherent minimization of wiring costs and transmission speeds within the brain connectome (Budd and Kisvárday, 2012). Motor areas project into the caudal, dorsolateral tip of the STN because they lie closest to those areas, whereas more rostral premotor areas project into the more rostral parts of the STN. The more ventral limbic belt projects into medial tip of the STN, simply because the 'limbic' fibers then do not hinder the projections from more dorsal cortical regions.

Topographic organization
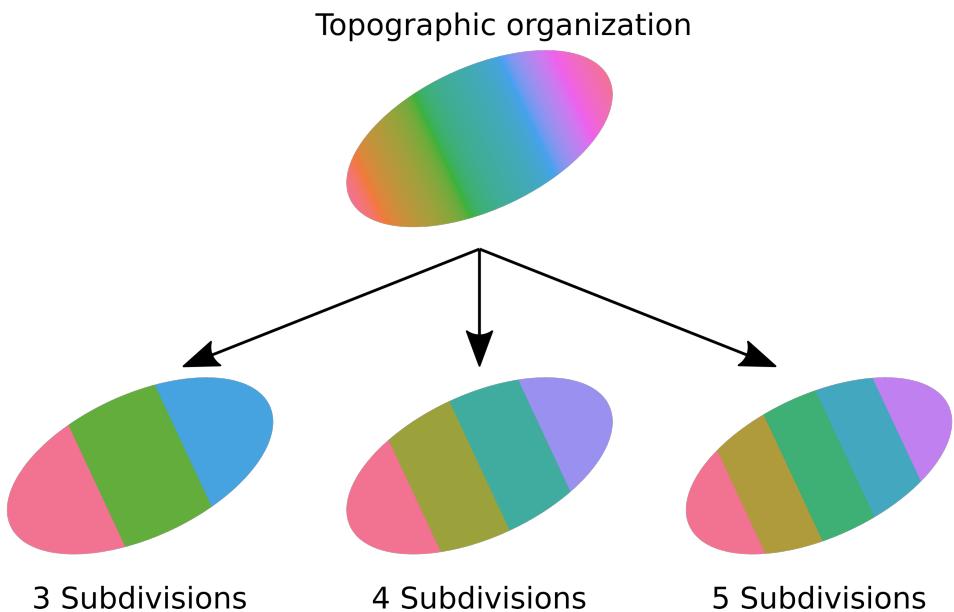
Figure 1: Schematic illustration of the discretization of topographic organization. A topographic map can easily be discretized in three, four, or five subdivisions, but one could argue that this is not a useful representation of the underlying, continuous organization (Jbabdi et al., 2013).

In such a view, the STN might integrate information from different cortical areas in an unspecific manner and the particular topography of the input of these areas is not that relevant. This 'unspecific integration hypothesis' is in line with multiple neurocomputational models of basal ganglia functioning, where the STN acts like a *global*, *unspecific* brake on motor output in response to unexpected events (Aron, 2011), *summates* neural activity corresponding to alternative action patterns (Bogacz and Gurney, 2007), or acts as a *global coordinator* for "emotional component synchronization" *across different brains structures* (Péron et al., 2013). Furthermore, this model fits with empirical microstructural data: (a) The dendrites of STN neurons arborize widely across the STN, which means single neurons could integrate signals coming from relatively distant cortical areas (Yelnik and Percheron, 1979; Parent and Hazrati, 1995b). (b) The terminal fields of cortical areas projecting *into* the STN span relatively large areas of the STN, and overlap with terminal fields from other cortical areas (Haynes and Haber, 2013). (c) Projections terminals *from* the STN, into the GPi, GPe, SNr, and striatum are relatively diffuse (Parent and Hazrati, 1993; 1995b; Mink, 1996; Sato et al., 2000). Such diffuse projections suggest that separate signals that are projected into specific parts of the STN might be integrated downstream, especially via the reciprocal connections between STN and GPe (Joel and Weiner, 1994; 1997). (d) Lastly, this model of unspecific integration also fits with the fMRI results presented in Chapter 8. These results suggest that activity in the different parts of the STN is equally related to different aspects of perceptual decision making. In sum, neurocomputational models, the cytoarchitectonic structure of the STN, as well as the functional imaging experiment presented in Chapter 8 support a model of a homogeneous non-specific integrative function throughout the STN.

However, in Chapter 3 we have shown that, next to a topographical pattern of cortical connectivity, there are also topographical patterns in iron concentrations in the STN, as measured by QSM. Furthermore, in Chapter 4 we have shown that there are also topographical patterns in some immunocytochemical stainings of the STN. How to reconcile these topographical patterns in the STN with a functional model of 'non-specific integration'? Several ideas come to mind: (a) First, the ventromedial STN borders directly to the lateral hypothalamus (LH), an important part of the limbic system. The border between the LH and the STN is hard to define, because cell populations originating from the LH and STN are overlapping (Haynes and Haber, 2013). It is possible that the presence of cells originating from the LH contribute to some of the observed immunocytochemical and MRI image gradients from the ventromedial tip of the STN, intermingled with the LH, versus other parts of the STN. For example, the LH is highly innervated by serotonergic projections originating from the raphe nuclei (Parent et al., 2010) and we found increased concentrations of serotonin transporters specifically in the ventromedial tip of the STN. (b) Second, the STN is surrounded by some major neuromodulatory pathways, which can enter the STN for various reasons. For example, the increased expression of tyrosine hydroxylase (TH) in the dorsal part of the STN that we found in Chapter 4 has been described before and has been linked to dopaminergic projections originating from nigrostrial pathway (Hedreen, 1999; Cragg et al., 2004). However, the density of these dopaminergic axons is very low compared to the striatum, the main target of the nigrostriatal pathway. The functional relevance of these dopaminergic projections into the STN has therefore been questioned by multiple authors. Possibly, the dopaminergic projections are just 'accidentally' splitting from the massive nigrostriatal pathway that lies dorsal of the STN or are mere passing fibers (Hedreen, 1999; Cragg et al., 2004; Redgrave et al., 2010; Alkemade et al., 2015). (c) Third, some of the patterns found in the immunocytochemical stainings might simply be due to differences in cell density or metabolic rate across the STN. Cell density in the STN is higher in the ventromedial part (Yelnik and Percheron, 1979; Hardman et al., 2002b; Lévesque and Parent, 2005) and aligns with the major axis of immunocytochemical differences that was found in Chapter 4. However, such differences in cell density are hardly evidence for functional specialization. In sum, the immunocytochemical staining patterns and related MRI images suggest a heterogeneous pattern of cell populations throughout the STN, but it remains to be seen if this heterogeneity in microstructure is functionally relevant in terms of the processing of 'limbic', 'associative', and 'motor' information.

Another stream of data that has been important for the idea of functional specialization in the STN are the effects of DBS electrode placement on electrophysiological recordings and clinical outcome measures (Mallet et al., 2007; Greenhouse et al., 2011; 2013; Horn et al., 2017). It has been shown that oscillations in the 'beta' frequency band (15-30Hz), which play an important role in suppression of the motor system (van Wijk et al., 2012), show highest power in electrodes that are located near the dorsolateral tip of the STN (Horn et al., 2017). This part of the STN has now even been called a potential "sweet spot" for DBS in PD patients (Horn et al., 2017), because clinical outcome measures are better for DBS electrodes that were placed near this dorsolateral, 'sensorimotor' zone. However, multiple studies suggest that best clinical outcome is actually achieved by stimulation *outside the STN*, in the white matter bundles slightly dorsal of the STN, which are part of larger motor networks, such as the pallidothalamic bundle and the cerebellothalamic tract (Saint-Cyr et al., 2002; Voges et al., 2002; Herzog et al., 2004; Plaha et al., 2006; Butson et al., 2011; Contarino et al., 2017). Similarly, it has been suggested that local field potentials, such as recorded with DBS electrodes, can pick up on neural signals not only from gray matter, but also from nearby fiber bundles (Mercier et al., 2017). Such white matter signals would explain why the highest peak in recorded beta power

can be found on the very border of the dorsolateral tip of the STN, if not outside of it (Horn et al., 2017). Furthermore, some studies suggest that 'limbic' side effects of DBS are due to stimulation in limbic structures ventromedial to the STN, such as the ventral tegmental area (VTA), substantia nigra (SN), and LH (Coenen et al., 2009). In sum, evidence for functional specialization that comes from DBS electrode recordings or DBS stimulation is severely limited by the spatial fidelity of these methods. It is plausible that 'motor' versus 'non-motor' effects of DBS are due to stimulation of 'motor' white matter bundles just dorsal of the STN versus stimulation inside the STN or limbic structures, such as the VTA, SN, and LH, that lie ventromedial to the STN. In sum, no strong evidence for functional specialization *within* the STN can be drawn from DBS studies.

SUBDIVISIONS OR NO SUBDIVISIONS?

In the above, I have argued that, from a functional viewpoint, the STN might be a homogeneous nucleus that integrates information that comes from different cortical regions to influence the global dynamics of the basal ganglia and there are no functional subdivisions to be found within the STN. However, with the scarce data currently available, the existence of functional subdivisions cannot be ruled out completely. The topographic patterns we found in immunocytochemical stains and QSM images could be functionally relevant. Future work should try to reconstruct the histochemical patterns described in Chapter 4 *in vivo*, using quantitative MRI parameters and mathematical models (Weiskopf et al., 2015) and see if these reconstructed patterns are predictive of functional STN activity patterns, measured with DBS electrodes or fMRI. If so, this should be taken as evidence for functional specialization within the STN. If not, this should be taken as evidence that, from a functional viewpoint, the STN is a homogenous structure that probably integrates information from a wide array of sources.

More generally, both theorists and experimentalists should better distinguish between, on the one hand, *structural* properties of the STN, such as topographic organization of cortical connections and histochemical properties, and, on the other hand, the *functional* role of the STN and its structural subzones. Although brain function has to follow from brain structure, this mapping is not trivial and should not be taken for granted (Jonas and Kording, 2017). Furthermore, in the interpretation of data, it is essential to acknowledge the severe limitations that are inherent to any data stream, especially when it considers a nucleus that is so small and is surrounded by so many other distinct gray and white matter structures as the STN.

FUTURE WORK

The structural and functional internal organization of the STN remains an unsolved problem, but recent work, including the work presented in this thesis, has made some significant strides in unravelling its structure and function. I will now discuss two main directions for future work.

First, theoretical work should aim for a more precise model of not only the structural organization of the STN, but also the computational role that possible subdivisions or a cortical topography in the STN could play (Marr, 1982). Linking neural measurements to formal models of decision-making, such as the diffusion decision model (DDM; Turner et al., 2015; Forstmann et al., 2016) and the multihypothesis sequential probability ratio test (MSPRT; Bogacz and

Gurney, 2007), might be a useful starting point. However, there are still some thorny outstanding issues in the use of such models. For example, recent electrophysiological work in monkeys has shown that basal ganglia nodes, unlike some cortical counterparts, show non-linear accumulation signals that do not correspond to the internal mechanisms of established, more abstract sequential sampling models such as the DDM (Ding and Gold, 2013) and can only be explained by more complex models including highly non-linear neuronal dynamics (Wong and Wang, 2006; Ding and Gold, 2013).

More generally, it still remains unclear how to *precisely* interpret relationships between neural measurements and cognitive latent variables as estimated by abstract cognitive models like the DDM, because of their very different levels of description (Poldrack, 2015; Lebreton and Palminteri, 2016). For example, if during a perceptual decision-making task, an area negatively correlates with evidence accumulation rates, is this area directly involved in evidence accumulation, error monitoring, or part of the default mode network (O'Reilly and Mars, 2011; Turner et al., 2015)? And, if we want to learn more about the implementation of computational processes in the brain, should we look at within- or across-subject variability of behaviour and neural measures? Or both? In any case, these two levels of variability can potentially give very different answers (Molenaar, 2004; Kievit et al., 2013). For models that are less abstract and more closely resemble neural architecture, like the mapping of the MSPRT equations to the basal ganglia (Bogacz and Gurney, 2007), the leaky competing accumulator model (Usher and McClelland, 2001), or even neural network models (Wong and Wang, 2006), the mapping between neural measurements and internal model parameters might be more straightforward. However, the increased complexity of neurally plausible models often makes their parameters trade-off and the inverse problem (estimating cognitive parameters from behaviour) becomes intractable (Miletić et al., 2017). This precludes more complex models from being used in a traditional model-based cognitive neuroscience approach, which hinges on the quantification of inter- or intra-subject variability in latent parameters (Forstmann and Wagenmakers, 2015). Maybe a shift from inter- and intra-individual to inter- and intra-stimulus variability, as used in encoding models of visual cortex could be a fruitful future direction (van Gerven, 2017).

Another technique that could aid theoretical development is the automated meta-analysis of neuroimaging papers (Yarkoni et al., 2011). Such data-driven meta-analyses have shown that some brain activation patterns can be clustered and related to specific cognitive constructs by manifold learning, with little a-priori assumptions (Poldrack et al., 2012). However, an important limitation of such meta-analyses is their very crude spatial resolution, since they are based on activation coordinate tables, rather than the original activation maps. This might make them unsuitable for the study of smaller subcortical nuclei (Keuken et al., 2014b).

A second direction of research should be dedicated to the further improvement of neuroimaging techniques for subcortex. As the first chapters of this thesis have shown, structural imaging of the STN at 7 T yields images of very high quality and some of the internal structure of STN can already be resolved in vivo. However, Chapter 6 and 8 showed that the functional imaging of the STN (and subcortex in general) is currently lagging behind. Although we found robust task-related BOLD effects in average signal of anatomical ROIs in Chapter 8, voxelwise analyses did not show any robust activation clusters. The limited BOLD sensitivity in STN is probably due to both high noise (see Chapter 6), as well as relatively small task-related BOLD signal changes in subcortex (see Ances et al., 2008). Both problems could be tackled by increasing the signal-to-noise ratio for functional imaging protocols in the subcortex. Two potential approaches to achieve this are a further increase of field strength (Budde et al., 2013)

and the use of customized coils that show better sensitivity in the subcortex, such as a monopole or dipole antenna array (Wiggins et al., 2012; Hong et al., 2013). However, both these approaches come with additional challenges, such as further increased B0 field inhomogeneity effects (Budde et al., 2013; van der Zwaag et al., 2016), increased B1+ inhomogeneity, reduced field-of-views, and heating issues (Wiggins et al., 2012; Hong et al., 2013).

We can currently not exclude that in the study described in Chapter 8, different subregions of the STN showed similar BOLD activation patterns because of blurring of the activity of different neural populations by neurovascular coupling and spin dephasing (Shmuel et al., 2007). Future work should investigate the extent of such blurring in the subcortex and explore alternative functional sequences like VASO (Huber et al., 2016) and spin echo sequences (Budde et al., 2013), which have shown to be more spatially specific to underlying neural activity than gradient echo sequences (Turner, 2016). Unfortunately, the increased spatial specificity that is gained by such sequences, come with inherently decreased signal-to-noise ratios and it remains to be seen if these sequences show enough sensitivity in the basal ganglia.

Lastly, to further investigate the functional relevance of the histochemical patterns presented in Chapter 4, these patterns should be related to functional activation patterns measured with fMRI. To do so, mathematical models mapping quantitative MRI parameters and microstructural properties should be developed (Stüber et al., 2014; Weiskopf et al., 2015). The data presented in Chapter 4 could serve as a starting point for estimating the parameters of such models.

Appendix A

SUPPLEMENTARY MATERIALS FOR CHAPTER 4

MATERIALS AND METHODS

TISSUE FIXATION

All brain tissues were collected within a 4 year period from the Netherlands Brain Bank with a <8h post mortem interval before brain autopsy. Tissues were obtained in accordance with BrainNet Europe's Code of Conduct for brain banking (Klioueva et al., 2015). Clinicopathological information is presented in Supplementary Table S1.

Supplementary Table S1: Clinicopathological data

NBB#	Age (y)	Sex	PMD (h:m)	Fix (days)	Cause of death, clinical diagnosis
12-062	88	M	05:40	Nd	Ischemic bowel rupture, aortic stenosis, femoropopliteal bypass, hypercholesterolemia, cardiorenal syndrome, ischaemic cardiomyopathy, atrial fibrillation, tauopathy*
12-082	101	F	05:10	Nd	Cachexia, cataract, TIA, mitral valve insufficiency, osteoporosis, coxarthrosis, kyphosis, decubitus, dehydration, AD Braak score 4C*
12-104	79	M	06:30	Nd	Respiratory insufficiency, type 2 diabetes, nephropathy
13-095	101	F	06:15	57	Pneumonia, cardiac failure, angina pectoris, cataract, hysterectomy, cholecystectomy, type 2 diabetes, coxarthrosis, spondylosis, conjunctivitis, COPD, bullous pemphigoid
14-037	101	F	07:27	57	Renal insufficiency, urinary tract infection, gasteroenteritis, scoliosis, atrial fibrillation, cataract, prosthetic hip, AD Braak score 4C*
14-051	92	M	07:45	57	Cardiac failure, type 2 diabetes, polyneuropathy, decubitus, ascites, liver cirrhosis, cataract, COPD, prosthetic hips
14-069	73	M	04:25	56	Pneumonia, COPD, hypercholesterolemia, atrial fibrillation, aortofemoral bypass, PCTA, cataract, spondylosis, esophagitis, prostate carcinoma, hyperthyroidism, decubitus
15-033	93	M	07:40	59	Cardiac failure, aortic stenosis, cardiac decompensation, macular degeneration, basal cell carcinoma
15-035	73	M	08:00	56	Pneumonia, cardiac failure, pneumonia, myelodysplastic syndrome, fungal infection
15-055	72	F	06:50	55	Respiratory insufficiency, polymyalgia, polio, ovarium carcinoma, ileus, osteoporosis

*Determined post mortem, AD=Alzheimer's disease, Fix=fixation duration, nd= not determined, PTCA=percutaneous transluminal coronary angioplasty, PMD=post mortem delay, TIA=transient ischemic attack, y=years

We fixated the tissue for approximately 8 weeks in 10% formalin (10x V/V). After initial formalin fixation tissues were transferred to phosphate buffered saline [PBS (pH ~ 6.6-7.0): 145 mM NaCl, 9 mM disodium phosphate (Na_2HPO_4 cat.no. 71640, Sigma-Aldrich, St. Louis, MO, USA),

2 mM sodium phosphate ($NaH_2PO_4.H_2O$, cat. no. S9638, Sigma-Aldrich, St. Louis, MO, USA)] containing 0.02% sodium azide to prevent fungal growth until further processing.

MRI OF THE TISSUE

For ultra-high resolution magnetic resonance imaging (MR), tissues were transferred to Fomblin, which is proton free and therefore shows no MR signal and is susceptibility matched to the tissue (Benveniste et al., 2000; D'Arceuil and de Crespigny, 2007; D'Arceuil et al., 2007; Klioueva et al., 2015). MRI scans were created using a 7 Tesla (T) Siemens whole-body MR scanner with a custom-built 80-mm dual loop miniCP coil (Weiss et al., 2015).

MRI SEQUENCE PARAMETERS

The T_1 maps were based on the magnetization-prepared 2 rapid acquisition gradient echoes (MP2RAGE) sequence which was acquired with the following sequence parameters: 104 axial slices with an acquisition time (TA) of 2:24 hours (repetition time (TR) = 3000ms; echo time (TE) =3.07ms; inversion times TI1/TI2 = 180/900 ms; flip angle = 8°/8°; bandwidth =350 Hz/Px; voxel size = 0.2 mm isotropic). The T_2* maps were based on a multi-echo gradient echo (GRE) fast low angle shot (FLASH) sequence which was acquired with the following parameters: 104 axial slices with a TA of 1:02:26; TR:500ms; TE: 4.67, 11.77, 18.87, 25.97, 33.07, 40.17, 47.27, 54.37ms; flip angle: 79°; bandwidth: 320Hz/Px; phase and slice partial Fourier of 6/8; voxel size 0.2 mm isotropic. Finally, a single echo GRE FLASH was acquired to delineate the STN and calculate the quantitative susceptibility mapping (QSM) which was acquired with the following parameters: 352 axial slices with a TA of 10:24:50; TR:500ms; TE: 20ms; flip angle: 79°; bandwidth: 40Hz/Px; phase and slice partial Fourier of 6/8; voxel size 0.06 mm isotropic. The coil combination of phase data was done automatically by the scanner vendor software (version VB17).

QUANTITATIVE MRI

The T_1 maps were created using the MP2RAGE sequence which incorporates two volumes with different inversion times (the INV1 and INV2 volumes), which can be combined into a single T_1-weighted volume or used to estimate the T_1 values (Marques et al., 2010). The T_2* map was created by fitting a linear least squares function in log-space to the eight TEs of the FLASH images (Weiskopf et al., 2014), solving the following equation for T2*:

$$S(TE) = S_0 e^{-TE/T2*}.$$

The QSM was calculated using the 0.06 mm T_2*-weighted volume by unwrapping the phase data and removal of the background phase using iHARPERELLA (Li et al., 2015). Then the quantitative susceptibility was estimated using the iLSQR method as implemented in STIsuite (V 2.2; Li et al., 2011).

MRI REGISTRATION STEPS

The target space for the MRI volumes was the stacked block face (see below) which was converted from a tiff image to NifTi. The stacked tiff image was loaded in MIPAV (McAuliffe et al., 2001) here the color information was removed by conversion to a gray image with an equal

weight per RGB channel. The tissue was manually masked to remove the background tissue and exported to NifTi with an 0.014 mm in-plane resolution and 0.3 mm slice thickness.

0.06MM T_2*–WEIGHTED TO BLOCK FACE REGISTRATION

The 0.06 mm T_2*-weighted magnitude image together with the block face stack image was opened in MIPAV and viewed in triplanar view. A minimum of four landmarks around the STN (such as distinct branching of blood vessels) were identified for each individual sample in both images and used for nonlinear thin plate spline landmark registration using trilinear interpolation (Bookstein, 1989). Landmark registration was necessary as other automatic registration algorithms implemented in either FSL, MIPAV, or ANTs failed to result in a satisfactory registration. The QSM and manual parcellations of the STN were transformed to block face space using the non-linear transformation matrix and trilinear and nearest neighbor interpolation respectively.

T_2* MAPS TO BLOCK FACE REGISTRATION

To improve the registration between the T_2* map and 0.06 mm T_2*-weighted volume an average magnitude volume was created of the eight T_2*-weighted volumes. This average T_2*-weighted volume was linearly registered to the 0.06 mm T_2*-weighted volume using a correlation cost function, 6 degrees of freedom (DoF), and trilinear interpolation as implemented in FLIRT (Jenkinson and Smith, 2001; FSL 5.0.9; Jenkinson et al., 2002). The T_2* map was transformed to the block face space using the resulting linear transformation matrix in combination with the nonlinear transformation matrix from the landmark registration step with trilinear interpolation.

T_1 MAPS TO BLOCK FACE REGISTRATION

First, an average volume was created of the two inversion volumes, which was linearly registered to the 0.06 mm T_2*-weighted volume using a mutual cost function, 6 DoF, and trilinear interpolation as implemented in FLIRT (Jenkinson and Smith, 2001; FSL 5.0.9; Jenkinson et al., 2002). The T_1 map was transformed to block face in a similar fashion as the T_2* map.

PROCESSING OF THE TISSUE

After scanning, tissues were transferred back to PBS with 0.02% sodium azide (cat.no. S-2002, Sigma-Aldrich, St. Louis, MO, USA) until further processing. Following dehydration, tissues were embedded in paraffin, after which 6 micrometer thick serial coronal sections were cut covering the entire rostrocaudal axis of the STN. While processing, block face imaging was performed (at an interval of 50 sections), which provides an intermediate step crucial for registration of individual sections to MRI space. This was done using a camera mounted in front of the microtome.

At the block face imaging level, sections were mounted on Menzel-Gläser Superfrost plus object slides (Cat. no. J1800AMNZ, Thermo Scientific, Braunschweig, Germany) and stained with thionine (Thionine acetate: cat. no. 1.15929.0025, Merck, Darmstadt, Germany) for anatomical orientation. Sections were stained with thionine at systematic 300 micrometer

intervals, which allowed us to identify the borders of the STN using a light microscope. Consecutive sections containing the STN were used for staining of individual protein markers using immunocytochemical procedures for Neurofilament H (SMI-32), Synaptophysin (SYN), Tyrosine Hydroxylase (TH), Vesicular Glutamate Transporter 1 (VGLUT1), Glutamate Decarboxylase 65/67 (GAD65/67), GABA-A receptor subunit alpha 3 (GABRA3), Serotonin Transporter (SERT), Parvalbumin (PARV), Calretinin (CALR), Transferrin (TRANSF), and Ferritin (FERR) (see Table S2).

Supplementary Table S2: Primary antibody characteristics

Primary Ab	Dilution	Protein	Function	Source	Specificity
Pilots studies					
NPY	1:1,000	Neuropeptide Y	Neurotransmitter, affects cortical excitability, stress response, food intake, circadian rhythms, and cardiovascular function	Niepke, NIN	IEF, preadsorptions, omission primary Ab, ICC (van der Beek et al., 1992)
CRH	1:100,000	Corticotropin releasing hormone	Peptide hormone/neurotransmitter involved in the stress-response	PFU83, Free of University Amsterdam	Preadsorptions, preimmune serum testing, omission primary Ab, ICC (Raadsheer et al., 1993; Erkut et al., 1995)
ORXA	1:20,000	Orexin A	Peptide hormone involved in sleep regulation	H003-30,Phoenix Pharmaceuticals	Preadsorptions, dot blots, ICC (Fronczek et al., 2005)
VIP	1:1,000	Vasoactive intestinal peptide	Peptide hormone involved in circadian rhythmicity	Viper, NIN	IEF, preadsorptions, omission primary Ab, ICC (van der Beek et al., 1992)
Aromatase	1:1,500	Aromatase	Enzyme involved in estrogen synthesis	Narom, NIN	ICC (Ishunina et al., 2005)
ChAT	0.180555556	Choline acetyl transferase	Enzyme involved in acetylcholine synthesis		ICC (Dubelaar et al., 2004)

(Specificity for ChAT): ICC, WB (Bar-Peled et al., 1997; Fernyhough et al., 1999; Brownlees et al., 2000; Gveric et al., 2001; Van den Haute et al., 2001; Van der Gucht et al., 2003; Weigum et al., 2003; Mahad et al., 2009; Veeranna et al., 2010; Jablonska et al., 2012; Sareen et al., 2012)

Ab=antibody, ELISA=enzyme-linked immunosorbent assay, ICC=immunocytochemistry, IEF=isoelectric focusing, WB=Western Blotting

Supplementary Table S2 (continued)

Primary Ab	Dilution	Protein	Function	Source	Specificity
Distribution studies					
SMI-32	1:2,000	Neurofilament H	Major cytoskeletal component	SMI-32, Covance	ICC, WB, ELISA (Nagatsu et al., 1964; Sager et al., 2000; Hara et al., 2008; van Vliet et al., 2009; Gottschall et al., 2010; Eftekhari and Edvinsson, 2011; Purushothuman et al., 2013)
SYN	0.215277778	Synaptophysin	Major synaptic vesicle protein	A0010, DAKO	ICC, WB (Perez et al., 2002; Kanaan et al., 2007; Morrow et al., 2007; Mastrobeardino et al., 2009; Dobi et al., 2010; Thomsen et al., 2010; Addis et al., 2011; Mulcahy et al., 2012; Rothmond et al., 2012)
TH	1:1,500	Tyrosine hydroxylase	Rate limiting enzyme in dopamine production (69)	MAb318, Millipore	ICC, WB (Kirvell et al., 2006; Zhou et al., 2006; Ribic et al., 2010; Zander et al., 2010; Larsson et al., 2012; Kempf et al., 2013; Nair et al., 2013; Sun et al., 2013)
VGLUT1	1:10,000	Vesicular glutamate transporter 1	Sodium dependent phosphate transporter, glutamate signalling (79)	135302, Synaptic Systems	ICC, WB (Hédou et al., 2000; Yamada et al., 2002; Dracheva et al., 2004; Rodriguez-Contreras, 2005; Kiss et al., 2007; Bragina et al., 2008; Idrissi and L'Amoreaux, 2008; Yeo et al., 2010; Gavin et al., 2011; Yang et al., 2011; Joshi et al., 2012; Padgett et al., 2012; Gao et al., 2013)
GAD65/67	0.25	Glutamate decarboxylase 65/67	Enzyme that catalyzes glutamate to GABA conversion	Ab1511 Millipore	ICC, WB (Hédou et al., 2000; Yamada et al., 2002; Dracheva et al., 2004; Rodriguez-Contreras, 2005; Kiss et al., 2007; Bragina et al., 2008; Idrissi and L'Amoreaux, 2008; Yeo et al., 2010; Gavin et al., 2011; Yang et al., 2011; Joshi et al., 2012; Padgett et al., 2012; Gao et al., 2013)

Ab=antibody, ELISA=enzyme-linked immunosorbent assay, ICC=immunocytochemistry, IEF=isoelectric focusing, WB=Western Blotting

Supplementary Table S2 (continued)

Primary Ab	Dilution	Protein	Function	Source	Specificity
GABRA3	0.2153	GABA-A receptor subunit alpha 3	Receptor subunit	AGA-003, Alomone Labs	ICC, WB (Caspary et al., 2013; Park et al., 2013; Zhou et al., 2013; Seo and Leitch, 2014)
SERT	1:5,000	Serotonin transporter	Determines serotonin availability in the synaptic cleft (106)	MAb5618, Millipore	ICC, WB (Bauman et al., 2000; Ramsey and DeFelice, 2002; Serafeim et al., 2002; Henry et al., 2003; Borgers et al., 2014)
PARV	1:2,500	Parvalbumin	Calcium binding protein	195004, Synaptic Systems	ICC (Andrioli et al., 2007; Gross et al., 2011; Mallet et al., 2012; Massi et al., 2012; Huang et al., 2013; Lee et al., 2013)
CALR	0.354166667	Calretinin	Calcium binding protein	6B3, Swant	ICC, WB (Schiffmann et al., 1999; Lavenex et al., 2009; Fuentealba et al., 2010; Lancaster et al., 2013)
TRANSF	1:4,000	Transferrin	Iron binding glycoprotein	Ab9538, Abcam	ICC, WB (Zawadzka et al., 2010)
FERR	1:1,500	Ferritin	Iron binding protein expressed in oligodendrocytes (122, 123)	sc-14416, Santa Cruz	ICC, WB (Saunders et al., 2007; Vidal et al., 2008; Duan et al., 2009; Li et al., 2009; Sengupta et al., 2009)

Ab=antibody, ELISA=enzyme-linked immunosorbent assay, ICC=immunocytochemistry, IEF=isoelectric focusing, WB=Western Blotting

Each section was stained using a single antibody. In short: Paraffin was cleared from the slides using xylene and tissues were rehydrated using a graded series of alcohols. After rinsing in distilled water, antigen retrieval was performed using heat treatment (Shi et al., 1997), and pre-incubation was performed if appropriate. Subsequent incubation in the primary antibody was performed overnight in a humidified chamber in Supermix [(SUMI): TBS containing 0.25% gelatin (cat. no. 1.04078.1000, Merck, Darmstadt, Germany) and 0.5% Triton X-100 (cat.no. X100, Sigma-Aldrich, St. Loius, MO, USA)]. After rinsing in Tris buffered saline [(TBS): 150 mM NaCl (cat. no. 1.06404.1000, Merck, Darmstadt, Germany), 50 mM Tris-HCl, pH 7.6 (Trizma cat.no. T1503, Sigma-Aldrich, St. Louis, MO, USA)], sections were incubated in an appropriate biotinylated secondary antibody (Vector laboratories Inc., Burlingame, CA, USA), followed by incubation in avidine-biotinylated-complex (VECTASTAIN ABC Kit: cat. no. PK-6100, Vector laboratories Inc., Burlingame, CA, USA) and visualization of the staining using diaminobenzidine amplified with nickel ammonium sulphate [DAB: cat.no. D5637, Sigma-Aldrich, St. Louis, MO, USA; Ammonium nickel(II) sulfate: BDH Chemicals, UK] as a chromogen resulting in an intense purple precipitate as described previously (Alkemade et al., 2005a; 2005b; 2012a; 2012b). Sections were cover slipped using Entellan (Cat.no. 1.0791.0500, Merck, Darmstadt, Germany).
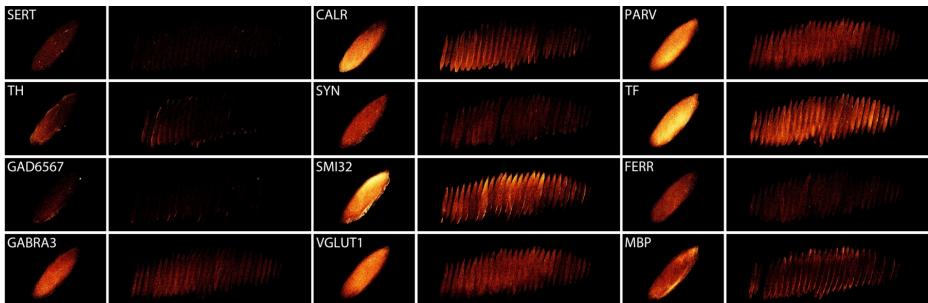
IMAGE PROCESSING

Block face images were restacked using image J (1.48V) and Stackreg (Thevenaz et al., 1998). Tissue borders were manually outlined in the block face image, since the more caudal tissue was visible in the paraffin resulting in limited contrast that did not allow reliable automatic parcellation of the tissue in the field of view.

All stained sections were digitally imaged using a slide scanner (Ventana, Roche). The appropriate image was selected and the image was adjusted to allow registration of the protein markers to the appropriate block face images. Image conversion was performed to exclude contrast in the tissue and to allow registration based on shape of the tissue. This was done because the contrast information obtained from the block face image was substantially different from that obtained from staining. Images were registered using a scaled rotation, followed by an affine transformation. Transformation matrices were saved. All transformations were visually inspected, and if the results were insufficient, as evidenced by clear jumps of the sections within the reconstructed STN structure, images were registered using a rigid body transformation followed by an affine registration. If registration was still deemed to be insufficient, images were discarded. Overall registration of #12-062, 12-082, and 12-104 was deemed insufficient, and these specimens were excluded from further analyses.

THRESHOLDING OF THE STAINING

A histogram based thresholding procedure was applied to remove background signal from the immunocytochemistry procedure on the red channel of the stained images in ImageJ, by creating a RGB-stack, followed by the default thresholding procedure implemented in ImageJ. Threshold settings were determined experimentally [CALR (0, 95), FER (0, 127), GABRA (0, 134), GAD6567 (51, 112), MBP (0, 130), PARV (41, 133), SERT (0, 165), SMI (0, 156), SYN (0, 162), TRANSF (0, 110), TH (0, 155), VGLUT1 (0, 140)]. The thresholded images were converted using the binary mask functions to which subsequently the scaled rotation and affine transformation matrices, and if appropriate, the rigid body and affine transformation matrices were applied (see Fig. S1 for an example).

Supplementary Figure 1. Example of a single specimen showing the reconstructions of immunoreactivity for serotonin transporter (SERT), calretinin (CALR), parvalbumin (PARV), tyrosine hydroxylase (TH), synaptophysin (SYN), transferrin (TF), glutamic acid decarboxylase (GAD65/67), neurofilament H (SMI32), ferritin (FERR), GABA receptor subunit A3 (GABRA3), vesicular glutamate transporter 1 (VGLUT1), myelin basic protein (MBP), and a combination of individual reconstructions. Small images represent Z-stacks showing maximum intensity of immunoreactivity. Larger images illustrate the distribution of immunoreactivity over the rostro-caudal axis of the STN.

## DELINEATION OF THE STN IN STAINED SECTIONS
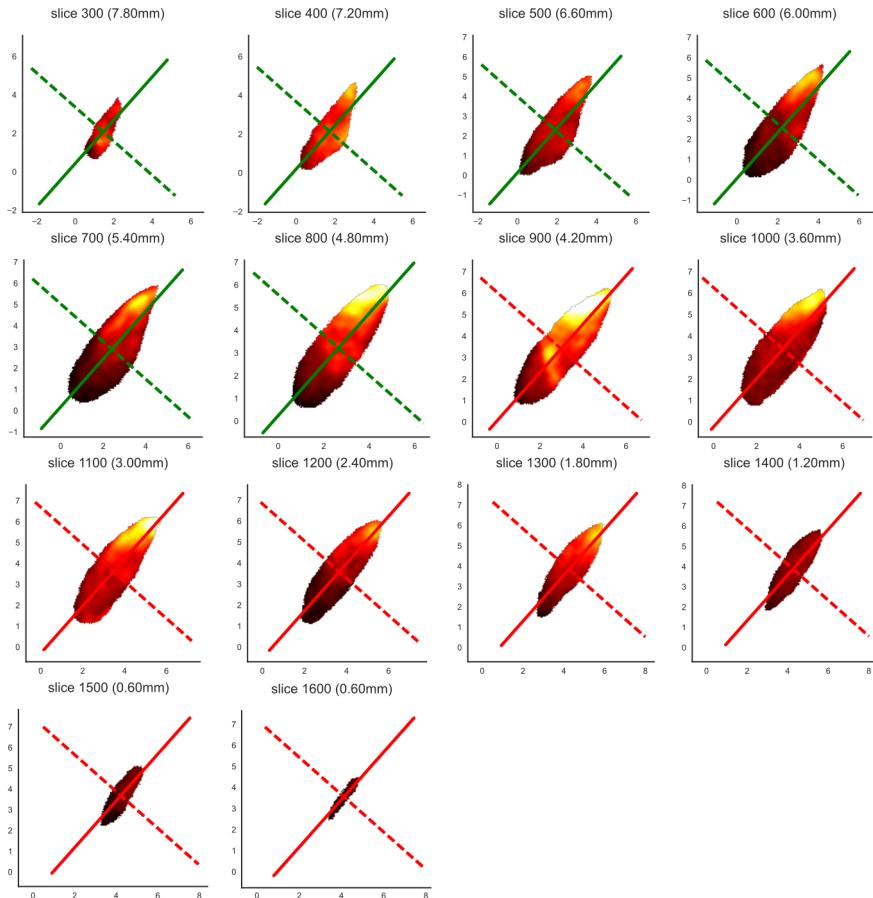
Two independent raters delineated the STN over the entire rostrocaudal axis of the STN using PARV and SMI32 images. This yielded 4 STN for each level. The area included in the STN in a minimum of 3 masks was used for further analyses. Consequently, only images for which both PARV and SMI32 sections were available, were used in further analyses.

QUANTITATIVE ANALYSES OF IMMUNOREACTIVITY

Immunocytochemical and MRI images were analyzed in a common intra-individual space, based on the block face images. These images had a resolution of 0.014 mm isotropic in the cutting plane, and 0.3 mm between adjacent slices. For the immunocytochemical images, the thresholded and transformed images constructed using imageJ were analyzed. These images were smoothed with a Gaussian kernel with a full-width half maximum (FWHM) of 0.3 mm (Szeliski, 2010; de Hollander et al., 2014a). This smoothing procedure was performed to (i) increase signal-to-noise ratio, and (ii) focus the analyses on topological patterns in the order of 0.1 – 1 mm, rather than patterns in structures much smaller than the STN. To make sure that image intensities outside of the STN mask were not included in the analyses, the smoothing kernel was always truncated outside of the STN mask and normalized.

CONSISTENCY OF IMMUNOREACTIVITY PATTERNS

To analyze the data of 7 different STN specimens in a common interindividual space, they were subdivided in 27 sectors. These sectors were based on two cuts over three axes, resulting in three domains for every axis. The first axis followed the cutting plane (anterior-posterior). The two other axes were defined by a principal component analysis (Bishop, 2006) on the 2D coordinates over all slices. The resulting axes were visually inspected and were consistently identified as a main laterodorsal->medioventral axis and a dorsomedial -> ventromedial axis (see Fig. S2 for an example).

Supplementary Figure 2. Main PCA axis overlaid on SMI32 images. The solid line indicates the main dorsolateral-ventromedial axis in the 2D plane, and the dotted line indicates the axis orthogonal to that axis. The green lines lie in the rostral half of the specimen, whereas the red lines lie in the caudal half of the specimen.

The intra-individual sectors were used to test whether specific sectors showed increased expression for specific markers. To do this, within every specimen, for every marker, the 27 sectors were demeaned and standardized, so that their mean was 0 and their standard deviation was 1. Then, for every sector, a one-sampled t-test was performed over the 7 STN specimens. Results were corrected for multiple comparisons using the False Discovery Rate correction. Sectors that robustly and consistently showed increased or decreased marker expression should show significant t-values.

For visualization purposes, we also made a "group STN template", by iteratively linearly registering the binary masks based on the PARV and SMI32 towards the average image of each other (see also de Hollander et al., 2017). We then transformed all the individual staining intensity images to this space, after which we could make "group maps" of these staining intensities (see Fig. 4 of Chapter 4).

As an exploratory analysis, for every specimen separately, the marker intensities were correlated over all voxels, using Pearson correlation. This yielded a 12 x 12 correlation matrix for all 7 specimens. These correlations matrices were averaged over specimens to get a correlation matrix that showed the average correlations-across-space over the 7 specimens. A Hierarchical linking clustering algorithm was used, with an average linkage criterion and Euclidian distances (using the Python libraries Scipy, 0.18.1(Jones et al., n.d.) and Seaborn, 0.7.1 (Waskom et al., 2015)). This analysis yielded a dendogram that described (groups of) clusters of protein markers that showed similar spatial expression patterns.

MIXTURE MODELS

To test how many components of intensity distributions could be found within individual marker protein stains, a set of mixture models was fitted to the empirical intensity distribution for every stain and specimen separately. Specifically, a mixture of exponentially-modified Gaussians was fitted (exGauss; Grushka, 1972). ExGauss distributions are bounded to be above zero and have a positive skew, just like the image intensities of the marker proteins. They are defined as the convolution of the normal density and exponential density functions. They can, to some extent, be theoretically motivated as an appropriate distribution for the data at hand, because many biological growth processes can be described as an exponential process, and the spatial smoothing that was applied to the image can be approximated as a convolution with a Gaussian distribution in intensity space. The density function of an exGauss distribution is as follow:

$$\text{exGauss}(x; \mu, \sigma, \lambda) = \frac{\lambda}{2} e^{\frac{\lambda}{2}(2\mu + \lambda\sigma^2 - 2x)} \text{erfc}(\frac{\mu + \lambda\sigma^2 - x}{\sqrt{2}\sigma})$$

where erfc is the complementary error function, defined as:

$$\text{erfc}(x) = 1 - \text{erf}(x)$$

$$= \frac{2}{\sqrt{\pi}} \int_{x}^{\infty} e^{-t^2} \, dt$$

The likelihood function of the complete mixture model was now as follows:

$$f(x; \mu, \sigma, \lambda, p) = \sum_{c=1}^{k} p_c \, \text{exGauss}(x; \mu_c, \sigma_c, \lambda_c)$$

Where $\mu, \sigma,$ and λ are vectors of size k (corresponding to the number of clusters) that describe the shapes of the different exGauss distributions. p is a vector of size k with summing up to one. It describes the proportion of every exGauss distribution in the mixture. For every marker and specimen, 10,000 intensity values were randomly sampled from within the STN mask and rescaled so that the minimum value was 0, and the maximum value was 1. Then, the maximum-likelihood parameters of the exGauss-mixture were found using the differential evolution optimization algorithm (DE; Storn and Price, 1997), as implemented in Scipy, using 100 walkers

and up to 500 optimization iterations. After DE optimizations, the best set of parameters was further "polished" using sequential least squares programming (SLSQP; Kraft, 1988). All elements of the vector p were bounded to be above 0.05, to prevent "null models" where one of the clusters has a proportion of (close to) 0 (Frühwirth-Schnatter, 2006). For every marker and specimen, models varying in number of clusters k from 1-6 were fitted.

To select the most appropriate number of clusters for the different protein markers, we resorted to three different model selection criteria. The first one was based on the Akaike Information Criterion (AIC; Akaike, 1974) and the Bayesian Information Criterion (BIC; Schwarz, 1978). Both are a weighted sum of the likelihood of the data under the estimated model and the number of parameters, where models that have high likelihood but a small number of parameters are preferred. However, information criteria hinge on assumptions and should be interpreted with caution (Vandekerckhove et al., 2014).

Therefore, we also resorted to a second method of model selection: cross-validation within-specimens. Specifically, we fitted the mixture models on half of the slices in a specimen (i.e., the even slices), and assessed the likelihoods of the other half of the slices (i.e., the uneven slices). Mixture models that generalize well should show a higher likelihood than models that overfit the data. However, a problem of this approach in our data is that alternating sections from the same specimen do not represent independent samples, breaking down an assumption of cross-validation (Arlot and Celisse, 2010).

A third method of model selection was therefore also applied: cross-validation across specimens. A model was fit for one individual specimen, and then tested on the other specimens. To overcome scaling issues, the intensity values of the test specimen were linearly scaled, by minimizing the Kolgomorov-Smirnoff statistic between the test and training distributions (using the Simplex optimization algorithm). Again, well-generalizable models should show a relatively high likelihood on held-out specimens. This technique assumes that different specimens should show intensity distributions with identical underlying generative distributions. This does not take variability in biological systems into account: it is likely that even when robust clusters exist within the STN, their exact proportions, as well as that of the (non-linear) scaling of intensity values after digital imaging vary across specimens. In sum, all method selection approaches used have limitations, which we have attempted to overcome, at least partly, by reporting multiple methods.

Another way of interpreting the mixture models is to investigate the estimated parameters of the different models (if we assume a specific number of clusters: where do they come to lie?). For example, assuming a fixed number of clusters, to what extent do these clusters overlap? Therefore, we fitted mixture models with 1-6 clusters and counted which proportion of voxels had a probability of less than 95% of belonging to one *specific* clusters, i.e., how many voxels could not exclusively be attributed to a single cluster. If this proportion of voxels is high, one could argue that if clusters are present in the data, they show substantial overlap.

In line with earlier work (de Hollander et al., 2014a), we analysed the gradient magnitude images of the marker proteins. These images indicate, for every voxel, to what extent the image intensity changes compared to neighboring voxels. If there are clear borders present, a subset voxels with a very high gradient value is expected. To assess this, we fitted ExGauss mixture models to the gradient images. Again, three different types of model comparison were applied and the proportion of strong cluster assignments was calculated.
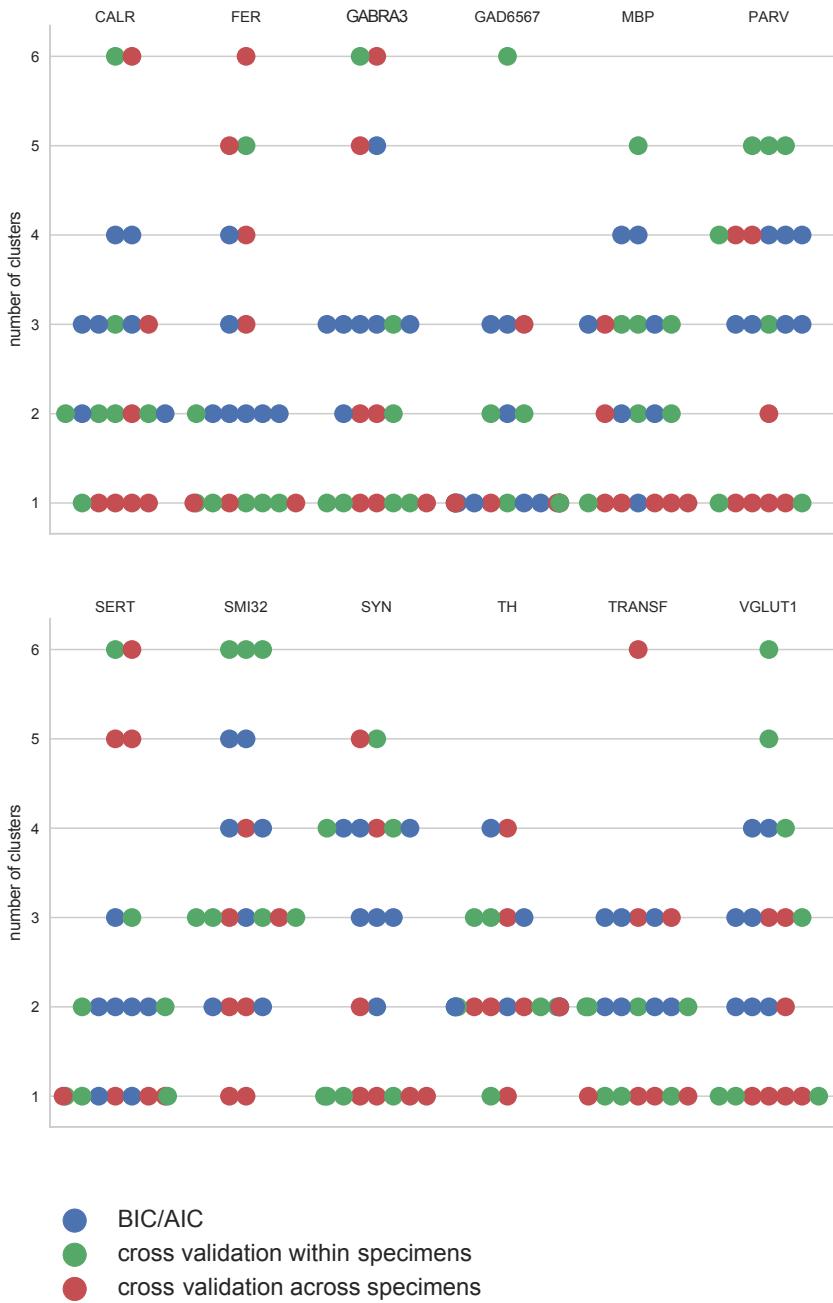
MAPPING BETWEEN QMRI AND IMMUNOHISTOCHEMISTRY

Finally, we related quantitative MRI parameters to the densitometric data. A promising direction of MRI research is "*in vivo* histology" (Weiskopf et al., 2015), where researchers aim to model histological features in healthy human subjects using MR signals and a forward model. To investigate the feasibility of such an approach for the patterns obtained in this study, we fit linear models predicting relative densitometric values (normalized between 0 and 1), based on different combinations of quantitative T_1, T_2*, and QSM parameters (and a constant intercept).

EXTENDED RESULTS
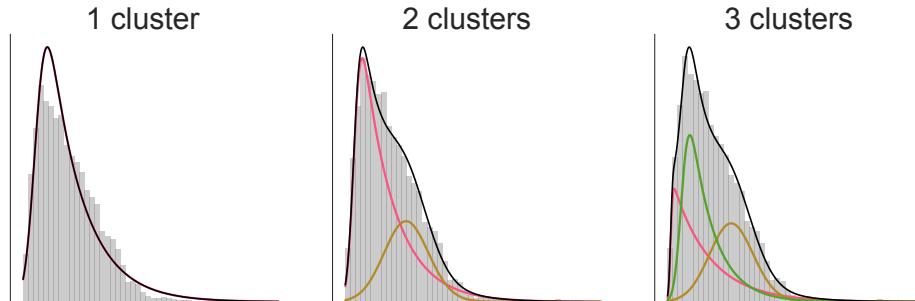
MIXTURE MODELS

When densitometric values were used as input to a mixture model, different model selection techniques suggested different numbers of clusters for the same specimens (see Supplementary Fig. 3).
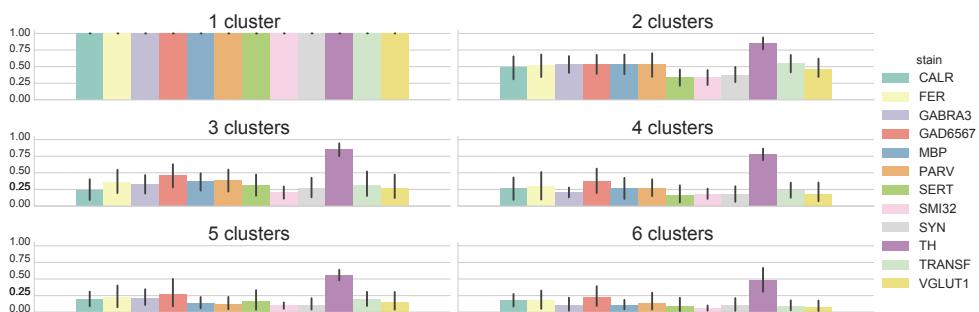
Supplementary Figure 3. Number of exGauss components in protein marker intensity images, according to different model comparison techniques. Note that different methods suggest a different numbers of clusters, with little consistency. Cross-validation within-specimens: models are cross-validated across even and uneven slices in the same specimen; Cross-validation across specimens: models are cross-validated across specimens; BIC/AIC: model selection using Bayesian and Akaike information.

One could argue that maybe all models are mis-specified and are not able to meaningfully describe the data. However, plotting the predicted intensity distributions over the actual intensity distributions suggest the model fits reasonably well (see Supplementary Fig. 4).
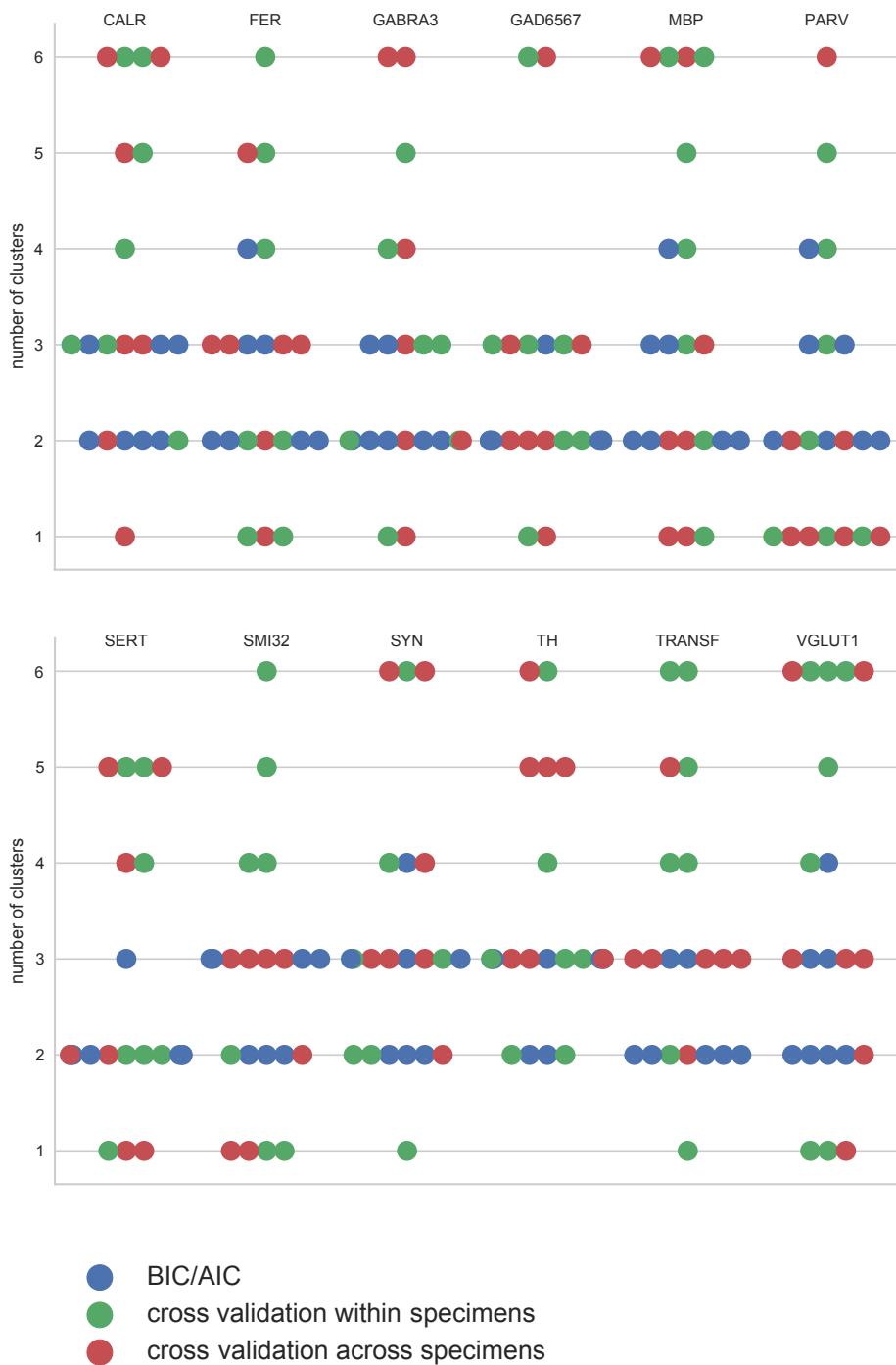
Supplementary Figure 4. ExGauss mixture model predictions overlaid on empirical intensity distribution of CALR marker expression for a representative subject.

We estimated the proportion of voxels that can be attributed to only a single cluster with more than 95% probability, to assess how much potential clusters are overlapping. It turns out that for most stains, approximately only 50% of the voxels can clearly be attributed to a single cluster. The only exception is TH, which showed expression only in the dorsal border of the STN and shows low expression in other parts of the STN (see Supplementary Fig. 5). This led us to conclude that even if there are meaningful clusters in the data, they must be highly overlapping (see also main text).
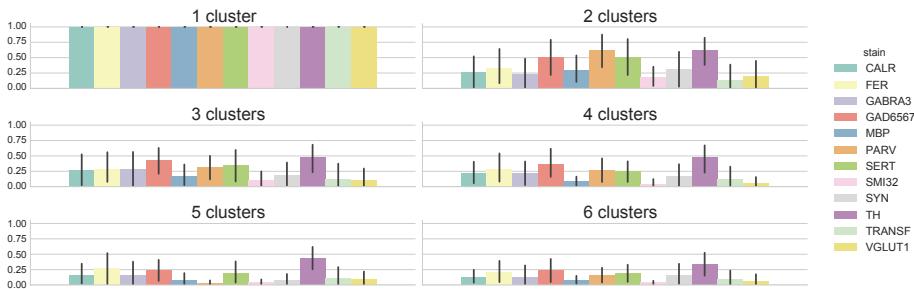
Supplementary Figure 5. Proportion of voxels that can be assigned to one specific cluster with more than 95% probability. Error bars indicate 95% bootstrapped confidence interval.

When we applied mixture models to the gradient images, we found a similar pattern as in the raw intensity images: the different model selection techniques did not converge on a specific number of clusters (see Supplementary Fig. 6).

Supplementary Figure 6. Most likely number of components in the gradient image according to different model comparisons techniques.
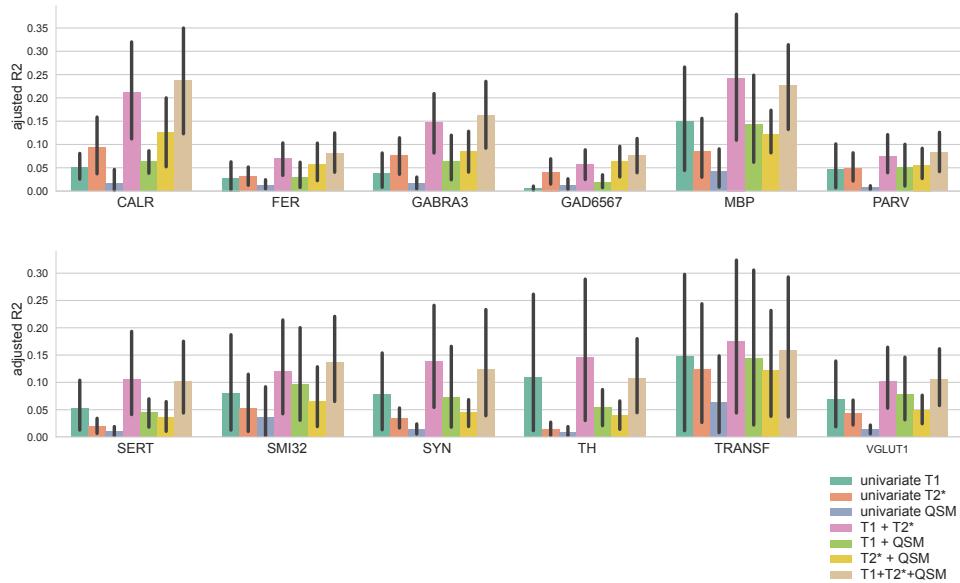
Also for the gradient images, parameter estimates suggested that any possible clusters in gradient size are highly overlapping: approximately 50% of the voxels could not be attributed to a specific component (see Supplementary Fig. 7). This is in line with the hypothesis of "transition zones", where multiple neuronal populations are present, rather than a model where there are hard borders between subsequent subzones (Haynes and Haber, 2013).

Supplementary Figure 7. Proportion of voxels in the gradient images that can be assigned to one specific cluster with more than 95% probability. Error bars indicate 95% bootstrapped confidence interval

MAPPING BETWEEN QMRI AND IMMUNOCYTOCHEMISTRY

When we fitted linear models predicting staining intensities based on qMRI parameters, a linear model including all three parameters showed the highest proportion of explained variance (R^2) of the image intensities, but not meaningfully more than a model including only T_1 and T_2^* estimates (see Supplementary Fig. 8). This suggests that, at least in the STN and using MRI data at a very high resolution, QSM conveys no additional information about the underlying immunocytochemical properties, compared to T_1 and T_2^* alone.

Supplementary Figure 8. R-squared (R^2) of general linear models that predict relative staining intensities for different marker proteins, based on different combinations of T_1, T_2*, and QSM. For many marker proteins, a model including all three qMRI measures can predict relative staining to a relatively high degree, but its performance is similar to a model including only T_1 and T_2*. Error bars indicate bootstrapped 95% confidence interval, based on all 7 specimens.

Appendix B

SUPPLEMENTARY MATERIALS FOR CHAPTER 6

Supplementary Table S1 Frequentist and Bayesian statistics for test whether parameter estimate is different from zero.

protocol	condition	frequentist					BF10			
		1	2	3	3 (n = 5)	4	1	2	3	4
GPe_L	go	t(4) = -1.78, p=.150	t(4) = -1.78, p=.150	t(19) = 6.39, p<.001*	t(4) = 5.27, p=.006*	t(9) = 0.46, p=.655	1.03	0.41	9.94	0.34
	stop_inhibit	t(4) = -1.46, p=.219	t(4) = -1.46, p=.219	t(19) = 4.73, p<.001*	t(4) = 2.68, p=.055	t(9) = 0.58, p=.576	0.8	0.53	2.06	0.36
	stop_respond	t(4) = -1.05, p=.354	t(4) = -1.05, p=.354	t(19) = 6.29, p<.001*	t(4) = 5.46, p=.005*	t(9) = 0.95, p=.368	0.59	0.48	11	0.45
GPe_R	go	t(4) = -3.39, p=.028	t(4) = -3.39, p=.028	t(19) = 4.77, p<.001*	t(4) = 1.77, p=.152	t(9) = 1.09, p=.306	3.4	0.45	1.02	0.5
	stop_inhibit	t(4) = -1.19, p=.300	t(4) = -1.19, p=.300	t(19) = 4.58, p<.001*	t(4) = 2.35, p=.079	t(9) = -1.32, p=.221	0.66	0.58	1.61	0.61
	stop_respond	t(4) = -1.70, p=.165	t(4) = -1.70, p=.165	t(19) = 4.97, p<.001*	t(4) = 2.24, p=.089	t(9) = 1.72, p=.120	0.97	0.41	1.48	0.93
GPi_L	go	t(4) = -1.61, p=.183	t(4) = -1.61, p=.183	t(19) = 4.81, p<.001*	t(4) = 2.37, p=.077	t(9) = 0.04, p=.968	0.9	0.42	1.64	0.31
	stop_inhibit	t(4) = -0.98, p=.384	t(4) = -0.98, p=.384	t(19) = 3.06, p=.006*	t(4) = 2.64, p=.058	t(9) = 0.51, p=.620	0.57	0.5	2.01	0.35
	stop_respond	t(4) = -1.30, p=.264	t(4) = -1.30, p=.264	t(19) = 2.79, p=.012*	t(4) = 1.98, p=.118	t(9) = 1.90, p=.090	0.71	0.47	1.21	1.14
GPi_R	go	t(4) = -1.28, p=.269	t(4) = -1.28, p=.269	t(19) = 4.60, p<.001*	t(4) = 1.62, p=.180	t(9) = 0.45, p=.661	0.7	1.06	0.91	0.34
	stop_inhibit	t(4) = -0.64, p=.557	t(4) = -0.64, p=.557	t(19) = 2.37, p=.029*	t(4) = 2.02, p=.114	t(9) = -0.79, p=.448	0.47	20	1.24	0.4
	stop_respond	t(4) = -1.72, p=.161	t(4) = -1.72, p=.161	t(19) = 4.24, p<.001*	t(4) = 2.15, p=.098	t(9) = 1.09, p=.305	0.98	2.7	1.38	0.5

Supplementary Table S1 (continued)

protocol		frequentist 1	2	3	3 (n = 5)	4	BF10 1	2	3	4
RN_L	go	t(4) = 0.16, p=.878	t(4) = 0.16, p=.878	t(19) = 5.55, p<.001*	t(4) = 3.09, p=.036	t(9) = 0.03, p=.979	0.4	0.46	2.78	0.31
	stop_inhibit	t(4) = -0.06, p=.956	t(4) = -0.06, p=.956	t(19) = 5.89, p<.001*	t(4) = 3.56, p=.024	t(9) = -0.02, p=.982	0.4	0.4	3.81	0.31
	stop_respond	t(4) = 0.04, p=.970	t(4) = 0.04, p=.970	t(19) = 6.16, p<.001*	t(4) = 4.68, p=.009	t(9) = -0.17, p=.869	0.4	0.4	7.33	0.31
RN_R	go	t(4) = 0.18, p=.865	t(4) = 0.18, p=.865	t(19) = 5.88, p<.001*	t(4) = 2.82, p=.048	t(9) = -0.05, p=.964	0.4	0.64	2.28	0.31
	stop_inhibit	t(4) = -0.04, p=.969	t(4) = -0.04, p=.969	t(19) = 5.18, p<.001*	t(4) = 3.32, p=.029	t(9) = -0.56, p=.591	0.4	0.4	3.24	0.35
	stop_respond	t(4) = -1.93, p=.125	t(4) = -1.93, p=.125	t(19) = 6.98, p<.001*	t(4) = 4.21, p=.014	t(9) = 2.79, p=.021	1.17	0.43	5.64	3.45
SN_L	go	t(4) = 1.23, p=.286	t(4) = 1.23, p=.286	t(19) = 4.05, p<.001*	t(4) = 2.20, p=.093	t(9) = -0.34, p=.743	0.68	0.4	1.43	0.32
	stop_inhibit	t(4) = -0.30, p=.782	t(4) = -0.30, p=.782	t(19) = 3.52, p=.002*	t(4) = 3.59, p=.023	t(9) = -0.18, p=.864	0.41	0.41	3.87	0.31
	stop_respond	t(4) = -1.94, p=.125	t(4) = 0.29, p=.784	t(19) = 4.46, p<.001*	t(4) = 2.71, p=.053	t(9) = 0.52, p=.619	1.17	0.41	116	0.35
SN_R	go	t(4) = 0.03, p=.976	t(4) = -1.30, p=.265	t(19) = 4.83, p<.001*	t(4) = 2.05, p=.109	t(9) = -1.07, p=.313	0.4	0.71	241	0.49
	stop_inhibit	t(4) = 0.80, p=.470	t(4) = -0.34, p=.752	t(19) = 4.24, p<.001*	t(4) = 3.10, p=.036	t(9) = -1.27, p=.237	0.51	0.42	75	0.58
	stop_respond	t(4) = -1.03, p=.361	t(4) = -0.68, p=.536	t(19) = 6.17, p<.001*	t(4) = 3.28, p=.030	t(9) = 0.31, p=.761	0.59	0.48	3352	0.32

Supplementary Table S1 (continued)

protocol		frequentist					BF10			
		1	2	3	3 (n = 5)	4	1	2	3	4
STN_L	go	t(4) = 0.94, p=.402	t(4) = -0.96, p=.392	t(19) = 4.54, p<.001*	t(4) = 4.56, p=.010	t(9) = 1.04, p=.327	0.55	0.56	135	0.48
	stop_inhibit	t(4) = 0.35, p=.747	t(4) = -1.77, p=.152	t(19) = 4.54, p<.001*	t(4) = 3.70, p=.021	t(9) = 2.54, p=.032	0.42	1.02	135	2.49
	stop_respond	t(4) = -0.29, p=.786	t(4) = -0.98, p=.385	t(19) = 6.50, p<.001*	t(4) = 24.47, p<.001*	t(9) = 1.25, p=.242	0.41	0.57	6296	0.58
STN_R	go	t(4) = -0.93, p=.404	t(4) = 0.53, p=.624	t(19) = 4.35, p<.001*	t(4) = 3.80, p=.019	t(9) = 4.00, p=.003	0.55	0.45	93	16
	stop_inhibit	t(4) = -0.83, p=.451	t(4) = 0.54, p=.618	t(19) = 3.56, p=.002*	t(4) = 3.77, p=.020	t(9) = 1.78, p=.109	0.52	0.45	19	0.99
	stop_respond	t(4) = -0.46, p=.668	t(4) = 0.71, p=.515	t(19) = 5.03, p<.001*	t(4) = 5.90, p=.004*	t(9) = 2.73, p=.023	0.43	0.49	365	3.17
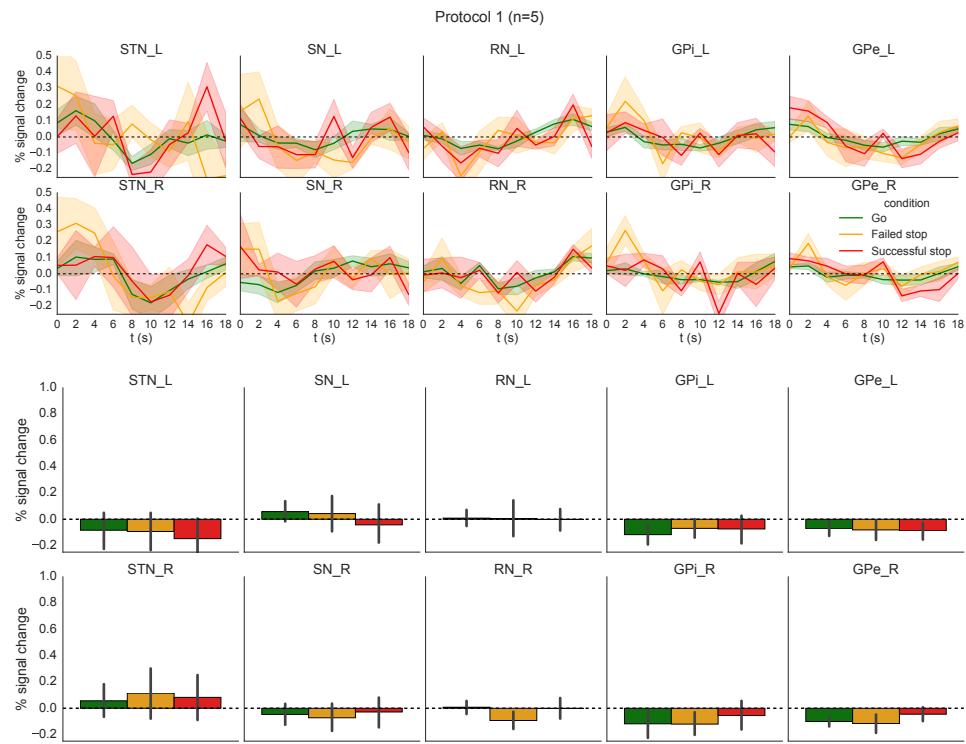
Supplementary Table S2 Frequentist and Bayesian statistics for test whether parameter estimate is different between conditions.

| mask	Protocol contrast	frequentist 1	2	3	3 (n = 5)	4	BF10 1	2	3	3 (n = 5)	4
GPe_L	**stop_inhibit > non_stop**	t(4) = -1.11, p=.329	t(4) = -0.16, p=.879	t(19) = -1.52, p=.144	t(4) = -0.12, p=.908	t(9) = 0.01, p=.995	0.62	0.4	0.63	0.4	0.31
	stop_respond > non_stop	t(4) = -0.67, p=.538	t(4) = -0.08, p=.938	t(19) = 1.40, p=.176	t(4) = 3.48, p=.025*	t(9) = 0.72, p=.487	0.48	0.4	0.54	3.6	0.38
	stop_respond > stop_inhibit	t(4) = 0.72, p=.512	t(4) = 0.18, p=.865	t(19) = 3.36, p=.003*	t(4) = 2.28, p=.085	t(9) = 0.73, p=.487	0.49	0.4	13	1.53	0.39
GPe_R	**stop_inhibit > non_stop**	t(4) = -0.56, p=.604	t(4) = 1.43, p=.227	t(19) = 0.57, p=.577	t(4) = 2.47, p=.069	t(9) = -2.32, p=.046	0.45	0.78	0.27	1.77	1.88
	stop_respond > non_stop	t(4) = 0.11, p=.914	t(4) = -0.21, p=.846	t(19) = 3.08, p=.006*	t(4) = 2.13, p=.100	t(9) = 0.09, p=.927	0.4	0.4	7.63	1.36	0.31
	stop_respond > stop_inhibit	t(4) = 0.42, p=.698	t(4) = -1.80, p=.146	t(19) = 2.58, p=.018*	t(4) = 1.25, p=.278	t(9) = 1.93, p=.085	0.43	1.05	3.12	0.69	1.19
GPi_L	**stop_inhibit > non_stop**	t(4) = 0.57, p=.597	t(4) = 0.57, p=.600	t(19) = -1.13, p=.271	t(4) = 1.73, p=.158	t(9) = 0.94, p=.373	0.45	0.45	0.41	0.99	0.44
	stop_respond > non_stop	t(4) = -1.02, p=.365	t(4) = 0.95, p=.396	t(19) = 0.55, p=.591	t(4) = 1.35, p=.248	t(9) = 2.19, p=.056	0.58	0.56	0.27	0.74	1.62
	stop_respond > stop_inhibit	t(4) = -1.00, p=.373	t(4) = 0.07, p=.948	t(19) = 1.14, p=.267	t(4) = 0.32, p=.768	t(9) = 1.32, p=.219	0.58	0.4	0.41	0.41	0.61
GPi_R	**stop_inhibit > non_stop**	t(4) = -2.08, p=.106	t(4) = 2.50, p=.067	t(19) = -1.42, p=.173	t(4) = 0.29, p=.784	t(9) = -1.30, p=.227	1.31	1.81	0.55	0.41	0.6
	stop_respond > non_stop	t(4) = -1.76, p=.153	t(4) = -0.03, p=.976	t(19) = 0.74, p=.466	t(4) = 1.65, p=.175	t(9) = 1.13, p=.288	1.01	0.4	0.3	0.93	0.52
	stop_respond > stop_inhibit	t(4) = -0.88, p=.428	t(4) = -1.27, p=.275	t(19) = 1.68, p=.110	t(4) = 0.76, p=.489	t(9) = 2.52, p=.033	0.53	0.69	0.76	0.5	2.44

Supplementary Table S2 (continued)
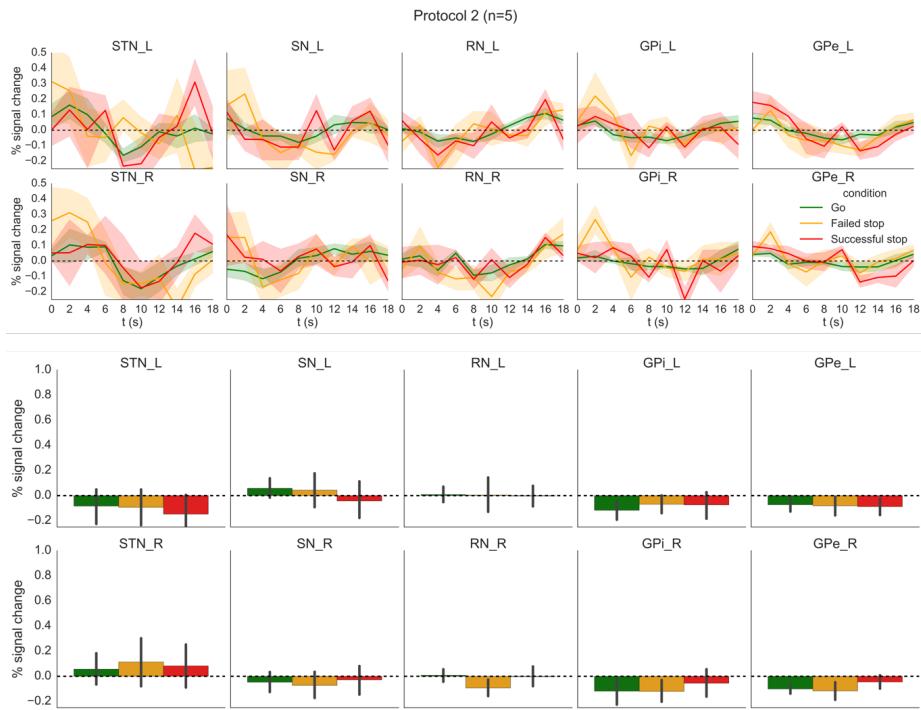
| mask	Protocol contrast	frequentist 1	2	3	3 (n = 5)	4	BF10 1	2	3	3 (n = 5)	4
RN_L	**stop_inhibit > non_stop**	t(4) = -0.30, p=.782	t(4) = -0.22, p=.837	t(19) = 1.57, p=.132	t(4) = 2.22, p=.090	t(9) = -0.07, p=.946	0.41	0.41	0.67	1.46	0.31
	stop_respond > non_stop	t(4) = -0.41, p=.703	t(4) = -0.03, p=.980	t(19) = 4.66, p<.001*	t(4) = 5.68, p=.005*	t(9) = -0.24, p=.815	0.43	0.4	173	12	0.32
	stop_respond > stop_inhibit	t(4) = -0.20, p=.851	t(4) = 0.08, p=.938	t(19) = 2.38, p=.028*	t(4) -0.05, p=.959	t(9) = -0.13, p=.897	0.4	0.4	2.2	0.4	0.31
RN_R	**stop_inhibit > non_stop**	t(4) = -0.98, p=.382	t(4) = -0.28, p=.790	t(19) = 1.16, p=.260	t(4) = 2.93, p=.043	t(9) = -0.55, p=.595	0.57	0.41	0.42	2.47	0.35
	stop_respond > non_stop	t(4) = -1.30, p=.263	t(4) = -1.40, p=.234	t(19) = 5.22, p<.001*	t(4) = 3.42, p=.027*	t(9) = 2.52, p=.033	0.71	0.77	531	3.47	2.43
	stop_respond > stop_inhibit	t(4) = -0.69, p=.530	t(4) = -1.25, p=.279	t(19) = 3.70, p=.002*	t(4) = -0.09, p=.933	t(9) = 3.65, p=.005*	0.48	0.69	25	0.4	10
SN_L	**stop_inhibit > non_stop**	t(4) = -0.14, p=.896	t(4) = -0.83, p=.454	t(19) = 0.83, p=.416	t(4) = 1.57, p=.190	t(9) = 0.29, p=.779	0.4	0.52	0.32	0.88	0.32
	stop_respond > non_stop	t(4) = -1.04, p=.357	t(4) = -0.09, p=.934	t(19) = 3.26, p=.004*	t(4) = 2.65, p=.057	t(9) = 1.50, p=.168	0.59	0.4	11	2.02	0.73
	stop_respond > stop_inhibit	t(4) = -0.90, p=.419	t(4) = 0.38, p=.726	t(19) = 1.93, p=.069	t(4) = -0.06, p=.955	t(9) = 0.88, p=.400	0.54	0.42	1.08	0.4	0.43
SN_R	**stop_inhibit > non_stop**	t(4) = 0.84, p=.450	t(4) = 0.21, p=.843	t(19) = 1.26, p=.224	t(4) = 1.71, p=.163	t(9) = -0.86, p=.410	0.52	0.4	0.46	0.98	0.42
	stop_respond > non_stop	t(4) = -0.74, p=.499	t(4) = -0.32, p=.765	t(19) = 5.72, p<.001*	t(4) = 3.56, p=.024*	t(9) = 1.42, p=.188	0.49	0.41	1423	3.8	0.68
	stop_respond > stop_inhibit	t(4) = -1.63, p=.178	t(4) = -0.39, p=.718	t(19) = 2.38, p=.028*	t(4) = 0.30, p=.778	t(9) = 2.24, p=.052	0.92	0.42	2.19	0.41	1.72

Supplementary Table S2 (continued)
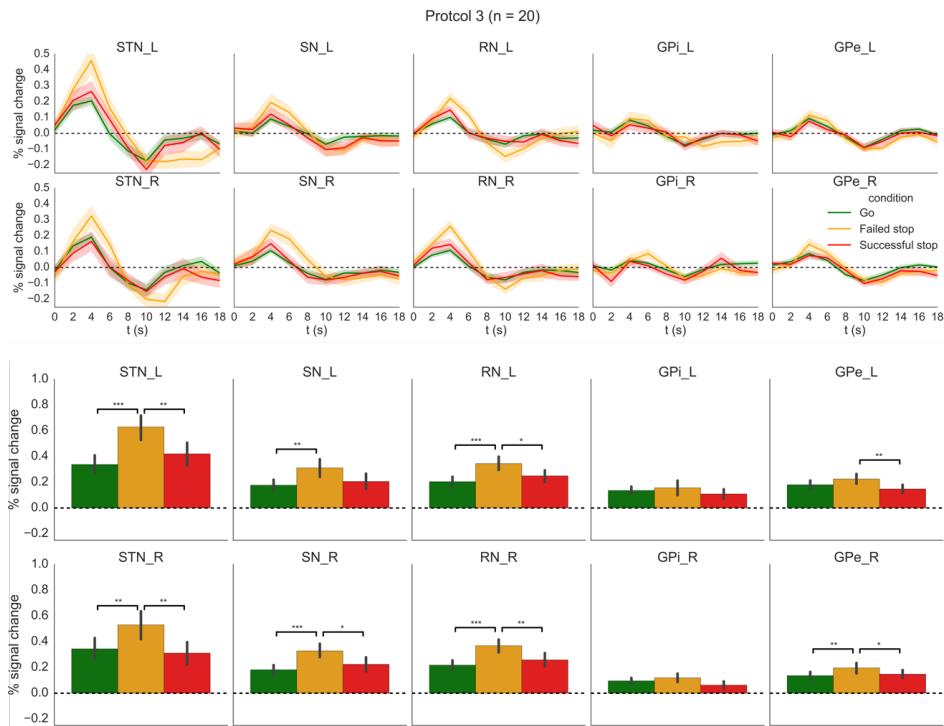
| mask	Protocol contrast	frequentist 1	2	3	3 (n = 5)	4	BF10 1	2	3	3 (n = 5)	4
STN_L	stop_inhibit > non_stop	t(4) = -0.35, p=.747	t(4) = -0.63, p=.564	t(19) = 1.48, p=.154	t(4) = 1.25, p=.278	t(9) = 1.79, p=.108	0.42	0.47	0.6	0.69	1
	stop_respond > non_stop	t(4) = -1.07, p=.344	t(4) = -0.08, p=.939	t(19) = 4.29, p<.001*	t(4) = 8.33, p=.001*	t(9) = 1.09, p=.305	0.6	0.4	82	34	0.5
	stop_respond > stop_inhibit	t(4) = -3.68, p=.021	t(4) = 0.51, p=.637	t(19) = 2.95, p=.008*	t(4) = 1.09, p=.337	t(9) = -0.79, p=.447	4.09	0.44	6.05	0.61	0.4
STN_R	stop_inhibit > non_stop	t(4) = -0.64, p=.558	t(4) = 0.34, p=.754	t(19) = -0.87, p=.394	t(4) = 0.42, p=.696	t(9) = -0.73, p=.481	0.47	0.42	0.33	0.43	0.39
	stop_respond > non_stop	t(4) = 0.28, p=.796	t(4) = 0.31, p=.769	t(19) = 3.35, p=.003*	t(4) = 9.17, p=.001*	t(9) = -1.75, p=.114	0.41	0.41	13	45	0.96
	stop_respond > stop_inhibit	t(4) = 0.70, p=.525	t(4) = 0.20, p=.851	t(19) = 3.18, p=.005*	t(4) = 2.11, p=.102	t(9) = -0.03, p=.976	0.48	0.4	9.23	1.34	0.31
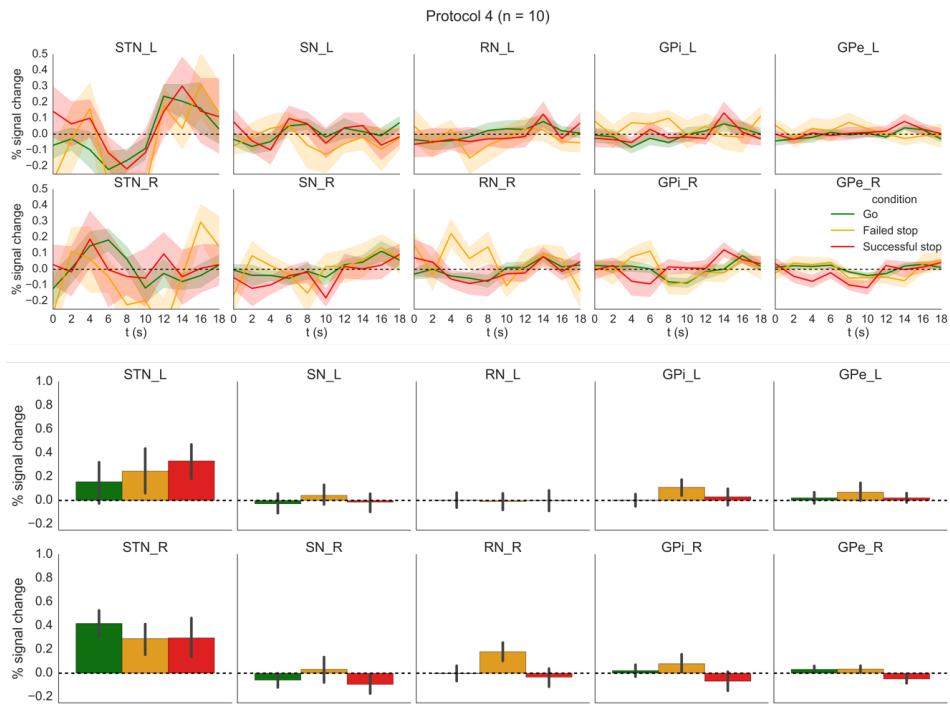
Supplementary Figure 1. Raw task-locked mean time series (top) and corresponding GLM parameter estimates (bottom) for protocol 1. Shaded area and error bars indicate 67% bootstrapped confidence interval. Green corresponds to go trials, orange to failed stop trials, and red to successful stop trials.

Supplementary Figure 2. Raw task-locked mean time series (top) and corresponding GLM parameter estimates (bottom) for protocol 2. Shaded area and error bars indicate 67% bootstrapped confidence interval. Green corresponds to go trials, orange to failed stop trials, and red to successful stop trials.

Supplementary Figure 3. Raw task-locked mean time series (top) and corresponding GLM parameter estimates (bottom) for protocol 3. Shaded area and error bars indicate 67% bootstrapped confidence interval. Green corresponds to go trials, orange to failed stop trials, and red to successful stop trials. * =p < 0.05, ** = p< 0.01, ** = p<0.001

Supplementary Figure 4. Raw task-locked mean time series (top) and corresponding GLM parameter estimates (bottom) for protocol 4. Shaded area and error bars indicate 67% bootstrapped confidence interval. Green corresponds to go trials, orange to failed stop trials, and red to successful stop trials.

Appendix C

SUPPLEMENTARY MATERIALS FOR CHAPTER 8

BEHAVIORAL DDM MODEL FITS

Fifteen versions of the DDM were fit to the data and quantitatively compared using the DIC, which are presented in Supplementary Table S1. The group parameter posteriors of the winning model are presented in Supplementary Table S2.
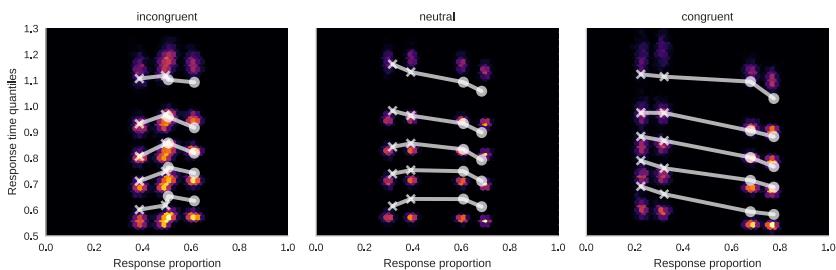
Plotting the empirical response time quantiles against the posterior predictive quantiles of the winning model shows that this model fits the empirical data adequately (Figure S1). However, the fastest quantiles of the RT distributions are slightly overestimated and the slowest quantiles slightly underestimated. Importantly, the time difference between the last two empirical response time quantiles is not much bigger than the difference between earlier quantiles, for both correct and error trials. This is an unusual pattern for response time distributions (Luce, 1986), which tend to have long extending tails (large skewness), but similar patterns have been reported before in paradigms with high time-pressure and are considered a hallmark of an "urgency" signal (Noorbaloochi et al., 2015; Boehm et al., 2016; de Hollander, 2016). The limited skewness is probably reflected in an unusually large value for across-trial variability in non-decision time (st; approximately 0.5s; see Table S2). Large values for this parameter effectively result in a convolution of the DDM RT distribution with a uniform distribution, making the resulting distribution more normal and less-skewed. We would argue that an "urgency model" could account for these more precisely, and might be a better "process model" (Lewandowsky and Farrell, 2010). However, since the goal here was to quantify inter- and interindividual differences in the integration of prior information and susceptibility to degraded stimulus information, we consider the DDM is an adequate "measurement model".

Supplementary Table S1: Deviance Information Criterion (DIC) for 12 different HDDM models: models with a lower DIC better account for the data, penalizing for the number of parameters. Sv: across-variability in drift rate; sz: across-trial variability in start point; st: across-trial variability in non-decision time.

across-trial variability bias manipulation	DIC				
	none	sv	sz	sv and sz	sv, sz, st
drift	8966	8895	8967	8893	5501
startpoint	9098	9029	9097	9027	5462
both	8903	8824	8904	8823	5437

Table S2: Mean and interquartile ranges of group posteriors of main parameters of DDM; a: threshold; v: drift rate; t: non-decision-time; z: start point of accumulation; sv: across-trial variability in drift rate; sz: across trial variability in start point; st: across-trial variability in non-decision time.

	Mean	25%	50%	75%
a	1.019	0.986	1.017	1.049
v (easy)	1.171	1.026	1.166	1.315
v (hard)	0.56	0.397	0.556	0.723
t	0.611	0.593	0.611	0.629
z (congruent)	0.581	0.553	0.579	0.607
z (incongruent)	0.438	0.414	0.437	0.461
sv	1.025	0.945	1.026	1.106
sz	0.082	0.041	0.079	0.118
st	0.503	0.496	0.503	0.51

Supplementary Figure 1. Empirical RT quantiles overlaid on posterior predictive distributions generated by the full HDDM**.** The x-axis of this plot corresponds to the proportion of responses, and the y-axis corresponds to response time quantiles. The 5 white lines indicate 0.1, 0.3, 0.5, 0.7, and 0.9 RT quantiles. The four x-values per line correspond to easy error responses, hard error responses, hard correct responses, and easy correct responses. Crosses indicate erroneous responses, whereas circles indicate correct responses. Underlying intensity values correspond to posterior predictive mass. Larger overlap between empirical (white crosses and dots) and predicted (colored posterior predictive mass) means better model fit. These model fits are, in our opinion, adequate for the goal at hand (quantify intra- and interindividual differences in behavior), but the response time of fast correct responses are slightly underestimated, whereas the slowest responses are slightly overestimated.

# REGRESSION DDM USING TRIAL–WISE FMRI REGRESSORS: THE PROBLEM OF COLLINEARITY
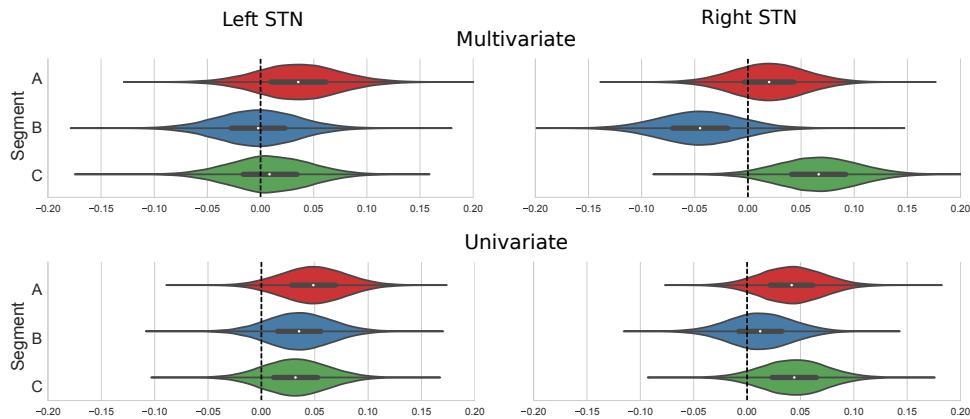
Originally, we planned to estimate a single model that included trial-to-trial BOLD estimates for all three STN segments in a hemisphere. For example, for the left hemisphere:

$$z(t) = 0.5\, b + cue(t){:}\, z_{congruency} + cue(t){:}\, z_{bold,STN\_L\_A} * BOLD_{STN_{L_A},cue}(t)$$
$$+ cue(t){:}\, z_{bold,STN\_L\_B} * BOLD_{STN\_L\_B,cue}(t) + cue(t){:}\, z_{bold,STN\_L\_C}$$
$$* BOLD_{STN\_L\_C,cue}(t)$$
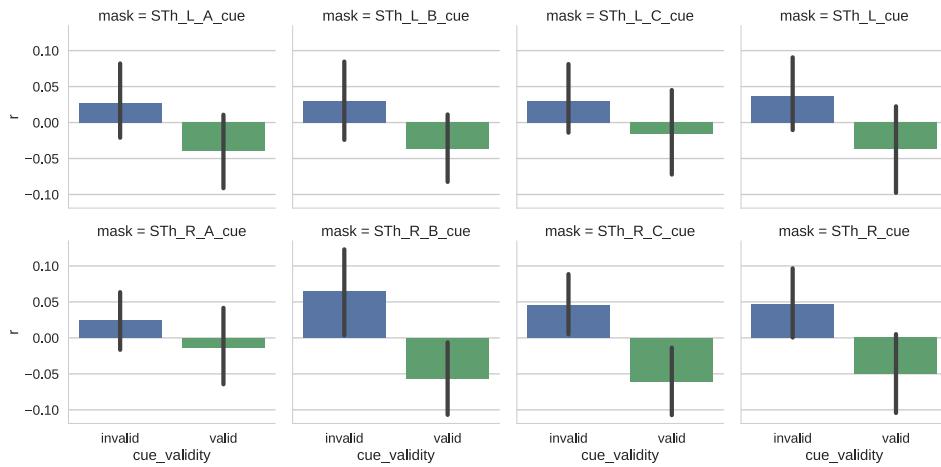
The inclusion of all three segments per hemisphere in the same model would be useful, because it allows to sample from the posterior of the *difference* of the regression slopes of two segments, marginalized over all other parameters, rather than comparing the posteriors of two separate models, which were sampled independently. However, due to very high collinearity of the BOLD signal in the three segments, such a model turned out to be infeasible.

When fitting this 'multivariate' regression HDDM including single trial BOLD estimates of all three segments, left STN activity was marginally predictive of trial-to-trial variability in start point shifts: 82% of the posterior mass of the slope of segment A was larger than 0, for segment B this was 48%, and for segment C it was 59% (see Figure S2, top). For the right STN, an unexpected pattern was found: the slopes of segment A (71%) and segment C (96%) were positive, whereas the slope of segment B was negative (12% of the slope posterior mass was larger than 0; also see Figure S2, top). This second result is counter-intuitive and we feared it might be an artefact. Note that in general linear models, different regressors are assumed to be independent. However, the single trial BOLD amplitude estimates of the three different segments are highly correlated (with a correlation of approximately 0.43 – 0.56). Ignoring this correlation between different regressors (i.e., segments) could potentially lead to inaccurate model estimates (Bishop, 2006; see e.g. Turner et al., 2013 for an approach that does model covariance in the neural data). Therefore, we also fitted models for each segment separately, where start point shifts toward the cued bound are predicted only by one specific segment at a time. This model resulted in more credible parameter estimates (Figure S2; bottom row).

A post-hoc model-free analysis aligned with the pattern observed in the univariate, rather than the multivariate model: for all segments in the right STN, averaged over subjects, cue-related STN activity was *positively* correlated with RT on trials with incongruent cues, whereas it was *negatively* correlated with RT on trials with a congruent cue (see figure S3). This pattern did not reverse for segment B of the right STN, like it did in the multivariate HDDM parameter estimates. This strengthens the belief that the multivariate model leads to invalid inference, because it fails to model covariance between different neural measures and thus we only present results of the univariate model in the main text.

Supplementary Figure S2. Estimated posterior distributions for the group slope parameter of the trial-to-trial variability BOLD activity, regressed on the *start point* in the HDDM. The top row visualizes the posteriors for the slopes of segment A, B, and C for left and right STN, when the slopes of the three segments are fit together in a single *multivariate* model. The negative slope for segment B is probably an artefact of the failure of the model to account for covariance between neural sources, since model-free analysis of the correlation between BOLD amplitudes and RT does not predict this pattern. The bottom row illustrates the same posteriors, but now for separate "univariate" models where only one segment is included. Note that the negative slope for Segment B is now estimated to be positive.

Supplementary Figure S3: Correlation coefficient between trial-to-trial cue-locked BOLD amplitude and reaction time for invalid and valid trials, averaged across subjects. Error bars are bootstrapped 95% confidence intervals.

REFERENCES

Aarts E, Verhage M, Veenvliet JV, Dolan CV, van der Sluis S (2014) A solution to dependency: using multilevel analysis to accommodate nested data. Nat Neurosci 17:491–496.

Abdul-Rahman HS, Gdeisat MA, Burton DR, Lalor MJ, Lilley F, Moore CJ (2007) Fast and robust three-dimensional best path phase unwrapping algorithm. Appl Opt 46:6623–6635.

Accolla EA, Dukart J, Helms G, Weiskopf N, Kherif F, Lutti A, Chowdhury R, Hetzer S, Haynes J-D, Kühn AA, Draganski B (2014) Brain tissue properties differentiate between motor and limbic basal ganglia circuits. Human Brain Mapping 35:5083–5092.

Accolla EA, Herrojo Ruiz M, Horn A, Schneider G-H, Schmitz-Hübsch T, Draganski B, Kühn AA (2016) Brain networks modulated by subthalamic nucleus deep brain stimulation. Brain 139:2503–2515.

Addis RC, Hsu F-C, Wright RL, Dichter MA, Coulter DA, Gearhart JD (2011) Efficient Conversion of Astrocytes to Functional Midbrain Dopaminergic Neurons Using a Single Polycistronic Vector Muotri AR, ed. PLoS ONE 6:e28719.

Akaike H (1974) A new look at the statistical model identification. IEEE transactions on automatic control 19:716–723.

Alexander GE, Crutcher MD (1990) Functional architecture of basal ganglia circuits: neural substrates of parallel processing. Trends in Neurosciences 13:266–271.

Alexander GE, Crutcher MD, DeLong MR (1991) Basal ganglia-thalamocortical circuits: parallel substrates for motor, oculomotor,"prefrontal" and 'limbic' functions. Progress in brain research 85:119–146.

Alexander GE, DeLong MR, Strick PL (1986) Parallel organization of functionally segregated circuits linking basal ganglia and cortex. Annu Rev Neurosci 9:357–381.

Alexander WH, Brown JW (2011) Medial prefrontal cortex as an action-outcome predictor. Nature Neuroscience 14:1338–1344.

Alkemade A (2013) Subdivisions and anatomical boundaries of the subthalamic nucleus. The Journal of Neuroscience 33:9233–9234.

Alkemade A, Forstmann BU (2014) Do we need to revise the tripartite subdivision hypothesis of the human subthalamic nucleus (STN)? NeuroImage 95:326–329.

Alkemade A, Friesema EC, Unmehopa UA, Fabriek BO, Kuiper GG, Leonard JL, Wiersinga WM, Swaab DF, Visser TJ, Fliers E (2005a) Neuroanatomical Pathways for Thyroid Hormone Feedback in the Human Hypothalamus. J Clin Endocrinol Metab 90:4322–4334.

Alkemade A, Keuken MC, Forstmann BU (2013) A perspective on terra incognita: uncovering the neuroanatomy of the human subcortex. Front Neuroanat 7:40.

Alkemade A, Schnitzler A, Forstmann BU (2015) Topographic organization of the human and non-human primate subthalamic nucleus. Brain Struct Funct 220:3075–3086.

Alkemade A, Unmehopa UA, Hessel EVS, Swaab DF, Kalsbeek A, Fliers E (2012a) Suppressor of cytokine signaling 3 in the human hypothalamus. Peptides 35:139–142.

Alkemade A, Vuijst CL, Unmehopa UA, Bakker O, Vennström B, Wiersinga WM, Swaab DF, Fliers E (2005b) Thyroid Hormone Receptor Expression in the Human Hypothalamus and Anterior Pituitary. J Clin Endocrinol Metab 90:904–912.

Alkemade A, Yi C-X, Pei L, Harakalova M, Swaab DF, la Fleur SE, Fliers E, Kalsbeek A (2012b) AgRP and NPY expression in the human hypothalamic infundibular nucleus correlate with body mass index, whereas changes in αMSH are related to type 2 diabetes. J Clin Endocrinol Metab 97:E925–E933.

Amunts K, Lepage C, Borgeat L, Mohlberg H, Dickscheid T, Rousseau M-É, Bludau S, Bazin P-L, Lewis LB, Oros-Peusquens A-M, Shah NJ, Lippert T, Zilles K, Evans AC (2013) BigBrain: an ultrahigh-resolution 3D human brain model. Science 340:1472–1475.

Amunts K, Zilles K (2015) Architectonic Mapping of the Human Brain beyond Brodmann. Neuron 88:1086–1107.

Ances BM, Leontiev O, Perthen JE, Liang C, Lansing AE, Buxton RB (2008) Regional differences in the coupling of cerebral blood flow and oxygen metabolism changes in response to activation:

Implications for BOLD-fMRI. NeuroImage 39:1510–1521.

Anderson JR (1992) Automaticity and the ACT* Theory. American Journal of Psychology 105.

Anderson JR (2007) How can the human mind occur in the physical universe? New York, NY, USA: Oxford University Press.

Anderson JR (2012) Tracking problem solving by multivariate pattern analysis and Hidden Markov Model algorithms. Neuropsychologia 50:487–498.

Anderson JR, Betts S, Ferris JL, Fincham JM (2010) Cognitive and metacognitive activity in mathematical problem solving: prefrontal and parietal patterns. Cognitive, Affective, & Behavioral Neuroscience 11:52–67.

Andrioli A, Alonso-Nanclares L, Arellano JI, DeFelipe J (2007) Quantitative analysis of parvalbumin-immunoreactive cells in the human epileptic hippocampus. Neuroscience 149:131–143.

Aquino D, Bizzi A, Grisoli M, Garavaglia B, Bruzzone MG, Nardocci N, Savoiardo M, Chiapparini L (2009) Age-related iron deposition in the basal ganglia: quantitative analysis in healthy subjects. Radiology 252:165–172.

Arendt D (2008) The evolution of cell types in animals: emerging principles from molecular studies. Nature Reviews Genetics 9:868–882.

Arlot S, Celisse A (2010) A survey of cross-validation procedures for model selection. Statist Surv 4:40–79.

Aron AR (2004) Human Midbrain Sensitivity to Cognitive Feedback and Uncertainty During Classification Learning. Journal of Neurophysiology 92:1144–1152.

Aron AR (2007) The Neural Basis of Inhibition in Cognitive Control. The Neuroscientist 13:214–228.

Aron AR (2011) From reactive to proactive and selective control: developing a richer model for stopping inappropriate responses. Biol Psychiatry 69:e55–e68.

Aron AR, Behrens TE, Smith S, Frank MJ, Poldrack RA (2007) Triangulating a Cognitive Control Network Using Diffusion-Weighted Magnetic Resonance Imaging (MRI) and Functional MRI. The Journal of Neuroscience 27:3743–3752.

Aron AR, Cai W, Badre D, Robbins TW (2015) Evidence Supports Specific Braking Function for Inferior PFC. Trends in Cognitive Sciences 19:711–712.

Aron AR, Herz DM, Brown P, Forstmann BU, Zaghloul K (2016) Frontosubthalamic Circuits for Control of Action and Cognition. The Journal of Neuroscience 36:11489–11495.

Aron AR, Poldrack RA (2006) Cortical and subcortical contributions to Stop signal response inhibition: role of the subthalamic nucleus. The Journal of Neuroscience 26:2424–2433.

Aron AR, Robbins TW, Poldrack RA (2014a) Inhibition and the right inferior frontal cortex: one decade on. Trends in Cognitive Sciences 18:177–185.

Aron AR, Robbins TW, Poldrack RA (2014b) Right inferior frontal cortex: addressing the rebuttals. Front Hum Neurosci 8:905.

Arsenault JT, Rima S, Stemmann H, Vanduffel W (2014) Role of the primate ventral tegmental area in reinforcement and motivation. Curr Biol 24:1347–1353.

Ashburner J, Friston K (1997) Multimodal image coregistration and partitioning—a unified framework. NeuroImage 6:209–217.

Avants B, Tustison N, Johnson H (2014) Advanced Normalization Tools (ANTS).

Avants BB, Tustison N, Song G (2009) Advanced normalization tools (ANTS). Insight J 2:1–35.

Azevedo FAC, Carvalho LRB, Grinberg LT, Farfel JM, Ferretti REL, Leite REP, Filho WJ, Lent R, Herculano-Houzel S (2009) Equal numbers of neuronal and nonneuronal cells make the human brain an isometrically scaled-up primate brain. J Comp Neurol 513:532–541.

Baecke S, Lützkendorf R, Mallow J, Luchtmann M, Tempelmann C, Stadler J, Bernarding J (2015) A proof-of-principle study of multi-site real-time functional imaging at 3T and 7T: Implementation and validation. Scientific Reports 5:8413.

Bar-Peled O, Ben Hur H, Biegon A, Groner Y, Dewhurst S, Furuta A, Rothstein JD (1997) Distribution of

glutamate transporter subtypes during human brain development. Journal of neurochemistry 69:2571–2580.

Barry RL, Coaster M, Rogers BP, Newton AT, Moore J, Anderson AW, Zald DH, Gore JC (2013) On the Origins of Signal Variance in FMRI of the Human Midbrain at High Field Yacoub E, ed. PLoS ONE 8:e62708.

Barry RL, Strother SC, Gatenby JC, Gore JC (2011) Data-driven optimization and evaluation of 2D EPI and 3D PRESTO for BOLD fMRI at 7 Tesla: I. Focal coverage. NeuroImage 55:1034–1043.

Baudrexel S, Witte T, Seifried C, Wegner von F, Beissner F, Klein JC, Steinmetz H, Deichmann R, Roeper J, Hilker R (2011) Resting state fMRI reveals increased subthalamic nucleus–motor cortex connectivity in Parkinson's disease. NeuroImage 55:1728–1738.

Bauman AL, Apparsundaram S, Ramamoorthy S, Wadzinski BE, Vaughan RA, Blakely RD (2000) Cocaine and antidepressant-sensitive biogenic amine transporters exist in regulated complexes with protein phosphatase 2A. The Journal of Neuroscience 20:7571–7578.

Bazin P-L, Cuzzocreo JL, Yassa MA, Gandler W, McAuliffe MJ, Bassett SS, Pham DL (2007) Volumetric neuroimage analysis extensions for the MIPAV software package. Journal of Neuroscience Methods 165:111–121.

Beauregard M, Lévesque J (2006) Functional Magnetic Resonance Imaging Investigation of the Effects of Neurofeedback Training on the Neural Bases of Selective Attention and Response Inhibition in Children with Attention-Deficit/Hyperactivity Disorder. Appl Psychophysiol Biofeedback 31:3–20.

Behrens TE, Sporns O (2012) Human connectomics. Current Opinion in Neurobiology 22:144–153.

Benveniste H, Kim K, Zhang L, Johnson GA (2000) Magnetic Resonance Microscopy of the C57BL Mouse Brain. NeuroImage 11:601–611.

Berns GS, McClure SM, Pagnoni G, Montague PR (2001) Predictability modulates human brain response to reward. The Journal of Neuroscience 21:2793–2798.

Bhatia KP, Marsden CD (1994) The behavioural and motor consequences of focal lesions of the basal ganglia in man. Brain 117:859–876.

Bishop CM (2006) Pattern Recognition and Machine Learning (Information Science and Statistics). Secaucus, NJ, USA: Springer-Verlag New York, Inc.

Boecker H, Jankowski J, Ditter P, Scheef L (2008) A role of the basal ganglia and midbrain nuclei for initiation of motor sequences. NeuroImage 39:1356–1369.

Boehler CN, Bunzeck N, Krebs RM, Noesselt T, Schoenfeld MA, Heinze H-J, Münte TF, Woldorff MG, Hopf J-M (2011a) Substantia Nigra Activity Level Predicts Trial-to-Trial Adjustments in Cognitive Control. Journal of Cognitive Neuroscience 23:362–373.

Boehler CN, Hopf JM, Krebs RM, Stoppel CM, Schoenfeld MA, Heinze HJ, Noesselt T (2011b) Task-Load-Dependent Activation of Dopaminergic Midbrain Areas in the Absence of Reward. The Journal of Neuroscience 31:4955–4961.

Boehm U, Hawkins GE, Brown S, van Rijn H, Wagenmakers E-J (2016) Of monkeys and men: Impatience in perceptual decision-making. Psychon Bull Rev 23:738–749.

Bogacz R, Gurney K (2007) The basal ganglia and cortex implement optimal decision making between alternative actions. Neural Comput 19:442–477.

Bogacz R, Usher M, Zhang J, McClelland JL (2007) Extending a biologically inspired model of choice: multi-alternatives, nonlinearity and value-based multidimensional choice. Philosophical Transactions of the Royal Society B: Biological Sciences 362:1655–1670.

Bogacz R, Wagenmakers E-J, Forstmann BU, Nieuwenhuis S (2010) The neural basis of the speed–accuracy tradeoff. Trends in Neurosciences 33:10–16.

Bonin von G, Shariff GA (1951) Extrapyramidal nuclei among mammals. A quantitative study. Journal of comparative Neurology 94:427–438.

Bookstein FL (1989) Principal warps: Thin-plate splines and the decomposition of deformations. IEEE Transactions on pattern analysis and machine intelligence 11:567–585.

Borgers AJ, Koopman KE, Bisschop PH, Serlie MJ, Swaab DF, Fliers E, la Fleur SE, Alkemade A (2014) Decreased serotonin transporter immunoreactivity in the human hypothalamic infundibular nucleus of overweight subjects. Front Neurosci 8:106.

Borst JP, Taatgen NA, Stocco A, van Rijn H (2010) The Neural Correlates of Problem States: Testing fMRI Predictions of a Computational Model of Multitasking Harrison BJ, ed. PLoS ONE 5:e12966.

Borst JP, Taatgen NA, van Rijn H (2011) Using a symbolic process model as input for model-based fMRI analysis: Locating the neural correlates of problem state replacements. NeuroImage 58:137–147.

Boyacioğlu R, Schulz J, Koopmans PJ, Barth M, Norris DG (2015) Improved sensitivity and specificity for resting state and task fMRI with multiband multi-echo EPI compared to multi-echo EPI at 7T. NeuroImage 119:352–361.

Bragina L, Marchionni I, Omrani A, Cozzi A, Pellegrini-Giampietro DE, Cherubini E, Conti F (2008) GAT-1 regulates both tonic and phasic GABA Areceptor-mediated inhibition in the cerebral cortex. Journal of neurochemistry 105:1781–1793.

Brett M, Taylor J, Burns C, Millman KJ, Perez F, Roche A, Thirion B, D'Esposito M (2009) NIPY: an open library and development framework for FMRI data analysis. NeuroImage 47:S196.

Brisch R, Saniotis A, Wolf R, Bielau H, Bernstein H-G, Steiner J, Bogerts B, Braun K, Braun AK, Jankowski Z, Kumaratilake J, Kumaritlake J, Henneberg M, Gos T (2014) The role of dopamine in schizophrenia from a neurobiological and evolutionary perspective: old fashioned, but still in vogue. Front Psychiatry 5:47.

Britten KH, Shadlen MN, Newsome WT, Movshon JA (1992) The analysis of visual motion: a comparison of neuronal and psychophysical performance. The Journal of Neuroscience 12:4745–4765.

Brodmann K (1909) Vergleichende Lokalisationslehre der Groshirnrinde. Leipzig: Barth.

Bronstein JM et al. (2011) Deep brain stimulation for Parkinson disease: an expert consensus and review of key issues. In, pp 165.

Brown SD, Heathcote A (2008) The simplest complete model of choice response time: Linear ballistic accumulation. Cognitive Psychology 57:153–178.

Brownlees J, Yates A, Bajaj NP, Davis D, Anderton BH, Leigh PN, Shaw CE, Miller CC (2000) Phosphorylation of neurofilament heavy chain side-arms by stress activated protein kinase-1b/Jun N-terminal kinase-3. J Cell Sci 113 (Pt 3):401–407.

Brunenberg EJL, Moeskops P, Backes WH, Pollo C, Cammoun L, Vilanova A, Janssen MLF, Visser-Vandewalle VERM, Haar Romeny ter BM, Thiran J-P, Platel B (2012) Structural and Resting State Functional Connectivity of the Subthalamic Nucleus: Identification of Motor STN Parts and the Hyperdirect Pathway Jiang T, ed. PLoS ONE 7:e39061.

Brydon L, Harrison NA, Walker C, Steptoe A, Critchley HD (2008) Peripheral Inflammation is Associated with Altered Substantia Nigra Activity and Psychomotor Slowing in Humans. Biol Psychiatry 63:1022–1029.

Budd JML, Kisvárday ZF (2012) Communication and wiring in the cortical connectome. Front Neuroanat 6:42.

Budde J, Shajan G, Zaitsev M, Scheffler K, Pohmann R (2013) Functional MRI in human subjects with gradient-echo and spin-echo EPI at 9.4 T. Magnetic Resonance Medicine 71:209–218.

Bunzeck N, Düzel E (2006) Absolute Coding of Stimulus Novelty in the Human Substantia Nigra/VTA. Neuron 51:369–379.

Bunzeck N, Schutze H, Stallforth S, Kaufmann J, Duzel S, Heinze HJ, Duzel E (2007) Mesolimbic Novelty Processing in Older Adults. Cerebral Cortex 17:2940–2948.

Butson CR, Cooper SE, Henderson JM, Wolgamuth B, McIntyre CC (2011) Probabilistic analysis of activation volumes generated during deep brain stimulation. NeuroImage 54:2096–2104.

Cabezas M, Oliver A, Lladó X, Freixenet J, Cuadra MB (2011) A review of atlas-based segmentation for magnetic resonance brain images. Computer Methods and Programs in Biomedicine 104:e158–e177.

Cai W, Ryali S, Chen T, Li CSR, Menon V (2014) Dissociable Roles of Right Inferior Frontal Cortex and Anterior Insula in Inhibitory Control: Evidence from Intrinsic and Task-Related Functional Parcellation, Connectivity, and Response Profile Analyses across Multiple Datasets. The Journal of Neuroscience 34:14652–14667.

Calamante F, Oh S-H, Tournier J-D, Park S-Y, Son Y-D, Chung J-Y, Chi J-G, Jackson GD, Park C-W, Kim Y-B, Connelly A, Cho Z-H (2013) Super-resolution track-density imaging of thalamic substructures: comparison with high-resolution anatomical magnetic resonance imaging at 7.0T. Human Brain Mapping 34:2538–2548.

Candela L, Castelli D, Manghi P, Tani A (2015) Data journals: A survey. J Assn Inf Sci Tec 66:1747–1762.

Carpenter MB, McMasters RE (1964) Lesions of the substantia nigra in the rhesus monkey. Efferent fiber degeneration and behavioral observations. Developmental Dynamics 114:293–319.

Carpenter MB, Peter P (1972) Nigrostriatal and nigrothalamic fibers in the rhesus monkey. Journal of comparative Neurology 144:93–115.

Caspary DM, Hughes LF, Ling LL (2013) Neurobiology of Aging. Neurobiology of Aging 34:1486–1496.

Cavanagh JF, Wiecki TV, Cohen MX, Figueroa CM, Samanta J, Sherman SJ, Frank MJ (2011) Subthalamic nucleus stimulation reverses mediofrontal influence over decision threshold. Nat Neurosci 14:1462–1467.

Chambers CD, Forstmann B, Pruszynski JA (2017) Registered reports at the European Journal of Neuroscience: consolidating and extending peer-reviewed study pre-registration. European Journal of Neuroscience 45:627–628.

Chase HW, Clark L (2010) Gambling Severity Predicts Midbrain Response to Near-Miss Outcomes. The Journal of Neuroscience 30:6180–6187.

Cho Z-H, Min H-K, Oh S-H, Han J-Y, Park C-W, Chi J-G, Kim Y-B, Paek SH, Lozano AM, Lee KH (2010) Direct visualization of deep brain stimulation targets in Parkinson disease with the use of 7-tesla magnetic resonance imaging. Journal of Neurosurgery 113:639–647.

Cho ZH, Kim YB, Han JY, Min HK (2008) New brain atlas—Mapping the human brain in vivo with 7.0 T MRI and comparison with postmortem histology: Will these images change modern medicine? International Journal of Imaging Systems and Technology 18:2–8.

Christen M, Bittlinger M, Walter H, Brugger P, Müller S (2012) Dealing With Side Effects of Deep Brain Stimulation: Lessons Learned From Stimulating the STN. AJOB Neuroscience 3:37–43.

Chu W-S, Furusato B, Wong K, Sesterhenn IA, Mostofi FK, Wei MQ, Zhu Z, Abbondanzo SL, Liang Q (2004) Ultrasound-accelerated formalin fixation of tissue improves morphology, antigen and mRNA preservation. Mod Pathol 18:850–863.

Coenen VA, Honey CR, Hurwitz T, Rahman AA, McMaster J, Bürgel U, Mädler B (2009) Medial forebrain bundle stimulation as a pathophysiological mechanism for hypomania in subthalamic nucleus deep brain stimulation for Parkinson's disease. Neurosurgery 64:1106–14–discussion1114–5.

Colpan ME, Slavin KV (2010) Parkinsonism and Related Disorders. Parkinsonism & Related Disorders 16:398–403.

Contarino MF, Speelman JD, De Bie RM, Schuurman PR, Van Den Munckhof P (2017) Bilateral cerebellorubrothalamic fibers stimulation for essential tremor? Mov Disord 26:1366.

Corlett PR, Aitken MRF, Dickinson A, Shanks DR, Honey GD, Honey RAE, Robbins TW, Bullmore ET, Fletcher PC (2004) Prediction error during retrospective revaluation of causal associations in humans: fMRI evidence in favor of an associative model of learning. Neuron 44:877–888.

Coxon JP, Goble DJ, Van Impe A, De Vos J, Wenderoth N, Swinnen SP (2010) Reduced Basal Ganglia Function When Elderly Switch between Coordinated Movement Patterns. Cerebral Cortex 20:2368–2379.

Coxon JP, Van Impe A, Wenderoth N, Swinnen SP (2012) Aging and Inhibitory Control of Action: Cortico-Subthalamic Connection Strength Predicts Stopping Performance. The Journal of Neuroscience

32:8401–8412.

Cragg SJ, Baufreton J, Xue Y, Bolam JP, Bevan MD (2004) Synaptic release of dopamine in the subthalamic nucleus. European Journal of Neuroscience 20:1788–1802.

Cyron D (2016) Mental Side Effects of Deep Brain Stimulation (DBS) for Movement Disorders: The Futility of Denial. Front Integr Neurosci 10:1722.

D'Arceuil H, de Crespigny A (2007) The effects of brain tissue decomposition on diffusion tensor imaging and tractography. NeuroImage 36:64–68.

D'Arceuil HE, Westmoreland S, de Crespigny AJ (2007) An approach to high resolution diffusion tensor imaging in fixed primate brain. NeuroImage 35:553–565.

Daugherty AM, Haacke EM, Raz N (2015) Striatal Iron Content Predicts Its Shrinkage and Changes in Verbal Working Memory after Two Years in Healthy Adults. The Journal of Neuroscience 35:6731–6743.

Dawe RJ, Bennett DA, Schneider JA, Vasireddi SK, Arfanakis K (2009) Postmortem MRI of human brain hemispheres: T2 relaxation times during formaldehyde fixation. Magnetic Resonance Medicine 61:810–818.

de Hollander G (2016) Combining Computational Models of Cognition and Neural Data to Learn about Mixed Task Strategies. The Journal of Neuroscience 36:1–3.

de Hollander G, Forstmann BU, Brown SD (2016) Different Ways of Linking Behavioral and Neural data via Computational Cognitive Models. Biological Psychiatry: CNNI 1:101–109.

de Hollander G, Keuken MC, Bazin P-L, Weiss M, Neumann J, Reimann K, Wähnert M, Turner R, Forstmann BU, Schäfer A (2014a) A gradual increase of iron toward the medial-inferior tip of the subthalamic nucleus. Human Brain Mapping 35:4440–4449.

de Hollander G, Keuken MC, Forstmann BU (2015) The subcortical cocktail problem; mixed signals from the subthalamic nucleus and substantia nigra. PLoS ONE.

de Hollander G, Keuken MC, van der Zwaag W, Forstmann BU, Trampel R (2017) Comparing functional MRI protocols for small, iron-rich basal ganglia nuclei such as the subthalamic nucleus at 7 T and 3 T. Human Brain Mapping 38:3226–3248.

de Hollander G, Wagenmakers E-J, Waldorp L (2014b) An antidote to the imager's fallacy, or how to identify brain areas that are in limbo. PLoS ONE.

de Koning PP, Figee M, Van Den Munckhof P, Schuurman PR, Denys D (2011) Current Status of Deep Brain Stimulation for Obsessive-Compulsive Disorder: A Clinical Review of Different Targets. Curr Psychiatry Rep 13:274–282.

De Martino F, Moerel M, van de Moortele P-F, Uğurbil K, Goebel R, Yacoub E, Formisano E (2013) Spatial organization of frequency preference and selectivity in the human inferior colliculus. Nature Communications 4:1386.

de Zwart JA, van Gelderen P, Kellman P, Duyn JH (2002) Application of sensitivity-encoded echo-planar imaging for blood oxygen level-dependent functional brain imaging. Magnetic Resonance Medicine 48:1011–1020.

Deichmann R, Good CD, Josephs O, Ashburner J, Turner R (2000) Optimization of 3-D MP-RAGE Sequences for Structural Brain Imaging. NeuroImage 12:112–127.

Deistung A, Schäfer A, Schweser F, Biedermann U, Turner R, Reichenbach JR (2013) Toward in vivo histology: A comparison of quantitative susceptibility mapping (QSM) with magnitude-, phase-, and $R2^*$-imaging at ultra-high magnetic field strength. NeuroImage 65:299–314.

DeLong MR, Crutcher MD, Georgopoulos AP (1985) Primate globus pallidus and subthalamic nucleus: functional organization. Journal of Neurophysiology 53:530–543.

DeLong MR, Wichmann T (2007) Circuits and circuit disorders of the basal ganglia. Arch Neurol 64:20–24.

Derey K, Valente G, de Gelder B, Formisano E (2015) Opponent Coding of Sound Location (Azimuth) in Planum Temporale is Robust to Sound-Level Variations. Cerebral Cortex 26:450–464.

Derrfuss J, Mar RA (2009) Lost in localization: The need for a universal coordinate database. NeuroImage

48:1–7.

DeSimone K, Viviano JD, Schneider KA (2015) Population Receptive Field Estimation Reveals New Retinotopic Maps in Human Subcortex. The Journal of Neuroscience 35:9836–9847.

Devos D, Szurhaj W, Reyns N, Labyt E, Houdayer E, Bourriez JL, Cassim F, Krystkowiak P, Blond S, Destée A, Derambure P, Defebvre L (2006) Predominance of the contralateral movement-related activity in the subthalamo-cortical loop. Clin Neurophysiol 117:2315–2327.

Di Chiara G, Bassareo V (2007) Reward system and addiction: what dopamine does and doesn't do. Curr Opin Pharmacol 7:69–76.

Dice LR (1945) Measures of the amount of ecologic association between species. Ecology 26:297–302.

Ding L, Gold JI (2013) The basal ganglia's contributions to perceptual decision making. Neuron 79:640–649.

Dobi A, Margolis EB, Wang HL, Harvey BK, Morales M (2010) Glutamatergic and Nonglutamatergic Neurons of the Ventral Tegmental Area Establish Local Synaptic Contacts with Dopaminergic and Nondopaminergic Neurons. The Journal of Neuroscience 30:218–229.

Dormont D, Ricciardi KG, Tandé D, Parain K, Menuel C, Galanaud D, Navarro S, Cornu P, Agid Y, Yelnik J (2004) Is the subthalamic nucleus hypointense on T2-weighted images? A correlation study using MR imaging and stereotactic atlas data. AJNR Am J Neuroradiol 25:1516–1523.

Dorsey ER, Constantinescu R, Thompson JP, Biglan KM, Holloway RG, Kieburtz K, Marshall FJ, Ravina BM, Schifitto G, Siderowf A, Tanner CM (2007) Projected number of people with Parkinson disease in the most populous nations, 2005 through 2030. Neurology:384–386.

Dracheva S, Elhakem SL, McGurk SR, Davis KL, Haroutunian V (2004) GAD67 and GAD65 mRNA and protein expression in cerebrocortical regions of elderly patients with schizophrenia. J Neurosci Res 76:581–592.

Duan W, Zhang R, Guo Y, Jiang Y, Huang Y, Jiang H, Li C (2009) Nrf2 activity is lost in the spinal cord and its astrocytes of aged mice. In Vitro Cellular \& Developmental Biology-Animal 45:388–397.

Duann JR, Ide JS, Luo X, Li CSR (2009) Functional Connectivity Delineates Distinct Roles of the Inferior Frontal Cortex and Presupplementary Motor Area in Stop Signal Inhibition. The Journal of Neuroscience 29:10171–10179.

Dubelaar EJG, Verwer RWH, Hofman MA, Van Heerikhuize JJ, Ravid R, Swaab DE (2004) ApoE epsilon4 genotype is accompanied by lower metabolic activity in nucleus basalis of Meynert neurons in Alzheimer patients and controls as indicated by the size of the Golgi apparatus. J Neuropathol Exp Neurol 63:159–169.

Dunbar R (1992) Neocortex size as a constraint on group size in primates. Journal of human evolution 22:469–493.

Dunnen den WFA, Staal MJ (2005) Anatomical alterations of the subthalamic nucleus in relation to age: A postmortem study. Mov Disord 20:893–898.

Dutch Brain Bank. (n.d.) Dutch Brain Bank. Available at: http://www.brainnank.nl [Accessed May 11, 2017].

Duyn JH (2012) The future of ultra-high field MRI and fMRI for study of the human brain. NeuroImage 62:1241–1248.

Dyvorne H, O'Halloran R, Balchandani P (2015) Ultrahigh field single-refocused diffusion weighted imaging using a matched-phase adiabatic spin echo (MASE). Magnetic Resonance Medicine 75:1949–1957.

D'Ardenne K, Eshel N, Luka J, Lenartowicz A, Nystrom LE, Cohen JD (2012) Role of prefrontal cortex and the midbrain dopamine system in working memory updating. Proc Natl Acad Sci USA 109:19900–19909.

D'Ardenne K, Lohrenz T, Bartley KA, Montague PR (2013) Computational heterogeneity in the human mesencephalic dopamine system. Cognitive, Affective, & Behavioral Neuroscience 13:747–756.

Eapen M, Zald DH, Gatenby JC, Ding Z, Gore JC (2011) Using High-Resolution MR Imaging at 7T to Evaluate the Anatomy of the Midbrain Dopaminergic System. American Journal of Neuroradiology 32:688–

694.

Edelstein WA, Glover GH, Hardy CJ, Redington RW (1986) The intrinsic signal-to-noise ratio in NMR imaging. Magnetic Resonance Medicine 3:604–618.

Eftekhari S, Edvinsson L (2011) Calcitonin gene-related peptide (CGRP) and its receptor components in human and rat spinal trigeminal nucleus and spinal cord at C1-level. BMC Neurosci 12:112.

Eickhoff S, Nichols TE, Van Horn JD, Turner JA (2016) Sharing the wealth: Neuroimaging data repositories. NeuroImage 124:1065–1068.

Eickhoff SB, Stephan KE, Mohlberg H, Grefkes C, Fink GR, Amunts K, Zilles K (2005) A new SPM toolbox for combining probabilistic cytoarchitectonic maps and functional imaging data. NeuroImage 25:1325–1335.

Elolf E, Bockermann V, Gringel T, Knauth M, Dechent P, Helms G (2007) Improved Visibility of the Subthalamic Nucleus on High-Resolution Stereotactic MR Imaging by Added Susceptibility (T2*) Contrast Using Multiple Gradient Echoes. American Journal of Neuroradiology 28:1093–1094.

Engel SA, Glover GH, Wandell BA (1997) Retinotopic organization in human visual cortex and the spatial precision of functional MRI. Cereb Cortex 7:181–192.

Erika-Florence M, Leech R, Hampshire A (2014) A functional network perspective on response inhibition and attentional control. Nature Communications 5:1–12.

Erkut ZA, Hofman MA, Ravid R, Swaab DF (1995) Increased activity of hypothalamic corticotropin-releasing hormone neurons in multiple sclerosis. J Neuroimmunol 62:27–33.

Fasano A, Lozano AM (2015) Deep brain stimulation for movement disorders. Current Opinion in Neurology 28:423–436.

Federative Committee on Anatomical Terminology (1998) Terminologia anatomica : international anatomical terminology. Stuttgart: Thieme.

Federau C, Gallichan D (2016) Motion-Correction Enabled Ultra-High Resolution In-Vivo 7T-MRI of the Brain Lin F-H, ed. PLoS ONE 11:e0154974.

Fernyhough P, Gallagher A, Averill SA, Priestley JV (1999) Aberrant neurofilament phosphorylation in sensory neurons of rats with diabetic neuropathy. Diabetes 48.

Fiedler A, Reinert T, Morawski M, Brückner G, Arendt T, Butz T (2007) Intracellular iron concentration of neurons with and without perineuronal nets. Nuclear Instruments and Methods in Physics Research Section B: Beam Interactions with Materials and Atoms 260:153–158.

Finlay BL, Workman AD (2013) Human exceptionalism. Trends in Cognitive Sciences 17:199–201.

Fischl B, Salat DH, Busa E, Albert M, Dieterich M (2002) Whole brain segmentation: automated labeling of neuroanatomical structures in the human brain. Neuron 33:341–355.

Fischl B, van der Kouwe A, Destrieux C, Halgren E, Ségonne F, Salat DH, Busa E, Seidman LJ, Goldstein J, Kennedy D, Caviness V, Makris N, Rosen B, Dale AM (2004) Automatically parcellating the human cerebral cortex. Cereb Cortex 14:11–22.

Fleming SM, Thomas CL, Dolan RJ (2010a) Overcoming status quo bias in the human brain. Proc Natl Acad Sci USA 107:6005–6009.

Fleming SM, Whiteley L, Hulme OJ, Sahani M, Dolan RJ (2010b) Effects of Category-Specific Costs on Neural Systems for Perceptual Decision-Making. Journal of Neurophysiology 103:3238–3247.

Forstmann BU (2010) The neural substrate of prior information in perceptual decision making: a model-based analysis. Front Hum Neurosci 4.

Forstmann BU, Anwander A, Schäfer A, Neumann J, Brown S, Wagenmakers E-J, Bogacz R, Turner R (2010) Cortico-striatal connections predict control over speed and accuracy in perceptual decision making. Proc Natl Acad Sci USA 107:15916–15920.

Forstmann BU, de Hollander G, van Maanen L, Alkemade A, Keuken MC (2017) Towards a mechanistic understanding of the human subcortex. Nat Rev Neurosci 18:57–65.

Forstmann BU, Dutilh G, Brown S, Neumann J, Cramon Von DY, Ridderinkhof KR, Wagenmakers E-J (2008)

Striatum and pre-SMA facilitate decision-making under time pressure. Proc Natl Acad Sci USA 105:17538–17542.

Forstmann BU, Keuken MC, Jahfari S, Bazin P-L, Neumann J, Schäfer A, Anwander A, Turner R (2012) Cortico-subthalamic white matter tract strength predicts interindividual efficacy in stopping a motor response. NeuroImage 60:370–375.

Forstmann BU, Keuken MC, Schäfer A, Bazin P-L, Alkemade A, Turner R (2014) Multi-modal ultra-high resolution structural 7-Tesla MRI data repository. Sci Data 1:140050.

Forstmann BU, Ratcliff R, Wagenmakers E-J (2016) Sequential Sampling Models in Cognitive Neuroscience: Advantages, Applications, and Extensions. Annu Rev Psychol 67:641–666.

Forstmann BU, Wagenmakers E-J (2015) An Introduction to Model-Based Cognitive Neuroscience. Springer.

Forstmann BU, Wagenmakers E-J, Eichele T, Brown S, Serences JT (2011) Reciprocal relations between cognitive neuroscience and formal cognitive models: opposites attract? Trends in Cognitive Sciences 15:272–279.

Frahm J, Haase A, Matthaei D (1986) Rapid NMR imaging of dynamic processes using the FLASII technique. Magnetic Resonance Medicine 3:321–327.

Frank MJ (2005) Dynamic dopamine modulation in the basal ganglia: a neurocomputational account of cognitive deficits in medicated and nonmedicated Parkinsonism. Journal of Cognitive Neuroscience 17:51–72.

Frank MJ (2006) Hold your horses: A dynamic computational role for the subthalamic nucleus in decision making. Neural Networks 19:1120–1136.

Frank MJ, Claus ED (2006) Anatomy of a decision: Striato-orbitofrontal interactions in reinforcement learning, decision making, and reversal. Psychological Review 113:300–326.

Frank MJ, Gagne C, Nyhus E, Masters S, Wiecki TV, Cavanagh JF, Badre D (2015) fMRI and EEG Predictors of Dynamic Decision Parameters during Human Reinforcement Learning. The Journal of Neuroscience 35:485–494.

Frank MJ, Samanta J, Moustafa AA, Sherman SJ (2007) Hold Your Horses: Impulsivity, Deep Brain Stimulation, and Medication in Parkinsonism. Science 318:1309–1312.

Fronczek R, Lammers GJ, Balesar R, Unmehopa UA, Swaab DF (2005) The Number of Hypothalamic Hypocretin (Orexin) Neurons Is Not Affected in Prader-Willi Syndrome. J Clin Endocrinol Metab 90:5466–5470.

Frost R, Hess AT, Okell TW, Chappell MA, Tisdall MD, van der Kouwe AJW, Jezzard P (2015) Prospective motion correction and selective reacquisition using volumetric navigators for vessel-encoded arterial spin labeling dynamic angiography. Magnetic Resonance Medicine 76:1420–1430.

Frühwirth-Schnatter S (2006) Finite mixture and Markov switching models. Springer Science & Business Media.

Fuentealba P, Klausberger T, Karayannis T, Suen WY, Huck J, Tomioka R, Rockland K, Capogna M, Studer M, Morales M, Somogyi P (2010) Expression of COUP-TFII Nuclear Receptor in Restricted GABAergic Neuronal Populations in the Adult Rat Hippocampus. The Journal of Neuroscience 30:1595–1609.

Fussenich M (1967) Vergleichend anatomische studien uber den nucleus subthalamicus(corpus Luys) bei primaten. Diss & Vogt Institut fuer Hirnforschung, Neustadt/Albert-Ludwigs Universitaet Frieburg.

Fuster JM (2001) The prefrontal cortex--an update: time is of the essence. Neuron 30:319–333.

Gaetan C, Guyon X (2010) Spatial Statistics and Modeling. Springer.

Gao S-F, Klomp A, Wu J-L, Swaab DF, Bao A-M (2013) Journal of Affective Disorders. Journal of Affective Disorders 149:422–425.

Gavin DP, Sharma RP, Chase KA, Matrisciano F, Dong E, Guidotti A (2011) Growth Arrest and DNA-Damage-Inducible,Beta (GADD45b)-Mediated DNA Demethylation in Major Psychosis. 37:531–542.

Gazzaniga MS, Ivry RB, Mangun GR (2007) Cognitive neuroscience (Gazzaniga MS, Ivry RB, Mangun GR,

eds). Cambridge, Massachutes: MIT Press.

Gelman A, Carlin JB, Stern HS, Rubin DB (2014a) Bayesian data analysis. Taylor & Francis.

Gelman A, Hwang J, Vehtari A (2014b) Understanding predictive information criteria for Bayesian models. Statistics and Computing.

Gelman A, Stern H (2006) The Difference Between "Significant" and 'Not Significant' is not Itself Statistically Significant. The American Statistician 60:328–331.

Geyer S, Turner R (2015) Microstructural parcellation of the human cerebral cortex. Springer.

Glasser MF, Coalson TS, Robinson EC, Hacker CD, Harwell J, Yacoub E, Uğurbil K, Andersson J, Beckmann CF, Jenkinson M, Smith SM, Van Essen DC (2016a) A multi-modal parcellation of human cerebral cortex. Nature 536:171–178.

Glasser MF, Goyal MS, Preuss TM, Raichle ME, Van Essen DC (2014) Trends and properties of human cerebral cortex: Correlations with cortical myelin content. NeuroImage 93:165–175.

Glasser MF, Smith SM, Marcus DS, Andersson JLR, Auerbach EJ, Behrens TEJ, Coalson TS, Harms MP, Jenkinson M, Moeller S, Robinson EC, Sotiropoulos SN, Xu J, Yacoub E, Uğurbil K, Van Essen DC (2016b) The Human Connectome Project's neuroimaging approach. Nat Neurosci 19:1175–1187.

Glasser MF, Sotiropoulos SN, Wilson JA, Coalson TS, Fischl B, Andersson JL, Xu J, Jbabdi S, Webster M, Polimeni JR, Van Essen DC, Jenkinson M, Consortium FTW-MH (2013) The minimal preprocessing pipelines for the Human Connectome Project. NeuroImage 80:105–124.

Glimcher PW (2004) Decisions, uncertainty, and the brain: The science of neuroeconomics. MIT press.

Glover GH (1999) Deconvolution of impulse response in event-related BOLD fMRI. NeuroImage 9:416–429.

Glover GH, Li TQ, Ress D (2000) Image-based method for retrospective correction of physiological motion effects in fMRI: RETROICOR. Magn Reson Med 44:162–167.

Gonzalez-Castillo J, Saad ZS, Handwerker DA, Inati SJ, Brenowitz N, Bandettini PA (2012) Whole-brain, time-locked activation with simple tasks revealed using massive averaging and model-free analysis. Proc Natl Acad Sci USA 109:5487–5492.

Gorgolewski K, Burns CD, Madison C, Clark D, Halchenko YO, Waskom ML, Ghosh SS (2011) Nipype: a flexible, lightweight and extensible neuroimaging data processing framework in python. Frontiers in Neuroinformatics 5:13.

Gorgolewski KJ, Mendes N, Wilfling D, Wladimirow E, Gauthier CJ, Bonnen T, Ruby FJM, Trampel R, Bazin P-L, Cozatl R, Smallwood J, Margulies DS (2015) A high resolution 7-Tesla resting-state fMRI test-retest dataset with cognitive and physiological measures. Sci Data 2:140054.

Gottschall PE, Ajmo JM, Eakin AK, Howell MD, Mehta H, Bailey LA (2010) Panel of synaptic protein ELISAs for evaluating neurological phenotype. Exp Brain Res 201:885–893.

Graybiel AM (1998) The basal ganglia and chunking of action repertoires. Neurobiol Learn Mem 70:119–136.

Greenhouse I, Gould S, Houser M, Aron AR (2013) Stimulation of contacts in ventral but not dorsal subthalamic nucleus normalizes response switching in Parkinson's disease. Neuropsychologia 51:1302–1309.

Greenhouse I, Gould S, Houser M, Hicks G, Gross J, Aron AR (2011) Stimulation at dorsal and ventral electrode contacts targeted at the subthalamic nucleus has different effects on motor and emotion functions in Parkinson's disease. Neuropsychologia 49:528–534.

Griswold MA, Jakob PM, Heidemann RM, Nittka M, Jellus V, Wang J, Kiefer B, Haase A (2002) Generalized autocalibrating partially parallel acquisitions (GRAPPA). Magnetic Resonance Medicine 47:1202–1210.

Groiss SJ, Wojtecki L, Südmeyer M, Schnitzler A (2009) Deep brain stimulation in Parkinson's disease. Ther Adv Neurol Disord 2:20–28.

Gross A, Sims RE, Swinny JD, Sieghart W, Bolam JP, Stanford IM (2011) Differential localization of GABAA receptor subunits in relation to rat striatopallidal and pallidopallidal synapses. European Journal of

Neuroscience 33:868–878.

Grushka E (1972) Characterization of exponentially modified Gaussian peaks in chromatography. Anal Chem 44:1733–1738.

Guitart-Masip M, Chowdhury R, Sharot T, Dayan P, Düzel E, Dolan RJ (2012) Action controls dopaminergic enhancement of reward representations. Proc Natl Acad Sci USA 109:7511–7516.

Guitart-Masip M, Fuentemilla L, Bach DR, Huys QJM, Dayan P, Dolan RJ, Duzel E (2011) Action Dominates Valence in Anticipatory Representations in the Human Striatum and Dopaminergic Midbrain. The Journal of Neuroscience 31:7867–7875.

Gurney K, Prescott TJ, Redgrave P (2001) A computational model of action selection in the basal ganglia. I. A new functional anatomy. Biol Cybern 84:401–410.

Gveric D, Hanemaaijer R, Newcombe J, van Lent NA, Sier CF, Cuzner ML (2001) Plasminogen activators in multiple sclerosis lesions: implications for the inflammatory response and axonal damage. Brain 124:1978–1988.

Haase A, Frahm J, Matthaei D, Hanicke W, Merboldt KD (1985) FLASH imaging. Rapid NMR imaging using low flip-angle pulses. J Magn Reson (1969-1992) 67:258–266.

Haber SN (2003) The primate basal ganglia: parallel and integrative networks. Journal of Chemical Neuroanatomy 26:317–330.

Haber SN (2014) The place of dopamine in the cortico-basal ganglia circuit. Neuroscience 282:248–257.

Hahn A, Kranz GS, Seidel E-M, Sladky R, Kraus C, Küblböck M, Pfabigan DM, Hummer A, Grahl A, Ganger S, Windischberger C, Lamm C, Lanzenberger R (2013) Comparing neural response to painful electrical stimulation with functional MRI at 3 and 7T. NeuroImage 82:336–343.

Hale JR, Brookes MJ, Hall EL, Zumer JM, Stevenson CM, Francis ST, Morris PG (2010) Comparison of functional connectivity in default mode and sensorimotor networks at 3 and 7T. Magn Reson Mater Phy 23:339–349.

Hamani C, Saint-Cyr JA, Fraser J, Kaplitt M, Lozano AM (2004) The subthalamic nucleus in the context of movement disorders. Brain 127:4–20.

Hampshire A (2015) Putting the brakes on inhibitory models of frontal lobe function. NeuroImage 113:340–355.

Hampshire A, Sharp DJ (2015) Contrasting network and modular perspectives on inhibitory control. Trends in Cognitive Sciences 19:445–452.

Hanes DP, Schall JD (1996) Neural control of voluntary movement initiation. Science 274:427–430.

Hanke M, Baumgartner FJ, Ibe P, Kaule FR, Pollmann S, Speck O, Zinke W, Stadler J (2014) A high-resolution 7-Tesla fMRI dataset from complex natural stimulation with an audio movie. Sci Data 1:140003.

Hara A, Aoki H, Taguchi A, Niwa M, Yamada Y, Kunisada T, Mori H (2008) Neuron-like Differentiation and Selective Ablation of Undifferentiated Embryonic Stem Cells Containing Suicide Gene with Oct-4 Promoter. Stem Cells and Development 17:619–628.

Hardman CD, Halliday GM, McRitchie DA, Morris JG (1997) The subthalamic nucleus in Parkinson's disease and progressive supranuclear palsy. J Neuropathol Exp Neurol 56:132–142.

Hardman CD, Henderson JM, Finkelstein DI, Horne MK, Paxinos G, Halliday GM (2002a) Comparison of the basal ganglia in rats, marmosets, macaques, baboons, and humans: Volume and neuronal number for the output, internal relay, and striatal modulating nuclei. J Comp Neurol 445:238–255.

Hardman CD, Henderson JM, Finkelstein DI, Horne MK, Paxinos G, Halliday GM (2002b) Comparison of the basal ganglia in rats, marmosets, macaques, baboons, and humans: Volume and neuronal number for the output, internal relay, and striatal modulating nuclei. J Comp Neurol 445:238–255.

Hartmann-von Monakow A, Akert K, Künzle H (1978) Projections of the precentral motor cortex and other cortical areas of the frontal lobe to the subthalamic nucleus in the monkey. Exp Brain Res 33:395–403.

Hauptmann G, Lauter G, Söll I (2016) Detection and signal amplification in zebrafish RNA FISH. Methods

98:50–59.

Hawkins GE, Forstmann BU, Wagenmakers E-J, Ratcliff R, Brown SD (2015a) Revisiting the Evidence for Collapsing Boundaries and Urgency Signals in Perceptual Decision-Making. The Journal of Neuroscience 35:2476–2484.

Hawkins GE, Mittner M, Boekel W, Heathcote A, Forstmann BU (2015b) Toward a model-based cognitive neuroscience of mind wandering. Neuroscience 310:290–305.

Haynes WIA, Haber SN (2013) The Organization of Prefrontal-Subthalamic Inputs in Primates Provides an Anatomical Substrate for Both Functional Specificity and Integration: Implications for Basal Ganglia Models and Deep Brain Stimulation. The Journal of Neuroscience 33:4804–4814.

Heckemann RA, Hajnal JV, Aljabar P, Rueckert D, Hammers A (2006) Automatic anatomical brain MRI segmentation combining label propagation and decision fusion. NeuroImage 33:115–126.

Hedreen JC (1999) Tyrosine hydroxylase-immunoreactive elements in the human globus pallidus and subthalamic nucleus. J Comp Neurol 409:400–410.

Heekeren HR, Marrett S, Bandettini PA, Ungerleider LG (2004) A general mechanism for perceptual decision-making in the human brain. Nature 431:859–862.

Heidemann RM, Anwander A, Feiweier T, Knösche TR, Turner R (2012) k-space and q-space: Combining ultra-high spatial and angular resolution in diffusion imaging using ZOOPPA at 7T. NeuroImage 60:967–978.

Heimann T, Meinzer H-P (2009) Medical Image Analysis. Medical image analysis 13:543–563.

Hennig J, Speck O (2012) High-field MR imaging. Springer.

Henry LK, Adkins EM, Han Q, Blakely RD (2003) Serotonin and Cocaine-sensitive Inactivation of Human Serotonin Transporters by Methanethiosulfonates Targeted to Transmembrane Domain I. Journal of Biological Chemistry 278:37052–37063.

Herculano-Houzel S (2012) The remarkable, yet not extraordinary, human brain as a scaled-up primate brain and its associated cost. Proc Natl Acad Sci USA 109:10661–10668.

Herz DM, Christensen MS, Bruggemann N, Hulme OJ, Ridderinkhof KR, Madsen KH, Siebner HR (2014) Motivational Tuning of Fronto-Subthalamic Connectivity Facilitates Control of Action Impulses. The Journal of Neuroscience 34:3210–3217.

Herzog J, Fietzek U, Hamel W, Morsnowski A, Steigerwald F, Schrader B, Weinert D, Pfister G, Müller D, Mehdorn HM, Deuschl G, Volkmann J (2004) Most effective stimulation site in subthalamic deep brain stimulation for Parkinson's disease. Mov Disord 19:1050–1054.

Hédou G, Chasserot-Golaz S, Kemmel V, Gobaille S, Roussel G, Artault JC, Andriamampandry C, Aunis D, Maitre M (2000) Immunohistochemical studies of the localization of neurons containing the enzyme that synthesizes dopamine, GABA, or gamma-hydroxybutyrate in the rat substantia nigra and striatum. J Comp Neurol 426:549–560.

Ho TC, Brown S, Serences JT (2009) Domain General Mechanisms of Perceptual Decision Making in Human Cortex. The Journal of Neuroscience 29:8675–8687.

Hong S-M, Park JH, Woo M-K, Kim Y-B, Cho Z-H (2013) New design concept of monopole antenna array for UHF 7T MRI. Magnetic Resonance Medicine 71:1944–1952.

Horn A, Neumann W-J, Degen K, Schneider G-H, Kühn AA (2017) Toward an electrophysiological "sweet spot" for deep brain stimulation in the subthalamic nucleus. Human Brain Mapping 35:5083.

Hu S, Tseng Y-C, Winkler AD, Li C-SR (2013) Neural bases of individual variation in decision time. Human Brain Mapping 35:2531–2542.

Huang L, Garcia I, Jen H-I, Arenkiel BR (2013) Reciprocal connectivity between mitral cells and external plexiform layer interneurons in the mouse olfactory bulb. Front Neural Circuits 7:32.

Huber L, Ivanov D, Guidi M, Turner R, Uludağ K, Möller HE, Poser BA (2016) Functional cerebral blood volume mapping with simultaneous multi-slice acquisition. NeuroImage 125:1159–1168.

Huber L, Ivanov D, Krieger SN, Gauthier C (2013) Measurements of cerebral blood volume and BOLD signal

during hypercapnia and functional stimulation in humans at 7T: application to calibrated BOLD.

Huettel SA, Song AW, McCarthy G (2009) Functional Magnetic Resonance Imaging. Sinauer Associates.

Idrissi El A, L'Amoreaux WJ (2008) Selective resistance of taurine-fed mice to isoniazide-potentiated seizures: In vivo functional test for the activity of glutamic acid decarboxylase. Neuroscience 156:693–699.

Ineichen C, Glannon W, Temel Y, Baumann CR, Sürücü O (2014) A critical reflection on the technological development of deep brain stimulation (DBS). Front Hum Neurosci 8:730.

Insel TR, Landis SC, Collins FS (2013) The NIH brain initiative. Science 340:687–688.

International Human Genome Sequencing Consortium (2004) Finishing the euchromatic sequence of the human genome. Nature 431:931–945.

Ishunina TA, van Beurden D, van der Meulen G, Unmehopa UA, Hol EM, Huitinga I, Swaab DF (2005) Diminished aromatase immunoreactivity in the hypothalamus, but not in the basal forebrain nuclei in Alzheimer's disease. Neurobiology of Aging 26:173–194.

Jablonska B, Scafidi J, Aguirre A, Vaccarino F, Nguyen V, Borok E, Horvath TL, Rowitch DH, Gallo V (2012) Oligodendrocyte Regeneration after Neonatal Hypoxia Requires FoxO1-Mediated p27Kip1 Expression. The Journal of Neuroscience 32:14775–14793.

Jahanshahi M, Obeso I, Rothwell JC, Obeso JA (2015) A fronto-striato-subthalamic-pallidal network for goal-directed and habitual inhibition. Nat Rev Neurosci 16:719–732.

Jahfari S, Waldorp L, van den Wildenberg WPM, Scholte HS, Ridderinkhof KR, Forstmann BU (2011) Effective Connectivity Reveals Important Roles for Both the Hyperdirect (Fronto-Subthalamic) and the Indirect (Fronto-Striatal-Pallidal) Fronto-Basal Ganglia Pathways during Response Inhibition. The Journal of Neuroscience 31:6891–6899.

Jbabdi S, Sotiropoulos SN, Behrens TE (2013) The topographic connectome. Current Opinion in Neurobiology 23:207–215.

Jenkinson M (2004) Improving the registration of B0-disorted EPI images using calculated cost function weights. NeuroImage 22:e1544–e1545.

Jenkinson M, Bannister P, Brady M, Smith S (2002) Improved Optimization for the Robust and Accurate Linear Registration and Motion Correction of Brain Images. NeuroImage 17:825–841.

Jenkinson M, Smith S (2001) A global optimisation method for robust affine registration of brain images. Medical image analysis 5:143–156.

Joel D, Weiner I (1994) The organization of the basal ganglia-thalamocortical circuits: open interconnected rather than closed segregated. Neuroscience 63:363–379.

Joel D, Weiner I (1997) The connections of the primate subthalamic nucleus: indirect pathways and the open-interconnected scheme of basal ganglia-thalamocortical circuitry. Brain Res Brain Res Rev 23:62–78.

Johansen-Berg H (2013) Human connectomics — What will the future demand? NeuroImage 80:541–544.

Jonas E, Kording KP (2017) Could a Neuroscientist Understand a Microprocessor? PLoS Comput Biol 13:e1005268.

Jones DK, Knösche TR, Turner R (2013) White matter integrity, fiber count, and other fallacies: The do"s and don"ts of diffusion MRI. NeuroImage 73:239–254.

Jones E, Oliphant T, Peterson P, Others (n.d.) Scipy. Available at: http://www.scipy.org/.

Joshi D, Fung SJ, Rothwell A, Weickert CS (2012) Higher gamma-aminobutyric acid neuron density in the white matter of orbital frontal cortex in schizophrenia. Biol Psychiatry 72:725–733.

Kanaan NM, Kordower JH, Collier TJ (2007) Age-related accumulation of Marinesco bodies and lipofuscin in rhesus monkey midbrain dopamine neurons: Relevance to selective neuronal vulnerability. J Comp Neurol 502:683–700.

Kandel ER, Schwartz JH, Jessell TM, Siegelbaum SA (2000) Principles of neural science.

Kanowski M, Voges J, Buentjen L, Stadler J, Heinze HJ, Tempelmann C (2014) Direct Visualization of

Anatomic Subfields within the Superior Aspect of the Human Lateral Thalamus by MRI at 7T. American Journal of Neuroradiology 35:1721–1727.

Karachi C, Grabli D, Baup N, Mounayar S, Tandé D, François C, Hirsch EC (2009) Dysfunction of the subthalamic nucleus induces behavioral and movement disorders in monkeys. Mov Disord 24:1183–1192.

Karachi C, Yelnik JRM, Tand D, Tremblay LO, Hirsch EC, Fran ois C (2005) The pallidosubthalamic projection: An anatomical substrate for nonmotor functions of the subthalamic nucleus in primates. Mov Disord 20:172–180.

Kempf C, Staudt T, Bingen P, Horstmann H, Engelhardt J, Hell SW, Kuner T (2013) Tissue Multicolor STED Nanoscopy of Presynaptic Proteins in the Calyx of Held Mothet J-P, ed. PLoS ONE 8:e62893.

Keren NI, Taheri S, Vazey EM, Morgan PS, Granholm A-CE, Aston-Jones GS, Eckert MA (2015) Histologic validation of locus coeruleus MRI contrast in post-mortem tissue. NeuroImage 113:235–245.

Kerl HU, Gerigk L, Brockmann MA, Huck S, Al-Zghloul M, Groden C, Hauser T, Nagel AM, Nölte IS (2013) Imaging for deep brain stimulation: The zona incerta at 7 Tesla. World J Radiol 5:5–16.

Kerl HU, Gerigk L, Huck S, Al-Zghloul M, Groden C, Nölte IS (2012a) Visualisation of the zona incerta for deep brain stimulation at 3.0 Tesla. Clin Neuroradiol 22:55–68.

Kerl HU, Gerigk L, Pechlivanis I, Al-Zghloul M, Groden C, Nölte I (2012b) The subthalamic nucleus at 3.0 Tesla: choice of optimal sequence and orientation for deep brain stimulation using a standard installation protocol. Journal of Neurosurgery 117:1155–1165.

Kerl HU, Gerigk L, Pechlivanis I, Al-Zghloul M, Groden C, Nölte IS (2012c) The subthalamic nucleus at 7.0 Tesla: evaluation of sequence and orientation for deep-brain stimulation. Acta Neurochir 154:2051–2062.

Keuken MC, Bazin PL, Backhouse K, Beekhuizen S, Himmer L, Kandola A, Lafeber JJ, Prochazkova L, Trutti A, Schäfer A, Turner R, Forstmann BU (2017) Effects of aging on [Formula: see text], [Formula: see text], and QSM MRI values in the subcortex. Brain Struct Funct.

Keuken MC, Bazin PL, Crown L, Hootsmans J, Laufer A, Müller-Axt C, Sier R, van der Putten EJ, Schäfer A, Turner R, Forstmann BU (2014a) Quantifying inter-individual anatomical variability in the subcortex using 7T structural MRI. NeuroImage 94:40–46.

Keuken MC, Bazin PL, Schäfer A, Neumann J, Turner R, Forstmann BU (2013) Ultra-High 7T MRI of Structural Age-Related Changes of the Subthalamic Nucleus. The Journal of Neuroscience 33:4896–4900.

Keuken MC, Forstmann BU (2015) A probabilistic atlas of the basal ganglia using 7 T MRI. Data in Brief 4:577–582.

Keuken MC, Mueller-Axt C, Langner R, Eickhoff SB, Forstmann BU, Neumann J (2014b) Brain networks of perceptual decision-making: an fMRI ALE meta-analysis. Front Hum Neurosci 8.

Keuken MC, Uylings HBM, Geyer S, Schäfer A, Turner R, Forstmann BU (2012) Are there three subdivisions in the primate subthalamic nucleus? Front Neuroanat 6:14.

Keuken MC, van Maanen L, Bogacz R, Schäfer A, Neumann J, Turner R, Forstmann BU (2015) The subthalamic nucleus during decision-making with multiple alternatives. Human Brain Mapping 36:4041–4052.

Kievit RA, Frankenhuis WE, Waldorp LJ, Borsboom D (2013) Simpson's paradox in psychological science: a practical guide. Frontiers in Psychology 4.

Kim J, Lenglet C, Duchin Y, Sapiro G, Harel N (2014) Semiautomatic segmentation of brain subcortical structures from high-field MRI. IEEE J Biomed Health Inform 18:1678–1695.

Kirsch P, Schienle A, Stark R, Sammer G, Blecker C, Walter B, Ott U, Burkart J, Vaitl D (2003) Anticipation of reward in a nonaversive differential conditioning paradigm and the brain reward system:. NeuroImage 20:1086–1095.

Kirvell SL, Esiri M, Francis PT (2006) Down-regulation of vesicular glutamate transporters precedes cell loss

and pathology in Alzheimer's disease. Journal of neurochemistry 98:939–950.

Kiss J, Halász B, Csáki Á, Liposits Z, Hrabovszky E (2007) Vesicular glutamate transporter 2 protein and mRNA containing neurons in the hypothalamic suprachiasmatic nucleus of the rat. Brain Research Bulletin 74:397–405.

Kitajima M, Korogi Y, Kakeda S, Moriya J, Ohnari N, Sato T, Hayashida Y, Hirai T, Okuda T, Yamashita Y (2008) Human subthalamic nucleus: evaluation with high-resolution MR imaging at 3.0 T. Neuroradiology 50:675–681.

Kleinschmidt A, Toni I (2004) Functional magnetic resonance imaging of the human motor cortex. Motor Cortex in Voluntary Movements: A Distributed System for Distributed Functions:49–84.

Klioueva NM, Rademaker MC, Dexter DT, Al-Sarraj S, Seilhean D, Streichenberger N, Schmitz P, Bell JE, Ironside JW, Arzberger T, Huitinga I (2015) BrainNet Europe's Code of Conduct for brain banking. Journal of Neural Transmission:1–4.

Knutson B, Adams CM, Fong GW, Hommer D (2001) Anticipation of increasing monetary reward selectively recruits nucleus accumbens. The Journal of Neuroscience 21:RC159.

Koopmans PJ, Barth M, Orzada S, Norris DG (2011) Multi-echo fMRI of the cortical laminae in humans at 7T. NeuroImage 56:1276–1285.

Krack P, Hariz MI, Baunez C, Guridi J, Obeso JA (2010) Deep brain stimulation: from neurology to psychiatry? Trends in Neurosciences 33:474–484.

Kraft D (1988) A software package for sequential quadratic programming. Forschungsbericht- Deutsche Forschungs- und Versuchsanstalt fur Luft- und Raumfahrt.

Krebs RM, Boehler CN, Roberts KC, Song AW, Woldorff MG (2012) The Involvement of the Dopaminergic Midbrain and Cortico-Striatal-Thalamic Circuits in the Integration of Reward Prospect and Attentional Task Demands. Cerebral Cortex 22:607–615.

Krebs RM, Heipertz D, Schuetze H, Duzel E (2011) Novelty increases the mesolimbic functional connectivity of the substantia nigra/ventral tegmental area (SN/VTA) during reward anticipation: Evidence from high-resolution fMRI. NeuroImage 58:647–655.

Krebs RM, Schott BH, Duzel E (2009) Personality Traits Are Differentially Associated withPatterns of Reward and Novelty Processing in theHuman Substantia Nigra/Ventral Tegmental Area. BPS 65:103–110.

Kretzschmar H (2009) Brain banking: opportunities, challenges and meaning for the future. Nat Rev Neurosci 10:70–78.

Kruschke JK (2011) Doing Bayesian Data Analysis: A Tutorial with R and BUGS. Barlington: Academic Press.

Kundu P, Inati SJ, Evans JW, Luh W-M, Bandettini PA (2012) Differentiating BOLD and non-BOLD signals in fMRI time series using multi-echo EPI. NeuroImage 60:1759–1770.

Kühn AA, Hariz MI, Silberstein P, Tisch S, Kupsch A, Schneider GH, Limousin-Dowsey P, Yarrow K, Brown P (2005) Activation of the subthalamic region during emotional processing in Parkinson disease. Neurology 65:707–713.

Kühn AA, Kempf F, Brücke C, Gaynor Doyle L, Martinez-Torres I, Pogosyan A, Trottenberg T, Kupsch A, Schneider GH, Hariz MI, Vandenberghe W, Nuttin B, Brown P (2008) High-Frequency Stimulation of the Subthalamic Nucleus Suppresses Oscillatory   Activity in Patients with Parkinson's Disease in Parallel with Improvement in Motor Performance. The Journal of Neuroscience 28:6165–6173.

Lambert C, Zrinzo L, Nagy Z, Lutti A, Hariz M, Foltynie T, Draganski B, Ashburner J, Frackowiak R (2012) Confirmation of functional zones within the human subthalamic nucleus: Patterns of connectivity and sub-parcellation using diffusion weighted imaging. NeuroImage 60:83–94.

Lambert C, Zrinzo L, Nagy Z, Lutti A, Hariz M, Foltynie T, Draganski B, Ashburner J, Frackowiak R (2015) Do we need to revise the tripartite subdivision hypothesis of the human subthalamic nucleus (STN)? Response to Alkemade and Forstmann. NeuroImage 110:1–2.

Lancaster JL, Tordesillas-Gutiérrez D, Martinez M, Salinas F, Evans A, Zilles K, Mazziotta JC, Fox PT (2007) Bias between MNI and Talairach coordinates analyzed using the ICBM-152 brain template. Human

Brain Mapping 28:1194–1205.

Lancaster MA, Renner M, Martin C-A, Wenzel D, Bicknell LS, Hurles ME, Homfray T, Penninger JM, Jackson AP, Knoblich JA (2013) Cerebral organoids model human brain development and microcephaly. Nature 501:373–379.

Lange H, Thörner G, Hopf A, Schröder KF (1976) Morphometric studies of the neuropathological changes in choreatic diseases. Journal of the Neurological Sciences 28:401–425.

Langkammer C, Schweser F, Krebs N, Deistung A, Goessler W, Scheurer E, Sommer K, Reishofer G, Yen K, Fazekas F, Ropele S, Reichenbach JR (2012) Quantitative susceptibility mapping (QSM) as a means to measure brain iron? A post mortem validation study. NeuroImage 62:1593–1599.

Larsson M, Sawada K, Morland C, Hiasa M, Ormel L, Moriyama Y, Gundersen V (2012) Functional and Anatomical Identification of a Vesicular Transporter Mediating Neuronal ATP Release. Cerebral Cortex 22:1203–1214.

Lavenex P, Lavenex PB, Bennett JL, Amaral DG (2009) Postmortem changes in the neuroanatomical characteristics of the primate brain: Hippocampal formation. J Comp Neurol 512:27–51.

Lebreton M, Palminteri S (2016) Revisiting the assessment of inter-individual differences in fMRI activations-behavior relationships. bioRxiv.

Lee MD, Wagenmakers E-J (2014) Bayesian cognitive modeling: A practical course.

Lee YJ, Yan BC, Park JH, Ahn JH, Kim IH, Lee J-C, Lee HY, Kim Y-M, Won M-H, Cho JH (2013) Differences of calcium binding proteins immunoreactivities in the young hippocampal CA1 region from the adult following transient ischemic damage. Journal of the Neurological Sciences 326:40–47.

Lefranc M, Derrey S, Merle P, Tir M, Constans J-M, Montpellier D, Macron JM, Le Gars D, Peltier J, Baledentt O (2014) High-resolution 3-dimensional T2*-weighted angiography (HR 3-D SWAN): an optimized 3-T magnetic resonance imaging sequence for targeting the subthalamic nucleus. Neurosurgery 74:615–627.

Lehericy S (2005) Motor control in basal ganglia circuits using fMRI and brain atlas approaches. Cerebral Cortex 16:149–161.

Lenglet C, Abosch A, Yacoub E, De Martino F, Sapiro G, Harel N (2012) Comprehensive in vivo Mapping of the Human Basal Ganglia and Thalamic Connectome in Individuals Using 7T MRI Bankiewicz K, ed. PLoS ONE 7:e29153.

Leunissen I, Coxon JP, Geurts M, Caeyenberghs K, Michiels K, Sunaert S, Swinnen SP (2012) Disturbed cortico-subcortical interactions during motor task switching in traumatic brain injury. Human Brain Mapping 34:1254–1271.

Lewandowsky S, Farrell S (2010) Computational modeling in cognition: Principles and practice. Sage.

Lévesque J, Beauregard M, Mensour B (2006) Effect of neurofeedback training on the neural substrates of selective attention in children with attention-deficit/hyperactivity disorder: A functional magnetic resonance imaging study. Neurosci Lett 394:216–221.

Lévesque J-C, Parent A (2005) GABAergic interneurons in human subthalamic nucleus. Mov Disord 20:574–584.

Li W, Wu B, Liu C (2011) Quantitative susceptibility mapping of human brain reflects spatial variation in tissue composition. NeuroImage 55:1645–1656.

Li W, Wu B, Liu C (2015) iHARPERELLA: an improved method for integrated 3D phase unwrapping and background phase removal. In, pp 3313.

Li Z, Chen-Roetling J, Regan RF (2009) Increasing expression of H- or L-ferritin protects cortical astrocytes from hemin toxicity. Free Radical Research 43:613–621.

Limousin P, Pollak P, Benazzouz A, Hoffmann D, Le Bas J-F, Brousolle E, Perret JE, Benabid AL (1995) Effect on parkinsonian signs and symptoms of bilateral subthalamic nucleus stimulation. The Lancet 345:91–95.

Linnman C, Moulton EA, Barmettler G, Becerra L, Borsook D (2012) Neuroimaging of the periaqueductal

gray: State of the field. NeuroImage 60:505–522.

Liu T, Spincemaille P, de Rochefort L, Kressler B, Wang Y (2009) Calculation of susceptibility through multiple orientation sampling (COSMOS): A method for conditioning the inverse problem from measured magnetic field map to susceptibility source image in MRI. Magnetic Resonance Medicine 61:196–204.

Lo C-C, Wang X-J (2006) Cortico–basal ganglia circuit mechanism for a decision threshold in reaction time tasks. Nat Neurosci 9:956–963.

Logan GD, Cowan WB (1984) On the ability to inhibit thought and action: A theory of an act of control. Psychological Review 91:295.

Logan GD, Cowan WB, Davis KA (1984) On the ability to inhibit simple and choice reaction time responses: a model and a method. Journal of Experimental Psychology: Human Perception and Performance 10:276–291.

Logothetis NK (2008) What we can do and what we cannot do with fMRI. Nature 453:869–878.

Lohmann G (1998) Volumetric image analysis.

Lohmann G, Stelzer J, Neumann J, Ay N, Turner R (2013) "More Is Different" in Functional Magnetic Resonance Imaging: A Review of Recent Data Analysis Techniques. Brain Connectivity 3:223–239.

Lourens MAJ, Meijer HGE, Contarino MF, van den Munckhof P, Schuurman PR, van Gils SA, Bour LJ (2013) Functional neuronal activity and connectivity within the subthalamic nucleus in Parkinson's disease. Clin Neurophysiol 124:967–981.

Lozano AM, Lipsman N (2013) Probing and Regulating Dysfunctional Circuits Using Deep Brain Stimulation. Neuron 77:406–424.

Lu H, Golay X, Pekar JJ, van Zijl PCM (2003) Functional magnetic resonance imaging based on changes in vascular space occupancy. Magnetic Resonance Medicine 50:263–274.

Luce RD (1986) Response times. Oxford University Press.

MacQueen J (1967) Some methods for classification and analysis of multivariate observations. In, pp 281–297.

Mahad DJ, Ziabreva I, Campbell G, Lax N, White K, Hanson PS, Lassmann H, Turnbull DM (2009) Mitochondrial changes within axons in multiple sclerosis. Brain 132:1161–1174.

Mai JK, Majtanik M, Paxinos G (2015) Atlas of the human brain. New York: Academic Press.

Maitra R, Ramler IP (2010) A k-mean-directions algorithm for fast clustering of data on the sphere. Journal of Computational and Graphical Statistics 19:377–396.

Makris N, Swaab DF, van der Kouwe A, Abbs B, Boriel D, Handa RJ, Tobet S, Goldstein JM (2013) Volumetric parcellation methodology of the human hypothalamus in neuroimaging: Normative data and sex differences. NeuroImage 69:1–10.

Mallet L, Schüpbach M, N'Diaye K, Remy P, Bardinet E, Czernecki V, Welter M-L, Pelissolo A, Ruberg M, Agid Y (2007) Stimulation of subterritories of the subthalamic nucleus reveals its role in the integration of the emotional and motor aspects of behavior. Proc Natl Acad Sci USA 104:10661–10666.

Mallet N, Micklem BR, Henny P, Brown MT, Williams C, Bolam JP, Nakamura KC, Magill PJ (2012) Dichotomous Organizationof the External Globus Pallidus. Neuron 74:1075–1086.

Mansfield EL, Karayanidis F, Jamadar S, Heathcote A, Forstmann BU (2011) Adjustments of Response Threshold during Task Switching: A Model-Based Functional Magnetic Resonance Imaging Study. The Journal of Neuroscience 31:14688–14692.

Manyika J, Chui M, Brown B, Bughin J, Dobbs R (2011) Big Data: The Next Frontier for Innovation, Competition, and Productivity. McKinsey Global Institute, McKinsey&Company.

Marani E, Heida T, Lakke EA, Usunoff KG (2008) The Subthalamic Nucleus. Springer.

Marchand WR, Lee JN, Suchy Y, Garn C, Chelune G, Johnson S, Wood N (2012) Functional architecture of the cortico-basal ganglia circuitry during motor task execution: Correlations of strength of functional connectivity with neuropsychological task performance among female subjects. Human Brain

Mapping 34:1194–1207.

Mardia KV, Jupp PE (2000) Directional statistics. Wiley.

Marin JM, Robert CP (2014) Bayesian essentials with R.

Markram H (2012) The human brain project. Scientific American 306:50–55.

Marques JP, Kober T, Krueger G, van der Zwaag W, van de Moortele P-F, Gruetter R (2010) MP2RAGE, a self bias-field corrected sequence for improved segmentation and T1-mapping at high field. NeuroImage 49:1271–1281.

Marr D (1982) Vision: A computational approach. Freeman & Co., San Francisco.

Mars RB, Shea NJ, Kolling N, Rushworth MFS (2012) Model-based analyses: Promises, pitfalls, and example applications to the study of cognitive control. The Quarterly Journal of Experimental Psychology 65:252–267.

Martin JH, Leonard ME, Radzyner H (1989) Neuroanatomy: text and atlas. Elsevier New York.

Martuzzi R, van der Zwaag W, Farthouat J, Gruetter R, Blanke O (2012) Human finger somatotopy in areas 3b, 1, and 2: A 7T fMRI study using a natural stimulus. Human Brain Mapping 35:213–226.

Massey LA, Miranda MA, Zrinzo L, Al-Helli O, Parkes HG, Thornton JS, So PW, White MJ, Mancini L, Strand C, Holton JL, Hariz MI, Lees AJ, Revesz T, Yousry TA (2012) High resolution MR anatomy of the subthalamic nucleus: Imaging at 9.4T with histological validation. NeuroImage 59:2035–2044.

Massi L, Lagler M, Hartwich K, Borhegyi Z, Somogyi P, Klausberger T (2012) Temporal Dynamics of Parvalbumin-Expressing Axo-axonic and Basket Cells in the Rat Medial Prefrontal Cortex In Vivo. The Journal of Neuroscience 32:16496–16502.

Mastroberardino PG, Hoffman EK, Horowitz MP, Betarbet R, Taylor G, Cheng D, Na HM, Gutekunst C-A, Gearing M, Trojanowski JQ, Anderson M, Chu CT, Peng J, Greenamyre JT (2009) Neurobiology of Disease. Neurobiology of Disease 34:417–431.

McAuliffe MJ, Lalonde FM, McGarry D, Gandler W, Csaky K, Trus BL (2001) Medical Image Processing, Analysis and Visualization in clinical research. In, pp 381–386.

McCoy RC, Wakefield J, Akey JM (2017) Impacts of Neanderthal-Introgressed Sequences on the Landscape of Human Gene Expression. Cell 168:916–927.e12.

Menz MM, Buchel C, Peters J (2012) Sleep Deprivation Is Associated with Attenuated Parametric Valuation and Control Signals in the Midbrain during Value-Based Decision Making. The Journal of Neuroscience 32:6937–6946.

Mercier MR, Bickel S, Megevand P, Groppe DM, Schroeder CE, Mehta AD, Lado FA (2017) Evaluation of cortical local field potential diffusion in stereotactic electro-encephalography recordings: A glimpse on white matter signal. NeuroImage 147:219–232.

Mestres-Missé A, Trampel R, Turner R, Kotz SA (2017) Uncertainty and expectancy deviations require cortico-subcortical cooperation. NeuroImage 144:23–34.

Mestres-Missé A, Turner R, Friederici AD (2012) An anterior–posterior gradient of cognitive control within the dorsomedial striatum. NeuroImage 62:41–47.

Michalareas G, Vezoli J, van Pelt S, Schoffelen J-M, Kennedy H, Fries P (2016) Alpha-Beta and Gamma Rhythms Subserve Feedback and Feedforward Influences among Human Visual Cortical Areas. Neuron 89:384–397.

Middleton FA, Strick PL (1994) Anatomical evidence for cerebellar and basal ganglia involvement in higher cognitive function. Science 266:458–461.

Middleton FA, Strick PL (2000) Basal ganglia and cerebellar loops: motor and cognitive circuits. Brain Res Brain Res Rev 31:236–250.

Middleton FA, Strick PL (2001) A revised neuroanatomy of frontal-subcortical circuits. In, pp 44–58. The Guilford Press New York.

Middleton FA, Strick PL (2002) Basal-ganglia "projections" to the prefrontal cortex of the primate. Cereb Cortex 12:926–935.

Miletić S, Turner BM, Forstmann BU (2017) Parameter recovery for the Leaky Competing Accumulator model. Journal of Mathematical Psychology 76:25–50.

Mink JW (1996) The basal ganglia: focused selection and inhibition of competing motor programs. Progress in Neurobiology 50:381–425.

Mittner M, Boekel W, Tucker AM, Turner BM, Heathcote A, Forstmann BU (2014) When the brain takes a break: a model-based analysis of mind wandering. The Journal of Neuroscience 34:16286–16295.

Molenaar PCM (2004) A Manifesto on Psychology as Idiographic Science: Bringing the Person Back Into Scientific Psychology, This Time Forever. Measurement: Interdisciplinary Research & Perspective 2:201–218.

Monchi O, Petrides M, Strafella AP, Worsley KJ, Doyon J (2006) Functional role of the basal ganglia in the planning and execution of actions. Ann Neurol 59:257–264.

Montgomery E Jr (2012) The epistemology of deep brain stimulation and neuronal pathophysiology. Front Integr Neurosci 6.

Montgomery EB Jr, Gale JT (2008) Mechanisms of action of deep brain stimulation (DBS). Neuroscience and Biobehavioral Reviews 32:388–407.

Moore EF (1956) Gedanken-experiments on sequential machines. Automata studies 34:129–153.

Morelli JN, Runge VM, Ai F, Attenberger U, Vu L, Schmeets SH, Nitz WR, Kirsch JE (2011) An image-based approach to understanding the physics of MR artifacts. RadioGraphics 31:849–866.

Morey RD, Rouder JN (2015) BayesFactor: An R package for computing Bayes factors in common research designs. bayesfactorpclr-forger-projectorg Available at: http://bayesfactorpcl.r-forge.r-project.org/ [Accessed January 15, 2015].

Morrow BA, Roth RH, Redmond DE Jr., Sladek JR Jr., Elsworth JD (2007) Apoptotic natural cell death in developing primate dopamine midbrain neurons occurs during a restricted period in the second trimester of gestation. Experimental Neurology 204:802–807.

Mottershead JP, Schmierer K, Clemence M, Thornton JS, Scaravilli F, Barker GJ, Tofts PS, Newcombe J, Cuzner ML, Ordidge RJ, McDonald WI, Miller DH (2003) High field MRI correlates of myelin content and axonal density in multiple sclerosis. Journal of Neurology 250:1293–1301.

Mulcahy P, O'Doherty A, Paucard A, O'Brien T, Kirik D, Dowd E (2012) Development and characterisation of a novel rat model of Parkinson's disease induced by sequential intranigral administration of AAV-α-synuclein and the pesticide, rotenone. Neuroscience 203:170–179.

Mulder MJ, van Maanen L, Forstmann BU (2014) Perceptual decision neurosciences - a model-based review. Neuroscience 277:872–884.

Mulder MJ, Wagenmakers E-J, Ratcliff R, Boekel W, Forstmann BU (2012) Bias in the Brain: A Diffusion Model Analysis of Prior Probability and Potential Payoff. The Journal of Neuroscience 32:2335–2343.

Mumford JA, Turner BO, Ashby FG, Poldrack RA (2012) Deconvolving BOLD activation in event-related designs for multivoxel pattern classification analyses. NeuroImage 59:2636–2643.

Murphy K, Bodurka J, Bandettini PA (2007) How long to scan? The relationship between fMRI temporal signal to noise ratio and necessary scan duration. NeuroImage 34:565–574.

Murray GK, Corlett PR, Clark L, Pessiglione M, Blackwell AD, Honey G, Jones PB, Bullmore ET, Robbins TW, Fletcher PC (2007) Substantia nigra/ventral tegmental reward prediction error disruption in psychosis. Mol Psychiatry 13:267–276.

Nagatsu T, Levitt M, Udenfriend S (1964) Tyrosine Hydroxylase: the Initial Step in Norepinephrine Biosynthesis. J Biol Chem 239:2910–2917.

Nair R, Lauks J, Jung S, Cooke NE, de Wit H, Brose N, Kilimann MW, Verhage M, Rhee J (2013) Neurobeachin regulates neurotransmitter receptor trafficking to synapses. J Cell Biol 200:61–80.

Nakano K (2000) Neural circuits and topographic organization of the basal ganglia and related regions. Brain Dev 22 Suppl 1:S5–S16.

Neath AA, Cavanaugh JE (2006) A Bayesian approach to the multiple comparisons problem. Journal of

Data Science 4:131–146.

Nieuwenhuis S, Forstmann BU, Wagenmakers E-J (2011) Erroneous analyses of interactions in neuroscience: a problem of significance. Nature Publishing Group 14:1105–1107.

Nieuwenhuis S, Ridderinkhof KR, Talsma D, Coles MGH, Holroyd CB, Kok A, van der Molen MW (2002) A computational account of altered error processing in older age: dopamine and the error-related negativity. Cognitive, Affective, & Behavioral Neuroscience 2:19–36.

Nieuwenhuys R (2012) The myeloarchitectonic studies on the human cerebral cortex of the Vogt–Vogt school, and their significance for the interpretation of functional neuroimaging data. Brain Struct Funct 218:303–352.

Nishimoto S, Vu AT, Naselaris T, Benjamini Y, Bin Yu, Gallant JL (2011) Reconstructing Visual Experiences from Brain Activity Evoked by Natural Movies. Curr Biol 21:1641–1646.

Niv Y (2009) Journal of Mathematical Psychology. Journal of Mathematical Psychology 53:139–154.

Noorbaloochi S, Sharon D, McClelland JL (2015) Payoff Information Biases a Fast Guess Process in Perceptual Decision Making under Deadline Pressure: Evidence from Behavior, Evoked Potentials, and Quantitative Model Comparison. The Journal of Neuroscience 35:10989–11011.

Norris DG (2006) Principles of magnetic resonance assessment of brain function. J Magn Reson Imaging 23:794–807.

O'Reilly JX, Woolrich MW, Behrens TEJ, Smith SM, Johansen-Berg H (2012) Tools of the trade: psychophysiological interactions and functional connectivity. Social Cognitive and Affective Neuroscience 7:604–609.

O'Toole AJ, Jiang F, Abdi H, Pénard N, Dunlop JP, Parent MA (2007) Theoretical, statistical, and practical perspectives on pattern-based classification approaches to the analysis of functional neuroimaging data. Journal of Cognitive Neuroscience 19:1735–1752.

Obeso JA, Rodríguez-Oroz MC, Benitez-Temino B, Blesa FJ, Guridi J, Marin C, Rodriguez M (2008) Functional organization of the basal ganglia: Therapeutic implications for Parkinson's disease. Mov Disord 23:S548–S559.

Ogawa S, Lee TM, Kay AR, Tank DW (1990) Brain magnetic resonance imaging with contrast dependent on blood oxygenation. Proc Natl Acad Sci USA 87:9868–9872.

Oldfield RC (1971) The assessment and analysis of handedness: the Edinburgh inventory. Neuropsychologia 9:97–113.

O'Doherty JP, Dayan P, Friston KJ, Critchley H, Dolan RJ (2003) Temporal difference models and reward-related learning in the human brain. Neuron 38:329–337.

O'Doherty JP, Dayan P, Schultz J, Deichmann R, Friston KJ, Dolan RJ (2004) Dissociable roles of ventral and dorsal striatum in instrumental conditioning. Science 304:452–454.

O'Reilly JX, Mars RB (2011) Computational neuroimaging: localising Greek letters? Comment on Forstmann et al. Trends in Cognitive Sciences 15:450.

Padgett CL, Lalive AL, Tan KR, Terunuma M, Munoz MB, Pangalos MN, Martínez-Hernández J, Watanabe M, Moss SJ, Luján R, Lüscher C, Slesinger PA (2012) Methamphetamine-Evoked Depression of GABA. Neuron 73:978–989.

Parent A (1990) Extrinsic connections of the basal ganglia. Trends in Neurosciences 13:254–258.

Parent A, Hazrati L-N (1995a) Functional anatomy of the basal ganglia. I. The cortico-basal ganglia-thalamo-cortical loop. Brain Research Reviews 20:91–127.

Parent A, Hazrati L-N (1995b) Functional anatomy of the basal ganglia. II. The place of subthalamic nucleus and external pallidium in basal ganglia circuitry. Brain Research Reviews 20:128–154.

Parent A, Hazrati LN (1993) Anatomical aspects of information processing in primate basal ganglia. Trends in Neurosciences 16:111–116.

Parent A, Smith Y (1987) Organization of efferent projections of the subthalamic nucleus in the squirrel monkey as revealed by retrograde labeling methods. Brain Research 436:296–310.

Parent M, Wallman M-J, Descarries L (2010) Distribution and ultrastructural features of the serotonin innervation in rat and squirrel monkey subthalamic nucleus. European Journal of Neuroscience 31:1233–1242.

Park HJ, Kim CH, Park ES, Park B, Oh SR, Oh MK, Park CI, Lee JD (2013) Increased GABA-A Receptor Binding and Reduced Connectivity at the Motor Cortex in Children with Hemiplegic Cerebral Palsy: A Multimodal Investigation Using 18F-Fluoroflumazenil PET, Immunohistochemistry, and MR Imaging. Journal of Nuclear Medicine 54:1263–1269.

Parkes LM, Schwarzbach JV, Bouts AA, Deckers RHR, Pullens P, Kerskens CM, Norris DG (2005) Quantifying the spatial resolution of the gradient echo and spin echo BOLD response at 3 Tesla. Magnetic Resonance Medicine 54:1465–1472.

Patenaude B, Smith SM, Kennedy DN, Jenkinson M (2011) A Bayesian model of shape and appearance for subcortical brain segmentation. NeuroImage 56:907–922.

Pauli WM, Larsen T, Collette S, Tyszka JM, Seymour B, O'Doherty JP (2015) Distinct Contributions of Ventromedial and Dorsolateral Subregions of the Human Substantia Nigra to Appetitive and Aversive Learning. The Journal of Neuroscience 35:14220–14233.

Penke L, Hernandéz MCV, Maniega SM, Gow AJ, Murray C, Starr JM, Bastin ME, Deary IJ, Wardlaw JM (2012) Brain iron deposits are associated with general cognitive ability and cognitive aging. Neurobiology of Aging 33:510–517.e512.

Percheron G, Filion M (1991) Parallel processing in the basal ganglia: up to a point. Trends in Neurosciences 14:55–59.

Perez RG, Waymire JC, Lin E, Liu JJ, Guo F (2002) A role for α-synuclein in the regulation of dopamine biosynthesis. The Journal of Neuroscience 22:3090–3099.

Peters AM, Brookes MJ, Hoogenraad FG, Gowland PA, Francis ST, Morris PG, Bowtell R (2007) T2* measurements in human brain at 1.5, 3 and 7 T. Magnetic Resonance Imaging 25:748–753.

Péron J, Frühholz S, Vérin M, Grandjean D (2013) Subthalamic nucleus: A key structure for emotional component synchronization in humans. Neuroscience and Biobehavioral Reviews 37:358–373.

Pfeuffer J, van de Moortele P-F, Yacoub E, Shmuel A, Adriany G, Andersen P, Merkle H, Garwood M, Uğurbil K, Hu X (2002) Zoomed Functional Imaging in the Human Brain at 7 Tesla with Simultaneous High Spatial and High Temporal Resolution. NeuroImage 17:272–286.

Plaha P, Ben-Shlomo Y, Patel NK, Gill SS (2006) Stimulation of the caudal zona incerta is superior to stimulation of the subthalamic nucleus in improving contralateral parkinsonism. Brain 129:1732–1747.

Plantinga BR, Temel Y, Roebroeck A, Uludağ K, Ivanov D, Kuijf ML, Haar Romenij ter BM (2014) Ultra-high field magnetic resonance imaging of the basal ganglia and related structures. Frontier in Human Neuroscience 8:876.

Polders DL, Leemans A, Hendrikse J, Donahue MJ, Luijten PR, Hoogduin JM (2011) Signal to noise ratio and uncertainty in diffusion tensor imaging at 1.5, 3.0, and 7.0 Tesla. J Magn Reson Imaging 33:1456–1463.

Poldrack RA (2006) Region of interest analysis for fMRI. Social Cognitive and Affective Neuroscience 2:67–70.

Poldrack RA (2015) Developmental Cognitive Neuroscience. Accident Analysis and Prevention 11:12–17.

Poldrack RA, Fletcher PC, Henson RN, Worsley KJ, Brett M, Nichols TE (2008) Guidelines for reporting an fMRI study. NeuroImage 40:409–414.

Poldrack RA, Gorgolewski KJ (2014) Making big data open: data sharing in neuroimaging. Nature Publishing Group 17:1510–1517.

Poldrack RA, Mumford JA, Nichols TE (2011) Statistical modelling: Single subject analysis. In: Handbook of Functional MRI analysis, 1st ed. (Poldrack RA, Mumford JA, Nichols TE, eds), pp 70–99. Cambridge: Cambridge Univ Press.

Poldrack RA, Mumford JA, Schonberg T, Kalar D, Barman B, Yarkoni T (2012) Discovering Relations Between Mind, Brain, and Mental Disorders Using Topic Mapping Sporns O, ed. PLoS Comput Biol 8:e1002707.

Polimeni JR, Fischl B, Greve DN, Wald LL (2010) Laminar analysis of 7T BOLD using an imposed spatial activation pattern in human V1. NeuroImage 52:1334–1346.

Poline J-B, Breeze JL, Ghosh S, Gorgolewski K, Halchenko YO, Hanke M, Haselgrove C, Helmer KG, Keator DB, Marcus DS, Poldrack RA, Schwartz Y, Ashburner J, Kennedy DN (2012) Data sharing in neuroimaging research. Frontiers in Neuroinformatics 6:9.

Pollock H, Hutchings M, Weller RO, Zhang ET (1997) Perivascular spaces in the basal ganglia of the human brain: their relationship to lacunes. J Anat 191 (Pt 3):337–346.

Preuschoff K, Bossaerts P, Quartz SR (2006) Neural Differentiation of Expected Reward and Risk in Human Subcortical Structures. Neuron 51:381–390.

Prodoehl J, Yu H, Wasson P, Corcos DM, Vaillancourt DE (2008) Effects of Visual and Auditory Feedback on Sensorimotor Circuits in the Basal Ganglia. Journal of Neurophysiology 99:3042–3051.

Pruessmann KP, Weiger M, Scheidegger MB, Boesiger P (1999) SENSE: sensitivity encoding for fast MRI. Magn Reson Med 42:952–962.

Purcell BA, Heitz RP, Cohen JY, Schall JD, Logan GD, Palmeri TJ (2010) Neurally constrained modeling of perceptual decision making. Psychological Review 117:1113–1143.

Purcell BA, Schall JD, Logan GD, Palmeri TJ (2012) From salience to saccades: multiple-alternative gated stochastic accumulator model of visual search. The Journal of Neuroscience 32:3433–3446.

Purushothuman S, Marotte L, Stowe S, Johnstone DM, Stone J (2013) The Response of Cerebral Cortex to Haemorrhagic Damage: Experimental Evidence from a Penetrating Injury Model Norris CM, ed. PLoS ONE 8:e59740.

Qin Y, Sohn MH, Anderson JR, Stenger VA, Fissell K, Goode A, Carter CS (2003) Predicting the practice effects on the blood oxygenation level-dependent (BOLD) function of fMRI in a symbolic manipulation task. Proc Natl Acad Sci USA 100:4951–4956.

R Core Team (2015) R: A Language and Environment for Statistical Computing. Vienna, Austria: R Foundation for Statistical Computing.

Raadsheer FC, Sluiter AA, Ravid R, Tilders FJ, Swaab DF (1993) Localization of corticotropin-releasing hormone (CRH) neurons in the paraventricular nucleus of the human hypothalamus; age-dependent colocalization with vasopressin. Brain Research 615:50–62.

Rakic P (2009) Evolution of the neocortex: a perspective from developmental biology. Nat Rev Neurosci 10:724–735.

Ramsey IS, DeFelice LJ (2002) Serotonin transporter function and pharmacology are sensitive to expression level: evidence for an endogenous regulatory factor. J Biol Chem 277:14475–14482.

Ratcliff R (1978) A theory of memory retrieval. Psychological Review 85:59–108.

Ratcliff R, McKoon G (2008) The diffusion decision model: theory and data for two-choice decision tasks. Neural Comput 20:873–922.

Ratcliff R, Rouder JN (1998) Modeling response times for two-choice decisions. Psychological Science 9:347–356.

Ratcliff R, Tuerlinckx F (2002) Estimating parameters of the diffusion model: approaches to dealing with contaminant reaction times and parameter variability. Psychon Bull Rev 9:438–481.

Ravid R, Van Zwieten EJ, Swaab DF (1992) Brain banking and the human hypothalamus—factors to match for, pitfalls and potentials. Progress in brain research 93:83–95.

Ray Li C-S, Yan P, Sinha R, Lee T-W (2008) Subcortical processes of motor response inhibition during a stop signal task. NeuroImage 41:1352–1363.

Redgrave P, Prescott TJ, Gurney K (1999) The basal ganglia: a vertebrate solution to the selection problem? Neuroscience 89:1009–1023.

Redgrave P, Rodriguez M, Smith Y, Rodriguez-Oroz MC, Lehericy S, Bergman H, Agid Y, DeLong MR, Obeso

JA (2010) Goal-directed and habitual control in the basal ganglia: implications for Parkinson's disease. Nat Rev Neurosci 11:760–772.

Ribic A, Zhang M, Schlumbohm C, Mätz-Rensing K, Uchanska-Ziegler B, Flügge G, Zhang W, Walter L, Fuchs E (2010) Neuronal MHC Class I Molecules are Involved in Excitatory Synaptic Transmission at the Hippocampal Mossy Fiber Synapses of Marmoset Monkeys. Cell Mol Neurobiol 30:827–839.

Robinson DA (1992) Implications of neural networks for how we think about brain function. Behavioral and brain sciences.

Robinson S, Basso G, Soldati N, Sailer U, Jovicich J, Bruzzone L, Kryspin-Exner I, Bauer H, Moser E (2009) A resting state network in the motor control circuit of the basal ganglia. BMC Neurosci 10:137.

Robitaille P-M, Berliner L (2007) Ultra high field magnetic resonance imaging. Springer Science & Business Media.

Rodriguez-Contreras A (2005) Axodendritic Contacts onto Calcium/Calmodulin-Dependent Protein Kinase Type II-Expressing Neurons in the Barn Owl Auditory Space Map. The Journal of Neuroscience 25:5611–5622.

Rodriguez-Oroz MC, Jahanshahi M, Krack P, Litvan I, Macias R, Bezard E, Obeso JA (2009) Initial clinical manifestations of Parkinson's disease: features and pathophysiological mechanisms. The Lancet Neurology 8:1128–1139.

Rodriguez-Oroz MC, Rodriguez M, Guridi J, Mewes K, Chockkman V, Vitek J, DeLong MR, Obeso JA (2001) The subthalamic nucleus in Parkinson's disease: somatotopic organization and physiological characteristics. Brain 124:1777–1790.

Rothmond DA, Weickert CS, Webster MJ (2012) Developmental changes in human dopamine neurotransmission: cortical receptors and terminators. BMC Neurosci 13:18.

Rouault TA (2001) Iron on the brain. nature genetics 28:299–299.

Rouder JN, Morey RD, Speckman PL, Province JM (2012) Default Bayes factors for ANOVA designs. Journal of Mathematical Psychology 56:356–374.

Rumelhart DE, Hinton GE, McClelland JL (1986a) A General Framework for Parallel Distributed Processing. In: Parallel Distributed Processing: Explorations in the Microstructure of Cognition (Vol. 1) (Rumelhart DE, McClelland JL, the PDP Research Group, eds), pp 45–76. Cambridge, MA: MIT Press.

Rumelhart DE, Hinton GE, Williams RJ (1986b) Learning Internal Representations by Error Propagation. In: Parallel Distributed Processing: Explorations in the Microstructure of Cognition (Vol. 1) (Rumelhart DE, McClelland JL, the PDP Research Group, eds), pp 318–362. Cambridge, MA: MIT Press.

Sacchet MD, Knutson B (2013) Spatial smoothing systematically biases the localization of reward-related brain activity. NeuroImage 66:270–277.

Sager TN, Hansen AJ, Laursen H (2000) Correlation between N-acetylaspartate levels and histopathologic changes in cortical infarcts of mice after middle cerebral artery occlusion. J Cereb Blood Flow Metab 20:780–788.

Saint-Cyr JA, Hoque T, Pereira LCM, Dostrovsky JO, Hutchison WD, Mikulis DJ, Abosch A, Sime E, Lang AE, Lozano AM (2002) Localization of clinically effective stimulating electrodes in the human subthalamic nucleus on magnetic resonance imaging. Journal of Neurosurgery 97:1152–1166.

Saranathan M, Tourdias T, Bayram E, Ghanouni P, Rutt BK (2014) Optimization of white-matter-nulled magnetization prepared rapid gradient echo (MP-RAGE) imaging. Magnetic Resonance Medicine 73:1786–1794.

Sareen D, Ebert AD, Heins BM, McGivern JV, Ornelas L, Svendsen CN (2012) Inhibition of Apoptosis Blocks Human Motor Neuron Cell Death in a Stem Cell Model of Spinal Muscular Atrophy Gillingwater TH, ed. PLoS ONE 7:e39113.

Sasahira M, Asakura T, Niiro M, Haruzono A, Hirakawa W, Matsumoto T, Fujimoto T (1995) Functional magnetic resonance imaging of the human motor cortex. Neurol Med Chir (Tokyo) 35:277–284.

Sato F, Parent M, Levesque M, Parent A (2000) Axonal branching pattern of neurons of the subthalamic

nucleus in primates. J Comp Neurol 424:142–152.

Saunders GC, Horigan V, Tout AC, Windl O (2007) Identification of a proteinase K resistant protein for use as an internal positive control marker in PrP Western blotting. Research in Veterinary Science 83:157–164.

Schall JD (2004) On Building a Bridge Between Brain and Behavior. Annu Rev Psychol 55:23–50.

Schäfer A, Forstmann BU, Neumann J, Wharton S, Mietke A, Bowtell R, Turner R (2011) Direct visualization of the subthalamic nucleus and its iron distribution using high-resolution susceptibility mapping. Human Brain Mapping 33:2831–2842.

Schäfer A, Wharton S, Gowland P, Bowtell R (2009) Using magnetic field simulation to study susceptibility-related phase contrast in gradient echo MRI. NeuroImage 48:126–137.

Schiffmann SN, Cheron G, Lohof A, d'Alcantara P, Meyer M, Parmentier M, Schurmans S (1999) Impaired motor coordination and Purkinje cell excitability in mice lacking calretinin. Proc Natl Acad Sci USA 96:5257–5262.

Schlaier JR, Habermeyer C, Warnat J, Lange M, Janzen A, Hochreiter A, Proescholdt M, Brawanski A, Fellner C (2011) Discrepancies between the MRI- and the electrophysiologically defined subthalamic nucleus. Acta Neurochir 153:2307–2318.

Schmierer K, Wheeler-Kingshott CAM, Tozer DJ, Boulby PA, Parkes HG, Yousry TA, Scaravilli F, Barker GJ, Tofts PS, Miller DH (2008) Quantitative magnetic resonance of postmortem multiple sclerosis brain before and after fixation. Magnetic Resonance Medicine 59:268–277.

Schott BH (2004) Activation of Midbrain Structures by Associative Novelty and the Formation of Explicit Memory in Humans. Learning & Memory 11:383–387.

Schott BH, Minuzzi L, Krebs RM, Elmenhorst D, Lang M, Winz OH, Seidenbecher CI, Coenen HH, Heinze HJ, Zilles K, Duzel E, Bauer A (2008) Mesolimbic Functional Magnetic Resonance Imaging Activations during Reward Anticipation Correlate with Reward-Related Ventral Striatal Dopamine Release. The Journal of Neuroscience 28:14311–14319.

Schultz W, Dayan P, Montague PR (1997) A neural substrate of prediction and reward. Science 275:1593–1599.

Schwarz G (1978) Estimating the dimension of a model. The Annals of Statistics 6:461–464.

Schweser F, Deistung A, Lehr BW, Reichenbach JR (2011) Quantitative imaging of intrinsic magnetic tissue properties using MRI signal phase: An approach to in vivo brain iron metabolism? NeuroImage 54:2789–2807.

Schweser F, Deistung A, Reichenbach JR (2016) Foundations of MRI phase imaging and processing for Quantitative Susceptibility Mapping (QSM). Zeitschrift fßr Medizinische Physik 26:6–34.

Scientific Data (2014) More bang for your byte. Sci Data 1:140010.

Seabold S, Perktold J (2010) Statsmodels: Econometric and statistical modeling with python. In, pp 57–61.

Sengupta R, Burbassi S, Shimizu S, Cappello S, Vallee RB, Rubin JB, Meucci O (2009) Morphine Increases Brain Levels of Ferritin Heavy Chain Leading to Inhibition of CXCR4-Mediated Survival Signaling in Neurons. The Journal of Neuroscience 29:2534–2544.

Seo S, Leitch B (2014) Altered thalamic GABA A-receptor subunit expression in the stargazer mouse model of absence epilepsy. Epilepsia 55:224–232.

Serafeim A, Grafton G, Chamba A, Gregory CD, Blakely RD, Bowery NG, Barnes NM, Gordon J (2002) 5-Hydroxytryptamine drives apoptosis in biopsylike Burkitt lymphoma cells: reversal by selective serotonin reuptake inhibitors. Blood 99:2545–2553.

Setsompop K, Feinberg DA, Polimeni JR (2016) Rapid brain MRI acquisition techniques at ultra-high fields. NMR Biomed 29:1198–1221.

Shapiro EM, Sharer K, Skrtic S, Koretsky AP (2006) In vivo detection of single cells by MRI. Magn Reson Med 55:242–249.

Shattuck DW, Mirza M, Adisetiyo V, Hojatkashani C, Salamon G, Narr KL, Poldrack RA, Bilder RM, Toga AW

(2008) Construction of a 3D probabilistic atlas of human cortical structures. NeuroImage 39:1064–1080.

Shen W-G, Wang H-Y, Lin Z-G, Shen H, Chen X-G, Fu Y-L, Gao W-P (2009) Stereotactic localization and visualization of the subthalamic nucleus. Chinese medical journal 122:2438–2443.

Shenoy P, Yu AJ (2011) Rational decision-making in inhibitory control. Front Hum Neurosci 5:48.

Shi SR, Cote RJ, Taylor CR (1997) Antigen retrieval immunohistochemistry: past, present, and future. J Histochem Cytochem 45:327–343.

Shi SR, Key ME, Kalra KL (1991) Antigen retrieval in formalin-fixed, paraffin-embedded tissues: an enhancement method for immunohistochemical staining based on microwave oven heating of tissue sections. J Histochem Cytochem 39:741–748.

Shmuel A, Yacoub E, Chaimow D, Logothetis NK, Uğurbil K (2007) Spatio-temporal point-spread function of fMRI signal in human gray matter at 7 Tesla. NeuroImage 35:539–552.

Shohamy D, Myers CE, Kalanithi J, Gluck MA (2008) Basal ganglia and dopamine contributions to probabilistic category learning. Neuroscience and Biobehavioral Reviews 32:219–236.

Sladky R, Friston KJ, Tröstl J, Cunnington R, Moser E, Windischberger C (2011) Slice-timing effects and their correction in functional MRI. NeuroImage 58:588–594.

Smith SM (2002) Fast robust automated brain extraction. Human Brain Mapping 17:143–155.

Smith SM, Fox PT, Miller KL, Glahn DC, Fox PM, Mackay CE, Filippini N, Watkins KE, Toro R, Laird AR (2009) Correspondence of the brain's functional architecture during activation and rest. Proc Natl Acad Sci USA 106:13040–13045.

Smith SM, Jenkinson M, Woolrich MW, Beckmann CF, Behrens TEJ, Johansen-Berg H, Bannister PR, De Luca M, Drobnjak I, Flitney DE, Others (2004) Advances in functional and structural MR image analysis and implementation as FSL. NeuroImage 23:S208–S219.

Sodickson DK, Manning WJ (1997) Simultaneous acquisition of spatial harmonics (SMASH): fast imaging with radiofrequency coil arrays. Magn Reson Med 38:591–603.

Sohn MH, Goode A, Stenger VA, Carter CS, Anderson JR (2003) Competition and representation during memory retrieval: Roles of the prefrontal cortex and the posterior parietal cortex. Proc Natl Acad Sci USA 100:7412–7417.

Solem JE (2012) Programming Computer Vision with Python. Sebastopol, California, USA: O'Reilly Media.

Sporns O (2013) The human connectome: Origins and challenges. NeuroImage 80:53–61.

Sporns O, Tononi G, Kötter R (2005) The Human Connectome: A Structural Description of the Human Brain. PLoS Comput Biol 1:e42.

Spraker MB, Yu H, Corcos DM, Vaillancourt DE (2007) Role of Individual Basal Ganglia Nuclei in Force Amplitude Generation. Journal of Neurophysiology 98:821–834.

Steingroever H, Wetzels R, Wagenmakers E-J (2016) Bayes factors for reinforcement-learning models of the Iowa gambling task. Decision 3:115–131.

Stelzer J, Chen Y, Turner R (2013) Statistical inference and multiple testing correction in classification-based multi-voxel pattern analysis (MVPA): Random permutations and cluster size control. NeuroImage 65:69–82.

Stelzer J, Lohmann G, Mueller K, Buschmann T, Turner R (2014) Deficient approaches to human neuroimaging. Front Hum Neurosci 8:462.

Stephens M, Balding DJ (2009) Bayesian statistical methods for genetic association studies. Nature Reviews Genetics 10:681–690.

Storn R, Price K (1997) Differential evolution–a simple and efficient heuristic for global optimization over continuous spaces. Journal of global optimization 11:341–359.

Strotmann B, Heidemann RM, Anwander A, Weiss M, Trampel R, Villringer A, Turner R (2013) High-resolution MRI and diffusion-weighted imaging of the human habenula at 7 tesla. J Magn Reson Imaging 39:1018–1026.

Stucht D, Danishad KA, Schulze P, Godenschweger F, Zaitsev M, Speck O (2015) Highest Resolution In Vivo Human Brain MRI Using Prospective Motion Correction Kassubek J, ed. PLoS ONE 10:e0133921.

Stüber C, Morawski M, Schäfer A, Labadie C, Wähnert M, Leuze C, Streicher M, Barapatre N, Reimann K, Geyer S, Spemann D, Turner R (2014) Myelin and iron concentration in the human brain: A quantitative study of MRI contrast. NeuroImage 93:95–106.

Sullivan EV, Adalsteinsson E, Rohlfing T, Pfefferbaum A (2009) Relevance of Iron Deposition in Deep Gray Matter Brain Structures to Cognitive and Motor Performance in Healthy Elderly Men and Women: Exploratory Findings. Brain Imaging Behav 3:167–175.

Sun C, Zhang L, Chen G (2013) An unexpected role of neuroligin-2 in regulating KCC2 and GABA functional switch. Mol Brain 6:23.

Sutton RS, Barto AG (1998) Introduction to Reinforcement Learning, 1st ed. Cambridge, MA, USA: MIT Press.

Szeliski R (2010) Computer Vision: Algorithms and Applications, 1st ed. New York, NY, USA: Springer-Verlag New York, Inc.

Tabelow K, Piëch V, Polzehl J, Voss HU (2009) High-resolution fMRI: Overcoming the signal-to-noise problem. Journal of Neuroscience Methods 178:357–365.

Tardif CL, Schäfer A, Trampel R, Villringer A, Turner R, Bazin P-L (2016) Open Science CBS Neuroimaging Repository: Sharing ultra-high-field MR images of the brain. NeuroImage 124:1143–1148.

Teller DY (1984) Linking propositions. Vision Research 24:1233–1246.

Temel Y, Blokland A, Ackermans L, Boon P, Kranen-Mastenbroek VHJM, Beuls EAM, Spincemaille GH, Visser-Vandewalle V (2005a) Differential effects of subthalamic nucleus stimulation in advanced Parkinson disease on reaction time performance. Exp Brain Res 169:389–399.

Temel Y, Blokland A, Steinbusch HWM, Visser-Vandewalle V (2005b) The functional role of the subthalamic nucleus in cognitive and limbic circuits. Progress in Neurobiology 76:393–413.

Temel Y, Kessels A, Tan S, Topdag A, Boon P, Visser-Vandewalle V (2006) Behavioural changes after bilateral subthalamic stimulation in advanced Parkinson disease: A systematic review. Parkinsonism & Related Disorders 12:265–272.

Temel Y, Visser-Vandewalle V, Aendekerk B, Rutten B, Tan S, Scholtissen B, Schmitz C, Blokland A, Steinbusch HWM (2005c) Acute and separate modulation of motor and cognitive performance in parkinsonian rats by bilateral stimulation of the subthalamic nucleus. Experimental Neurology 193:43–52.

Thevenaz P, Ruttimann UE, Unser M (1998) A pyramid approach to subpixel registration based on intensity. IEEE Trans Image Process 7:27–41.

Thivierge J-P, Marcus GF (2007) The topographic brain: from neural connectivity to cognition. Trends in Neurosciences 30:251–259.

Thomas C, Ye FQ, Irfanoglu MO, Modi P, Saleem KS, Leopold DA, Pierpaoli C (2014) Anatomical accuracy of brain connections derived from diffusion MRI tractography is inherently limited. Proc Natl Acad Sci USA 111:16574–16579.

Thomsen MS, Hay-Schmidt A, Hansen HH, Mikkelsen JD (2010) Distinct Neural Pathways Mediate 7 Nicotinic Acetylcholine Receptor-Dependent Activation of the Forebrain. Cerebral Cortex 20:2092–2102.

Tibshirani R, Walther G, Hastie T (2001) Estimating the number of clusters in a data set via the gap statistic. J R Stat Soc Series B Stat Methodol 63:411–423.

Tourdias T, Saranathan M, Levesque IR, Su J, Rutt BK (2014) Visualization of intra-thalamic nuclei with optimized white-matter-nulled MPRAGE at 7T. NeuroImage 84:534–545.

Trampel R, Bazin PL, Schäfer A, Heidemann RM, Ivanov D, Lohmann G, Geyer S, Turner R (2012) Laminar-specific fingerprints of different sensorimotor areas obtained during imagined and actual finger tapping. Proc Int Soc Magn Reson Med 20:663.

Triantafyllou C, Hoge RD, Krueger G, Wiggins CJ, Potthast A, Wiggins GC, Wald LL (2005) Comparison of physiological noise at 1.5 T, 3 T and 7 T and optimization of fMRI acquisition parameters. NeuroImage 26:243–250.

Triantafyllou C, Hoge RD, Wald LL (2006) Effect of spatial smoothing on physiological noise in high-resolution fMRI. NeuroImage 32:551–557.

Turner BM, Forstmann BU, Love BC, Palmeri TJ (2017) Approaches to analysis in model-based cognitive neuroscience. Journal of Mathematical Psychology 76:65–79.

Turner BM, Forstmann BU, Wagenmakers E-J, Brown SD, Sederberg PB, Steyvers M (2013) A Bayesian framework for simultaneously modeling neural and behavioral data. NeuroImage 72:193–206.

Turner BM, Rodriguez CA, Norcia TM, McClure SM, Steyvers M (2016) Why more is better: Simultaneous modeling of EEG, fMRI, and behavioral data. NeuroImage 128:96–115.

Turner BM, Sederberg PB (2014) A generalized, likelihood-free method for posterior estimation. Psychon Bull Rev 21:227–250.

Turner BM, van Maanen L, Forstmann BU (2015) Informing cognitive abstractions through neuroimaging: the neural drift diffusion model. Psychological Review 122:312–336.

Turner R (2016) Uses, misuses, new uses and fundamental limitations of magnetic resonance imaging in cognitive science. Philosophical Transactions of the Royal Society B: Biological Sciences 371:20150349.

Turner R, Geyer S (2014) Comparing like with like: the power of knowing where you are. Brain Connectivity 4:547–557.

Uludağ K, Müller-Bierl B, Uğurbil K (2009) An integrative model for neuronal activity-induced signal changes for gradient and spin echo functional imaging. NeuroImage 48:150–165.

Usher M, McClelland JL (2001) The time course of perceptual choice: the leaky, competing accumulator model. Psychological Review 108:550–592.

Vaillancourt DE, Mayka MA, Thulborn KR, Corcos DM (2004) Subthalamic nucleus and internal globus pallidus scale with the rate of change of force production in humans. NeuroImage 23:175–186.

Vaillancourt DE, Yu H, Mayka MA, Corcos DM (2007) Role of the basal ganglia and frontal cortex in selecting and producing internally guided force pulses. NeuroImage 36:793–803.

Van den Haute C, Spittaels K, Van Dorpe J, Lasrado R, Vandezande K, Laenen I, Geerts H, Van Leuven F (2001) Coexpression of Human cdk5 and Its Activator p35 with Human Protein Tau in Neurons in Brain of Triple Transgenic Mice. Neurobiology of Disease 8:32–44.

van der Beek EM, Pool CW, van Eerdenburg FJ, Sluiter AA, van der Donk HA, van den Hurk R, Wiegant VM (1992) Fc-mediated nonspecific staining of the porcine brain with rabbit antisera in immunocytochemistry is prevented by pre-incubation of the sera with proteins A and G. J Histochem Cytochem 40:1731–1739.

Van der Gucht E, Jacobs S, Kaneko T, Vandesande F, Arckens L (2003) Distribution and morphological characterization of phosphate-activated glutaminase-immunoreactive neurons in cat visual cortex. Brain Research 988:29–42.

van der Zwaag W, Da Costa SE, Zürcher NR, Adams RB, Hadjikhani N (2012) A 7 Tesla fMRI Study of Amygdala Responses to Fearful Faces. Brain Topogr 25:125–128.

van der Zwaag W, Francis S, Head K, Peters A, Gowland P, Morris P, Bowtell R (2009) fMRI at 1.5, 3 and 7 T: Characterising BOLD signal changes. NeuroImage 47:1425–1434.

van der Zwaag W, Jorge J, Butticaz D, Gruetter R (2015) Physiological noise in human cerebellar fMRI. Magn Reson Mater Phy 28:485–492.

van der Zwaag W, Schäfer A, Marques JP, Turner R, Trampel R (2016) Recent applications of UHF-MRI in the study of human brain function and structure: a review. NMR Biomed 29:1274–1288.

van Duijn S, Nabuurs RJA, van Rooden S, Maat-Schieman MLC, van Duinen SG, van Buchem MA, van der Weerd L, Natté R (2011) MRI artifacts in human brain tissue after prolonged formalin storage.

Magnetic Resonance Medicine 65:1750–1758.

Van Essen DC et al. (2012) The Human Connectome Project: A data acquisition perspective. NeuroImage 62:2222–2231.

Van Essen DC, Smith SM, Barch DM, Behrens TEJ, Yacoub E, Uğurbil K, Consortium FTW-MH (2013) The WU-Minn Human Connectome Project: An overview. NeuroImage 80:62–79.

van Gerven M (2017) A primer on encoding models in sensory neuroscience. Journal of Mathematical Psychology.

van Maanen L, Brown SD, Eichele T, Wagenmakers E-J, Ho T, Serences J, Forstmann BU (2011) Neural correlates of trial-to-trial fluctuations in response caution. The Journal of Neuroscience 31:17488–17495.

van Veen V, Krug MK, Carter CS (2008) The neural and computational basis of controlled speed-accuracy tradeoff during task performance. Journal of Cognitive Neuroscience 20:1952–1965.

van Vliet EA, Aronica E, Redeker S, Boer K, Gorter JA (2009) Decreased expression of synaptic vesicle protein 2A, the binding site for levetiracetam, during epileptogenesis and chronic epilepsy. Epilepsia 50:422–433.

van Wijk BCM, Beek PJ, Daffertshofer A (2012) Neural synchrony within the motor system: what have we learned so far? Front Hum Neurosci 6:252.

Vandekerckhove J, Matzke D, Wagenmakers E-J (2014) Model comparison and the principle of parsimony. In: The Oxford Handbook of Computational and Mathematical Psychology,, pp 300.

Veeranna, Kaji T, Boland B, Odrljin T, Mohan P, Basavarajappa BS, Peterhoff C, Cataldo A, Rudnicki A, Amin N, Li BS, Pant HC, Hungund BL, Arancio O, Nixon RA (2010) Calpain Mediates Calcium-Induced Activation of the Erk1,2 MAPK Pathway and Cytoskeletal Phosphorylation in Neurons. The American Journal of Pathology 165:795–805.

Verbruggen F, Logan GD (2009) Models of response inhibition in the stop-signal and stop-change paradigms. Neuroscience and Biobehavioral Reviews 33:647–661.

Verhagen J, Wagenmakers E-J (2014) Bayesian tests to quantify the result of a replication attempt. J Exp Psychol Gen 143:1457–1475.

Vermunt MW, Tan SC, Castelijns B, Geeven G, Reinink P, de Bruijn E, Kondova I, Persengiev S, Netherlands Brain Bank, Bontrop R, Cuppen E, de Laat W, Creyghton MP (2016) Epigenomic annotation of gene regulatory alterations during evolution of the primate brain. Nat Neurosci 19:494–503.

Vidal R, Miravalle L, Gao X, Barbeito AG, Baraibar MA, Hekmatyar SK, Widel M, Bansal N, Delisle MB, Ghetti B (2008) Expression of a Mutant Form of the Ferritin Light Chain Gene Induces Neurodegeneration and Iron Overload in Transgenic Mice. The Journal of Neuroscience 28:60–67.

Visser E, Keuken MC, Douaud G, Gaura V, Bachoud-Levi A-C, Remy P, Forstmann BU, Jenkinson M (2016a) Automatic segmentation of the striatum and globus pallidus using MIST: Multimodal Image Segmentation Tool. NeuroImage 125:479–497.

Visser E, Keuken MC, Forstmann BU, Jenkinson M (2016b) Automated segmentation of the substantia nigra, subthalamic nucleus and red nucleus in 7T data at young and old age. NeuroImage 139:324–336.

Voges J, Volkmann J, Allert N, Lehrke R, Koulousakis A, Freund H-J, Sturm V (2002) Bilateral high-frequency stimulation in the subthalamic nucleus for the treatment of Parkinson disease: correlation of therapeutic effect with anatomical electrode position. Journal of Neurosurgery 96:269–279.

Vogt O, Vogt C (1903) Zur anatomischen Gliederung des Cortex cerebri. J Psychol Neurol.

Wagenmakers E-J (2007) A practical solution to the pervasive problems of p values. Psychon Bull Rev 14:779–804.

Wagenmakers E-J, Forstmann BU (2014) Rewarding high-power replication research. Cortex 51:105–106.

Wagenmakers E-J, Wetzels R, Borsboom D, Van Der Maas HLJ, Kievit RA (2012) An Agenda for Purely Confirmatory Research. Perspectives on Psychological Science 7:632–638.

Wandell BA, Winawer J (2011) Vision Research. Vision Research 51:718–737.

Wang H-R (2014) "Publish or perish": Should this still be true for your data? Data in Brief 1:85–86.

Wargo CJ, Gore JC (2013) Localized high-resolution DTI of the human midbrain using single-shot EPI, parallel imaging, and outer-volume suppression at 7T. Magnetic Resonance Imaging 31:810–819.

Waskom M et al. (2015) seaborn: v0.6.0 (June 2015).

Wei W, Rubin JE, Wang XJ (2015) Role of the Indirect Pathway of the Basal Ganglia in Perceptual Decision Making. The Journal of Neuroscience 35:4052–4064.

Weigum SE, García DM, Raabe TD, Christodoulides N, Koke JR (2003) Discrete nuclear structures in actively growing neuroblastoma cells are revealed by antibodies raised against phosphorylated neurofilament proteins. BMC Neurosci 4:6.

Weiskopf N, Callaghan MF, Josephs O, Lutti A, Mohammadi S (2014) Estimating the apparent transverse relaxation time (R2(*)) from images with different contrasts (ESTATICS) reduces motion artifacts. Front Neurosci 8:278.

Weiskopf N, Mohammadi S, Lutti A, Callaghan MF (2015) Advances in MRI-based computational neuroanatomy. Current Opinion in Neurology 28:313–322.

Weiskopf N, Suckling J, Williams G, Correia MM, Inkster B, Tait R, Ooi C, Bullmore ET, Lutti A (2013) Quantitative multi-parameter mapping of R1, PD(*), MT, and R2(*) at 3T: a multi-center validation. Front Neurosci 7:95.

Weiss M, Alkemade A, Keuken MC, Műller-Axt C, Geyer S, Turner R, Forstmann BU (2015) Spatial normalization of ultrahigh resolution 7 T magnetic resonance imaging data of the postmortem human subthalamic nucleus: a multistage approach. Brain Struct Funct 220:1695–1703.

Welter M-L et al. (2014) Optimal target localization for subthalamic stimulation in patients with Parkinson disease. Neurology 82:1352–1361.

Wen X, Yao L, Fan T, Wu X, Liu J (2012) The spatial pattern of basal ganglia network: A resting state fMRI study. Proceedings of 2012 ICME International Conference on Complex Medical Engineering:43–46.

Wharton S, Schäfer A, Bowtell R (2010) Susceptibility mapping in the human brain using threshold-based k-space division. Magnetic Resonance Medicine 63:1292–1304.

Wiecki TV, Sofer I, Frank MJ (2013) HDDM: Hierarchical Bayesian estimation of the Drift-Diffusion Model in Python. Frontiers in Neuroinformatics 7:14.

Wiggins GC, Polimeni JR, Potthast A, Schmitt M, Alagappan V, Wald LL (2009) 96-Channel receive-only head coil for 3 Tesla: Design optimization and evaluation. Magnetic Resonance Medicine 62:754–762.

Wiggins GC, Zhang B, Lattanzi R, Chen G, Sodickson D (2012) The Electric Dipole Array: An Attempt to Match the Ideal Current Pattern for Central SNR at 7 Tesla. Proc Int Soc Magn Reson Med 20:1–1.

Williams NR, Foote KD, Okun MS (2014) Subthalamic Nucleus Versus Globus Pallidus Internus Deep Brain Stimulation: Translating the Rematch Into Clinical Practice. Mov Disord Clin Pract 1:24–35.

Wittmann BC, Bunzeck N, Dolan RJ, Düzel E (2007) Anticipation of novelty recruits reward system and hippocampus while promoting recollection. 38:194–202.

Wittmann BC, Schott BH, Guderian S, Frey JU, Heinze H-J, Düzel E (2005) Reward-Related fMRI Activation of Dopaminergic Midbrain Is Associated with Enhanced Hippocampus- Dependent Long-Term Memory Formation. Neuron 45:459–467.

Wong K-F, Wang X-J (2006) A recurrent network mechanism of time integration in perceptual decisions. The Journal of Neuroscience 26:1314–1328.

Woolrich MW, Jbabdi S, Patenaude B, Chappell M, Makni S, Behrens T, Beckmann C, Jenkinson M, Smith SM (2009) Bayesian analysis of neuroimaging data in FSL. NeuroImage 45:S173–S186.

Worsley KJ, Friston KJ (1995) Analysis of fMRI time-series revisited—again. NeuroImage 2:173–181.

Yacoub E, Shmuel A, Pfeuffer J, Van De Moortele PF, Adriany G, Andersen P, Vaughan JT, Merkle H, Ugurbil K, HU X (2001) Imaging brain function in humans at 7 Tesla. Magn Reson Med 45:588–594.

Yamada MK, Nakanishi K, Ohba S, Nakamura T, Ikegaya Y, Nishiyama N, Matsuki N (2002) Brain-derived

neurotrophic factor promotes the maturation of GABAergic mechanisms in cultured hippocampal neurons. The Journal of Neuroscience 22:7580–7585.

Yang K, Buhlman L, Khan GM, Nichols RA, Jin G, McIntosh JM, Whiteaker P, Lukas RJ, Wu J (2011) Functional Nicotinic Acetylcholine Receptors Containing 6 Subunits Are on GABAergic Neuronal Boutons Adherent to Ventral Tegmental Area Dopamine Neurons. The Journal of Neuroscience 31:2537–2548.

Yao B, Li T-Q, van Gelderen P, Shmueli K, de Zwart JA, Duyn JH (2009) Susceptibility contrast in high field MRI of human brain as a function of tissue iron content. NeuroImage 44:1259–1266.

Yarkoni T, Poldrack RA, Nichols TE, Van Essen DC, Wager TD (2011) Large-scale automated synthesis of human functional neuroimaging data. Nat Meth 8:665–670.

Yelnik J (2002) Functional anatomy of the basal ganglia. Mov Disord 17:S15–S21.

Yelnik J, Percheron G (1979) Subthalamic neurons in primates: a quantitative and comparative analysis. Neuroscience 4:1717–1743.

Yeo EJ, Cho YS, Paik SK, Yoshida A, Park MJ, Ahn DK, Moon C, Kim YS, Bae YC (2010) Ultrastructural analysis of the synaptic connectivity of TRPV1-expressing primary afferent terminals in the rat trigeminal caudal nucleus. J Comp Neurol 518:4134–4146.

Yoon JH, Minzenberg MJ, Raouf S, D'Esposito M, Carter CS (2013) Impaired prefrontal-basal ganglia functional connectivity and substantia nigra hyperactivity in schizophrenia. Biol Psychiatry 74:122–129.

Yu Y, FitzGerald THB, Friston KJ (2013) Working Memory and Anticipatory Set Modulate Midbrain and Putamen Activity. The Journal of Neuroscience 33:14040–14047.

Zander JF, Munster-Wandowski A, Brunk I, Pahner I, Gomez-Lira G, Heinemann U, Gutierrez R, Laube G, Ahnert-Hilger G (2010) Synaptic and Vesicular Coexistence of VGLUT and VGAT in Selected Excitatory and Inhibitory Synapses. The Journal of Neuroscience 30:7634–7645.

Zawadzka M, Rivers LE, Fancy SPJ, Zhao C, Tripathi R, Jamen F, Young K, Goncharevich A, Pohl H, Rizzi M, Rowitch DH, Kessaris N, Suter U, Richardson WD, Franklin RJM (2010) CNS-Resident Glial Progenitor/Stem CellsProduce Schwann Cells as well as Oligodendrocytes during Repair of CNS Demyelination. Stem Cell 6:578–590.

Zecca L, Youdim MBH, Riederer P, Connor JR, Crichton RR (2004) Iron, brain ageing and neurodegenerative disorders. Nat Rev Neurosci 5:863–873.

Zhou C, Huang Z, Ding L, Deel ME, Arain FM, Murray CR, Patel RS, Flanagan CD, Gallagher MJ (2013) Altered Cortical GABAA Receptor Composition, Physiology, and Endocytosis in a Mouse Model of a Human Genetic Absence Epilepsy Syndrome. Journal of Biological Chemistry 288:21458–21472.

Zhou J, Nannapaneni N, Shore S (2006) Vessicular glutamate transporters 1 and 2 are differentially associated with auditory nerve and spinal trigeminal inputs to the cochlear nucleus. J Comp Neurol 500:777–787.

Zwirner J, Möbius D, Bechmann I, Arendt T, Hoffmann K-T, Jäger C, Lobsien D, Möbius R, Planitzer U, Winkler D, Morawski M, Hammer N (2017) Subthalamic nucleus volumes are highly consistent but decrease age-dependently-a combined magnetic resonance imaging and stereology approach in humans. Human Brain Mapping 38:909–922.

NEDERLANDSE SAMENVATTING

In dit proefschrift beschrijf ik mijn promotieonderzoek, dat zich voornamelijk richtte op de structuur en functie van de subthalamische nucleus (STN) in de mens. De STN is onderdeel van de basale ganglia, een netwerk van kleine hersenkernen diep in het brein. De basale ganglia spelen een belangrijke rol in de controle van bewegingen en het nemen van snelle, perceptuele beslissingen. Een voorbeeld van zo'n snelle perceptuele beslissing is het herkennen van een specifiek gezicht in een groep mensen, of het wel of niet stoppen voor een oranje stoplicht. Bij patiënten met de ziekte van Parkinson functioneren de basale ganglia niet goed. Patiënten met de ziekte van Parkinson hebben bijvoorbeeld moeite met het 'starten' van bewegingen en hebben vaak ook last van tremor, een voortdurende schudbeweging van één of meerdere lichaamsdelen. *Deep Brain Stimulation (DBS)* is een belangrijke therapie bij patiënten met de ziekte van Parkinson in een vergevorderd stadium. Bij deze therapie wordt een kleine electrode aangebracht in de diepere structuren van de hersenen, meestal de STN. Deze structuren worden dan beïnvloed met elektrische stimulering via de electrode. Hoewel DBS van de STN de motor-symptomen van de ziekte van Parkinson vermindert, kunnen ook ernstige bijwerkingen optreden, zoals een achteruitgang in cognitie, depressie, en milde vormen van manie (*hypomanie*).

Volgens het *driedelige model van de STN* bestaat de STN uit drie subdivisies: een *associatief* deel, een *motor* deel, en een *limbisch* deel. Deze subdivisies zijn verbonden met specifieke gebieden aan de buitenkant van de hersen, de *cortex*. Omdat we weten dat deze gebieden in de cortex specifieke en zeer uiteenlopende functies hebben, denken sommige onderzoekers dat de verschillende subdivisies van de STN ook betrokken zijn bij specifieke functies. Het driedelige model van de STN biedt daarmee een verklaring voor de bijwerkingen van DBS: als de DBS-electrode niet alleen het motor deel, maar ook het associatieve deel of het limbische deel van de STN stimuleert, worden andere netwerken dan het motor-netwerk beïnvloed, en treden bijwerkingen op. Hoewel het driedelige model van de STN een elegante verklaring lijkt te bieden voor de bijwerkingen van DBS, is het model niet onomstreden. Als men de wat oudere wetenschappelijke literatuur grondig bekijkt, blijkt dat veel studies ook 2, 4, 5, of zelfs 10 subdivisies in de STN te beschrijven.

Vrijwel de enige manier waarop we momenteel de binnenkant van de hersenen in gezonde mensen kunnen onderzoeken is met behulp van MRI-scanners. De STN is echter relatief klein: ongeveer 100 kubieke millimeter (0.1 milliliter). Dit is ongeveer even groot als een bruine boon. Dat betekent dat de resolutie van de meeste MRI-scanners niet goed genoeg is om de STN duidelijk te onderscheiden van naburige kernen en witte stof-banen. Daar komt nog bij dat de STN ook minder goed van zijn omgeving is te onderscheiden dan gebieden in de cortex, omdat er diep in de hersen niet overal zo een consistente structuur van witte en grijze stof en cerebrospinaal vocht is als in de cortex en het cerebellum.

Een nieuwe generatie van MRI-scanners, zogenaamde *Ultra-High Field (UHF)* MRI-scanners, heeft daar verandering in gebracht. Alle MRI-scanners gebruiken een zeer sterk magnetisch veld om kleine verschillen in magnetische eigenschappen in het menselijk lichaam te visualiseren. Traditionele *3 Tesla* MRI-scanners die men in de meeste ziekenhuizen vindt, hebben een veldsterkte die ongeveer 60 000 keer zo sterk is als die van het magnetisch veld van de aarde. UHF MRI-scanners hebben een veldsterkte van ongeveer 140 000 keer die van de aarde (7 Tesla) of meer. Door die hogere veldsterkte kan men beelden van het brein maken met driedimensionale pixels (*voxels*) met een hoogte, lengte en breedte van slechts een halve millimeter. Voor mijn promotieonderzoek heb ik data verzameld met UHF MRI-scanners om

meer te begrijpen van de interne structuur van de STN en te kijken of het *driedelige model van de STN* inderdaad klopt.

Na een korte introductie begint dit proefschrift in hoofdstuk 2 met een recent *review*-artikel dat uiteenzet dat structuren diep in het brein een essentiële rol spelen in het functioneren van menselijke hersenen, maar dat ze lastig te zien zijn op standaard MRI-beelden en dat er ook maar weinig MRI-atlassen bestaan voor deze gebieden. Het laat ook zien welke technische ontwikkelingen, vooral gerelateerd aan UHF-MRI, gebruikt kunnen worden om deze situatie te verbeteren. Het stelt vervolgens dat, om de rol van diepe breinstructuren beter te begrijpen, het belangrijk is om formele, mathematische modellen van cognitie te gebruiken. Zulke formele modellen kunnen gebruikt worden om verschillen in cognitie tussen individuele proefpersonen kwantitatief te beschrijven, en deze verschillen vervolgens te relateren aan individuele verschillen in hersenactiviteit. Onze stelling is dat het relateren van individuele verschillen in cognitie en activiteit in het brein ons uiteindelijk meer kan leren over de werking van het brein, dan enkel naar hersenactiviteit te kijken, zonder formeel, kwantitatief *framework*. We stippen ook kort aan dat het beschikbaar stellen van data aan andere onderzoeksgroepen (*open data*) een veelbelovende manier is om meer MRI-onderzoekers zich op diepere breingebieden te laten richten.

Hoofdstuk 3 beschrijft een studie met een specifieke techniek, quantitative susceptibility mapping (QSM). Als je iets of iemand in het sterke magneetveld van een MRI-scanner legt, verandert de sterkte van dit magneetveld op een niet-homogene manier. QSM gebruikt speciale MRI-beelden om te kwantificeren in hoeverre het magnetisch veld verstoord wordt door specifieke gebieden in de hersenen. Er zijn allerlei eigenschappen in de hersenen die het magnetisch veld kunnen verstoren, maar vooral de aanwezigheid van ijzermoleculen kan een grote invloed hebben. We weten dat de STN veel ijzer bevat en dat de hoeveelheid ijzer in een hersengebied gerelateerd is aan het aantal en soort neuronale cellen die zich in dat hersengebied bevinden en dat het ons dus wat kan vertellen over de interne structuur van een hersengebied. De QSM-beelden die we van zowel levende proefpersonen als post-mortem weefsel hebben gemaakt, laten keer op keer zien dat de hoeveelheid ijzer groter is in het deel van de STN dat iets meer naar de binnenkant en voorkant van de hersenen ligt. Mathematische analyse van deze beelden laten zien dat de toename van ijzer in dit deel van de STN heel geleidelijk is. Nergens in de STN valt een duidelijk grens aan te wijzen tussen een 'ijzer-rijk' en 'ijzer-arm' gebied. We trekken hieruit de conclusie dat de STN niet-homogeen georganiseerd is, met mogelijke verschillende neuronale populaties, maar dat deze populaties in grote mate moeten overlappen.

In Hoofdstuk 4 wordt een studie beschreven waarin we post-mortem weefsel op verschillende manieren hebben gescand in de MRI-scanner. Ook hebben we hetzelfde materiaal behandeld met verschillende chemicaliën en daarna onder de microscoop bekeken en in digitale databestanden omgezet. Hieruit blijkt dat er verschillende soorten cellen in de STN aanwezig zijn en dat deze grotendeels langs dezelfde as als de ijzer-concentratie zijn georganiseerd (met meer cellen aan de voorkant van de STN). Mathematische analyse van de microscopische beelden laat opnieuw zien dat nergens in de STN sterke grenzen tussen neuronale populaties vallen aan te wijzen. Een veelbelovend resultaat is dat bepaalde magnetische eigenschappen die we met MRI kunnen meten kwantitatief te relateren zijn aan het soort neuronale populaties dat we met chemicaliën kunnen aantonen. Dit feit zou in de toekomst gebruikt kunnen worden om de neuronale populaties in levende proefpersonen te 'reconstrueren' aan de hand van de gemeten magnetische eigenschappen.

In de daaropvolgende hoofdstukken gaat deze thesis vooral over de functie van de STN, en niet alleen meer over de interne structuur. Zo beschrijft Hoofdstuk 5 een meta-analyse van de wetenschappelijke literatuur waarin functionele MRI (fMRI) is gebruikt. Met fMRI kan men hersenactiviteit in (diepere) hersenstructuren meten aan de hand van de hoeveelheid verbruikt zuurstof in het bloed. Het beschrijft de scanparameters en analysemethoden die men heeft gebruikt in MRI-studies die activiteit rapporteren in de STN en de direct aangrenzende subtantia nigra (SN). Uit onze meta-analyse blijkt dat de gerapporteerde activatie-coördinaten vaak niet overeenkomen met de locatie van de STN of SN in het brein zoals we die met UHF-MRI hebben gevisualiseerd. Ook laten we met simulaties zien dat de gebruikte resolutie en analysemethoden vaak niet goed genoeg zijn om onderscheid te maken tussen activatie in de STN en SN.

In Hoofdstuk 6 worden een aantal functionele MRI (fMRI)-protocollen voor 7 Tesla-scanners vergeleken. Dit soort fMRI-protocollen zouden in staat moeten zijn om hersenactiviteit in diepere hersenstructuren te meten. Echter, onze studie laat zien dat 7 Tesla fMRI-protocollen die goed werken in de cortex, niet gevoelig genoeg zijn voor hersenactiviteit in diepere breinstructuren. Dit komt waarschijnlijk omdat (a) het signaal in deze gebieden meer ruis bevat, omdat ze verder af liggen van de antennes van de scanner, (b) een belangrijke magnetische eigenschap van de STN (de *T2*-relaxatie tijd*) erg verschilt van die in cortex, vanwege de hoge ijzerconcentratie en (c) de verschillen in verbruikt zuurstof kleiner zijn in diepere breinstructuren dan in cortex. We laten zien dat een specifiek 7 T fMRI-protocol voor de STN, met een iets lagere resolutie en een aantal aangepaste parameters, wel in staat is hersenactiviteit in de STN te meten. We laten ook zien dat een fMRI-protocol op een 3 Tesla-scanner, met eenzelfde resolutie, onmogelijk in staat is om hersenactiviteit in de STN te meten.

Hoofdstuk 7 is een wat conceptueler hoofdstuk dat beschrijft hoe cognitieve hersenwetenschappers hebben geprobeerd formele, wiskundige modellen van cognitie te koppelen aan neurale metingen. We beargumenteren eerst waarom het een goed idee is om zulke mathematische modellen van cognitieve processen te gebruiken in plaats van *verbale* theoriëen en waarom ze kunnen helpen in de interpretatie van neurale data, zoals bijvoorbeeld fMRI data. Dan beschrijven we een schaal van 'losse, kwalitatieve links' tussen mathematische cognitieve modellen en neurale data naar meer 'strakke, kwantitatieve links'. We beargumenteren dat strakkere, meer kwantitatievere links beter zijn dan meer kwalitatieve links, maar waarschuwen dat er wel een aantal belangrijke voorwaarden zijn aan het gebruikte cognitieve model, voordat strakkere links überhaupt mogelijk zijn. Ook beargumenteren we dat in deze links het modelleren van de neurale data vaak een ondergeschoven kindje blijft. Zo bevat de temporele dynamiek van de neurovasculaire response die we meten met fMRI waarschijnlijk veel informatie die momenteel niet wordt gebruikt.

Hoofdstuk 8 is een empirische fMRI-studie, waarin proefpersonen een taakje moesten doen dat een model vormt voor perceptuele beslissingen. Concreet kregen de proefpersonen een "wolk" van bewegende witte puntjes te zien en de taak van de proefpersonen was om aan te geven of de wolk naar links of naar rechts beweegt. Dit taakje wordt vaak gebruikt om perceptuele beslissingsprocessen beter te begrijpen en er zijn een aantal manipulaties waarvan we weten dat ze specifieke netwerken in de hersenen beïnvloeden. Zo hoopten we door de beslissingen makkelijker en moeilijker te maken een 'associatief' netwerk aan te spreken, door verschillende geldbeloningen voor verschillende antwoorden aan te bieden een 'limbisch' netwerk aan te spreken, en door proefpersonen hun antwoord te laten aangeven met hun linker- en rechterwijsvinger hoopten we linker- en rechterdelen van het motorsysteem aan te spreken.

Echter, we vonden geen bewijs dat activiteit in de STN wordt beïnvloed door de moeilijkheid van de stimulus of met welke hand proefpersonen een responseknop indrukten. We vonden wel bewijs dat activiteit in de STN correleert met de neiging van proefpersonen om eerder een antwoord te geven dat potentieel meer geld oplevert. Echter, verschillende delen van de STN waren precies even gevoelig voor deze manipulatie. Dit suggereert dat in het domein van perceptuele beslissingen, verschillende delen van de STN geen verschillende functies hebben.

In Hoofdstuk 9 kijk ik nog een keer terug op alle voorgaande hoofdstukken. De empirische studies die beschreven zijn in hoofdstuk 3, 4, en 8 zijn lastig te vereenzelvigen met het driedelige anatomische model van de STN. Nergens vinden we bewijs voor specifiek *drie* subdivisies en als er al subdivisies zijn, moeten deze waarschijnlijk in hoge mate overlappend zijn. Ik beschrijf een aantal invloedrijke papers waar het driedelige model van de STN op is gebaseerd, en constateer dat (a) ook in eerdere literatuur er weinig bewijs is voor het specifieke aantal van drie subdivisies in de STN, (b) dat veel literatuur over de basale ganglia in z'n geheel wellicht ten onrechte wordt gegeneraliseerd naar de STN in het bijzonder, en (c) dat vrijwel alle data die tot het driedelige model heeft geleid bijzonder voorzichtig geïnterpreteerd zou moeten worden en alleen was zegt over de structuur van subregio's in de STN en niet per se over hun functie. Ik stel een alternatieve interpretatie voor waarin de STN niet een specifiek aantal subdivisies kent, maar een meer *continue, topografische* representatie van de corticale gebieden die naar de STN projecteren bevat. Zo'n interpretatie komt ook overeen met andere neurocomputationele modellen van de basale ganglia die de STN vaak een meer globale en integratieve rol toebedelen. Ik eindig het hoofdstuk met een aantal suggesties voor toekomstig onderzoek en benadruk dat met name functionele MRI in de basale ganglia, en het de STN in het bijzonder, nog zeer in de kinderschoenen staat en dat meer technologisch en methodologisch onderzoek hard nodig is.

ACKNOWLEDGEMENTS

Like all PhD projects, also my PhD project sometimes felt like the life/career equivalent of a rollercoaster, with both many ups and downs and, fortunately, a lot of fun. If anything, the putative subdivisions of the STN brought me to many corners of the world and offered me countless unforgettable experiences. Finishing my A.I. master's back in 2012, I never could have imagined being in a prestigious institute in East-Germany in the middle of a Saturday night, completely on my own, to cut up some small piece of human brain tissue and put it into a cutting-edge multi-million euro MRI machine. Nor would I have known what it feels like to delve into a subject so deep that it becomes hard to keep seeing the big picture. Above all, I never would have dared to wish for meeting so many interesting people from all over the planet as I have. Wherever you are now, know that I am truly grateful for meeting all of you.

I will now thank some people specifically.

I first have to thank my promotor professor Birte Forstmann. Without her virtually endless drive, the projects described in this thesis would have never even taken place. I also thank my co-promotor Leendert van Maanen, who already supervised me as a Master's student. Leendert: thanks a lot for calming me down on those moments that becoming a scientist seemed like a pretty hopeless enterprise and always taking the time to put things in the perspective they needed.

I also would like to thank the members of the reading committee: Pilou Bazin, Tobias Donner, James Rowe, Richard Ridderinkhof, Robert Turner, and Lourens Waldorp. You are all amazing scientists that I highly respect and I am very honored that you took the time to read (and approve) my thesis.

A big hug to all the other members of the lab. We did some great work together, merging each other's strengths and doing some truly interdisciplinary research. Max, if anyone, you are clearly the academic equivalent of my big brother, with both a healthy dose of rivalry and a long list of great joint adventures (climbing along a rocky cliff above a rough Australian sea to name just one). Wouter, I was very happy to see you again at your PhD defense, taking no prisoners in the fight for a more honest science. I am sure you will do great in your new career as well. Anneke, thanks for putting up with all my desperate sighs and frantic foot-and-finger-drumming during those long rainy Tuesday afternoons and thank you for the countless practical tips on how to start living life like a grownup. Martijn, thank you for all our nice, sometimes much-needed after-work craft beers and laidback conversations. Jasper, you are the reason I ended up at this lab in the first place and you showed me how important it is to share your knowledge as a scientist (as well as showing a spine sometimes). Thank you for that! Matthias, you left Amsterdam years ago now, but I still miss you. You were my go-to-guy for technical questions and the only fellow computer science nerd in the lab, which offered great opportunities to bitch on various monstrosities like Matlab and Microsoft Word. Dilene, thanks for keeping my feet on the ground and always being critical. Guy, thank you for your endless patience in listening to my all-over-the-place ideas. I can barely think of any people that know the techniques and literature they work on with such precision. Yael, thank you for letting me get away a little bit from this hard-to-read, introvert subcortex and letting me in on your projects on sensory processing and conflict tasks. Anne, it was such a pleasure to see you grow from an ambitious bachelor student intern to a confident PhD student. I am sure you will do great things.

A substantial part of my PhD project took place outside of the Netherlands, mostly at the Max Planck institute for Human Cognitive and Brain Sciences in the great city of Leipzig, Germany

(or "Hypezig", as they say - slightly annoyed - in Berlin). From all the amazing people at the institute, I would especially like to thank Andreas Schäfer, Robert Trampel, Marcel Weiss, Jane Neumann, Domenica Wilfing and Elisabeth Wladimirow for helping me setting up the MRI experiments, showing me how to handle post-mortem brain tissue, and pointing me to the best Döner and Currywurst places in town. Also, thank you, Sofie, Lea, Andrea, Julia, and Janis, for offering me a place to crash and making me feel a little bit more at home.

During the first year of my PhD, I helped out with a little brain stimulation study at the University of California, Berkeley and although none of the resulting work was presented in this thesis (if tDCS stimulates anything, it is most definitely not the subcortex), I still want to thank Richard Ivry and Ludovica Labruna for this amazing opportunity, as well as Ian Greenhouse for insightful chats and almost taking me surfing (I got sick when me arrived to the beach; I swear it was not that I got nervous).

From down under, Newcastle, Australia: Frini Karayanidis, your hospitality is truly inspiring. I now finally know what a *real* BBQ should look like. And thank you, Scott Brown, for sharing your unique and inspiring blend of technical competence, Australian humor and appreciation of the bigger picture.

Closer to home, at the Spinoza Centre in Amsterdam: Wietske, thank you for thinking along, back in 2014, when for a moment it seemed that we might never measure a proper fMRI signal from the STN. You made me see that MR physics is a fascinating field in its own right and treating a MRI machine like a copier with a big green button is a very bad idea (although you told me that you think a MRI machine is endlessly more simple to use than a copier). Also, thanks for giving me a little more insight into the puzzling nature of the Swiss.

Speaking of Switzerland: large pieces of this thesis were prepared and written in Basel. Thanks to Jörg Rieskamp there is no place on earth where I have been more productive. Jörg, thank you for offering me a place to work when I was there. No other office I have worked in even comes close to the Swiss serenity and efficiency of your offices at the University of Basel (during my PhD, in just over 5 years, the lab moved 7 times within the University of Amsterdam). I also would like to thank Nathaniel Phillips, Mikhail Spektor, Janine Hoffart, Sebastian Olchewski, and Gilles Dutilh for being so much fun during extended, proper lunches and crazy nights in the best karaoke bar of Europe, the simply flawless "Don't Worry Be Happy Bar".

Tomas Knapen, thanks for offering me the opportunity to start a new chapter in my academic career, studying a much more superficial (and extravert?) part of the brain. I am sure we will do great things. Also, thank you, Martijn, Martin, and Daan for being the talented bunch of young scientists that you are and that I have the pleasure of working with now.

Arjan, sorry dat ik zoveel zeurde. Ik weet ook wel dat als ik net op mijn 'werk ' aankwam en met mijn eerste beker Coffee Company Cappucino nog even nrc.nl checkte, jij al weer twee klassen betweterende pubers verder was. Bedankt voor al die fijne stukjes fietsen!

"De Nerds": Arno, Thomas, Tom. Ik heb in de wetenschap nog niemand ontmoet met zulke intellectuele scherpte, creativiteit en computer skills al jullie drie. Er zijn hele grote wetenschappers aan jullie verloren gegaan. Maar dat geeft niet, want jullie shinen alle drie op jullie eigen manier. Ons weekendje in Berlijn heeft een prachtige thesis cover en een boel plezier

opgeleverd. Ik hoop dat we nog vele avondjes zullen hacken. Met een Berliner pilsje naast de laptop en af en toe wat machinegeweer-democratie brengende op ver afgelegen planeten.

Casper, Djuna, Doortje, Leanne: weet dat Karl's Popper superbelangrijk voor mij is geweest. Er is niets dat de stress van een lange dag subverdelingen in de STN vinden zo snel kan laten verdampen als een avondje met jullie in de oefenruimte. Geen ontdekking met MRI, presentatie op een groot congres, of high-impact paper zal ook maar in de buurt kunnen komen van ons optreden met Karl's Poppers in de Grote Zaal van Paradiso.

De bèta-gamma's, met het levensgrote risico dat ik iemand vergeet: Soraya, Andrea, Jessie, Lisa, Jan-Jaap, Simen, Ids, Freek, Vincent, Zsa Zsa, Dorus, Sander, Aukje. Wat een heerlijke groep zijn wij om mee op wintersport te gaan, Sinterklaas te vieren, of gewoon te wedijveren over werkelijk alles!

Sicco, bedankt voor je luisterend oor en je grote mond. Toen ik mijn paranimfen moest kiezen was onmiddellijk duidelijk dat jij er één van zou zijn.

Pap, mam, Charlie: jullie zijn de beste familie die ik me kan wensen. Ik zou nooit zijn gekomen waar ik ben zonder jullie onvoorwaardelijke steun en liefde, juist op die momenten dat het nodig is.

Laura, 'us' is literally the only thing during my PhD time that worked out *exactly* as I hoped. You brought the most beautiful thing that there is into my life. You are the smartest, the most beautiful. Thinking back of Swiss Alps, Manhattan streets, Sicilian roads, Basler beer cafés, and crappy DDM parameters, I am amazed at how many adventures we already experienced in these three years. And this is only just the beginning.

CURRICULUM VITAE

Gilles de Hollander was born in Amsterdam on the 24th of November, 1986. Between 1999 and 2005, he attended the Vossius Gymnasium in Amsterdam and obtained a VWO (pre-university) degree with a "Science & Health" and an "Science & Engineering" profile and additional courses in Philosophy and History. In 2010, he completed the interdisciplinary "Beta-Gamma" Bachelor, with a double major in Psychobiology and Artificial Intelligence at the University of Amsterdam. Subsequently, he finished his Master's degree in Artificial Intelligence at the University of Amsterdam in 2012, with a thesis on machine learning and functional MRI in the subthalamic nucleus, under the supervision of prof. dr. Birte U. Forstmann. From 2013 to 2017 he carried out his PhD Research described in this thesis, again under the supervision of prof. dr. Birte U. Forstmann. In the summer of 2017, he started his postdoctoral research on bistable perception and laminar-resolved fMRI in the lab of dr. Tomas Knapen at the Vrije Universiteit in Amsterdam.

LIST OF PUBLICATIONS

PUBLISHED

Alkemade, A.*, **de Hollander, G.,*** Keuken, M. C., & Schäfer, A. (2017). Comparison of T2*-weighted and QSM contrasts in Parkinson's disease to visualize the STN with MRI. *PLoS ONE 12(4), e0176130*.

de Hollander, G., Keuken, M. C., van der Zwaag, W., Forstmann, B. U., & Trampel, R. (2017). Comparing functional MRI protocols for small, iron-rich basal ganglia nuclei such as the subthalamic nucleus at 7 T and 3 T. *Human Brain Mapping*, *38*(6), 3226–3248.

Salzer, Y., **de Hollander, G.**, & Forstmann, B. U. (2017). Sensory neural pathways revisited to unravel the temporal dynamics of the Simon effect: A model-based cognitive neuroscience approach. *Neuroscience and Biobehavioral Reviews*, *77*, 48–57.

Forstmann, B. U., **de Hollander, G.**, van Maanen, L., Alkemade, A., & Keuken, M. C. (2017). Towards a mechanistic understanding of the human subcortex. *Nature Reviews Neuroscience*, *18*(1), 57–65.

de Hollander, G., Labruna, L., Sellaro, R., Trutti, A., Colzato, L. S., Ratcliff, R., Ivry, R. B., Forstmann, B.U. (2016). Transcranial Direct Current Stimulation Does Not Influence the Speed-Accuracy Tradeoff in Perceptual Decision-making: Evidence from Three Independent Studies. *Journal of Cognitive Neuroscience*, *28*(9), 1283–1294.

de Hollander, G. (2016). Combining Computational Models of Cognition and Neural Data to Learn about Mixed Task Strategies. *Journal of Neuroscience*, *36*(1), 1–3.

de Hollander, G., Forstmann, B. U., & Brown, S. D. Different ways of linking behavioral and neural data via computational cognitive models. *Biological Psychiatry: Cognitive Neuroscience and Neuroimaging 1 (2), 101-109*.

Karayanidis, F., Keuken, M. C., Wong, A., Rennie, J. L., **de Hollander, G.**, Cooper, P. S., Fulham, W.R., Lenroot, R., Parsons, M., Philips, N., Michie, P.T., Forstmann, B.U. (2016). The Age-ility Project (Phase 1): Structural and functional imaging and electrophysiological data repository. *NeuroImage*, *124*(Pt B), 1137–1142.

de Hollander, G., Keuken, M. C., & Forstmann, B. U. (2015). The subcortical cocktail problem; mixed signals from the subthalamic nucleus and substantia nigra. *PLoS ONe 10(3), e0120572*.

de Hollander, G., Wagenmakers, E.-J., Waldorp, L., & Forstmann, B. (2014). An Antidote to the Imager's Fallacy, or How to Identify Brain Areas That Are in Limbo. *PLoS ONE*, *9*(12), e115700.

de Hollander, G., Keuken, M. C., Bazin, P.-L., Weiss, M., Neumann, J., Reimann, K., Wähnert, M., Turner, R., Forstmann, B.U., Schäfer, A. (2014). A gradual increase of iron toward the medial-inferior tip of the subthalamic nucleus. *Human Brain Mapping*, *35*(9), 4440–4449.

de Hollander, G., & Marx, M. (2011). Summarization of meetings using word clouds. Presented at the 2016 IEEE Second International Conference on Multimedia Big Data (BigMM).

Zwinkels, T.*, **de Hollander, G.***, & Aizenberg, T.* (2008). Knowledge in Connection: A Cognitively Grounded Social Research Approach to Understanding Change in People's Knowledge Representations During Social Interaction. *International Journal of Interdisciplinary Social Sciences*, *3*(7), 71–78.

* equal contribution

IN PREPARATION/SUBMITTED

de Hollander, G., van Maanen, L. Trampel, R., Forstmann, B.U. A model-based 7T fMRI study investigating the role of different segments of the subthalamic nucleus during perceptual decision-making (in preparation)

Alkemade, A.*, **de Hollander, G.***, Keuken, M.C., Balesar, R., Swaab, D.F., Forstmann, B.U. The functional neuroanatomy of the human subthalamic nucleus (submitted)

Salzer, Y., **de Hollander, G.**, van Maanen, L., Forstmann, B.U. Neural feature representation accounts for errors in the Simon task: an fMRI model-based study (in preparation)